

THE MOBILE DOSIMETRIC TELESCOPE

A SMALL ACTIVE DOSIMETER FOR THE APPLICATION IN SPACE

– DEVELOPMENT, CALIBRATION AND MEASUREMENTS –

Dissertation

zur Erlangung des Doktorgrades

der Mathematisch-Naturwissenschaftlichen Fakultät

der Christian-Albrechts-Universität zu Kiel

vorgelegt von

Birgit Ritter

Kiel, 2013

Erster Gutachter: Prof. Dr. Bernd Heber
Zweiter Gutachter: PD Dr. Frank Wissmann
Tag der mündlichen Prüfung: 20.06.2013
Zum Druck genehmigt: 20.06.2013

Der Dekan

ZUSAMMENFASSUNG

Das Strahlungsfeld im erdnahen Orbit und auf Reise Flughöhen unterscheidet sich signifikant von der natürlichen Strahlungsumgebung am Erdboden. In Bodennähe setzt sich diese aus radioaktiven Zerfallsprodukten, aber auch aus in der Atmosphäre von kosmischer Strahlung erzeugten Sekundärteilchen zusammen. Auf Flughöhen besteht es aus einer komplexen Mischung von geladenen und neutralen Sekundärteilchen, während es im erdnahen Orbit auf der Höhe der Internationalen Raumstation von galaktisch kosmischer Primärstrahlung, solaren Teilchen und Teilchen aus dem Strahlungsgürteln der Erde dominiert wird. Damit stellt die Strahlenexposition eines der Hauptrisiken für Langzeitaufenthalte von Menschen im All dar und muss zur Abschätzung der Gesundheitsrisiken für Astronauten kontinuierlich überwacht werden. Dafür sind derzeit passive Personendosimeter und aktive Umgebungsstrahlungsmessgeräte im Einsatz. Ein tragbares aktives Personendosimeter wäre jedoch von Vorteil. Im Rahmen dieser Arbeit wird solch ein batteriebetriebenes, auf der Basis von Siliziumdetektoren arbeitendes Personendosimeter entwickelt und charakterisiert. Die Elektronik ist an die hohen Anforderungen des Strahlenfeldes auf der Internationalen Raumstation angepasst. Absorbierte Dosis sowie Dosisraten werden in Echtzeit gemessen und auf einem Display angezeigt. Die Daten werden zusätzlich auf einer Micro SD Karte für spätere Datenauswertungen gespeichert. Das Detektorsystem arbeitet mit zwei Siliziumdioden, angeordnet zu einer Teleskopkonfiguration. Zur Berechnung der absorbierten Dosis werden alle Teilchen, die in einer Diode gemessen werden berücksichtigt. Teilchen, die beide Dioden durchqueren haben eine beschränkte Wegstrecke im Detektor und ermöglichen die Bestimmung des linearen Energietransfers, aus dem der mittlere Qualitätsfaktor des Strahlenfeldes bestimmt wird. Dieser ist ein Maß für die biologische Wirksamkeit des Strahlenfeldes und ergibt zusammen mit der absorbierten Dosis eine Abschätzung der Äquivalentdosis.

Im Laufe dieser Arbeit werden zwei Prototypen des Mobile Dosimetric Telescope (MDT), mit den Bezeichnungen MDT-01-000-DLR-CAU und MDT-01-001-DLR-CAU mit der gleichen Elektronik in unterschiedlichen Gehäusen entwickelt, charakterisiert und ihre Arbeitsweise präsentiert. Die Kalibrierung erfolgt mit radioaktiven Isotopenquellen und Schwerionen am Beschleuniger. Fragmentmessungen von Schwerionen zeigen das hohe Ansprechvermögen des entwickelten Detektorsystems. Als Praxistests werden Messungen im Flugzeug auf Reise Flughöhen durchgeführt und relevante Dosisgrößen, sowie wichtige physikalische Strahlenfeldparameter abgeleitet. Zusätzlich zeigen einfache Simulationen die Anwendbarkeit des Detektors im erdnahen Orbit.

SUMMARY

The radiation field in low Earth orbit (LEO) and at aviation altitudes differs significantly from the radiation environment on Earth's surface. On ground it is dominated by radioactive decay products as well as by secondary particles produced by cosmic radiation in the atmosphere. At aviation altitudes the radiation field consists of a complex mixture of charged and neutral secondary particles, whereas further out, e.g. in LEO at the altitude of the International Space Station, primary galactic cosmic radiation, particles from the sun and from the radiation belts around Earth play a significant role. This makes the radiation exposure one of the main hazards for the health of humans in space and poses a limiting factor for long duration space flights. Hence it is essential to continuously monitor the radiation exposure of astronauts, which is currently conducted with passive personal dosimeters and active area monitors onboard the International Space Station. Portable active devices, which can be worn by the astronaut all the time, are however desirable.

In the course of this thesis a prototype for such a small size battery driven active personal dosimeter based on silicon detector technology is developed and its working principle is verified. The electronics is designed to match the requirements of the complex radiation field in LEO. The dosimeter measures absorbed dose and dose rates and includes a real time display as well as a micro SD card for data storage. The detector system is based on two silicon diodes arranged in a telescope configuration. The absorbed dose is obtained by considering all particles measured in either of the detectors. Particles traversing both diodes are recognized as coincidence events and enable to derive linear energy transfer spectra from which the quality factor of the radiation field can be determined. The quality factor gives information on the biological effectiveness of the radiation. With the information of absorbed dose and quality factor the dose equivalent can be estimated.

In the frame of this thesis two prototypes of the Mobile Dosimetric Telescope (MDT), MDT-01-000-DLR-CAU and MDT-01-001-DLR-CAU, are developed, comprising the same electronics in different housing and their working principle is presented. The detectors are characterized and calibrated with radioactive isotope sources and heavy ions. They are intensely tested in fragmentation measurements of heavy ions proving excellent detection capabilities of densely ionizing heavy ions. Field tests onboard aircraft within the mixed radiation field at aviation altitudes are successfully performed and important dose quantities and physical parameters of the radiation field are derived. Furthermore basic simulations show the applicability of the MDT in space.

CONTENTS

Zusammenfassung	III
Summary	IV
1. INTRODUCTION	1
Structure of Thesis	3
Author's Contribution	3
2. SCIENTIFIC BACKGROUND	5
2.1. Cosmic Radiation	5
2.1.1. Galactic Cosmic Ray Spectra Near Earth	5
2.1.2. Solar Modulation of Galactic Cosmic Rays	6
2.1.3. Solar Energetic Particle (SEP) Events	8
2.1.4. Influence of the Earth's Magnetic Field	8
2.1.5. Modification of the Radiation Field by the Earth's Atmosphere	11
2.2. Interaction of Particles with Matter	12
2.2.1. Heavy Charged Particles	12
2.2.2. Electrons	13
2.2.3. Energy Loss Distribution for Charged Particles	14
2.2.4. Photons	15
2.2.5. Neutrons	16
2.2.6. Shielding	17
2.3. Radiation Protection	17
2.3.1. Dose Quantities	18
2.3.2. The Radiation Exposure at Aviation Altitudes and in Low Earth Orbit (LEO)	21
2.3.3. Dosimeters	22
3. THE MOBILE DOSIMETRIC TELESCOPE	25

3.1.	Functional Description	25
3.1.1.	Functional Requirements	25
3.1.2.	Derived Requirements for the Detector Design	25
3.2.	Detector Design	27
3.3.	Development	30
3.4.	Electronics – Principle of Operation	33
3.4.1.	Power Supply	33
3.4.2.	Ground Planes	35
3.4.3.	Silicon Detectors	35
3.4.4.	Analog Electronics	36
3.4.5.	Digital Electronics	37
3.5.	Mechanical Setup of the Prototypes	40
3.5.1.	First Prototype: MDT-01-000-DLR-CAU	40
3.5.2.	Second Prototype: MDT-01-001-DLR-CAU	41
3.6.	Countermeasure for microphonic effects	42
3.7.	Characterization	45
3.7.1.	Resolution	45
3.7.2.	System Linearity	45
3.7.3.	Telescope and Geometry Factor	47
3.8.	Summary	50
4.	CALIBRATION	51
4.1.	Measurements with Radioactive Isotope Sources	51
4.1.1.	Americium-241	52
4.1.2.	Bismuth-207	54
4.2.	Measurements with Heavy Ions	55
4.2.1.	Irradiations	55
4.2.2.	Pulse Height Spectra and Fitting	57
4.3.	Calibration of the MDT	60
4.3.1.	High Gain	60
4.3.2.	Low Gain	61
4.3.3.	Results	63
5.	FRAGMENT MEASUREMENTS	65
5.1.	Measurements	65
5.2.	Results	67

5.2.1. Energy Depositions	67
5.2.2. Charge Identification	68
5.2.3. Test of the Linear Calibration Curve	70
5.2.4. Energy Loss Uncertainties	71
5.3. Summary	73
6. FLIGHT MEASUREMENTS	75
6.1. Materials and Methods	76
6.1.1. Measurements	76
6.1.2. Data Analysis	78
6.2. Long Distance Flights	80
6.2.1. Solar Activity During Flight Period	81
6.2.2. Count Rates	82
6.2.3. Altitude and Cutoff Rigidity Dependence of Count Rates	87
6.2.4. Dose Rates	96
6.2.5. Energy Deposition Spectra	103
6.2.6. LET Spectra	110
6.2.7. Absorbed Dose, Quality Factor, and Dose Equivalent	111
6.3. Summary	116
7. SIMULATIONS	119
7.1. Materials and Methods	119
7.2. Results	121
7.2.1. Energy Deposition of Coincidence Events	121
7.2.2. Dependence on Ion Energy	124
7.2.3. Comparison with Measurements	125
7.3. Summary	126
8. CONCLUSION	127
BIBLIOGRAPHY	133
LIST OF DATASHEETS	141
LIST OF ABBREVIATIONS	143
LIST OF FIGURES	149

LIST OF TABLES	151
APPENDIX A. MDT – DEVELOPMENT STEPS	155
APPENDIX B. MDT – CIRCUIT DIAGRAMS, TECHNICAL DRAWINGS, TABLES	161
APPENDIX C. CALIBRATION – FIGURES	173
APPENDIX D. CALIBRATION – TABLES	185
APPENDIX E. FLIGHT MEASUREMENTS – FIGURES	189
E.1. Count Rates	189
E.2. Dose Rates	194
E.3. Energy Deposition Spectra	196
E.4. Linear Energy Transfer Spectra	206
APPENDIX F. FLIGHT MEASUREMENTS – TABLES	211
APPENDIX G. ADDITIONAL FLIGHT MEASUREMENTS	213
G.1. First System Check	213
G.2. Periodic Behaviour of Count Rates	215
G.2.1. Count Rates of Parabolic Flight	215
G.2.2. Count Rates of Long Distance Flights	218
ACKNOWLEDGEMENT	221
CURRICULUM VITAE	223
EIDESSTÄTTLICHE ERKLÄRUNG	227

INTRODUCTION

In 1912 Viktor Franz Hess proved with his seventh balloon flight that the intensity of ionizing radiation increases with increasing altitude and deduced that the radiation source must be of extraterrestrial origin ("*...Die Ergebnisse der vorliegenden Beobachtungen scheinen am ehesten durch die Annahme erklärt werden zu können, daß eine Strahlung von sehr hoher Durchdringungskraft von oben her in unsere Atmosphäre dringt...*", Hess 1912). For his discovery of cosmic radiation he was awarded the Nobel prize in Physics in 1936. Exactly a hundred years after Hess' balloon flight the first man-made radiation detector (MSL/RAD) landed on Mars providing the first measurements of the radiation environment on the surface of another planet in our solar system (Hassler et al., 2012).

By now it is clear that the radiation exposure in space is one of the main hazards to human space flight, besides the influence of microgravity and psychological effects. First evidence of the effect of highly ionizing radiation was reported by astronauts of the Apollo 11 mission, when they observed light flashes in eyes every few minutes after a certain time of dark adaptation, resulting from the direct interaction of strongly ionizing radiation with the retina (Narici et al., 2004). Also a slight increase in the development of cataracts in astronauts is an effect observed in this context (first reported by Cucinotta et al. 2001). Despite the numerous biological experiments, the consequences of a continuous exposure are still not well understood and are subject to ongoing research. Hence the radiation environment onboard the International Space Station (ISS) is continuously monitored by radiation detectors for dosimetric purposes ensuring a solid risk estimation for astronauts.

But also the the investigation of fundamental physics and physical processes that can be deduced from sophisticated measurements of the radiation field are of great interest as the universe provides this unique experimental laboratory space in which processes can be observed that are not possible to investigate on Earth. An example is the Alpha Magnetic Spectrometer Experiment (AMS)¹ onboard ISS.

¹<http://www.ams02.org/>

The complexity and the huge energy range of the radiation field is however challenging for every radiation detector system, which is why detectors have to be designed carefully to match the requirements of their application in space.

Figure 1.1 gives an impression that cosmic radiation can not only pose a threat to the health of humans and provide exciting physics, but is occasionally also of great beauty. Solar wind particles can penetrate along the magnetic field lines of Earth deeper into the atmosphere, and produce visible light by the interaction with mainly oxygen atoms of the atmosphere. The resulting spatial patterns are not well understood yet, but fascinate nevertheless when observed from the Earth's surface as well as from space. The photograph of the Aurora Australis has been taken by an astronaut onboard the ISS above the southern Indian ocean.



Figure 1.1.: Aurora Australis photographed by an astronaut of the Expedition 29 crew members onboard the International Space Station on 17 September 2011. Image credit: NASA Human Space Flight Gallery².

The aim of this thesis is to develop as small size active radiation detector that can serve as an astronaut's dosimeter. As the verification in space is not easy to perform, measurements at a heavy ion accelerator facility and in aircraft at aviation altitudes are performed with the developed prototypes.

²<http://spaceflight.nasa.gov/gallery/images/station/crew-29/html/iss029e005904.html>

STRUCTURE OF THESIS

The following Chapter 2 gives a brief overview of the scientific context this work is embedded in. In Chapter 3 the development steps and the working principle of the developed detector, the Mobile Dosimetric Telescope (MDT), is introduced and the detector system is characterized. Subsequently Chapter 4 presents the calibration of the device, Chapter 5 and Chapter 6 show the performance of the MDT during measurements in an artificial mixed radiation field of heavy ions, created by fragment production from iron ions, and during measurements in the natural complex radiation field of Earth's atmosphere at cruising altitudes, respectively. In order to introduce the application of the MDT in space, Chapter 7 describes basic simulations of the detector in the radiation environment in space. Eventually Chapter 8 summarizes important results acquired in this thesis and emphasizes the importance of the in the frame of this thesis developed device.

The appendices provide additional information, like a detailed description of the development steps of the MDT (Appendix A) as well as circuit diagrams and mechanical drawings of the detector system (Appendix B). For completeness Appendices C to F give results in figures and tables for calibration and flight measurements, respectively, and Appendix G presents additional flight measurements.

AUTHOR'S CONTRIBUTION

The development of the electronics of the detector system proceeded in close collaboration with Karel Maršálek until board version 06.01 (Section 3.3) and afterwards by the author only. The author participated from the beginning in all respective tasks including designing of circuit diagrams and electronics board layouts, soldering, programming of microcontroller, testing of electronics, etc.

The mechanical design of prototype MDT-01-001 (Section 3.5) was developed together with Joachim Aeckerlein, who then created the CAD (computed-aided design) models and organized the manufacturing.

Simulations (Section 3.7.3 and Chapter 7) were supported by Jan Köhler, as stated in the corresponding sections.

All measurements, i.e. characterization of electronics (Section 3.7), calibration (Chapter 4), fragment (Chapter 5) and flight measurements (Chapter 6) and all data evaluation have been solely performed by the author.

SCIENTIFIC BACKGROUND

In the first section of this chapter the radiation environment and its respective sources in space and in the Earth's atmosphere (Section 2.1) are outlined. The subsequent section gives an overview of interaction processes of radiation with matter (Section 2.2) and in Section 2.3 some information for radiation protection purposes is presented with a focus on the radiation exposure onboard the International Space Station (ISS). The overviews are kept short to serve mainly as a reminder as there is numerous literature available, covering all topics discussed in a detailed manner. The corresponding references and reviews are given in the text.

2.1. COSMIC RADIATION

Earth is continuously bombarded by cosmic radiation of different origin. This radiation is modulated by the Earth's magnetic field and interacts with its atmosphere. In the consequence, the radiation field changes in energy, intensity and composition, depending on the position within the magnetosphere and atmosphere as well as on the altitude. The main components of the cosmic radiation close to Earth are galactic cosmic rays (GCR), solar wind, solar energetic particles (SEPs) and trapped radiation.

2.1.1. GALACTIC COSMIC RAY SPECTRA NEAR EARTH

GCR originate from outside the solar system and consist of 98 % nuclei and 2 % electrons. The hadronic component is composed of 87 % protons, 12 % Helium nuclei and of about 1 % heavier nuclei up to uranium, i.e. all stable nuclei are present (Simpson, 1983). Figure 2.1 shows typical energy spectra of selected ions in detail. For all species the energy spectra above a few GeV follow a power law over ten orders of magnitudes. Due to modulation of the lower energetic particles in the heliosphere (for a review see Potgieter 2011) the energy spectra show a maximum around 1 GeV u^{-1} . As it has been recently confirmed for example by the Fermi-LAT (Large Area Telescope)

experiment (e.g. Ackermann et al. 2013 and references therein), GCR are produced by supernovae, accelerated in their shock fronts to high velocities, and impinge nearly isotropically on Earth.

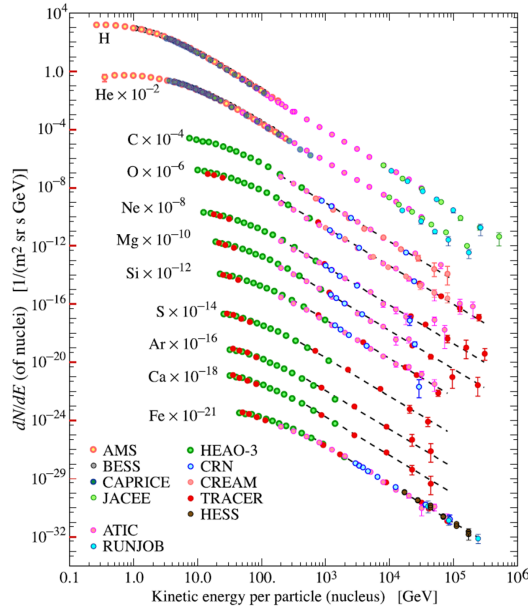


Figure 2.1.: Galactic cosmic ray fluxes for selected heavy ions. Figure credit: Particle Data Group (Beringer et al. (PDG), 2012a).

2.1.2. SOLAR MODULATION OF GALACTIC COSMIC RAYS

The sun emits continuously electromagnetic radiation as well as a stream of particles, the so-called solar wind (Biermann 1951, Parker 1958). It consists mainly of electrons, protons and few helium ions of low energies in the eV up to the keV range. The magnetic field of the sun is frozen in the solar wind and the region in space dominated by the solar wind interacting with the local interstellar medium is called the heliosphere. Due to small scale turbulences in the expanding solar wind and drifts in the large scale interplanetary magnetic field, the GCR spectrum is modulated within the heliosphere (a recent review is given by Heber 2011).

The sun follows a quasi periodic eleven year solar activity cycle that is reflected in the number of observed sunspots (Schwabe, 1843). It is induced by the reversal of the solar magnetic field about every eleven years. During the reversal process

the sun becomes more active showing an increased number of SEP events (next section). The resulting approximate 22-year solar magnetic cycle in which the sun returns to its previous magnetic field polarity was identified by Hale and Nicholson (1925) and is also called the Hale cycle. Neutron monitor count rates serve as a measure of GCR (e.g. Simpson 2000) and reflect both periodicities. Figure 2.2 shows the anti-correlation of sunspots and neutron monitor count rates in the eleven year solar cycle as due to stronger modulation of GCR during solar maximum the GCR intensity reduces. The neutron monitor count rates show additionally the 22-year magnetic cycle, visible in the alternately different count rate profile during solar minimum conditions. In times in which the solar magnetic field points towards sun in its northern hemisphere (e.g. in the 1960s, 1980s and during the last solar minimum), the neutron monitor count rates are more peaked than during times of the remaining solar minima shown in the figure, where the profile is flatter. These features arise as the solar magnetic field influences the drift direction of positively charged particles depending on the polarity of the sun. Detailed investigations and reviews can be found for example in Heber and Potgieter (2006), Potgieter et al. (2013) and references therein.

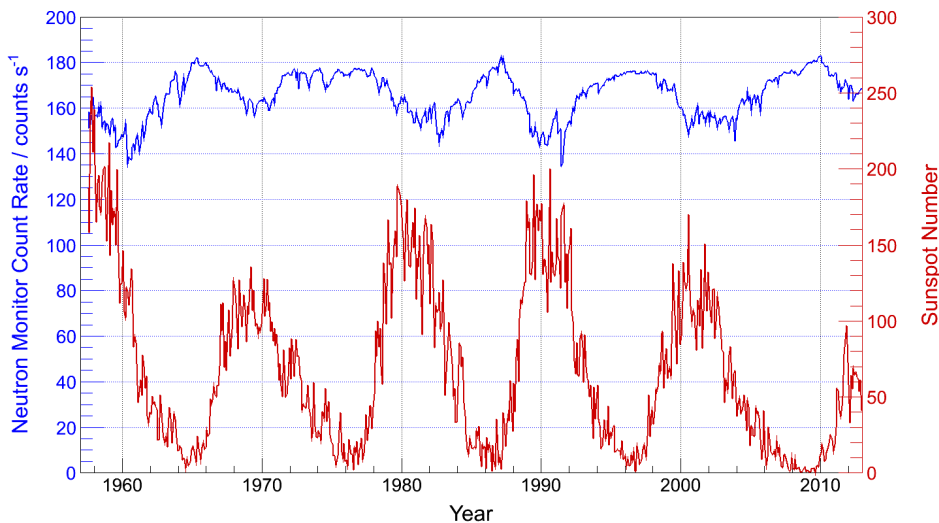


Figure 2.2.: The monthly averaged neutron monitor count rate from the neutron monitor in Kiel (data taken from <http://www.nmdb.eu>) as an indicator for GCR is shown in blue and the monthly averaged sunspot number (SIDC-team 1957-2012, <http://sidc.oma.be/sunspot-data/>) is shown in red.

2.1.3. SOLAR ENERGETIC PARTICLE (SEP) EVENTS

During solar maximum conditions an increased number of SEP events is observed. In the course of these events solar particles (i.e. mainly protons, electrons and few heavier particles) of high energies up to the GeV range are generated. Due to their energies and high intensities, SEP events could be immediately lethal to an astronaut floating in free space (Hellweg and Baumstark-Kahn, 2007). Depending on the magnetic field line geometry that determines the direction of travel of the particles and depending on the particle energy, SEPs can be detected by neutron monitors on ground in so-called Ground Level Events (GLE). SEP events can strongly influence the radiation environment in low Earth orbit (LEO) and can even affect the radiation exposure at aviation altitudes (compare Section 2.3.2).

2.1.4. INFLUENCE OF THE EARTH'S MAGNETIC FIELD

GEOMAGNETIC CUTOFF RIGIDITY

The Earth magnetic field has a shielding effect from charged particles (e.g. Smart and Shea 2005). In order to quantify the penetration ability of charged particles into the geomagnetic field, the magnetic rigidity R of the corresponding particle can be defined by

$$R = \frac{pc}{q}, \quad (2.1)$$

where pc is the momentum of the particle in electron volt and q its charge. Hence R is given in V or usually in GV. All particles with the same magnetic rigidity follow the same trajectory within a magnetic field. The geomagnetic cutoff rigidity R_c is defined as the minimum magnetic rigidity a particle requires to still penetrate the geomagnetic field. As it depends on the angle of incidence of the particle, it is usually referred to the vertical geomagnetic cutoff rigidity, assuming perpendicular incidence.

Figure 2.3 shows in contour lines the geomagnetic cutoff rigidity plotted on a world map. R_c ranges from 0 GV at the poles to 18 GV above India. The observed asymmetry coincides with a tilt in the geomagnetic dipole field component of Earth, discussed in the next paragraph. Figure 2.4 outlines impressively how the energy spectra of protons from the low energy part on are modulated in dependence of the particle rigidity (here given in GV c^{-1}) and on the shell parameter L . L is given by the distance of a magnetic field line from the center of Earth in the geomagnetic equatorial plane in units of Earth radii (e.g. Prölss 2004) and for a given altitude it is a measure of the

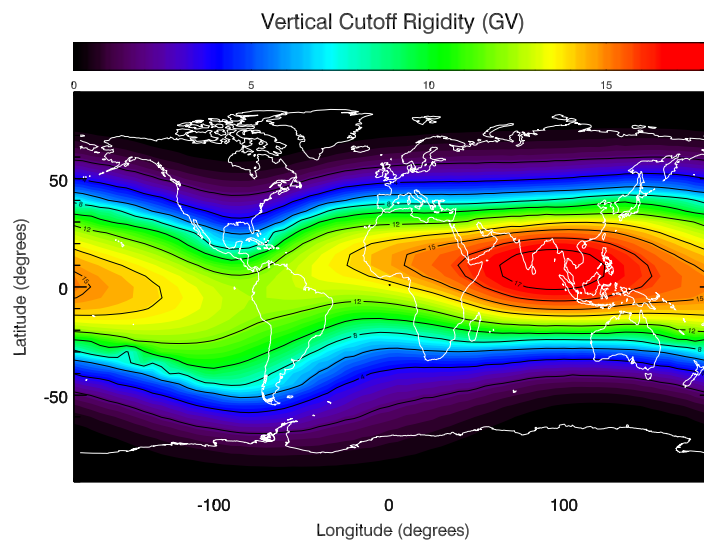


Figure 2.3.: Geomagnetic cutoff rigidity for the year 2010 at an altitude of 20 km. Figure credit: Herbst (2012).

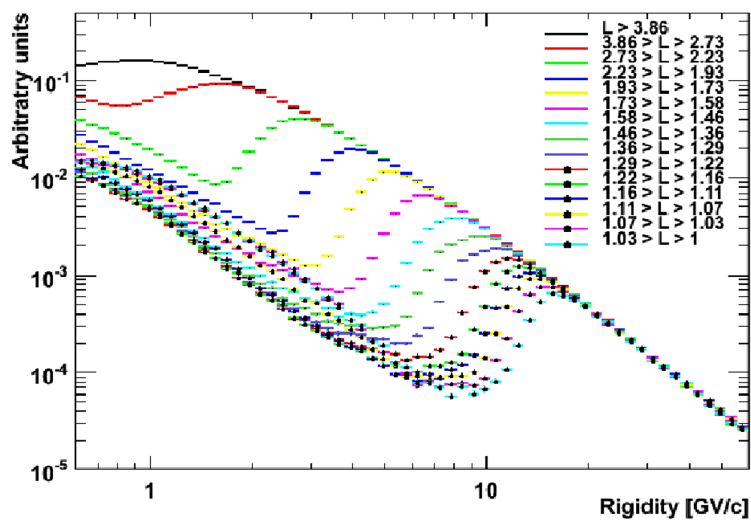


Figure 2.4.: Proton flux in dependence of the geomagnetic cutoff rigidity for different L-values measured by PAMELA. Figure courtesy: Picozza et al. (2013).

geomagnetic latitude. These measurements have been obtained with the PAMELA experiment (Payload for Antimatter Matter Exploration and Light-nuclei Astrophysics, e.g. Mocchiutti et al. 2009) at altitudes between 350 km and 610 km.

RADIATION BELTS

Cosmic radiation and albedo particles from the Earth's atmosphere can be trapped in the Earth's magnetic field. As a result, two radiation belts are formed that were discovered in 1958 (e.g. van Allen et al. 1959) and named after their discoverer van Allen. The inner van Allen belt consists mainly of protons of energies up to 600 MeV, whereas in the outer radiation belt predominantly electrons of energies up to 7 MeV are found (for a review see e.g. Reitz 2008). The high energetic part of the radiation belts is assumed to be generated by decaying neutrons that were produced in interactions of GCR with the atmosphere, referred to as the CRAND (Cosmic Ray Albedo Neutron Decay) process (Singer 1958a, Singer 1958b). Especially the outer belt is variable and highly influenced by the solar activity, e.g. SEP events.

Due to a tilt of the geomagnetic dipole axis towards the rotation axis by 11° and a displacement of their interception of about 500 km to the North with respect to the center of Earth, the proton belt reaches down to 200 km above the Eastern coast of South America, resulting in the so-called the South Atlantic Anomaly (SAA). The radiation belts are not of strong interest for aviation altitudes, but the International Space Station orbits Earth at altitudes between 350 km and 400 km with an inclination of 51.6° and passes the SAA five to six times per day (compare e.g. Wilson et al. 2007 and Section 2.3.2).

Figure 2.5 shows the van Allen belts at altitudes between 350 km and 610 km mapped

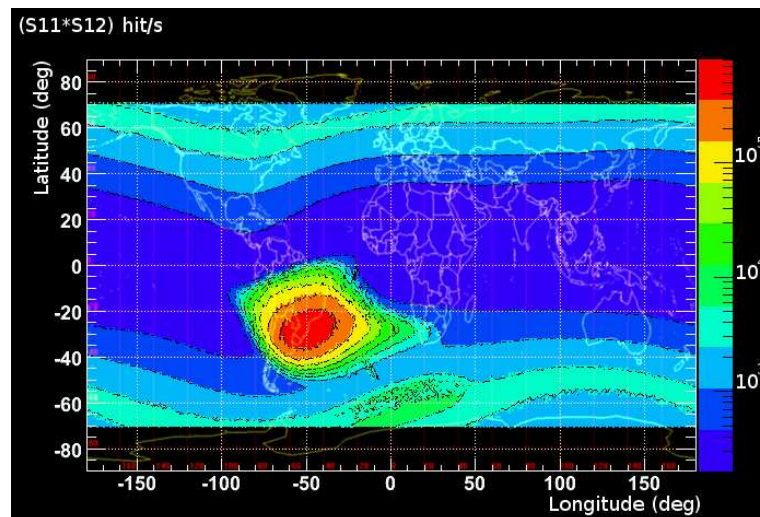


Figure 2.5.: Intensity of radiation belts, mapped by PAMELA (Picozza et al., 2013).

by the PAMELA experiment. At high latitudes the edges of the electron belt and above the South Atlantic in the region of the SAA the proton belt are visible.

2.1.5. MODIFICATION OF THE RADIATION FIELD BY THE EARTH'S ATMOSPHERE

Interaction of cosmic radiation with the atmosphere causes electromagnetic and hadronic cascades in which secondary particles are produced. An overview of some possible interaction processes involved for the individual particle species is given in the next section (Section 2.2). The particle flux in the atmosphere increases with increasing atmospheric depth, reaching a maximum in the first 100 g cm^{-2} , the so called Pfozter maximum (Pfozter, 1936). Below, the flux decreases continuously, as energy losses, absorption and decay processes dominate. Three major components of the mixed radiation field are distinguished, the hadronic, the photon-electron, and the muon component. The hadronic component arises from strong interactions of primary radiation with nuclei of atmospheric atoms. It therefore consists mainly of primary and secondary protons, neutrons and pions, but also kaons and hyperons are found. Photons and electrons are mainly produced in electromagnetic cascade showers that can be initiated from the decay of neutral pions. Muons are decay products of charged pions.

At aviation altitudes between 5 km and 12 km above ground, the radiation field consists of few primary particles and a number of secondaries and decay products, including for example photons, protons, electrons and positrons, neutrons, and muons (a recent overview is given by Beringer et al. (PDG) 2012a).

Due to their relativistic speed, muons can reach the surface of Earth before they decay and hence make the main component of galactic cosmic radiation secondaries above 100 MeV that can be observed on ground. Their decay products, electrons, contribute significantly to the hard component of the radiation field. Including also particles of lower energies, neutrons represent the main component at sea level with a broad energy distribution continuing also to high energies.

For this highly complex radiation field an extended compilation of existing data for the fluxes of individual particle species in dependence on the altitude and on their energies is provided by Grieder (2001).

2.2. INTERACTION OF PARTICLES WITH MATTER

The performance of every radiation detector depends on the interaction of the incoming radiation with the detecting material. The energy the particle loses during these interaction processes contributes to the signal of the detector.

Charged particles mainly lose energy due to ionization and bremsstrahlung, hadrons, including neutrons, interact also via nuclear processes, while photons follow the cross-sections for photo effect, Compton effect, and pair production.

In this section, heavy charged particles, electrons, photons, and neutrons are briefly discussed, also considering the interaction of each of these particles with silicon, as silicon serves as the particle detection material in this work.

If not stated otherwise, the descriptions follow the text books from Leo (1994), Knoll (1999), and Musiol et al. (1988).

2.2.1. HEAVY CHARGED PARTICLES

IONIZATION LOSSES

The interactions of charged particles with the absorbing material are dominated by coulomb interactions with the electrons of the target material. If these electrons can be assumed to be free and initially at rest compared to the incoming particle, the mean energy loss is described by the Bethe-Bloch formula, given in Equation 2.2.

$$-\frac{dE}{dx} = 2\pi N_a r_e^2 m_e c^2 \rho \frac{z}{A} \frac{Z^2}{\beta^2} \left[\ln \left(\frac{2m_e \gamma^2 v^2 W_{\max}}{I^2} \right) - 2\beta^2 - \delta - 2\frac{C}{z} \right], \quad (2.2)$$

where

N_a	Avogadro's number	Z	charge of incoming particle
r_e	classical radius of electron	v	velocity of incoming particle
m_e	mass of electron	β	v/c
ρ	density of target material	γ	$1/\sqrt{1-\beta^2}$
z	charge number of target material	W_{\max}	maximum energy transfer in single collision
A	mass number of target material	C	Shell correction
I	mean excitation potential	δ	Density correction
c	speed of light		

Two important additions are included here. At low energies, where the electrons of the absorbing material cannot be considered to be at rest, since the particle velocity is close to the orbital velocity of the electrons, the shell correction C is applied. It accounts for possible electron capture and therefore a lower effective charge of the incoming particle resulting in less energy loss. This correction is generally small. The density correction δ for high energies considers the polarization of the absorbing material along the path due to the electric field of the incoming particle. Hence more distant electrons are shielded from this electric field leading to a saturation of the energy loss. This effect becomes more important with denser materials.

FRAGMENTATION

Charged hadrons additionally lose energy by nuclear interactions, but these cross-sections are small compared to the energy loss by coulomb interactions. One possible interaction for direct nucleus-nucleus collisions of high energetic heavy ions is fragmentation, either of the projectile or of the target material nucleus or both. A commonly used model to describe the projectile fragmentation process in two stages is the abrasion-ablation model (e.g. Hüfner et al. 1975). When relativistic heavy ions collide, nucleons in the overlapping volume are sheared away (abrasion). The remaining part of the now excited heavy ion continues its path basically undisturbed with the same velocity as before. De-excitation of the fragment takes place through emission of one or several neutrons, protons and light nuclei as well as by fission and emission of gamma rays (ablation). While the production of fragmentation products that lost only few nucleons is attributed to peripheral collisions, complex break-up processes resulting in multi-fragmentation are mainly due to central nucleus-nucleus collisions (Gaimard and Schmidt, 1991). The probability of projectile fragmentation increases with increasing mass number of the target material (Westfall et al., 1979). Other than relativistic projectile fragments, fragments produced from the target material are short ranged. A comprehensive summary is for example given by the NCRP Report No. 153 (2006).

2.2.2. ELECTRONS

The description of the energy loss of electrons due to collisions requires certain modifications of the Bethe-Bloch formula. The incidence particle and the electron of the absorber material have the same masses, leading as one consequence to large deviations in the travel path. Furthermore the two collision partners need to be treated as

quantum-mechanically undistinguishable particles.

Additional to the collisional energy loss, bremsstrahlung needs to be considered. In general, every charged particle accelerated in a coulomb field loses energy through bremsstrahlung, but since this energy loss is inversely proportional to the mass m of the particle by m^{-2} , it is mainly important for electrons and positrons, respectively. The total energy loss is therefore written as sum of these two described terms

$$\left(\frac{dE}{dx}\right)_{\text{total}} = \left(\frac{dE}{dx}\right)_{\text{col}} + \left(\frac{dE}{dx}\right)_{\text{brems}}. \quad (2.3)$$

While losses due to ionization dominate at lower energies, bremsstrahlung is important at high energies, but also depend on the target material as it is proportional to Z^2 . The point, at which the two losses are equal is called critical energy E_c . In silicon, the critical energy is $E_c \approx 20 \text{ MeV}$. The critical energy for the next lighter charged particle, i.e. muons, lies at several hundred GeV.

2.2.3. ENERGY LOSS DISTRIBUTION FOR CHARGED PARTICLES

Charged particles lose energy along their path of travel by a large number of interactions. The number of collisions is subject to statistical fluctuations and the energy transfer can differ enormously in each collision. For a relatively long path length, the number of collisions is sufficiently large so that the energy loss distribution in the material results in a Gaussian distribution according to the central limit theorem. If the path length is restricted, e.g. by a thin detector, an asymmetric distribution is observed in which the mean energy loss does not coincide with the most probable energy loss that is found at lower energies than the mean. Rare events of large energy transfers in a single collision add to a long tail towards high energies. Under the assumption that in all individual collisions the electron of the target material can be considered to be free, that the energy transfer of the incoming particle is small compared to the particles energy, i.e. it does not slow down, and that the maximum energy transfer W_{max} in a single collision is infinite, Landau (1944) calculated the energy loss distribution for thin targets meaning a small number of collisions. In this theory, the mean energy loss is an ill-defined quantity. Vavilov (1957) extended this approach by inserting the real expression for the maximum energy transfer in order to describe energy losses for larger path lengths in which the number of collisions is still too low to approach a Gaussian distribution. It is convenient to define the parameter κ to decide which approach is suitable for a given application:

$$\kappa = \frac{\bar{\Delta}}{W_{\max}}, \quad (2.4)$$

where $\bar{\Delta}$ is the mean energy loss and W_{\max} the maximal energy transfer in a single collision as given in Equation 2.2.

For $\kappa \leq 0.01$ the Landau distribution is an appropriate approximation, for intermediate κ the approximation presented by Vavilov leads to good results, while for $\kappa \geq 10$ the energy loss distribution converges a Gaussian shape.

Figure 2.6 shows the energy loss distribution of oxygen ions with an energy of 400 MeV u^{-1} in a $300 \mu\text{m}$ thick silicon detector. The blue curve shows a fit according to Landau's theory, in green the Gaussian distribution is plotted. The Vavilov theory (shown in red) describes the distribution best with $\kappa = 0.6$. For fitting the data analysis software *ROOT* (Brun and Rademakers, 1996) was employed.

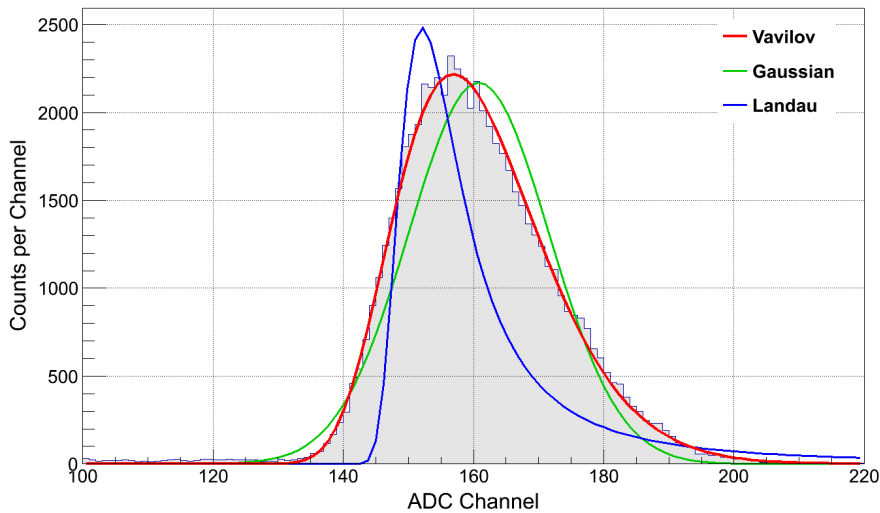


Figure 2.6.: The grey histogram shows the energy loss distribution of oxygen ions with an energy of 400 MeV u^{-1} in a $300 \mu\text{m}$ thick silicon diode. The colored curves show fit results for three different distribution theories. The Vavilov fit results in $\kappa = 0.6$.

2.2.4. PHOTONS

Other than charged particles, photon beams are not degraded in energy but attenuated in intensity as they traverse matter. All interactions that are discussed will either absorb the photon energy completely or remove the photon from the beam by scattering. This attenuation is given by an exponential behaviour.

Photons interact with matter via photo effect, Compton scattering or pair production, depending on their initial energy and on the absorber material. Interactions of a low energetic photon via photoelectric absorption can only occur with a bound electron of an atom in the target material because of momentum conservation. The photon transfers all energy to the electron and disappears completely. The cross-section for the photo effect is proportional to Z^n of the absorber, where n varies between 4 and 5.

Photons of intermediate energy undergo Compton scattering with electrons of the absorbing material. Thereby the photon is deflected from its incident direction and a part of its energy is transferred to the electron. The probability for this interaction increases with increasing Z of the target material.

As soon as the photon energy exceeds twice the rest-mass of electrons (1.022 MeV) pair production can occur, although this interaction becomes more important at higher energies. The photon interacts with the coulomb field of the atoms in the target material and is replaced by an electron-positron pair that undergoes further electromagnetic interactions in the absorber.

For silicon as target material, the photoelectric absorption dominates for photon energies below 60 keV. For intermediate energies the attenuation is dominated by the Compton effect, which is superseded by the pair production cross-section for photon energies higher than 15 MeV (calculated with *XCOM*¹, Berger et al. 1998).

2.2.5. NEUTRONS

Neutrons interact with the nucleus of the absorber material through short ranged forces. These interactions occur rarely compared to coulomb interactions by charged particles, but the energy transfer can be large. Energy or direction of the neutron is either changed significantly or it is replaced by secondary radiation that mostly consists of heavy charged particles depositing large amounts of energy in the detection material. Therefore, like for photons, a beam of neutrons is attenuated exponentially in intensity.

The interaction processes of neutrons are complex and dependent on their initial energy, but it can be distinguished between neutron-induced reactions, like (n,p), (n, α), (n,fission) or radiation capture, and elastic scattering. In a crude simplification, elastic scattering is more probable for fast neutrons with energies above 0.5 eV. The energy transfer to the collision partner E_R is described by

¹Photon Cross Section Database, <http://www.nist.gov/pml/data/xcom/index.cfm>

$$E_R = \frac{4A}{(1+A)^2} \cdot \cos^2 \theta \cdot E_n, \quad (2.5)$$

where E_n is the neutron energy, A is the mass number of the absorbing material and θ the incident angle. The expression becomes maximal for head-on collisions, where $\theta = 0$. A fast neutron can therefore lose all its energy in one collision with a hydrogen nucleus. For a silicon detector with $A_{Si} = 28$, the maximal energy transfer is about 13% of the neutron energy.

In detectors designed to measure neutrons, fast neutrons are moderated by proton-rich materials to energies in which nuclear reactions dominate and their secondary radiation is detected by proportional counters.

2.2.6. SHIELDING

Considering the interaction of GCR nuclei with shielding material for example on-board ISS, the shielding material should fulfil certain criteria. While fragmentation of GCR ions is desired as the energy loss by ionization decreases with lower charge number, the fragmentation of the shielding material is to be omitted to not create short ranged fragments. Furthermore the production of neutrons as well as the production of electron-positron pairs should be kept as low as possible. The best match for these requirements is a material with a low mean atomic mass (e.g. Sihver 2008). Plastic material with a high hydrogen content, like for example polyethylene (CH_2), provide a good compromise in this context.

2.3. RADIATION PROTECTION

When a human is exposed to ionizing radiation, radiation protection measures are necessary because of biological effects due to the interaction of the ionizing radiation with cellular DNA. Depending on the dose, these effects can either be deterministic or stochastic. While sparsely ionizing radiation rather results in single strand breaks, high energetic heavy ions often lead to double strand breaks in the double helix. Despite the fact that cells have efficient repair mechanisms (e.g. Hall and Giaccia 2011), especially in cases of an increased number of double strand breaks, these mechanisms can fail. Besides the desired error-free repair, possible biological endpoints are misrepair and cell death. Is the number of dead cells due to ionizing radiation significant, deterministic effects like radiation sickness occur. Exposure with low doses below deterministic thresholds are described by stochastic effects. In these

cases misrepair is worse than cell death, as it can lead to mutations that may result in late effects like tumor development or genetic defects. Stochastic effects can occur after a latency and their probability increases with increasing dose. An extended overview of the effects of ionizing radiation is given by Hellweg and Baumstark-Kahn (2007).

The International Commission on Radiological Protection (ICRP) is an independent organisation that aims to quantify and to estimate the severity of these effects and gives recommendations on limits for the exposure of radiation workers. In order to follow these recommendations the International Commission on Radiation Units and Measurements (ICRU) created a framework of units, guidelines of measurement techniques and working procedures that is continuously updated.

Considering especially the radiation exposure of astronauts in LEO, the National Council on Radiation Protection and Measurements (NCRP) published reports with guidelines and recommendations, NCRP Report No.132 (2000) and NCRP Report No.142 (2002).

In the following a number of dose quantities is introduced, the radiation exposure in space is described in more detail and an overview of the means of execution for radiation protection in space, i.e. dosimeters, is presented.

2.3.1. DOSE QUANTITIES

This section is supposed to give a short overview of only some of the commonly used dose quantities, as these will be applied later in this work. The description follows mainly the ICRU Report 84 (2010), where also a more detailed and extended summary of dose quantities can be found.

ABSORBED DOSE

The **absorbed dose** D describes the mean energy $d\bar{\epsilon}$ that is imparted in the mass element dm by ionizing radiation

$$D = \frac{d\bar{\epsilon}}{dm}. \quad (2.6)$$

Its unit is J kg^{-1} , but is usually named gray (Gy), where $1 \text{ Gy} = 1 \text{ J kg}^{-1}$ and $1 \text{ Gy} = 6.24 \cdot 10^{12} \text{ MeV kg}^{-1}$, respectively.

LINEAR ENERGY TRANSFER

The unrestricted **linear energy transfer** LET_{∞} refers to the electromagnetic stopping power and describes the energy dE that ionizing radiation deposits along the path dl it traverses the target material. It is strongly dependent on the type and the energy of the radiation. The often used quantity restricted linear energy transfer considers only the energy that is deposited along the particle's path and excludes all energies in excess of Δ that is transferred to electrons, which then become long range particles (δ -rays).

$$L_{\Delta} = \frac{dE_{\Delta}}{dl} \quad (2.7)$$

The SI unit of LET is J m^{-1} , but is usually expressed in $\text{keV } \mu\text{m}^{-1}$.

QUALITY FACTOR

After the ICRP Publication 103 (2007) the **quality factor** Q as a function of the unrestricted linear energy transfer is defined as

$$Q(LET) = \begin{cases} 1 & \text{for } LET < 10 \text{ keV } \mu\text{m}^{-1} \\ 0.32 \cdot LET - 2.2 & \text{for } 10 \text{ keV } \mu\text{m}^{-1} \leq LET \leq 100 \text{ keV } \mu\text{m}^{-1} \\ 300/\sqrt{LET} & \text{for } LET > 100 \text{ keV } \mu\text{m}^{-1} \end{cases} \quad (2.8)$$

and is a measure of the biological impact of the radiation considered. Its value has been derived empirically from biological experiments. Figure 2.7 shows Q as a function of LET .

DOSE EQUIVALENT

The product of absorbed dose D and quality factor Q is the biological relevant **dose equivalent** H

$$H = Q \cdot D = \int Q(LET) D_{LET} dLET. \quad (2.9)$$

As the quality factor is dimensionless, dose equivalent also has the quantity J kg^{-1} . To distinguish it from absorbed dose, it is named sievert (Sv), with $1 \text{ Sv} = 1 \text{ J kg}^{-1}$.

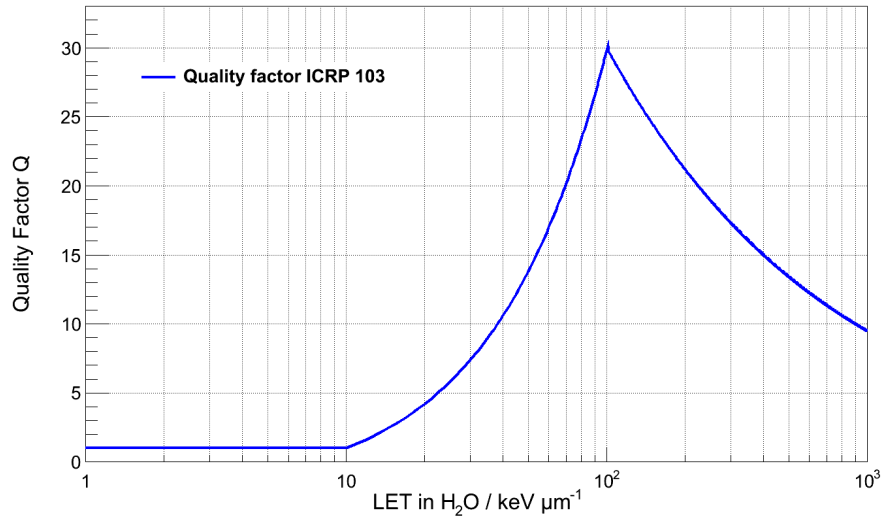


Figure 2.7.: Quality factor as a function of the linear energy transfer (ICRP Publication 103, 2007).

EFFECTIVE DOSE

The **effective dose** E is not a measurable quantity as it accounts not only for the different quality of radiation types, but also for the different sensitivity of organ tissues. For the application on Earth, ICRP Publication 103 (2007) uses radiation weighting factors w_R and tissue weighting factors w_T to define the effective dose as

$$E = \sum_T w_T \sum_R w_R D_{T,R}, \quad (2.10)$$

where $D_{T,R}$ is the mean absorbed dose in the corresponding organ or tissue T due to radiation of type R. The inner sum over R gives H_T , the equivalent organ dose. The sum over all organ tissue weighting factors w_T is one.

In space, the radiation weighting factors w_R are not applicable due to the different quality of the radiation compared to what is found on Earth. NCRP Report No. 132 (2000) and NCRP Report No. 142 (2002) therefore defines the effective dose as the sum over the dose equivalent (Equation 2.9) for specific organ tissues

$$E = \sum_T w_T \bar{H}_T, \quad (2.11)$$

where \bar{H}_T is the organ dose equivalent in the corresponding organ or tissue T.

As E also refers to energy deposition in a mass element, its unit is J kg^{-1} with the name sievert (Sv).

2.3.2. THE RADIATION EXPOSURE AT AVIATION ALTITUDES AND IN LOW EARTH ORBIT (LEO)

The Bundesamt für Strahlenschutz (BfS)² quotes the mean radiation exposure in Germany per year due to natural radiation sources to an effective dose of 2.1 mSv. This includes exposure from radon inhalation (1.1 mSv), radioactive material ingested with food (0.3 mSv), cosmic radiation (about 0.3 mSv depending on altitude) and terrestrial radiation (0.4 mSv). Exposure from artificial sources, like medical and technical applications, adds on average another 2.0 mSv per year.

At aviation altitudes the exposure is increased compared to ground and depends on altitude and latitude. Therefore the ICRP (ICRP Publication 60, 1991) recommended to regard aircrew as radiation workers and following Directive 96/29/EURATOM from the European Union the radiation exposure is regularly assessed by calculations and measurements (e.g. Lewis et al. 2004 and references therein). Although individual estimations and measurements vary, generally exposures come not close to reach the recommended values of ICRP of 100 mSv in 5 years (e.g. Goldhagen 2000). However in cases an SEP event results in a GLE, the radiation exposure can be strongly increased. For example Matthiä et al. (2009) show for the GLE 69 in 2005 that the radiation exposure at these altitudes during the event strongly depends on the position within the atmosphere and can increase by a factor of several hundreds on short time scales and still by a factor of two for a longer period of time.

The in LEO derived effective dose rates – based on the results from the MATROSHKA experiment – are of the order of 200 mSv yr⁻¹ for inside and of the order of 250 mSv yr⁻¹ for outside ISS (Berger et al., 2012).

The two main contributors are GCR and trapped radiation in the radiation belt when ISS is traversing the SAA. The trapped radiation can contribute one third up to half to the absorbed dose and about 15 % to 30 % to the dose equivalent (DOSIS/DOSIS 3D experiment, Burmeister et al. 2012), which is due to the different quality factors. The contribution from the SAA is strongly influenced by the altitude of the ISS and by the location inside ISS due to varying shielding (e.g. Jadrníčková et al. 2009, Reitz et al. 2005).

Figure 2.8 shows the elemental composition of GCR and the contribution of the individual ions to the absorbed dose and the dose equivalent of astronauts. Despite their

²<http://www.bfs.de>

low abundance, high Z particles contribute large parts of the total received absorbed dose and dose equivalent due to their large linear energy transfer that is proportional to Z^2 .

The dose limits for astronauts are set to dose levels corresponding to a three percent excess lifetime cancer mortality and depend on age and gender. The ten year career exposure limit of effective dose range from 0.4 Sv for a 25 year old female to 3.0 Sv for a 55 year old male (NCRP Report No. 132, 2000).

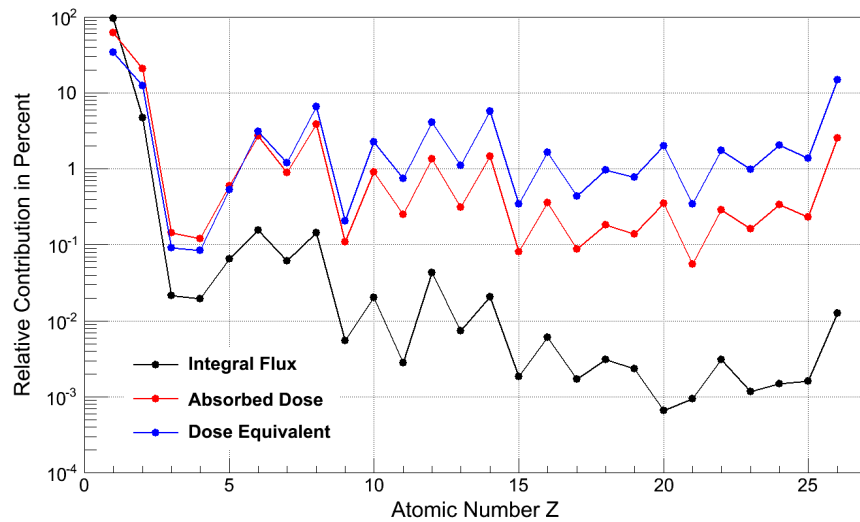


Figure 2.8.: The fluence of the elemental composition of GCR is given and their contribution to absorbed dose and dose equivalent. The data for the figure was provided by A. I. Mrigakshi.

2.3.3. DOSIMETERS

The radiation exposure of astronauts is continuously monitored by dosimeters. Area monitoring and personal dosimeters are both established in the space station. Extended overviews of radiation measurements onboard ISS are for example given by Berger (2008) and Zhou et al. (2009), but in the following four important detector principles are introduced briefly. As in this work silicon detectors are employed, their working principle is presented in more detail.

Personal dosimetry onboard the space station is currently carried out with passive dosimeters (e.g. Straube et al. 2010). These do not require a power source like active devices, but store the information of accumulated energy deposition in the detection

material. Other than active detectors, they are read out after a certain exposure time span and are usually brought back to Earth for evaluation. Commonly used is a combination of thermoluminescence detectors (TLDs) that are inorganic crystals and plastic nuclear track etch detectors (PNTDs) made of the tissue equivalent material CR-39.

TLDs store the deposited energy in imperfections in their lattice structure. By heating the detectors, they release this energy by light emission. The recorded light curves give a direct measure of the dose. After heating the TLDs are reset and can be used again.

Ionizing particles traversing PNTDs break the molecule chains of the polymer and leave a latent track behind. By chemical surface etching of the PNTDs these tracks form cones on the surface from which the linear energy transfer of the ionizing particle is deduced. While TLDs show excellent sensitivity to low LET particles, CR-39 detectors are applied for the high LET range. Spectra are usually merged at $10 \text{ keV } \mu\text{m}^{-1}$.

For area monitoring active and passive radiation detectors are employed. Active detectors are for example tissue equivalent proportional counters (TEPCs) and silicon detectors like the DOSTEL (Dosimetry Telescope). Both devices are placed stationary and are connected to power supply units of the station. The TEPC is an ionization chamber surrounded by tissue equivalent material in order to simulate the volume of human tissue the order of μm in diameter (e.g. Perez-Nunez and Braby 2011) and provides a direct measure of the lineal energy³.

The DOSTEL consists of two circular 6.93 cm^2 planar silicon detectors arranged in a telescope configuration (Beaujean et al., 1999). By restricting the opening of the aperture such, it is able to measure the linear energy transfer of charged particles (compare Section 3.1.2).

Silicon detectors consist of at least an n- and a p-doped component that build up an intrinsic electric field and a depleted zone in the junction region. Applying a bias voltage increases the depletion zone. An incoming ionizing particle creates electron-hole pairs in the sensitive volume that are pulled apart by the strong electric field. The number of free charge carriers is proportional to the energy loss of the ionizing particle in the detector. Silicon detectors provide an excellent energy resolution due to the small activation energy for electron-hole pairs of 3.6 eV. Compared to other semi-

³The lineal energy (ICRU Report 85, 2011) is the micro-dosimetric equivalent of the linear energy transfer.

conductor detectors they do not require cooling for operation. They are additionally highly qualified for portable applications, since they can be fabricated to small sizes and are easy to handle. However, as a silicon diode is a large capacitance, it is prone to microphonic effects that can be seen as a strong noise component on a short time scale, which needs to be considered when designing a personal dosimeter based on silicon detectors.

THE MOBILE DOSIMETRIC TELESCOPE

This chapter gives the functional description of the Mobile Dosimetric Telescope MDT (Section 3.1), its working principle (Section 3.2) and the prototype development (Section 3.3). The final technical design is presented including a detailed description of the electronics (Section 3.4) and the mechanical setup (Section 3.5). Section 3.6 introduces the countermeasure for microphonic effects and proves its performance. Finally, the response of the detector system to input signals is shown (Section 3.7).

3.1. FUNCTIONAL DESCRIPTION

3.1.1. FUNCTIONAL REQUIREMENTS

The aim of this work is to develop a prototype of a **small-size active personal dosimeter** based on **silicon detector technology** that is able to eventually serve as an astronaut's dosimeter. It needs to cover a broad **energy range** corresponding to the radiation field in low Earth orbit (LEO). This **battery** driven device has to measure **absorbed dose** as well as the **linear energy transfer** to enable calculations of dose equivalent. Section 3.1.2 explains these requirements and their realization in more detail.

3.1.2. DERIVED REQUIREMENTS FOR THE DETECTOR DESIGN

SMALL ACTIVE SILICON DETECTOR

Using silicon diodes as detection material has several advantages. They can be fabricated to small sizes and are relatively easy to handle. In bias mode operation, silicon detectors provide a high energy resolution and are capable of detecting ionizing radiation within a broad energy range. The signals coming from the detector are processed immediately and therefore enable to monitor the radiation exposure in real-time. The

silicon diodes used for this application have a thickness of $300\ \mu\text{m}$, which allows particles with a low linear energy transfer to deposit enough energy to be detected.

LINEAR ENERGY TRANSFER MEASUREMENTS

More than one detector is required to measure the linear energy transfer (LET), in order to know the path length the particle has traversed within the detector. For this radiation detector a telescope setup with two detectors is chosen (Figure 3.1). The two diodes are placed above each other with a defined distance between them. If a particle is detected in both diodes (coincidence event), its path length within the detector is restricted by the opening angle α of the setup. Hence a mean path length can be used to calculate LET from these coincidence events and to obtain the mean quality factor of the radiation field.

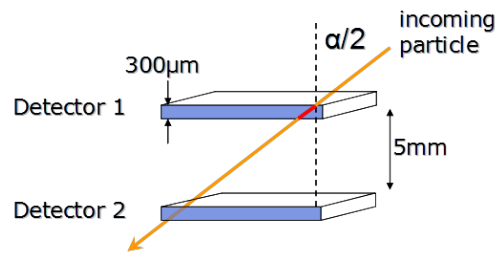


Figure 3.1.: Sketch of a telescope setup with two detectors for LET measurements.

ENERGY RANGE

The energy range of interest refers to particles with sufficient energy to ionize matter. This sets the lower threshold of detection to some 60 keV energy deposition in the diode, corresponding to the lower end of the Landau distribution of minimal ionizing protons. The high energy limit is defined by relativistic iron nuclei depositing about 70 MeV in $300\ \mu\text{m}$ silicon. Allowing an angle of incidence of about 60° doubles the distance travelled in the detector and sets the desired upper detection limit to 140 MeV energy deposition in silicon.

BATTERY OPERATIONAL TIME

The power consumption – and therefore the battery operational time – is given by several factors. Regarding digital signal processing, the power consumption is proportional to processing speed, i.e. the microcontroller (μC) clock frequency. For analog

components, like operational amplifiers, the bandwidth of the components is critical, effectively also resulting in processing speed. From DOSTEL (Dosimetry Telescope, Beaujean et al. 1999) measurements it is known that onboard the International Space Station count rates of maximal $100 \text{ counts s}^{-1} \text{ cm}^{-2}$ in the South Atlantic Anomaly (SAA) can be expected (e.g. Reitz et al. 2005). This is multiplied by a factor of 10 – to account for that particles do not come within regular intervals – and then taken as the lower speed limit of the digital electronics. Additionally all unnecessary features, e.g. backlight for the display, are omitted.

3.2. DETECTOR DESIGN

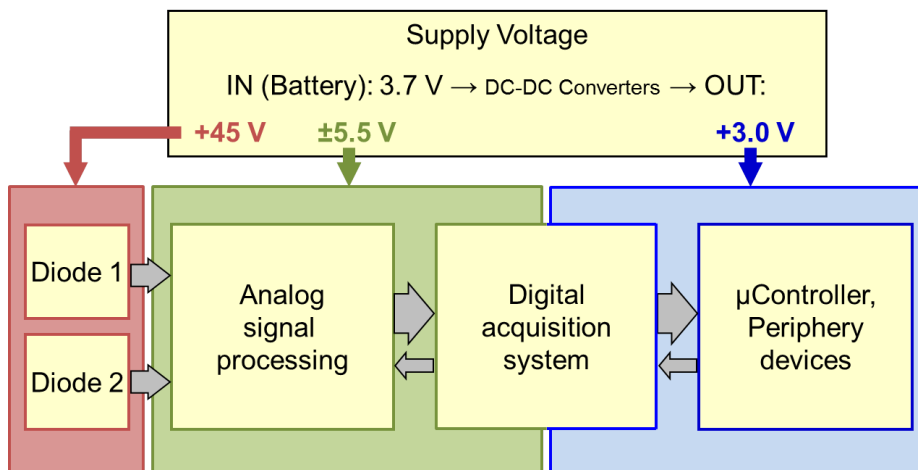


Figure 3.2.: Principle Block diagram of electronic detector setup. A detailed diagram can be found in Figure 3.3.

Figure 3.2 shows a simple block diagram that describes how the MDT works in principle. A rechargeable battery of 3.7 V provides the supply voltage. DC-DC converters generate from this input different voltages to power the bias voltage for the two silicon diodes (red), the analog electronics (green), and the voltage for the digital part of the instrument (blue).

The block diagram in Figure 3.3 gives a more detailed insight into the functioning of the described device. Components with a red, green, and blue frame are powered by the bias, analog, and digital supply voltage, respectively. Components with two colors receive both indicated supply voltages. The arrows of the digital signals are

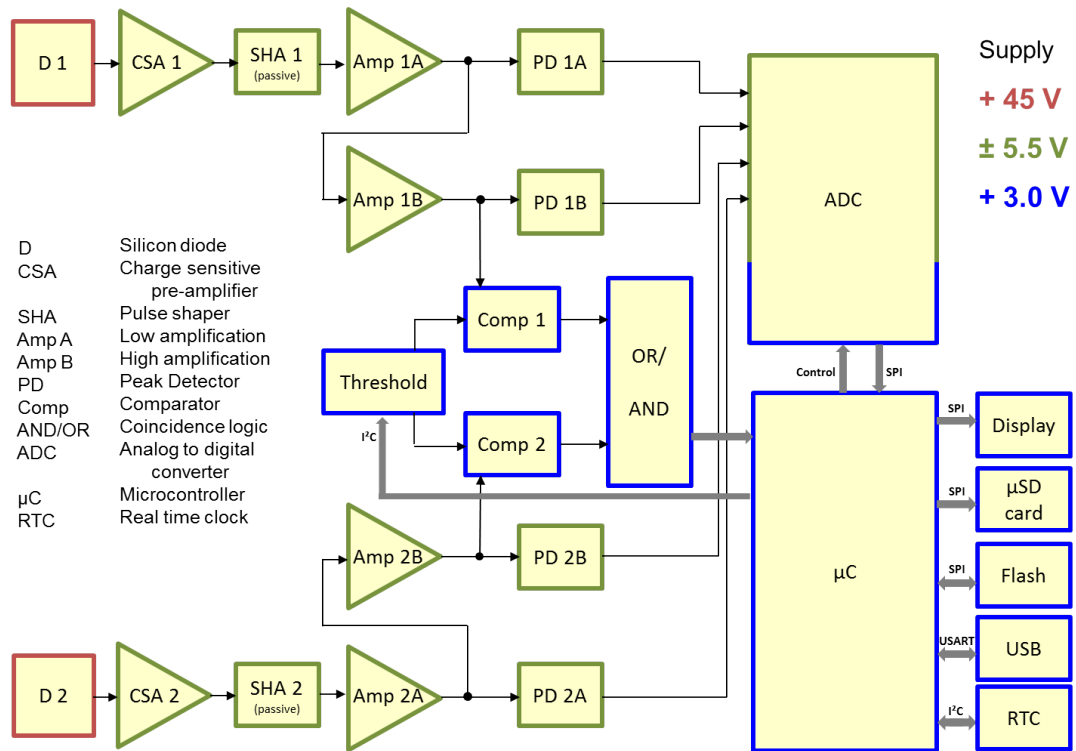


Figure 3.3.: Detailed block diagram of electronics design.

named by their communication protocol (SPI, USART, I²C)¹.

The two signal paths 1 and 2 for each detector are shown, starting on the left hand side with the silicon diodes (D), which are connected to the charge sensitive preamplifiers (CSA). The following electronics shapes (SHA) and amplifies the preamplifier signal in two subsequent amplification stages for low gain (Amp A) and high gain (Amp B). The amplitude of the signal is acquired by peak detectors (PD) and by an analog to digital converter (ADC), which is triggered and read out by the μ C. The μ C controls the detection threshold (Threshold) and processes all digital data (coincidence OR/AND, ADC values, battery voltage) further to transfer it to periphery devices (Display, μ SD card, USB interface)².

Figures 3.4 and 3.5 show the signal processing on the oscilloscope. The colored symbols on the very left indicate the signal baseline. In the blue bar at the top

¹SPI: Serial Peripheral Interface, USART: Universal Synchronous/Asynchronous Receiver Transmitter, I²C: Inter-Integrated Circuit

² μ SD card: Micro Secure digital Card, USB: Universal Serial Bus

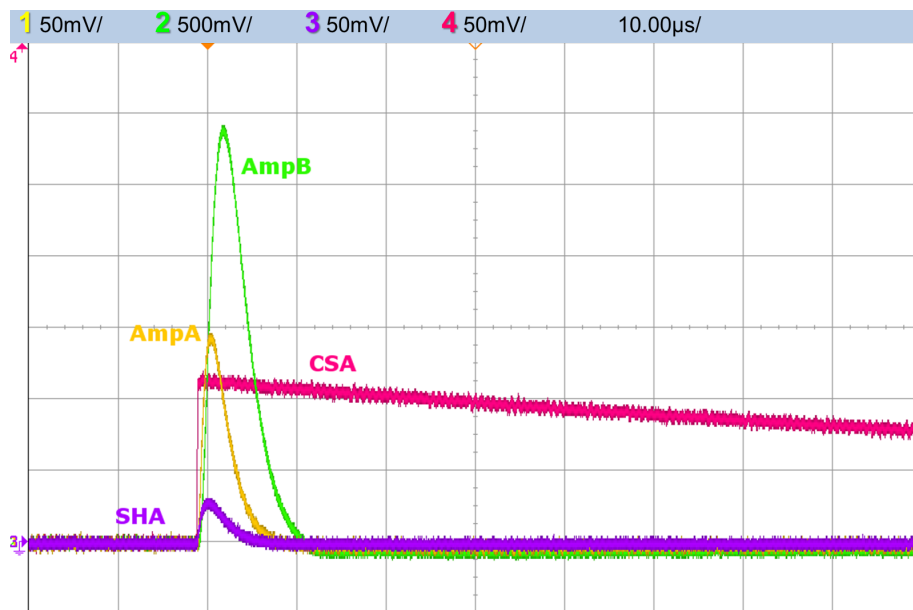


Figure 3.4.: Analog signal processing (I): (in the order of signal processing) Charge sensitive preamplifier (CSA, red), shaper (SHA, purple), low amplification stage (AmpA, yellow), and high amplification stage (AmpB, green).

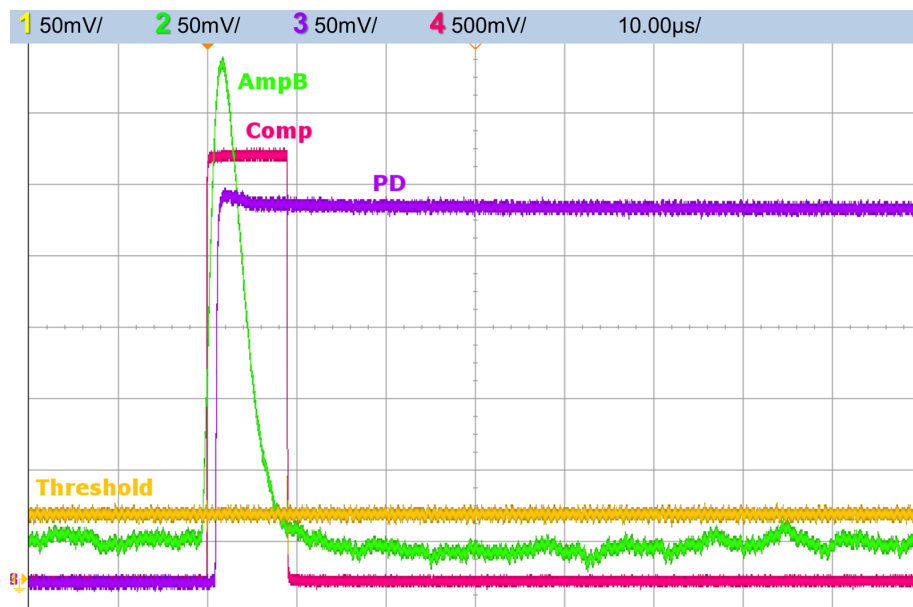


Figure 3.5.: Analog signal processing (II): High amplification stage (AmpB, green), peak hold detector (PD, purple), comparator (Comp, red), and Threshold (yellow).

the amplitude scaling for each signal is given in color code in mV per division. Also in the blue bar the time resolution is shown in μs per division. In Figure 3.4 the preamplifier signal (red) and the shaped and amplified pulse (purple SHA, green AmpA, yellow AmpB) can be seen. The preamplifier signal has an offset of -500mV and is shifted to superpose with the other signals. Except for the high amplification stage, all signals are scaled the same, while AmpB is minimized by a factor of ten to fit into the figure range. Figure 3.5 visualizes the shaped pulse from the high amplification stage (green AmpB), the corresponding peak detector (purple), the detection threshold (yellow), which has to be exceeded by the AmpB signal to trigger the comparator, and the comparator output (red) that serves as digital input signal for the μC . The input signals are decreased by about a factor of ten compared to Figure 3.4 in order to see the detection threshold. The comparator signal is minimized by a factor of ten for comprehension.

3.3. DEVELOPMENT

During the development of the MDT electronics hardware, eight iterations were performed resulting in eight different electronics boards. This section gives an overview of them, explaining briefly, what has been added, improved, and changed since the last version.

The boards are denoted with an increasing version number, e.g. 05.01, where the first two digits give the general version number (same form, fit, and function), while the last two digits were to be used for small changes during testing. The boards designed at the German Aerospace Center (DLR) (from version 01.01 on) are designed with the software tool *Eagle* by *Cadsoft*³ and the printed circuit board (PCB) layouts were sent to *PCB Pool*⁴ for manufacturing. Except for the latest board version (08.01), the assembly of the components (i.e. soldering) has been done at DLR to allow stepwise testing of each component.

Figure 3.6 shows photographs of all test and breadboards, while Table 3.1 summarizes shortly all versions, their sizes and the newly implemented features that are explained in detail in Appendix A.

³<http://www.cadsoft.de>

⁴<http://www.pcb-pool.com>

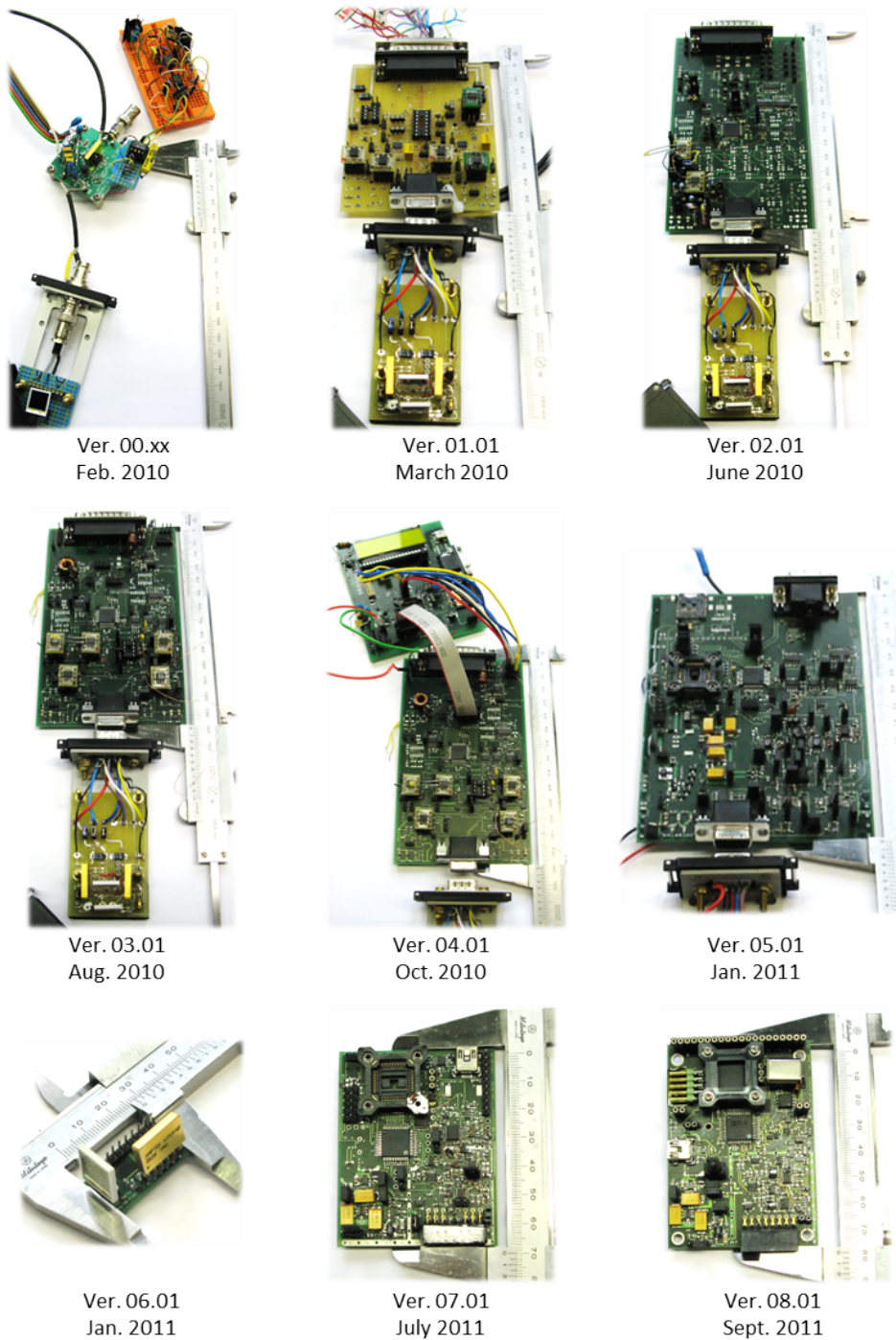


Figure 3.6.: Development summary for the electronics of the detector system: Board versions 00.xx to 08.01.

Table 3.1.: Development steps of the electronic boards for the detector system. Column 1 gives the board version, column 2 the length (L) and breadth (B) in cm and column 3 the application. P stands for preamplifier board, A for analog part and D for digital signal processing part. Column 4 lists shortly the added features for every version. **The final board versions are printed in bold.**

Board Version	Size (L × B) (cm × cm)	Board Type	New Features
00.xx		P, A	First design tests
01.01	6.4 × 4.0	P	Two preamplifiers and silicon diodes
	10.0 × 8.0	A	Active SHA/Amp, PD, and PD reset; test of PD reset
02.01	14.0 × 8.3	A	Passive SHA, 2 parallel Amp, digital potentiometer (threshold), ADC, coincidence logic, connectors to μC
03.01	14.0 × 8.3	A	Transformer for ± 5.5 V analog supply, new ADC
04.01	11.2 × 8.8	D	μC , μSD card, display, real time clock, RS-232 interface, new analog supply including charge pump and inverter
05.01	14.4 × 10.0	A/D	Combines version 03.01 and 04.01, generation of bias voltage for diodes, new μC
06.01	2.8 × 1.4	P	Separate boards for diode 1 and 2, size decreased, layout improved
07.01	7.0 × 5.5	A/D	Size decreased, assembled from top and bottom, amplification stages in sequence, RS-232 replaced by mini USB, flash memory, power switch, push button
08.01	7.9 × 5.5	A/D	Battery charger, additional small improvements

FINAL DETECTOR SETUP

The board versions 06.01 (preamplifier board) and 08.01 (analog and digital electronics board) are implemented into the final setup, i.e. two preamplifier boards for both diodes and one signal processing board for one detector system. Two prototypes are built with this electronic setup and are named with the designation **MDT-01-xxx-DLR-CAU**. 'xxx' denotes here the **two prototypes 000 and 001** that are employed for this thesis work and are described in more detail in the following sections.

3.4. ELECTRONICS – PRINCIPLE OF OPERATION

This description focusses on the final board versions **06.01**, the front end containing silicon detectors and preamplifier, and **08.01**, including the rest of the electronics.

The corresponding circuit diagrams of both boards are shown in Appendix B. For every paragraph the respective figure in the appendix is mentioned.

An overview of how the individual components are connected can also be found in the block diagrams in Figure 3.2 and in Figure 3.3. Figure 3.7 shows top and bottom of the signal processing board 08.01 indicating the different parts of the electronics.

Links to the datasheets for all electronic components can be found in the list of datasheets on page 141.

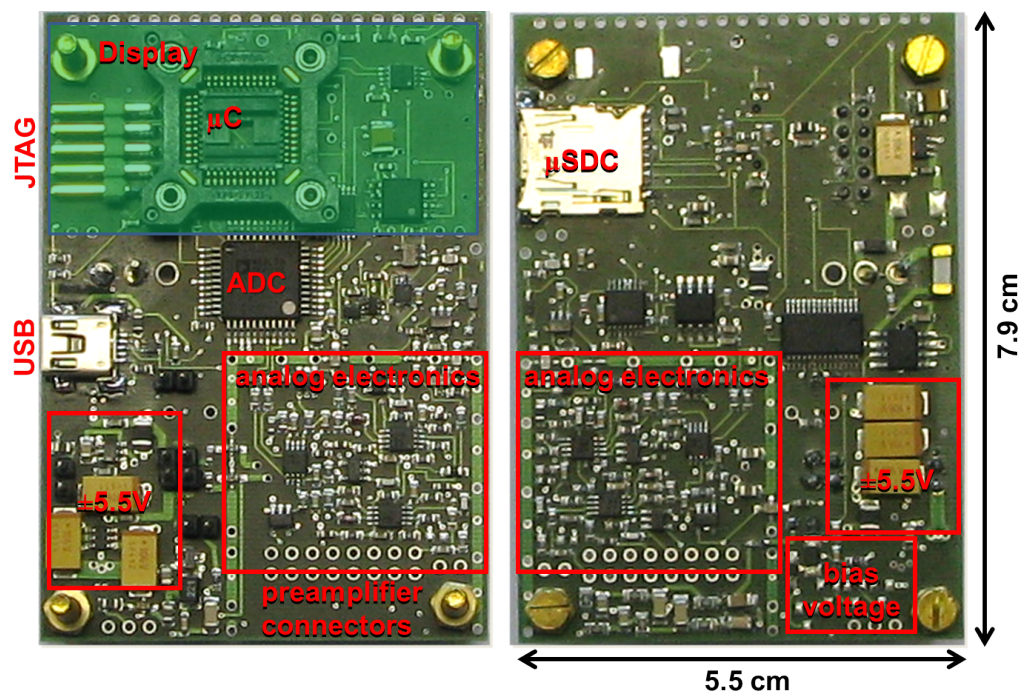


Figure 3.7.: Final breadboard of the prototype, board version 08.01, left top and right bottom of board.

3.4.1. POWER SUPPLY

The whole detector system is powered by rechargeable batteries. A 3.7 V Li-ion battery is used in MDT-01-001-DLR-CAU, and three AA-sized NiMH cells are used for MDT-01-000-DLR-CAU. From this, the bias voltage of 45 V for the silicon diodes, the

analog supply voltage of ± 5.5 V and the digital supply voltage of 3.0 V are generated. The battery is recharged inside the device via the USB interface (Figure B.1). The battery regulation current is set to 500 mA and fully charged the batteries provide 4.2 V. When using external power sources, the MDT can be powered with input voltages between 3.6 and 5.5 V.

During normal operation of the detector system, the MDT requires a constant current of 40 mA. When switching on the current increases to 180 mA for about one second (due to inrush current for the display and μ SD card access) and when the μ SD card is later accessed in the write mode, the current increases to 90 mA for less than a second. The battery voltage is monitored via a voltage divider that is connected to an internal analog to digital converter of the μ C (compare Section 3.4.5).

BIAS VOLTAGE

Silicon diodes require a stable bias voltage for proper function. This bias should fully deplete the active volume of the diode. Based on the datasheet of the diodes applied for this detector (S3590-19), the necessary bias voltage lies between 40 V (minimum for full depletion) and 100 V (break-down voltage). The current consumption due to the small leakage current of the diodes is negligible (nA range), but increases with increasing bias voltage.

The bias voltage is generated by a step-up voltage converter in discontinuous mode. The μ C uses pulse-width-modulation (PWM) for switching a field effect transistor to regulate the charging of an inductor, which is powered by +5.5 V. The duty cycle and frequency of the pulses, as well as the inductance of the inductor are critical parameters for the output voltage. Best results are obtained with an inductance of 150 to 220 μ H, a pulse width of 4 μ s and period of 2 ms. The bias voltage is tested without load for long term stability and it shows to be stable at 50 V. Zener diodes are chosen accordingly to stabilize the bias voltage to 45 V (Figure B.2).

ANALOG SUPPLY VOLTAGE

Analog electronics is powered by a symmetrical voltage of ± 5.5 V. The regulated charge pump for +5.5 V is fed by the battery through an inductor to suppress noise coming from the charge pump into the battery. Negative analog supply voltage is then generated from the +5.5 V line using a voltage inverter (Figure B.3).

Special attention is paid to the layout of this part of the circuitry as the switching frequency of the charge pump might interfere with the rest of the electronics.

DIGITAL SUPPLY VOLTAGE

A low drop out voltage regulator provides a constant voltage of 3.0 V for all digital components, since e.g. display and μ SD card operation are guaranteed in only a narrow supply voltage range (Figure B.4).

3.4.2. GROUND PLANES

As a measure of suppressing noise pick-up and cross-talk between signal lines on a PCB, ground planes are used. For the analog and the digital part two separate ground planes are chosen. They are connected via a 10 μ H inductor which prevents high frequency digital noise to enter the analog circuit.

The analog ground plane is connected to the conductive case of the prototype for shielding.

3.4.3. SILICON DETECTORS

The detector setup is based on two silicon PIN diodes (Figure 3.8), manufactured by *Hamamatsu Photonics*⁵. The sensitive area is 1 cm² for light, but extends to 1.21 cm² for ionizing radiation under the thin aluminium contact frame, which has to be taken into account for dose calculations. The thickness of the diodes is 300 μ m.

The diodes are connected reversely to the bias voltage to generate a maximal depletion zone. Incoming particles create electron-hole-pairs that are pulled apart in the strong electric field. The negative charge carriers of few thousands of electrons are the final signal to be processed further.

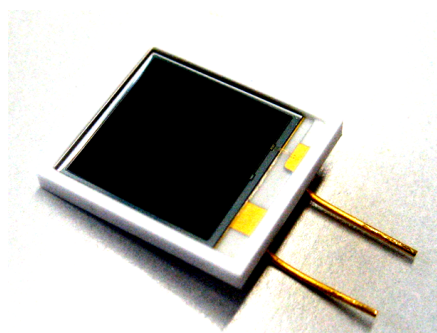


Figure 3.8.: Hamamatsu silicon diode S3590-19.

⁵<http://www.hamamatsu.com>

3.4.4. ANALOG ELECTRONICS

The signals of the analog signal processing chain are visualized in Figures 3.4 and 3.5.

CHARGE SENSITIVE PREAMPLIFIER

The charge sensitive preamplifier converts the charge coming from the detector proportionally into voltage. The capacitance of the feedback capacitor defines the conversion ratio. By default the preamplifiers have an internal feedback capacitance of 0.25 pF and a corresponding gain of 175 mV MeV^{-1} in silicon. For this application the feedback capacitance is increased to 2.25 pF, resulting in a theoretical conversion factor of energy in silicon of 19.4 mV MeV^{-1} . The feedback capacitor gives together with an external feedback resistor of $100 \text{ M}\Omega$ the time constant for the decay of the detected pulse of about $200 \mu\text{s}$ (Figure B.5).

The preamplifier boards with the silicon diodes are placed separately in an electrically shielded compartment.

SHAPERS

The output of the charge sensitive preamplifier is fed to a passive bandpass filter with a time constant τ of $1 \mu\text{s}$ (Figure B.6). The optimum for signal processing of silicon detectors is between $0.5 \mu\text{s}$ and $1 \mu\text{s}$, where the total noise as sum of the parallel and series noise becomes minimal. The parallel noise – parallel with the detector at the preamplifier input – occurs due to the leakage current from the detector and the gate of the FET, as well as due to thermal noise in the preamplifier feedback resistor and is proportional to $\sqrt{\tau}$. The series noise originates from thermal noise in the FET channel and is proportional to $\sqrt{\tau}^{-1}$.

This second order shaper reduces the amplitude of the signal by a factor of four.

PULSE AMPLIFIERS

The shaped signal is processed in two amplification stages for high and low energy depositions to cover the required dynamic range of nearly 3.5 decades. The first stage **low gain A** amplifies the shaped pulse by a factor of 8. The signal is split to feed on the one hand the low gain channel peak detector and on the other hand to be further amplified by the second amplification stage **high gain B** with a gain of about 30 (Figure B.6). The output of stage B propagates to the high gain peak detector. It is additionally compared to a threshold by a comparator, which, in case the signal

exceeds this threshold, signals the μC to start the process of measurement the peak voltage.

PEAK-HOLD DETECTORS

A peak-hold detector is used to artificially prolong the duration of the voltage peak coming from the amplifier by charging a capacitor. This peak prolongation is necessary for the ADC to measure the maximum amplitude of the peak. An operational amplifier buffers the voltage at the storage capacitor to prevent a discharge of the capacitor during the ADC conversion (Figure B.7). After the peak amplitude is digitized, the peak hold detector is reset by the μC .

3.4.5. DIGITAL ELECTRONICS

ANALOG TO DIGITAL CONVERTER (ADC)

The ADC is used to acquire the voltage of the shaped voltage pulse. A 12-bit simultaneously sampling ADC is chosen to convert the voltage of all four peak detectors at the same time. The conversion process is triggered by the μC . The upper eight bits of the ADC's parallel output are forwarded to a shift register that is read out by the μC via the SPI interface. The lower four bits are taken directly.

Since the maximum input signal amplitude of the ADC is slightly higher than 3 V and the reference voltage is 2.5 V, the signal is internally scaled down by a factor of two and the resulting ADC resolution is better than 11 bit, i.e. 2300 ADC channels. The circuit diagram is shown in Figure B.8.

MICROCONTROLLER, PERIPHERY DEVICES AND SOFTWARE

All digital processes are coordinated by the μC ATmega1284P. It runs with a clock frequency of 1.8432 MHz and is responsible for monitoring of the battery voltage, the control of the PWM for the diode bias voltage, setting of the detector threshold, the timing and control of the ADC, calculation, showing data to the display, and writing on the μSD card.

The μC program is written in the programming language C and transferred to the μC via the JTAG interface. In the following the program flow is described and thereby the periphery devices are introduced. The program flow chart of the working principle is given in Figure 3.9.

When the MDT is switched on, the input parameters are set (battery threshold, saving interval for μ SD card, detection threshold, battery check interval, timer resolution). The ADC is initialized and immediately put to sleep mode in order to save power, the communication interfaces (SPI, I²C, USART) are initialized, the PWM-generator for the bias voltage is started, time and date are read from the real time clock (RTC) and with this information a new folder is created on the μ SD card, in which the measurement data will be saved. The display is started, showing during the start process "Starting..." and the interrupts for particle event, timer overflow, and external interrupt are enabled. The timer is started and the main routine goes into an endless loop, in which dose and dose rates can be calculated, the display is updated with the calculated information with the time in minutes since start of the measurement. The main routine is interrupted only by the interrupt vectors.

The μ C program uses three interrupt vectors, the particle event interrupt, the timer interrupt, and an external interrupt.

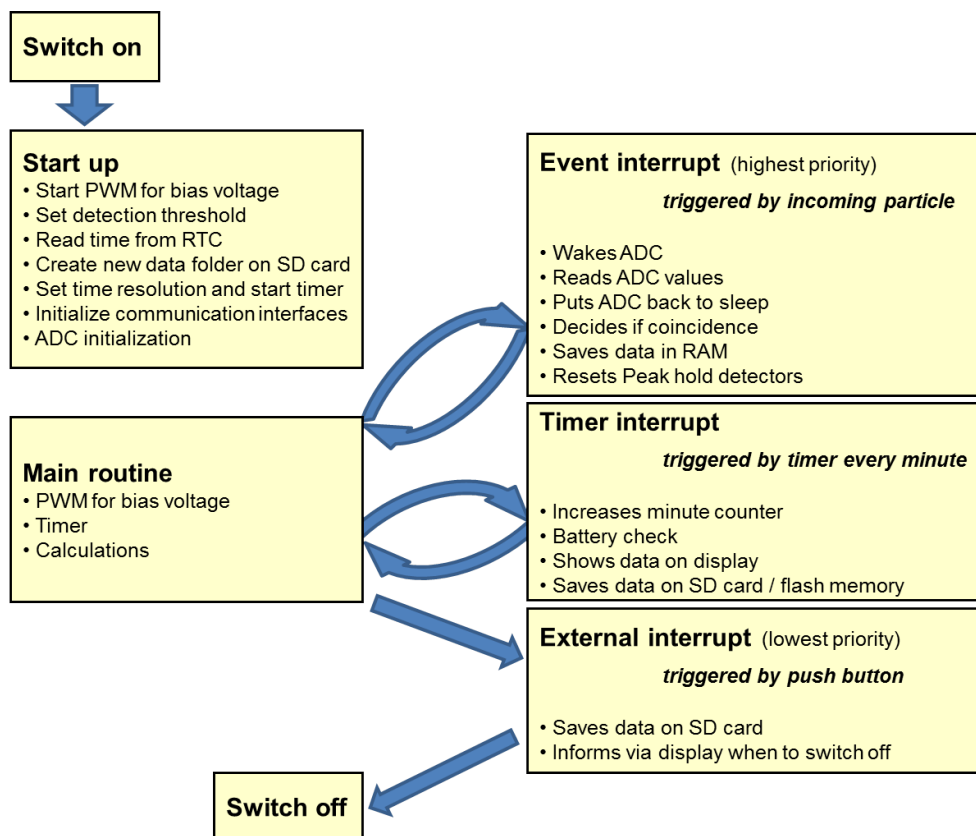


Figure 3.9.: Simplified block diagram of μ C program.

The event interrupt takes top priority, i.e. is always served first, and is triggered by any incoming particle that is detected above the detection threshold. The ADC is woken up to acquire the pulse amplitude and put back to sleep mode before the results are read out. The data is stored in a buffer, containing for every event the information of high and low gain of both diodes, a coincidence flag, and the time in minutes since switching on. After discharging all peak hold detectors, the μC goes back to the endless loop in the main routine. In case the MDT is not used for a mobile application, the information of each event can immediately be sent to a PC via USB. The duration of the interrupt routine adds up to about $440\ \mu\text{s}$. The ADC has the conversion finished already $33\ \mu\text{s}$ after the interrupt routine has started, but the data is read out serially by the SPI interface via the shift register, which takes another $300\ \mu\text{s}$ for all four channels. At the end of the interrupt routine, the interrupt flag is deleted, which means that any particle detected before is not considered.

Every minute the timer triggers the timer interrupt. The timer counter is incremented and depending on the saving and battery check interval, the data stored in the RAM is written to the flash memory or to the μSD card and the battery voltage is checked. If the battery voltage is below $3.6\ \text{V}$, it is checked again after one minute. In case the battery voltage is still too low, the display shows 'LOW BATTERY' and a new folder, named *Battery* is created on the μSD card, in which then subsequent data is saved. Lowest priority has the external interrupt that is triggered by the push button. All data on the flash memory and in the RAM is transferred to the μSD card. The display informs, when the saving process is over and the detector can be switched off without losing data.

The pin allocation table for the μC can be found in Table B.1 and the circuit diagram in Figure B.9 in the attachment.

DATA OUTPUT FORMAT

Every hour a new text file $Ri.TXT$ is created on the μSD card, where R stands for raw data and i is the incremented integer. Each ASCII file contains six columns. The first four columns are the ADC values of high (B) and low (A) gain of both diodes in the order 1B 1A 2B 2A. In column five the information is saved, if a coincidence event has occurred. Column six contains the time stamp of the corresponding event in minutes since starting the device.

Therefore the raw data files contain all available information and can be further processed.

3.5. MECHANICAL SETUP OF THE PROTOTYPES

The case of both prototypes is made of aluminium and is connected to the analog ground plane to act as EMC shielding for the system. Several openings for USB, μ SD card, JTAG, display, push button, and power switch are considered.

3.5.1. FIRST PROTOTYPE: MDT-01-000-DLR-CAU

The housing for the first prototype MDT-01-000-DLR-CAU (in the following referred to as MDT-01-000) consists of two plain aluminium boxes. The smaller box (*front end casing*) encloses the two silicon diodes and their preamplifier boards (Figure 3.10 left). The two preamplifier boards are placed on a carrier (Figure 3.13) and plugged into board version 08.01, the main board, by connectors through the front end casing's lid, which is glued to the main board and connected to its ground plane. Front end casing and main board are placed in another aluminium box (*detector case*) (Figure 3.10 right) and fixed by screws. The detector case has openings for USB, JTAG, and the μ SD card. The power switch is connected via cables to the lid of the box. To access the push button and see the display, the top cover of the detector has to be opened. Cables connect the board with the battery, which is placed externally.

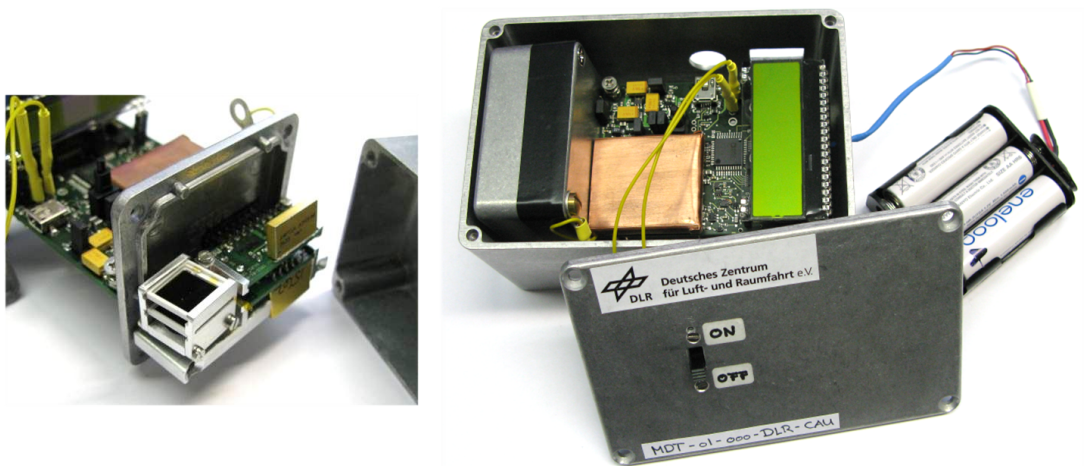


Figure 3.10.: The front end of MDT-01-000 (left) and the complete setup (right) are shown.

3.5.2. SECOND PROTOTYPE: MDT-01-001-DLR-CAU

For the second prototype MDT-01-001-DLR-CAU (in the following referred to as MDT-01-001) the case is carefully designed to fulfil several requirements and match dimensions of the electronics boards perfectly. The front end (diodes and preamplifier boards) is in a separate compartment of the case with an extra opening to plug in the preamplifier boards on the carrier separately. One part of the top wall of this compartment can be removed for irradiations with alpha particles in the vacuum chamber. Since the detector is still a prototype, the setup can be disassembled in a way that the electronics board can be accessed from top and from bottom to apply changes and run tests (Figure 3.11). In the bottom part of the case, a battery slot is implemented. On the top part the display is connected to the board by plug-in connectors and is removed for irradiations in vacuum, for exchanging the μC or for other tests on this part of the board. The top cover of the case has an opening for the display with a transparent protective cover. As in the previous prototype, the power switch is connected to the board via cables. Through a small hole the push button can be pressed with a thin stick (e.g. a ball pen). The openings for USB and JTAG are covered by small plastic caps. Figure 3.12 shows the detector from front and from back. The technical drawings for selected parts of this case (main case and front end carrier) are shown in Appendix B (Figure B.10 to B.15).

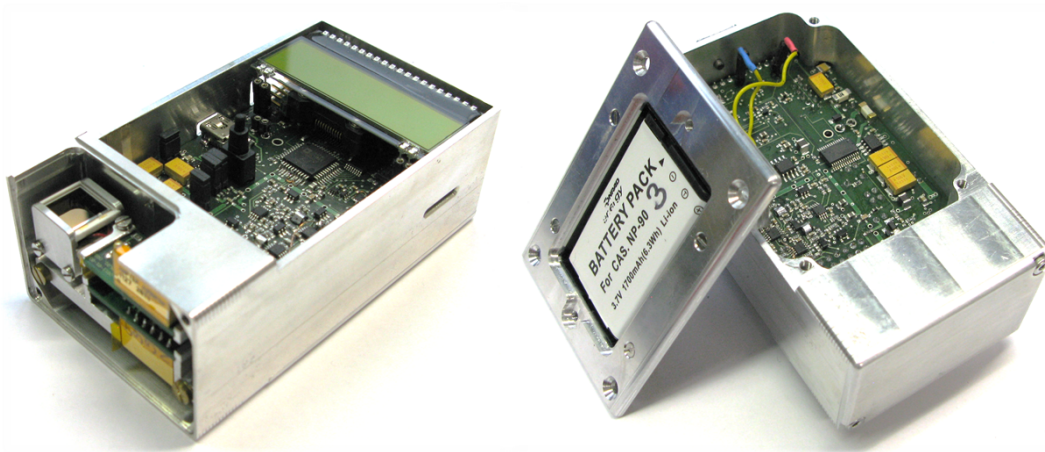


Figure 3.11.: MDT-01-001 disassembled from the top (left) and from the bottom (right). The separate front end compartment and the access to top and bottom side of the electronics board is visible. The battery slot is embedded in the bottom cover of the case.

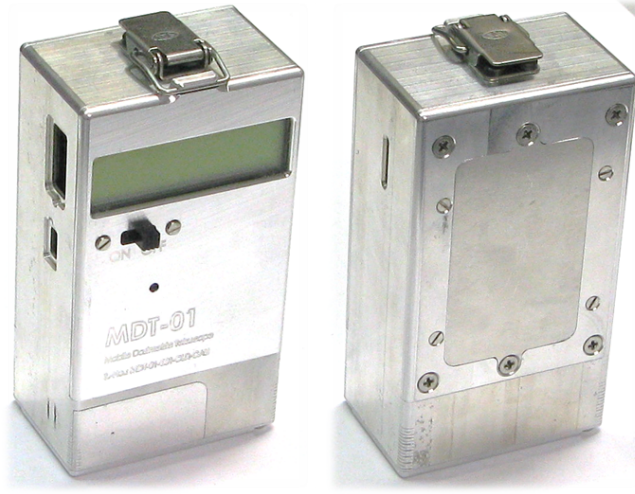


Figure 3.12.: The complete MDT-01-001 from front (left) and from back (right). On the left, the openings for JTAG (top) and the mini USB plug are visible, which are usually covered by plastic caps. On the right picture, the μ SD card slot can be seen.

3.6. COUNTERMEASURE FOR MICROPHONIC EFFECTS

Silicon diodes are sensitive to microphony, which poses a problem especially for mobile applications. Microphonic effects appear as a strong noise component on a short time scale and can for example be identified by an unexpected step increase in the count rate profile of the measurement.

Figure 3.13 shows the design of the front end carrier that has been developed for the MDT. The setup attempts to minimize microphonic effects as much as possible by decoupling the diodes mechanically from the rest of the detector. The diodes are connected to the bias voltage on the preamplifier boards by flexible cables. For the

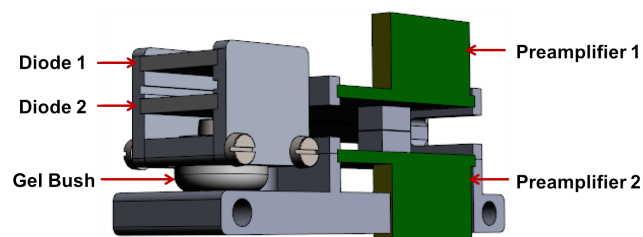


Figure 3.13.: Schematic view of the front end carrier with preamplifier boards and diodes in a telescope carrier that is buffered with a gel bush to prevent microphony.

mounting of the telescope configuration a gel bush is used that is designed by the manufacturer to damp tiny-load and micro vibration ([S] in the list of datasheets).

This design had not been implemented for the very first measurement onboard an aircraft with a test setup including breadboard version 05.01 and preamplifier board 06.01 (Figure A.2) that is presented in Appendix G.1. In the count rate profile of this flight, slight microphonic effects can be observed.

For testing of the countermeasure, the final prototype MDT-01-001 was used in its application as a personal dosimeter. It has been carried on the body during several hours during normal daily life activities, extended by jumping, running up and down the stairs and riding an old and shaky elevator. In order to provide a reference measure, not only the MDT, but also two additional silicon detectors of Liulin type (Dachev et al., 2007) were carried during the same activities. The Liulins work, like the MDT, with commercial Hamamatsu silicon diodes, but with about twice the detection area [S2744-08]. The positions of the three detectors on the body were interchanged during the day to omit a bias in the measurement.

Figure 3.14 shows the count rate profile of few hours of this test run. The count rates of the upper diode (D1) of the MDT are given red and of the lower diode (D2) in black. The results of the two Liulins are displayed in blue and green, respectively.

Liulin 1 is known to often show microphony, whereas Liulin 2 usually performs better (N. Santen, private communication). However, both Liulins reveal a strong response

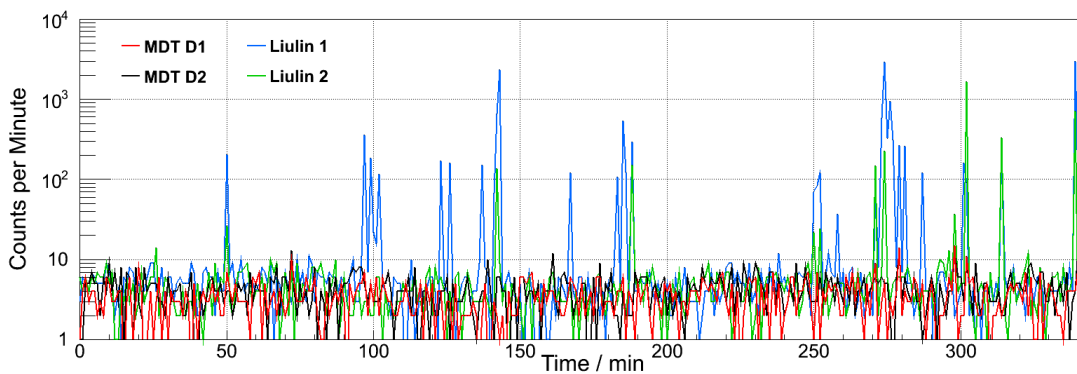


Figure 3.14.: Count rate profile of the test run for the microphonic countermeasure. The two silicon diodes of MDT-01-001 are given in red and black for the upper and lower diode. Liulin 1 and Liulin 2 are shown in blue and green. While the Liulins show a strong response to vibration and shocks, the MDT compensates well.

to motions related with the activities listed above (note the logarithmic scale of the count rates in the figure). The behaviour of the MDT is inconspicuous during the whole time. Besides the microphony, the count rates reflect the normal background radiation on Earth.

Additional measurements were performed within a shaking incubator (Infors HT Multitron, [SI] in list of datasheets) with 200 rounds per minute (rpm). Figure 3.15 shows in the left picture the MDT loosely taped to the carrier. In the right picture, the shaking incubator is captured in action. The MDT is indicated by the blue circle. This test could not be conducted with reference detectors, hence Figure 3.16 gives only the MDT count rate profiles of this test, proving its good performance.



Figure 3.15.: Vibration test with MDT-01-001 in a shaking incubator. The left panel shows the MDT taped to the carrier, the right panel shows the shaker in action and therefore appears to be blurry. The MDT is indicated by the blue ellipse.

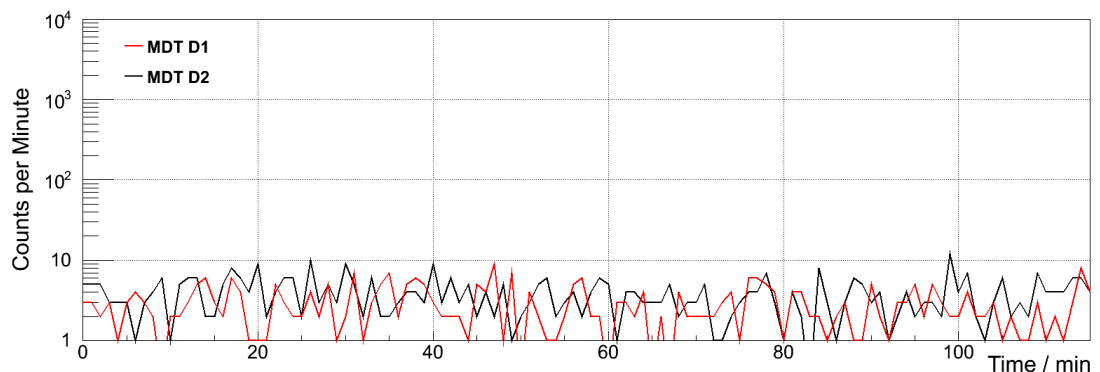


Figure 3.16.: MDT-01-001 count rate profile for measurement within the shaking incubator.

During measurements in aircraft that will be presented in Chapter 6, also no microphonic effects have been observed. It is understood that for space approval further tests are necessary, but the mechanical decoupling of the silicon diodes tested here is a major improvement compared to hard mounting of the sensitive detectors.

3.7. CHARACTERIZATION

Before the device can be calibrated with ionizing radiation, its behaviour is characterized. This includes electronic noise measurements defining the electronic resolution (Section 3.7.1) as well as the response of the electronics to different inputs (in frequency and amplitude, Section 3.7.2). For both measurements a signal generator (SG) is connected to the test input of the detector system. Negative step pulses with an exponential decay simulate incoming particles. Increasing the amplitude of the pulse simulates higher energy deposition in the detector.

Since the detector setup has a specific arrangement (telescope configuration), which has to be taken into account for measurements in a radiation field, the geometric properties are analyzed (Section 3.7.3).

3.7.1. RESOLUTION

Figure 3.17 shows the pulse height spectrum for a given input from the SG of 170 mV for the detector channel of the upper diode (diode 1) of prototype MDT-01-001 for low and for high gain. The peak is fitted by a Gaussian function, where the full width at half maximum (FWHM) is $\text{FWHM} = 2.355 \sigma$, with σ being the standard deviation. For high gain the FWHM is measured to about 6.5 channels and for low gain it results to 1 channel.

3.7.2. SYSTEM LINEARITY

The electronic system linearity (i.e. the electronics without the silicon detectors) shows how accurately the detector setup measures the deposited energy. In ideal case, this response is linear, but at least it has to be proportional, monotonous, and stable. The voltages at the test input range from 1 mV to 175 mV for the high amplification and 10 mV to 3.5 V for the low amplification stage.

Figure 3.18 shows the normalized result for high gain of the upper detector channel 1B of MDT-01-001. The error bars correspond to the FWHM of the test pulse peaks. Since

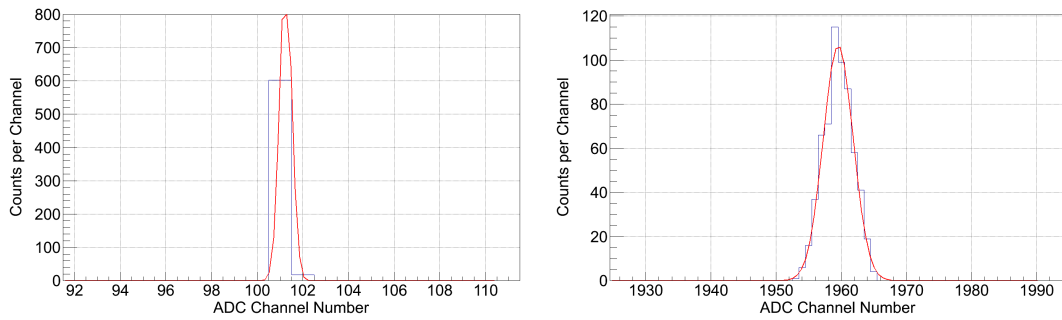


Figure 3.17.: Electronic resolution of the signal path for the upper diode of MDT-01-001, low gain A (left) and high gain B (right). Shown is the pulse height spectrum for an input voltage of 170 mV.

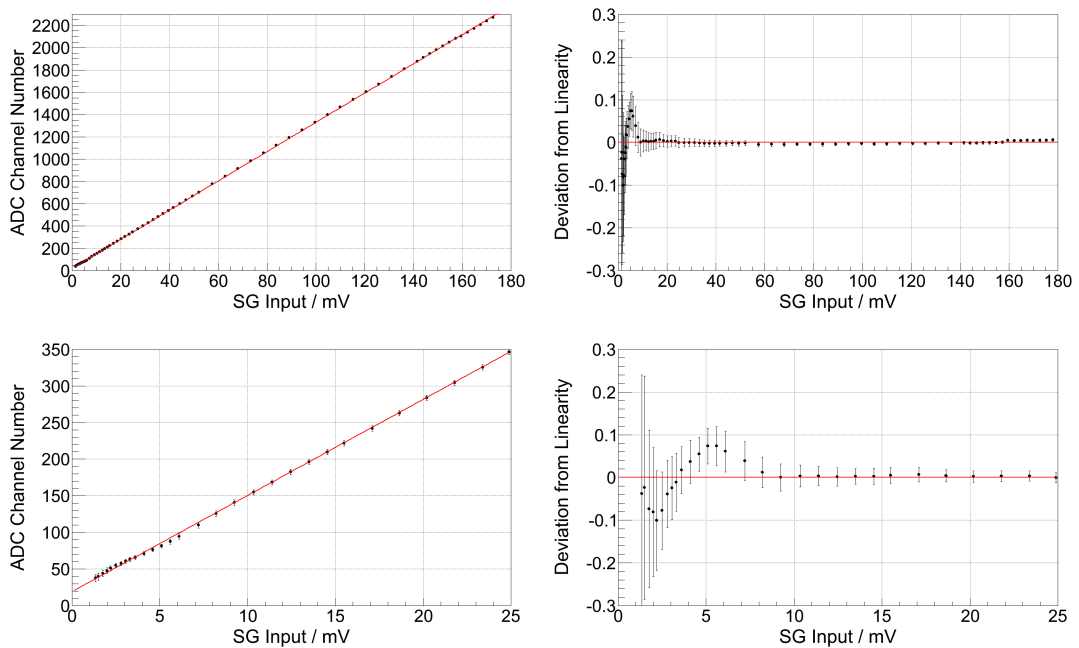


Figure 3.18.: Response of MDT-01-001 high gain channel 1B to input signals from the SG. The two top panels show the whole dynamic range of the channel, whereas the bottom panels zoom into the nonlinear range. In the left panels the direct output is plotted, which is normalized to show the relative deviation from a strict linear behaviour on the right panels. The red lines indicate an ideal linear response.

the electronic setup is the same for both detector channels and for low and for high gain, the performance is similar in all amplification stages for both detectors and only the results for one high gain channel is presented.

The first part of the dynamic range shows deviations from a strictly linear behaviour,

which is due to the nonlinear response of the peak detector for small signals. Since the high gain channels overlap with the nonlinear part of the low gain channels, only for high gain a correction for these deviations has to be applied.

The linear response of the detector setup including the silicon diodes will be shown in the calibration section (Chapter 4).

3.7.3. TELESCOPE AND GEOMETRY FACTOR

The response of every radiation detector depends on the detection material, the composition of the energy field it is applied for (i.e. particle species and particle energy) and on the detector's electronics. Additionally the geometrical configuration plays a role for the amount of energy that can be deposited in the detector as well as the pure count rate.

Considering the count rate, the dependence on the geometry is given by the geometry factor GF. The geometry factor is calculated by integrating over the upper hemisphere for an isotropic field distribution. With this field distribution the response of a planar detector follows according to Lambert's law the cosine of the angle of incidence θ that is defined with respect to the normal of the detector plane.

$$\text{GF} = \int \int \cos(\theta) \cdot \sin(\theta) \, d\theta \, d\phi \quad (3.1)$$

The detector introduced here is a telescope consisting of two rectangularly shaped planar silicon diodes.

For one single detector with a detection area A is after integrating Equation 3.1 simply given by (e.g. Sullivan 1971)

$$\text{GF}_{\text{single diode}} = \pi \cdot A \quad (3.2)$$

Considering the complete telescope, the geometry factor is not independent of ϕ , since the planar detectors are not spherically symmetric. To calculate, Sullivan (1971) provides an analytical approach. The expression in Equation (11) from this paper simplifies for two identical and squared diodes to⁶

⁶Note that for this simplification the formula remains unaffected by the Erratum (Sullivan, 1972).

$$\begin{aligned} \text{GF}_{\text{telescope}} = & d^2 \cdot \ln \left(\frac{d^2 + a^2}{d^2 (d^2 + 2a^2)} \right) - 4ad \cdot \arctan \left(\frac{a}{d} \right) \\ & + 4a(a^2 + d^2)^{\frac{1}{2}} \cdot \arctan \left(\frac{a}{(a^2 + d^2)^{\frac{1}{2}}} \right), \end{aligned} \quad (3.3)$$

where a is the edge length of the detectors and d the distance between them.

For the MDT setup, the area of each of the two Hamamatsu silicon diodes is $A = 1.21 \text{ cm}^2$, the edge length is $a = 1.1 \text{ cm}$, and the distance between the diodes is $d = 5 \text{ mm}$, resulting in the geometry factors

$$\text{GF}_{\text{single diode}} = 3.8 \text{ cm}^2 \text{ sr} \quad (3.4)$$

$$\text{GF}_{\text{telescope}} = 1.7 \text{ cm}^2 \text{ sr}. \quad (3.5)$$

The analytically obtained number for $\text{GF}_{\text{telescope}}$ is validated by a simple Monte Carlo program⁷ using the geometrical setup shown in Figure 3.19, in which the upper detector is chosen as source plane from which particles are shot in direction of the lower detector, while simulating an isotropic distribution. The relation of all particles that started in the upper detector to the particles that finally hit the lower detector, multiplied by the geometry factor of the upper detector gives the geometry factor of the whole telescope.

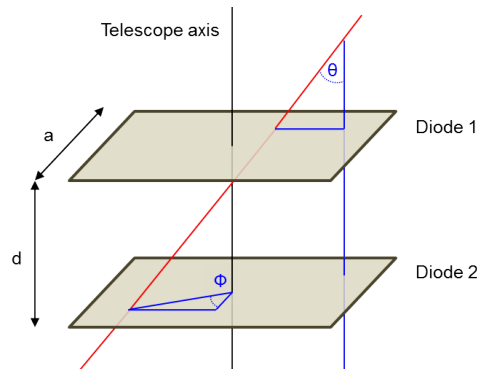


Figure 3.19.: Scheme of telescope setup with definition of θ and ϕ .

⁷J. Köhler (2012), private communication

From these simulations the number of particles that are detected can be shown in dependence on the angle of incidence θ , Figure 3.20(a). While for the single detector all angles of incidence $0^\circ < \theta < 90^\circ$ are allowed, the opening angle is restricted to 70° for the telescope geometry. The value is defined by the distance between the two diodes. The particle distribution for the single diode is shown in blue and for the telescope in red. Since the setup is not spherical symmetric, the response is also shown as a function of ϕ , Figure 3.20(b). Again, blue and red label single diode and telescope arrangement. The number of counts seen on the y-axes is in arbitrary units. Note that for the ϕ -dependence the number of particles is scaled down by a factor for better comparison and the y-axis is zoomed to show only the relevant section. The fact that the results for ϕ -dependence of single diodes is not completely constant is due to the limited number of particles used in the simulation. The increase for values of ϕ , where particles can traverse the telescope setup diagonally is clearly visible. Figure 3.21 shows the dependence on θ and ϕ together.

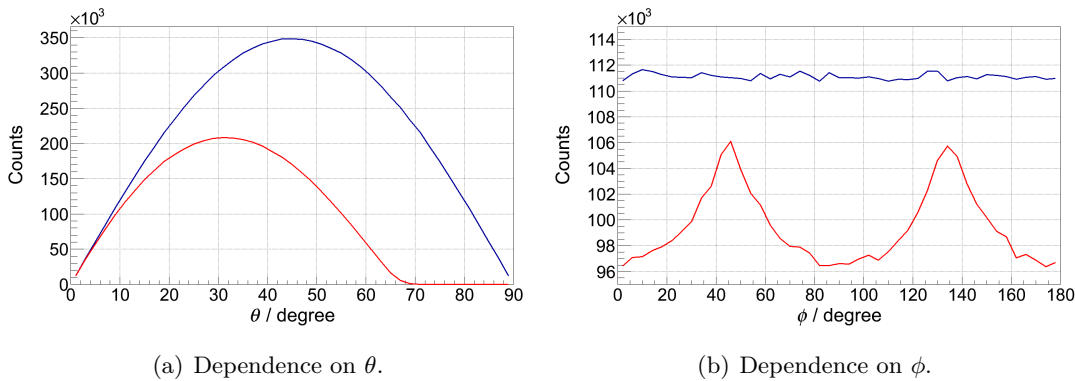


Figure 3.20.: The geometrical response in dependence on θ (a) and ϕ (b) is simulated for an isotropic field distribution and plotted for the single detector in blue and for telescope setup in red. For better visualisation the number of counts in (b) for the single diodes has been scaled down by a factor of two and the y-axis shows a zoom of the relevant section. The number of counts on the y-axes is in arbitrary units.

The mean incident angle for the telescope geometry for an isotropic radiation field is calculated to 32.45° , resulting for a detector thickness of $300 \mu\text{m}$ into a mean path length of $356 \mu\text{m}$ within an isotropic field distribution. The mean path length is required to calculate linear energy transfer spectra.

The maximum path length a particle can travel in one diode and still be detected in the second diode ($\theta = 70^\circ$) is $877 \mu\text{m}$.

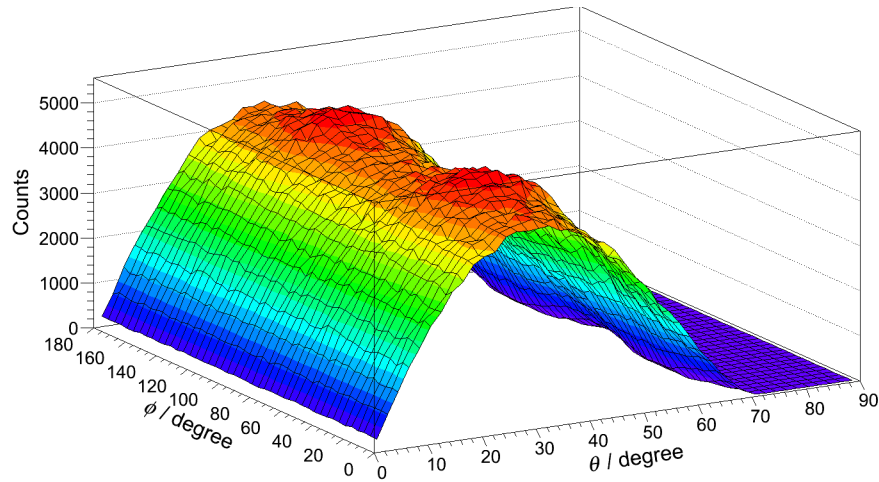


Figure 3.21.: Geometrical response of the telescope system – dependence on θ and ϕ . The number of counts of the y-axis is in arbitrary units.

3.8. SUMMARY

Within a number of development steps the electronics of the Mobile Dosimetric Telescope has been carefully designed from scratch to match the requirements of the radiation field in LEO in terms of speed and dynamic range as well as in terms of power consumption for the required battery operation. Eight electronics board versions have been developed, from which versions 06.01 and 08.01 are implemented in the final prototypes. Version 06.01 is the latest preamplifier board, while version 08.01 includes the rest of the signal processing analog and digital electronics. Two preamplifier boards, one for each of the two silicon diodes that build the telescope configuration, and one signal processing board are implemented in one prototype. Two prototypes with the same electronics are realized and labelled by MDT-01-xxx-DLR-CAU, where 'xxx' refers to the prototype versions '000' and '001'.

Due to time constraints and the process of development, the housing of both prototypes is different.

The electronics has been intensely tested with pulse generators and the geometrical setup of the telescope been quantified. A countermeasure for microphonic effects has been introduced and successfully tested.

In the following chapters the MDT is calibrated and measurements are performed in field tests.

CALIBRATION

The energy calibration of the Mobile Dosimetric Telescope (MDT) requires a variety of calibration sources as it covers an energy range of 3.5 orders of magnitude. For the low energy range, radioactive isotope sources provide an excellent source of mono-energetic particle radiation, such as gamma radiation, mono-energetic electrons, and alpha particles (Sections 4.1 and 4.3.1). However, even alpha particles from alpha decay do not exceed energies of approximately 6 MeV and are therefore not suitable for the calibration of the high energy range of the detector that is supposed to detect relativistic heavy particles from galactic cosmic radiation. The only possibility to simulate these on Earth are particle accelerators (Sections 4.2 and 4.3.2).

The calibration procedure presented in this chapter shows the details about diode 1 of MDT-01-001. The calibration procedure is representative for diode 2 of the same prototype as well as for both diodes of MDT-01-000. The corresponding figures for these can be found in Appendix C and the results for both MDTs are listed in Section 4.3.3.

As in the previous chapter high gain denotes the high amplification stage (B) covering small energy depositions in the detector, whereas low gain refers to the low amplification stage (A) detecting large energy depositions. Also diode 1 labels the top and diode 2 the bottom diode in the respective telescope arrangement.

4.1. MEASUREMENTS WITH RADIOACTIVE ISOTOPE SOURCES

For calibration of the low energy range, Americium-241 (^{241}Am) and Bismuth-207 (^{207}Bi) were used. Measurements with ^{241}Am were conducted at the Institute for Experimental and Applied Physics (IEAP)¹ at the Christian-Albrechts-University Kiel in Kiel (CAU) and at the Radiation Biology Department of the Institute of Aerospace

¹<http://www.ieap.uni-kiel.de/>

Medicine² at the German Aerospace Center (DLR) in Cologne. The measurements with ²⁰⁷Bi were performed at the CAU, Kiel, only.

4.1.1. AMERICIUM-241

The most dominant gamma line ²⁴¹Am emits has an energy of $\gamma = 60$ keV. Since this corresponds to the lower detection limit desired, it provides a suitable starting point for calibration. ²⁴¹Am has additionally three prominent alpha lines of $\alpha_1 = 5.389$ MeV, $\alpha_2 = 5.443$ MeV, and $\alpha_3 = 5.486$ MeV.

Figure 4.1 shows the 60 keV gamma line for diode 1 of detector MDT-01-001 in the high gain channel.

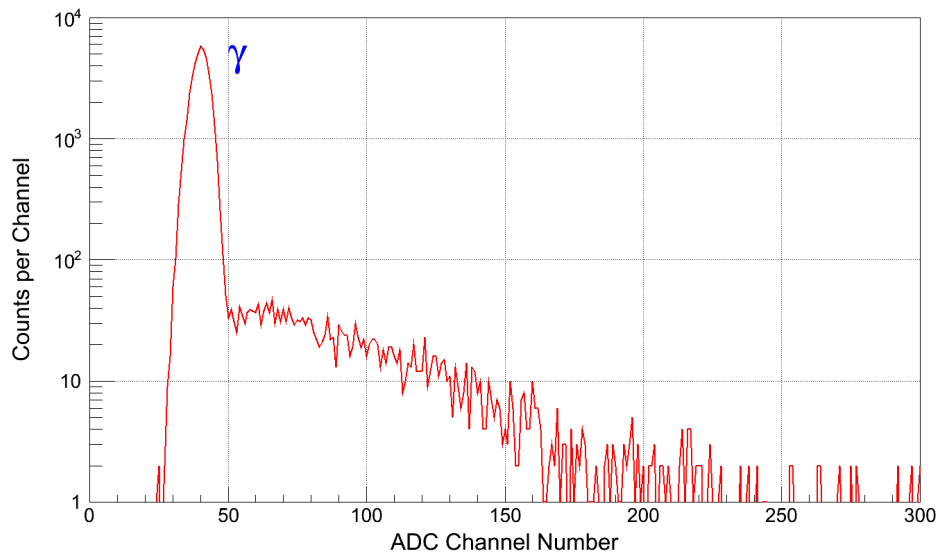


Figure 4.1.: 60 keV γ line of ²⁴¹Am, detected with diode 1 of MDT-01-001.

Measurements with alpha particles were conducted with the detector placed inside a vacuum chamber under a pressure of 0.1 mbar. The distance to the source was 5 cm, resulting in a maximum energy loss of less than 1 keV (calculated with *SRIM*³, Ziegler et al. 2012), which can be neglected.

Figures 4.2 and 4.3 show the three dominant alpha lines (α_1 , α_2 , α_3) of ²⁴¹Am. The satellite peak (**S**) on the left of the alpha lines in Figure 4.2 results from those

²<http://www.dlr.de/me/desktopdefault.aspx/tabid-1933/>

³The Stopping and Range of Ions in Matter, <http://www.srim.org>

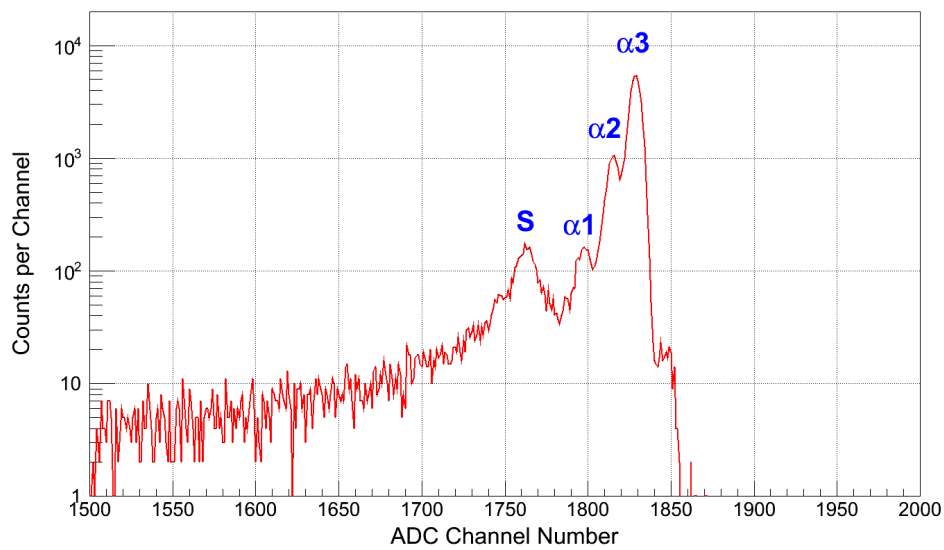


Figure 4.2.: ^{241}Am α lines and satellite peak (S) for MDT-01-001 diode 1.

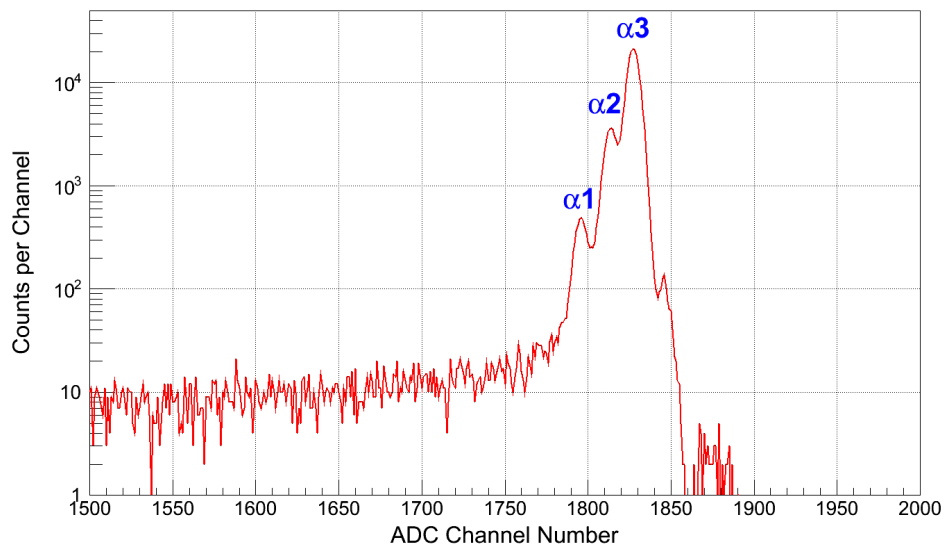


Figure 4.3.: Same as Figure 4.2, but the aluminum frame of the diode is covered to suppress the satellite peak.

alpha particles that traverse through the contact aluminium frame of the silicon diode (compare Section 3.4.3 and Figure 4.4). Covering this part of the diode during irradiation removes the satellite peak in the pulse height spectrum (Figure 4.3). By fitting the $\alpha 3$ line and the main satellite peak the energy loss of the particles can be

calculated, resulting in a thickness of the contact layer of $1.3 \mu\text{m} \pm 0.1 \mu\text{m}$. During measurements with heavy ions (Section 4.2) such a layer on the diode can lead to an energy loss shift for the ions traversing the frame before being detected. This would lead to an increase in the energy depositions from these ions and would be visible at higher energies with respect to the calibration peak. However the aluminium frame is sufficiently thin and no such effect is observed.

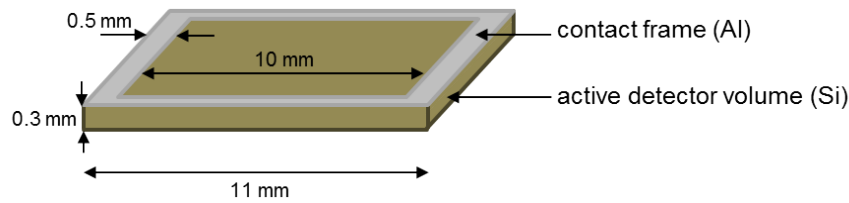


Figure 4.4.: Sketch of the silicon diode visualizing the aluminium contact frame, which is responsible for the satellite peak (S, Figure 4.2), since alpha particles traversing through the aluminium contact frame lose some of their energy before hitting the active detector material beneath.

For calibration all three main alpha lines and the gamma line were fitted by Gaussian distributions.

The measurements for detector MDT-01-000 and diode 2 of detector MDT-01-001 are shown in Figure C.1 to Figure C.3 and Figures C.4 to C.6 for γ and α lines, respectively, in Appendix C.

Fit results for all measurements are listed in Table D.1 in Appendix D.

4.1.2. BISMUTH-207

^{207}Bi shows six dominant lines from mono-energetic electrons that are created by internal conversion. Four of these lines are together in two pairs ($e_2 = 553.8 \text{ keV}$, $e_3 = 565.9 \text{ keV}$ and $e_5 = 1047.8 \text{ keV}$, $e_6 = 1059.8 \text{ keV}$). In this setup the paired lines overlap due to insufficient energy resolution which makes them not suitable for calibration. The two single lines ($e_1 = 481.7 \text{ keV}$ and $e_4 = 975.7 \text{ keV}$) are fitted by a Gaussian distribution, after the background has been subtracted by two power laws (Figure 4.5).

Measurements were done within a grounded metal box to shield the detector from light and with a distance of 4 to 6 cm between source and silicon diode resulting in

a mean energy loss of about 10 keV (calculated with *ESTAR*⁴, Berger et al. 2005), which is accounted for in the corresponding uncertainty estimation.

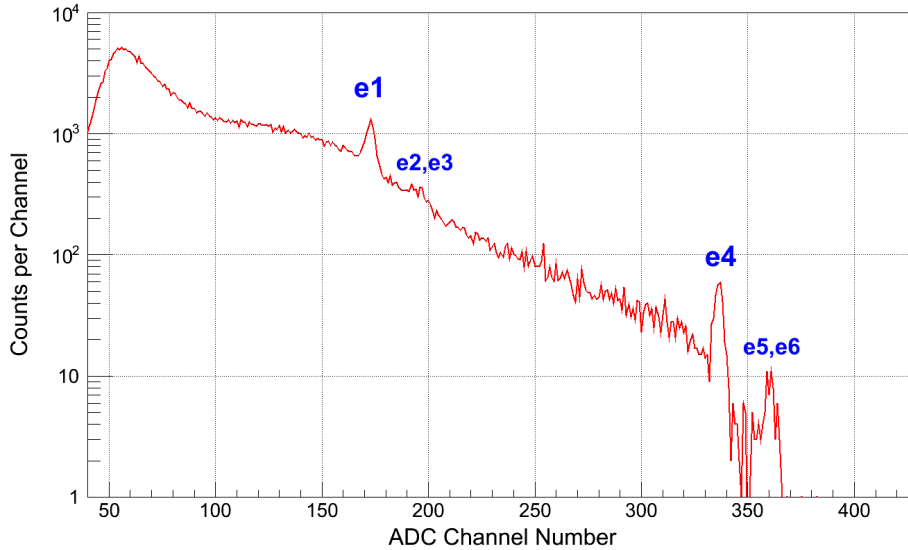


Figure 4.5.: ²⁰⁷Bi measurement for MDT-01-001 diode 1.

Figure C.7 to Figure C.9 in Appendix C show the results of bismuth measurement for the other diodes of the two MDT prototypes.

The fit results for bismuth measurements can be found in Table D.1 in Appendix D.

4.2. MEASUREMENTS WITH HEAVY IONS

4.2.1. IRRADIATIONS

Experiments with heavy ions were performed at the Heavy Ion Medical Accelerator (HIMAC) of the National Institute for Radiological Sciences (NIRS) in Chiba, Japan⁵. The facility is used for cancer therapy with charged particles and for related biological and physical experiments. Besides two linear accelerators, HIMAC contains two synchrotron rings that can accelerate ions from H to Xe to a maximum energy of 800 MeV u⁻¹.

⁴Stopping-power and range tables for electrons,

<http://physics.nist.gov/PhysRefData/Star/Text/ESTAR.html>

⁵<http://www.nirs.go.jp/ENG/index.html>

From the synchrotron, several beam lines lead to three therapy rooms and to different experimental irradiation rooms, like the physical and general purpose and the biological purpose room (in the following referred to as Physics and Biology room, respectively). Calibration measurements for the MDT were performed in both of these rooms. The ion beam in the Physics room is focussed to a diameter of 1 cm^2 , allowing irradiation of the MDTs subsequently only, while it is broadened to 10 cm^2 for applications in the Biology room, enabling irradiation of both MDTs at the same time. The beam has a pulse period of 3.3s with a spill duration of 0.5s to 1.5s, depending on the particle species and their energy. The number of particles per spill can be tuned to low intensities and is monitored by scintillation counters in front of the beam exit. The beam intensity for the measurements was chosen to 100 to 300 particles per spill. Thereby the electronics of the detector system is not overstrained, as it is designed for low intensities, especially from high energetic particles. Irradiations with the primary beam (i.e. without any absorber in the beam path, compare Chapter 5) of any specific ion have lasted for 15 min to 30 min to ensure good statistics.

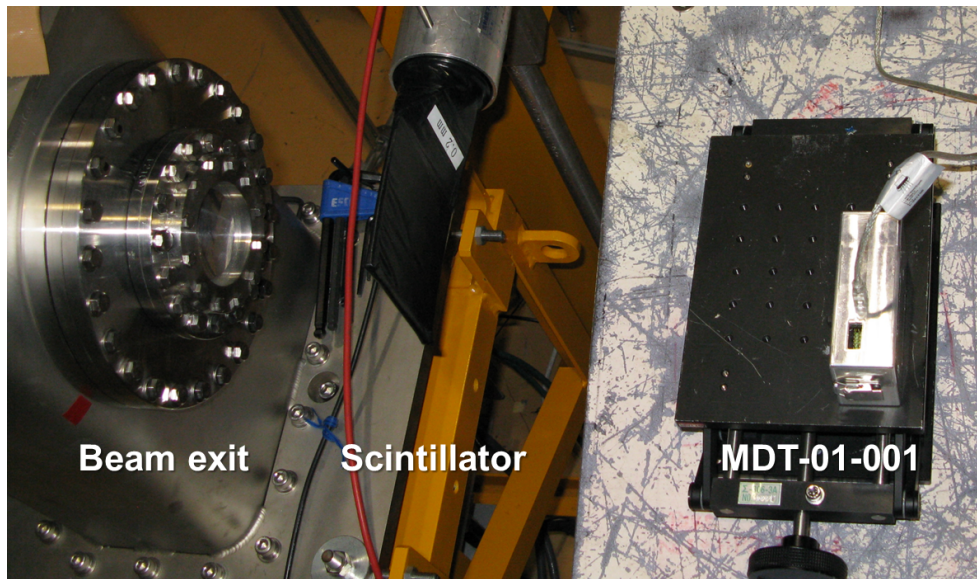


Figure 4.6.: Irradiation setup at HIMAC for detector MDT-01-001 in the Physics room, shown from the top. On the left hand side the beam exit is visible. The scintillation counter for beam monitoring is placed behind the beam exit. Downstream of the scintillator MDT-01-001 is connected via a USB cable with a laptop for online read-out.

Figure 4.6 shows the irradiation setup for MDT-01-001 in the Physics room. The detector is connected to a laptop via the USB interface for real-time read-out.

Table 4.1 gives an overview of the ions and their respective energy applied for this work. Calculations of the energy depositions of the heavy ions in each detector were performed with *SRIM*. The energy deposition in silicon given in the fifth column is calculated from the primary energy of the particles. For calibration, the energy loss in the beam path of the complete experiment setup (i.e. counting scintillator, air, aluminium case of prototype, top diode in case for the bottom diode) is taken into account when calculating the mean energy loss. The exact energies used for each prototype and each diode are listed in Table D.2 in Appendix D. Errors in the energy are calculated assuming an initial energy uncertainty of the incoming particles of 5%.

Table 4.1.: Overview of ions used for calibration. The table gives the ion species in the first column, followed by the energy per nucleon and the total energy. Also the energy loss in silicon is given as well as the total energy deposition in 300 μm thick silicon diodes. The comment in the last column denotes the experimental room at HIMAC, PH being the Physics and BIO the Biology room. The energy loss is calculated with *SRIM*.

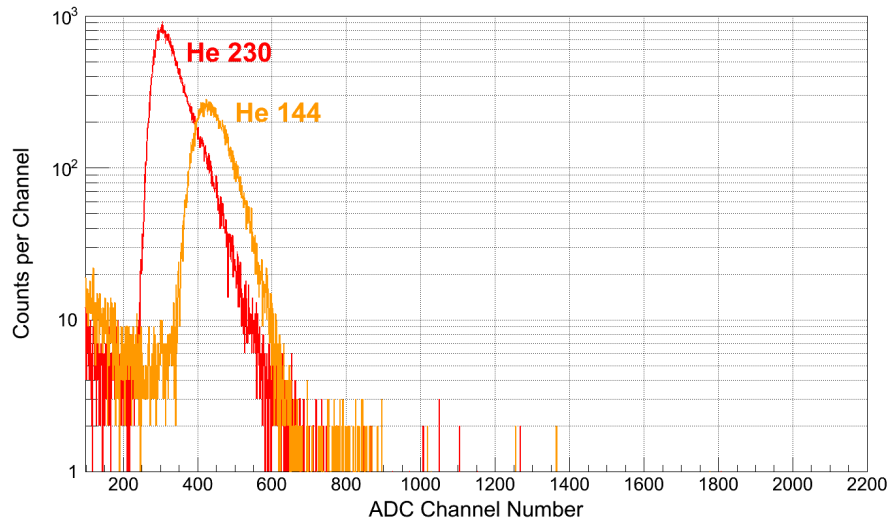
Ion	Energy (MeV u ⁻¹)	Total Energy (GeV)	Energy Loss in Si (keV μm^{-1})	Energy Deposition (MeV)	Comment
⁴ He	230	0.92	3.1	0.9	PH
⁴ He	144	0.58	4.2	1.3	BIO
¹⁴ N	400	5.6	27.7	8.3	PH
¹⁶ O	400	6.4	36.3	10.8	PH
²⁰ Ne	400	8.0	56.2	16.9	PH
²⁸ Si	600	16.8	94.2	28.3	PH
⁴⁰ Ar	400	16.0	190.9	57.3	PH
⁴⁰ Ar	290	11.6	225.8	67.7	PH
⁵⁶ Fe	490	28.0	341.9	102.6	PH

During beam time at HIMAC additional experiments were performed, in order to test, if the detector system is able to resolve individual fragments produced in an absorber between the beam exit and the detector. The measurements and results are presented in Chapter 5. The results are also applied for verification of the MDT calibration.

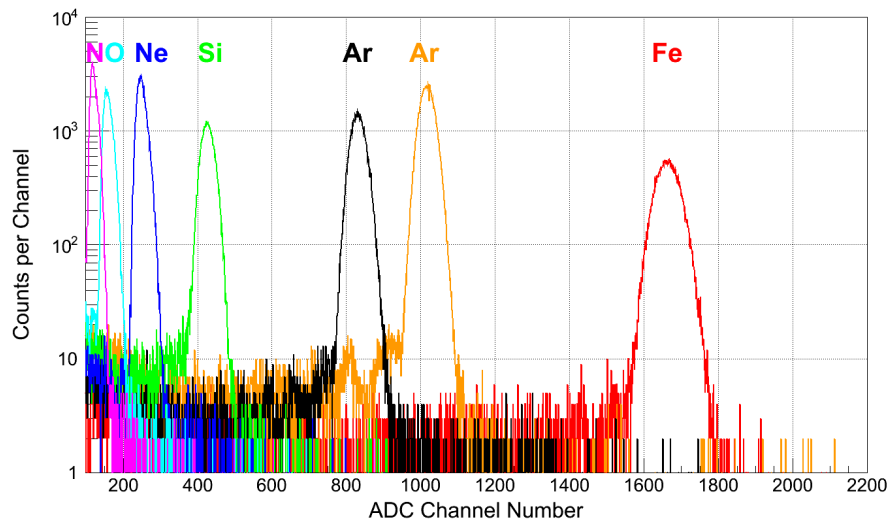
4.2.2. PULSE HEIGHT SPECTRA AND FITTING

The recorded pulse height spectra for diode 1 of MDT-01-001 are shown in Figure 4.7. Due to the low energy deposition of helium compared to other heavy ions, the pulse height spectra do not fall into the low gain range, but into the high gain range.

Spectra of heavy ion measurements with both diodes of MDT-01-000 and diode 2 of MDT-01-001 are shown in Figures C.10 to C.12 in Appendix C.



(a) High gain



(b) Low gain

Figure 4.7.: Pulse height spectra of measured ions for MDT-01-001 diode 1 in the high gain (a) and in the low gain channel (b). The corresponding ion energies, the energy depositions in the detector, and the fit results are listed in Table D.2 in Appendix D.

The pulse height spectra of each ion are fitted by a Vavilov distribution (Section 2.2.3). Figure 4.8 gives three examples of helium ($3 \text{ keV } \mu\text{m}^{-1}$), oxygen ($36 \text{ keV } \mu\text{m}^{-1}$) and

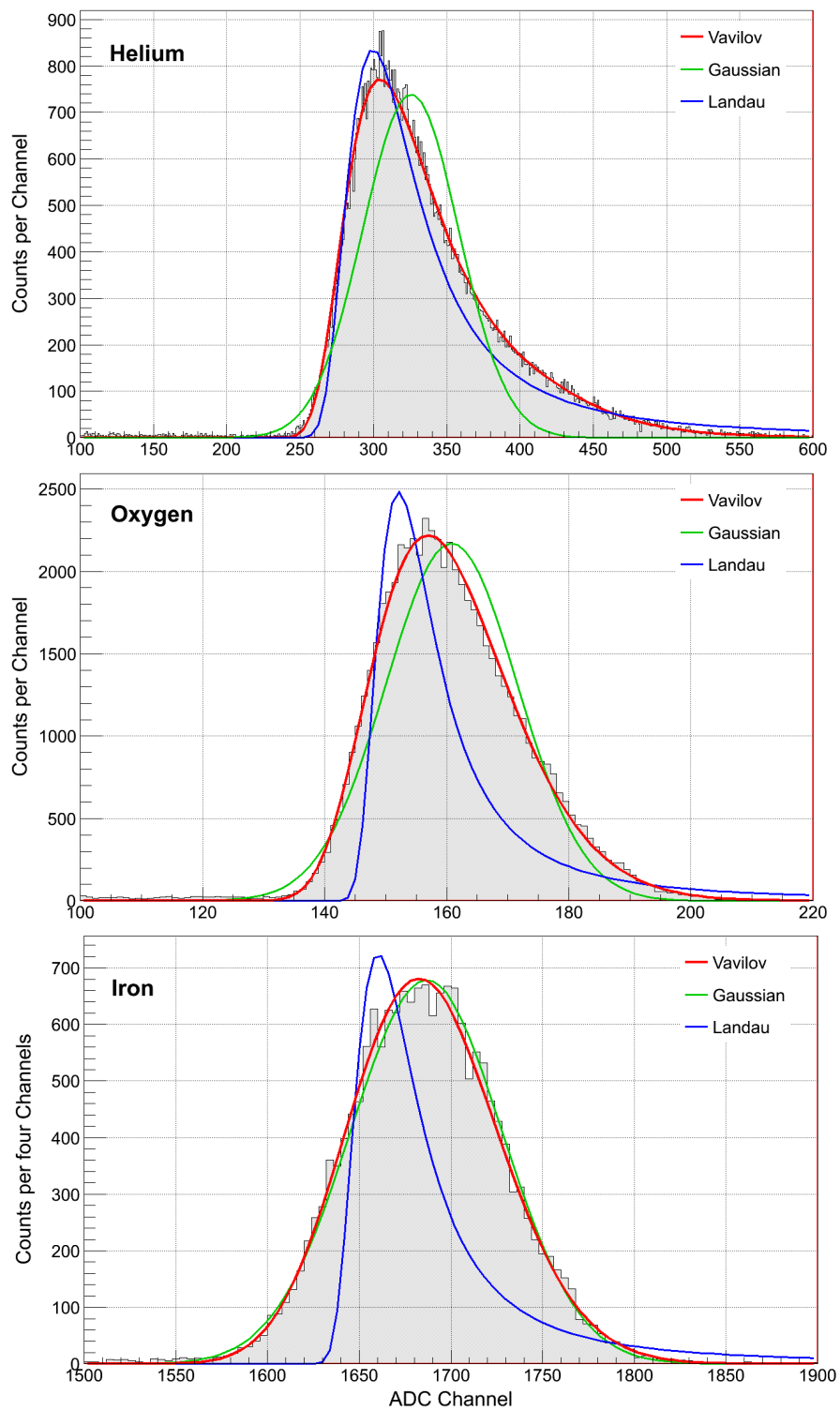


Figure 4.8.: Vavilov fit for measured helium of 230 MeV u^{-1} (top, high gain), oxygen of 400 MeV u^{-1} (middle, low gain) and iron of 490 MeV u^{-1} (bottom, low gain) for MDT-01-001 diode 1. Note that the energy loss in silicon covers about two orders of magnitude, i.e. about $3 \text{ keV } \mu\text{m}^{-1}$, $36 \text{ keV } \mu\text{m}^{-1}$ and $342 \text{ keV } \mu\text{m}^{-1}$ from top to bottom (Table 4.1).

iron ($342 \text{ keV } \mu\text{m}^{-1}$) that cover energy losses in silicon of two orders of magnitude. Additionally Landau and Gaussian distributions are plotted, showing how the shape of the energy loss distribution changes with increasing energy loss in the silicon detector. The Vavilov distribution is parameterized by the mean energy loss, $\beta^2 = v/c$ and κ (Equation 2.4). Since the incident energy of the ions is given, β^2 is used as an input parameter. The parameter κ for the three examples resulted in $\kappa_{\text{He}} = 0.14$, $\kappa_{\text{O}} = 0.61$ and $\kappa_{\text{Fe}} = 15$. The uncertainties exceed however 20%, as already slight changes in the shape of the distribution, e.g. due to binning of the data or the selection of the fitting window, have already a strong influence on the parameter. This hampers a quantitative evaluation of the parameters, although the expected trend that with increasing energy loss κ increases is confirmed. It becomes clear that for stabilizing the shape of the distribution and thereby providing good results for κ much higher statistics is required, which will be taken into account for upcoming measurements. As the distribution is also dependent on β^2 , a further investigation should focus on ions of the same energy per nucleon.

Fitting of the distributions was conducted with the data evaluation software *ROOT*⁶ (Brun and Rademakers, 1996), based on C⁺⁺. The provided mean of the distribution provided by the program is stable and is employed for calibration, using the standard deviation as uncertainty range. The fit results are given in Table D.2.

4.3. CALIBRATION OF THE MDT

4.3.1. HIGH GAIN

For the energy calibration of the high gain channels, measurements of 60 keV photons and alpha particles from ^{241}Am as well as mono-energetic electrons from ^{207}Bi are applied.

Figure 4.9 shows the linear calibration curve with the two Bi lines (e1 and e4, lower left) and the three alpha lines (upper right). For validation the results of HIMAC helium ion measurements (144 MeV u^{-1} and 230 MeV u^{-1}) are included in the figure (lower left with large errorbars). The linear calibration curve is not plotted for ADC channels below 120, since this nonlinear part was fitted with a polynomial function using the results from measurements with the signal generator (compare Section 3.7.2). Applying the result for 60 keV photons scales the voltage input of the signal generator

⁶<http://root.cern.ch/>

to the corresponding energy. Polynomial and linear part are then merged to calibrate the complete high gain channel.

The green 'X' in the upper right corner of Figure 4.9 shows the value that is taken to calibrate the transition to the low amplification channel (compare also Figure 4.10).

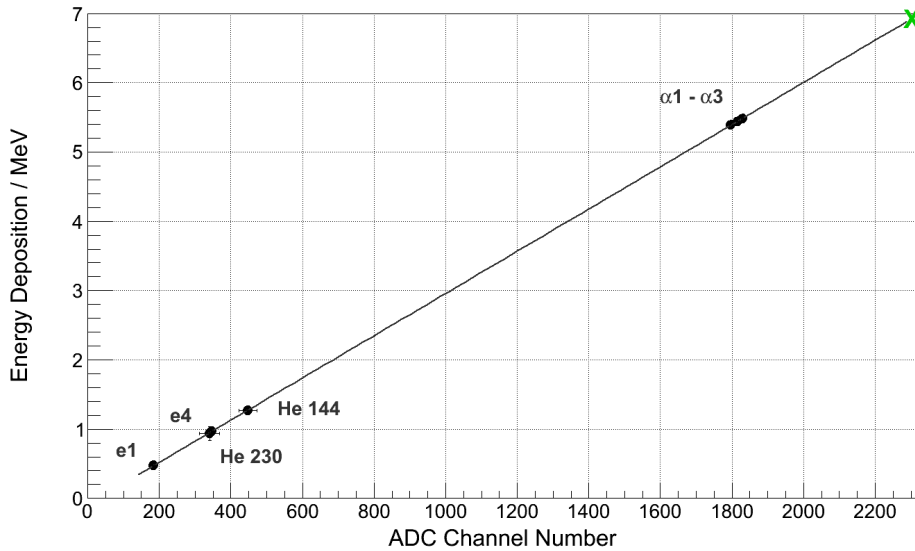


Figure 4.9.: High gain calibration curve for MDT-01-001 diode 1. The green 'X' denotes the transition point to low gain. The nonlinear part (Section 3.7.2) in the low energy range is excluded.

The high gain calibration curves of diode 2 of MDT-01-001 and of both diodes of MDT-01-000 are shown in Figures C.13 to C.15 in Appendix C.

4.3.2. LOW GAIN

In Figure 4.10 the linear calibration curve for the low gain channel 1A of detector MDT-01-001 is shown. All heavy ions measured in the low gain channel are included and are fit together with the calibrated transition to the high gain channel (green 'X', compare also Figure 4.9).

As mentioned before (Section 3.7.2), the nonlinear part of the low gain channel is completely covered by the high gain channel and does not need to be taken into account.

The results in the high energy range are not exactly on the linear calibration curve (Ar and Fe). This behaviour is the same in each low gain channel of both prototypes (compare also Figures C.16 to C.18 in Appendix C) and seems to be systematic.

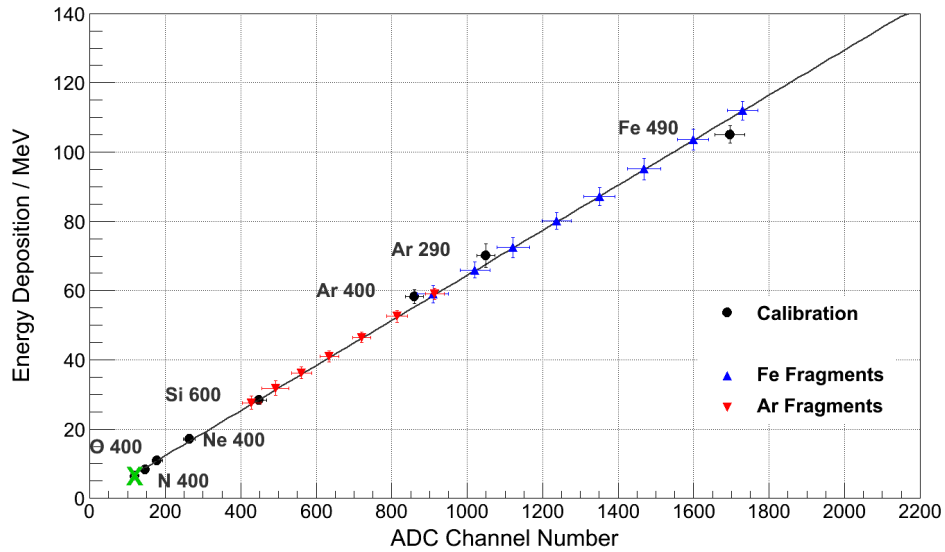


Figure 4.10.: Low gain calibration curve for MDT-01-001 diode 1. In black the calibration data is shown and the triangles represent fragmentation data that is discussed in Chapter 5. Blue triangles are iron fragments (from right to left: Fe, Mn, Cr, V, Ti, Sc, Ca, K), while the red triangles represent fragments from argon of 400 MeV u^{-1} (Ar, Cl, S, P, Si, Al, Mg). The green 'X' shows the transition point to high gain.

The linear response of the detector has been verified with test pulses from a signal generator (Section 3.7.2) over the complete dynamic range. To nevertheless exclude nonlinearities in the detector response, results from fragmentation measurements of Ar (400 MeV u^{-1} , red triangles) and Fe (490 MeV u^{-1} , blue triangles) are shown. The original calibration curve is applied to the fragment data and the uncertainties of the data points represent the FWHM of the respective fits in the ADC channel and in the energy calibrated data (Section 5.2.3). The fact that all fragments are linearly aligned prove the linearity and stability of the detector system. The fragment data is not employed for the actual calibration as the results (and therefore the uncertainties) are dependent on the primary particle that is already used for calibration. Additional uncertainty arises from the energy loss in the fragment producing absorber in the beam path.

The fragment measurement and identification are described in Chapter 5.

It is not clear where the discrepancies of argon and iron ions result from. Electronic nonlinearities are excluded by measurements with the signal generator and the fragment data, baseline drifts and gain changes in this order of magnitude between the mea-

measurements (they were taken at with a separation of few months) were not observed in other measurements during this time and are additionally highly unlikely to manifest in exactly the same way in all four diodes. Possible origins remain underestimated uncertainties in the energy of the ions or imperfections in the estimations of the energy depositions in the detector. Also systematic errors in the experimental setup are possible. Further measurements of ions in this mass and energy range are required. Nevertheless this hardly affects the results presented in the rest of this work, like the dose calculation from flight measurements presented in Chapter 6, as the energy depositions are mainly located in the high gain channel.

4.3.3. RESULTS

The linear calibration curves are fitted by

$$E_i = a \cdot ADC_i + b, \quad (4.1)$$

where E_i is the energy corresponding to the analog to digital converter value ADC_i . The fit parameters a and b for low and high gain are listed in Table D.3 in Appendix D. The calibration results for both prototypes are listed in Table 4.2, giving for each detector and diode the dynamic range of the ADC and the corresponding energy range for high and low gain separately.

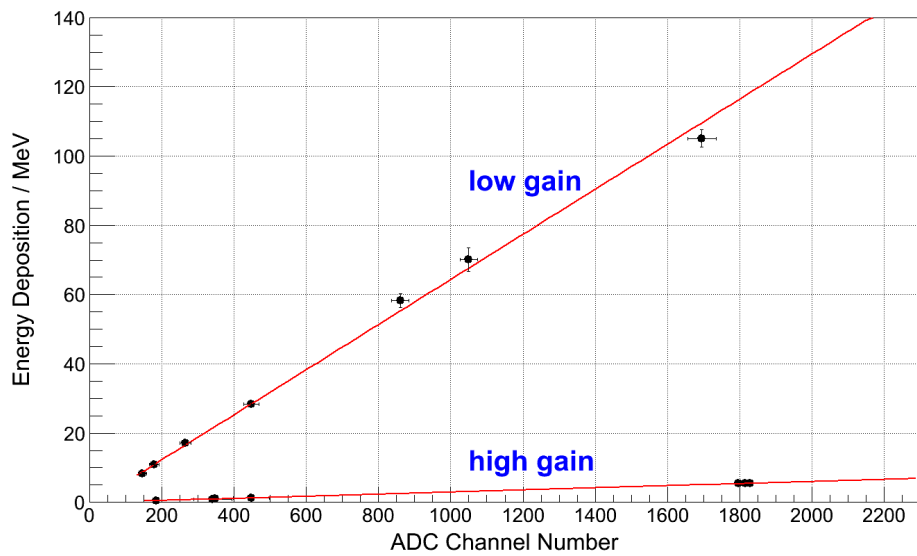
In general the linear fits do not intercept the origin for two reasons. The linear fits do not take into account the nonlinearity in this range and an artificial baseline offset is included for improved electronic performance.

To visualize the different energy ranges covered by the two amplification stages low and high gain, Figure 4.11 shows both calibration curves in one plot.

The calibration of both MDT prototypes led to satisfying results, as the envisaged energy range of more than 3.5 decades of measurable energy depositions from 0.06 MeV to about 140 MeV could be covered. Slight differences in the gains of each detector channel are expected and result from small uncertainties in the individual electronic components. It should be noted that not the silicon diodes are the limiting factor of the dynamic range, but the amplitude of the preamplifier and especially the response of the peak detector to small signals (compare e.g. Section 3.7.2).

Table 4.2.: Calibration results for MDT-01-000 and -001 for both diodes.

Detector	Diode	Amplification Channel	ADC Value Range	Energy Range MeV
MDT-01-000	1	high (B)	20 - 2300	0.06 - 6.66
		low (A)	107 - 2200	6.66 - 136.1
	2	high (B)	26 - 2300	0.06 - 6.51
		low (A)	104 - 2200	6.51 - 135.0
MDT-01-001	1	high (B)	40 - 2300	0.06 - 6.92
		low (A)	106 - 2200	6.92 - 142.2
	2	high (B)	48 - 2300	0.06 - 6.87
		low (A)	107 - 2200	6.87 - 140.1

**Figure 4.11.:** Low and high amplification for diode 1 of detector MDT-01-001.

FRAGMENT MEASUREMENTS

The interaction of cosmic radiation with the material of the International Space Station (ISS) modifies the primary spectra into an even more complex radiation field. Inside the space station, parts of the low energetic region of the spectra will be cut, but also cascades of secondary particles are produced, among them fragments of the primary heavy ions. Hence fragment measurements are an important tool to investigate these interactions and effects (e.g. Zeitlin et al. 2008).

Additionally, producing fragments with a high Z particle creates an approximate 'mono-energetic mixed' radiation field, as most of the heavy fragments can be assumed to have retained the velocity of the primary particle (Westfall et al., 1979), providing a useful tool to test the performance of the developed Mobile Dosimetric Telescope (MDT) within a radiation field that is composed of some of the high energetic constituents of the radiation field in low Earth orbit (LEO).

Section 5.1 describes the experimental setup and Section 5.2 presents the results on the energy deposition in the detectors (Section 5.2.1), before the individual fragments are identified by their charge (Section 5.2.2). The results are applied to the low gain calibration curve (Section 5.2.3) and finally uncertainties due to ionization losses in the fragment producing material are discussed (Section 5.2.4). Section 5.3 gives the summary.

5.1. MEASUREMENTS

Fragment measurements have been performed with both detectors for argon ions of 400 MeV u^{-1} and for iron ions of 490 MeV u^{-1} . The data presented here are from iron ion measurements with the prototype MDT-01-000. The procedure of measurements with heavy ions at the Heavy Ion Medical Accelerator (HIMAC) at the National Institute of Radiological Sciences (NIRS) in Japan has been described in Section 4.2. For calibration, the MDTs have been irradiated with a primary beam of 490 MeV u^{-1} iron ions. For fragmentation measurements a polyethylene (CH_2) absorber of 1 cm

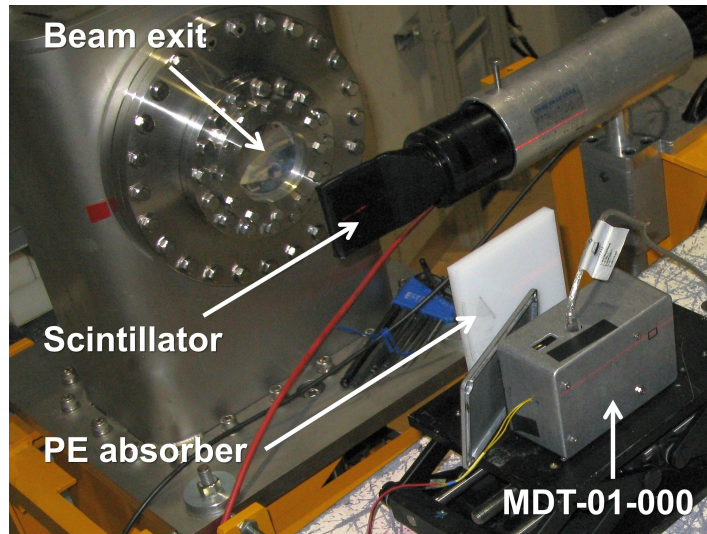


Figure 5.1.: Irradiation setup for fragment measurements with iron of 490 MeV u^{-1} and MDT-01-000. The beam exit is visible in the back on the left, downstream the beam line the counting scintillator (Section 4.2), the 1 cm thick polyethylene (PE) absorber, and the detector are placed.

thickness is inserted into the beam path (Figure 5.1). Iron ions passing through this absorber undergo interactions described in Section 2.2.1. The particles lose energy due to coulomb interactions with the polyethylene. This leads to an increase in the linear energy transfer and hence to a shift of the iron peak in the pulse height spectrum to higher energies by a few MeV, compared to the primary beam measurements. Additionally fragmentation due to direct nucleus-nucleus collisions occur. Heavy fragments with charge numbers Z close to the primary particle are produced by peripheral collisions. Individual nucleons and light fragments are removed from the projectile, but its direction of incidence remains mainly unchanged. In central collisions rather light fragments with a broader angular distribution are generated (Zeitlin et al., 1996b).

By choosing a relatively thin absorber of 1 cm of low mass number elements, the fragment production is not highly efficient, but the probability of multiple subsequent fragmentation processes is kept low. Additionally the fragment velocity distribution does not broaden further (Section 5.2.4), enabling a better charge identification of the produced particle species.

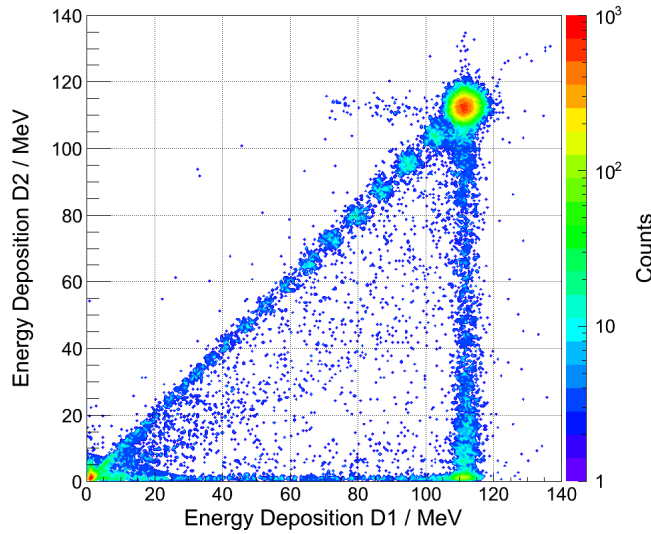


Figure 5.2.: Measurements of iron fragments. The number of events in arbitrary units is shown in color code in logarithmic scale.

5.2. RESULTS

5.2.1. ENERGY DEPOSITIONS

Figure 5.2 shows the two dimensional scatter plot of the energy depositions in diode 2 (D2, lower diode in telescope arrangement) versus the energy deposition in diode 1 (D1, upper diode) from fragmentation irradiations with iron nuclei. The number of events in color code is arbitrarily normalized to 1000 and shown in logarithmic scale. The spectrum still consists mainly of iron ions (prominent peak in the upper right). Along the angle bisector (45° line) towards lower energies, distinct spots are visible. These belong to nuclei that fragmented in the polyethylene absorber in front of the detector. Events that are detected below the angle bisector arise from particles that hit due to scattering processes only the edge of the second detector, from fragments or from other secondaries. Particles depositing energies according to the primary particle in the first, but less in the second diode ('vertical bar' structure below the iron peak in the figure) are fragments produced in the silicon or in the ceramic carrier of the first diode (compare also measurements from La Tessa 2007). The 1.1 mm thick ceramic carrier of the diodes extends under the complete area of the silicon layer (see datasheet of diode [S3590-19]), hence before a particle hits the second diode, it has to traverse this layer of diode 1 first.

Energy depositions at low energies are due to protons and other low ionizing secondaries. The protons can already be produced in the beam exit window (100 μm of aluminium) or in the counting scintillator in the beam path. This energy deposition component is also present during calibration irradiations with the primary beam.

5.2.2. CHARGE IDENTIFICATION

After fragmentation, more than one fragmentation product can hit the detector at the same time. A specific energy loss measured is therefore the sum of the energy losses of all participating fragments

$$\left(\frac{dE}{dx}\right)_{\text{detected}} = \sum_i \left(\frac{dE}{dx}\right)_i, \quad (5.1)$$

where i labels all individual fragmentation products hitting the detector. The energy loss of each particle integrated over the detector thickness results in the energy deposition in the detector, in the following denoted by E , hence Equation 5.1 becoming $E_{\text{detected}} = \sum_i E_i$.

From now on the consideration is restricted to particles detected along the angle bisector of the plot, as these can be assumed to be particles of the same type and energy passing both diodes perpendicularly.

For the assumption that the leading fragment (lf) with Z_{lf} within a few charge units of the primary particle dominates the energy deposition, Equation 5.1 can be approximated by

$$E_{\text{detected}} = \sum_i E_i \approx E_{\text{lf}}. \quad (5.2)$$

Since all leading fragments are rather heavy particles, their velocity does not differ significantly from the velocity of the primary particle. According to the Bethe-Bloch formula (Equation 2.2) the energy loss of heavy particles with charge Z is in the same target material then in first approximation solely dependent on Z^2 . Hence the ratio of the detected energy deposition of the leading fragment to the energy deposition of the primary particle $E_{\text{lf}}/E_{\text{p}}$ corresponds to the ratio of the squared charge number of the leading fragment Z_{lf}^2 to the squared charge number of the primary Z_{p}^2 , resulting in the relation

$$Z_{\text{lf}} \approx Z_{\text{p}} \cdot \sqrt{\frac{E_{\text{lf}}}{E_{\text{p}}}} \quad (5.3)$$

Z_p is equal to 26 and E_p for each diode is obtained by a Gaussian fit of the main peak. This approach is justified as due to the large energy transfer, the energy loss distribution has sufficiently approached a Normal distribution (compare Section 2.2.3 and Figure 4.8 in the previous chapter).

Generalizing Equation 5.3 by replacing the charge of the leading fragment by an effective charge and inserting for E_{lf} the complete energy deposition spectrum, the latter can be converted into charge yield, enabling the identification of the the leading fragments. The energy deposition spectrum is computed by the quadratic mean of the energy depositions in both diodes, improving the resolution.

The converted spectrum is shown in Figure 5.3. In order to improve the quality of the charge yield, only events within ten percent of the angle bisector of Figure 5.2 are taken into account.

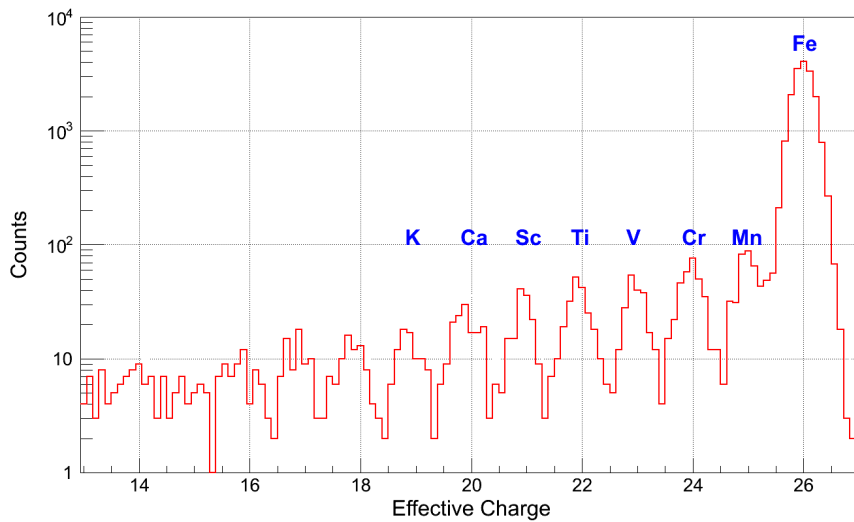


Figure 5.3.: Charge yield of fragment data measurement with iron ions.

Elements with Z lower than 26 are identified by their charge number down to $Z = 19$ (potassium), although even below fragments might be seen. But as the assumptions for the leading fragment analysis weakens with decreasing charge number, the effective charge does not coincide anymore completely with the leading fragment charge. The contribution of non-leading fragments becomes more important and in theory the leading fragment assumption breaks finally down at $Z_p/2$. Due to the fact that during beam time priority was always given to measurements with the primary beam and

also due to the ten percent cut, in Figure 5.3 statistics is already too low at $Z = 13$. Apart from increasing measurement time and choosing an absorber material of higher mass number elements, the separation of fragments to lower charge numbers than shown here can be achieved by placing the absorber more distant to the detector. As discussed, lighter nuclei are scattered out of the beam path more easily and would therefore contribute less to the energy deposition of the heavier fragment. This, however, would have resulted in lower intensities of the fragmented beam.

An additional effect contributing to peak broadening is the fact that not only charge changing nuclear interactions occur, but also individual neutrons are removed, i.e. isotopes of the primary or the fragments are produced. For example ^{56}Fe has according to the shell model of the nucleus two rather loosely bound neutrons above the magic number 28 (e.g. Musiol et al. 1988). However, the experiment presented here is neither sensitive to the isotope distribution of the fragments nor to ejected neutrons.

Furthermore the sometimes reported odd-even effect (e.g. Zeitlin et al. 1996a reports, whereas e.g. Westfall et al. 1979 explicitly does not) in the fragmentation process cannot be observed, which might be due to low statistics.

5.2.3. TEST OF THE LINEAR CALIBRATION CURVE

During energy calibration in the previous chapter deviations between measurements from iron and from argon nuclei were observed. Assuming a well known initial energy of the ions and a reliable estimate for the energy deposition in the detector, this could imply unstable and nonlinearly responding electronics.

The fragment peaks are fitted in the ADC channel pulse height spectra as well as in the energy calibrated pulse height spectra (Figure 5.4). The results for all diodes are listed in Tables D.4 and D.5 in Appendix D.

If the expected linear response of the detector system is not correct, the fragment data should not follow a straight line when the energy results are plotted versus the ADC channel numbers. This has been done for the iron fragment data presented in this chapter as well as for measurements of fragments from argon of 400 MeV u^{-1} that were produced in 2 cm of polyethylene.

The results are included in the calibration curves for both prototypes and both diodes (Figure 4.10 in Chapter 4 and Figures C.16 to C.18 in Appendix C) and show clearly a linear response.

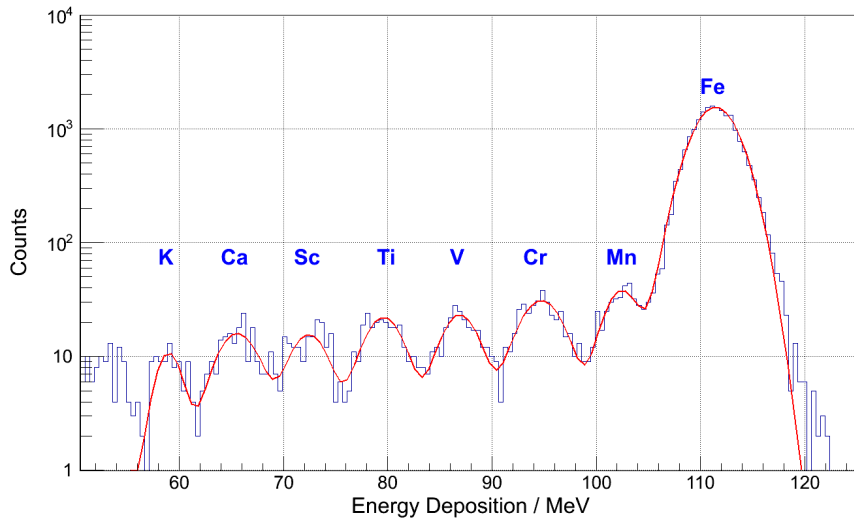


Figure 5.4.: Fitted pulse height spectrum of MDT-01-000 diode 1, of iron fragments after application of the energy calibration. The counts are given in counts per 0.5 MeV energy deposition.

5.2.4. ENERGY LOSS UNCERTAINTIES

The incident energy of a fragment hitting the detector changes depending on where in the polyethylene absorber it has been produced, as the energy loss of individual ion species is dependent on their charge number. In order to investigate how this affects the fragment measurements and if it can be deduced where in the absorber most fragments have been produced, two cases are considered (Figure 5.5).

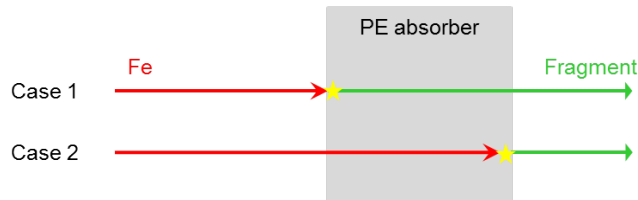


Figure 5.5.: Fragment production in polyethylene (PE) absorber.

In the first case (case1) the fragment is produced at the very beginning of the polyethylene absorber, in the second case (case2) at the very end. The calibration

curve derived in the previous chapter is applied to fit the iron peak from irradiations with the primary beam as well as to fit the remaining iron peak of the fragmentation measurement run. The resulting iron energies are 475 MeV u^{-1} before and 420 MeV u^{-1} behind the absorber. The energy loss of the fragments with an energy of 475 MeV u^{-1} in 1 cm of polyethylene is obtained from a basic GEANT4¹ (Agostinelli et al., 2003; Allison et al., 2006) simulation. By subtracting this energy loss the incident energy for all fragments produced in case 1 are obtained. For case 2 the incident energy is taken as 420 MeV u^{-1} .

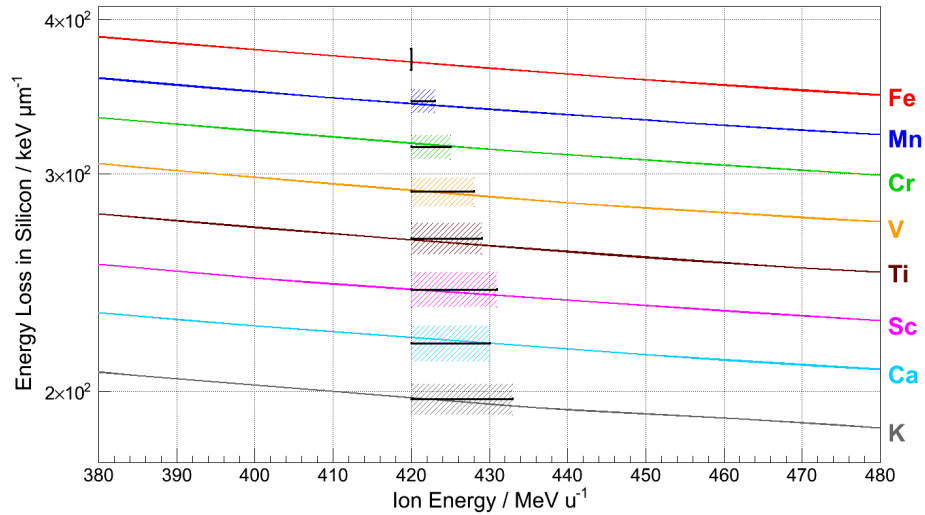


Figure 5.6.: Measured energy loss of iron and its fragmentation products in silicon in dependence on their energy. The upper and lower limit of the ion energy range are determined by case 1 and case 2 (Figure 5.5), respectively. The shaded areas in y-direction indicate the uncertainties deduced from the fits in Figure 5.4.

Figure 5.6 shows the energy loss curves in color coded solid lines for iron and all identified fragments in $\text{keV } \mu\text{m}^{-1}$ in silicon in dependence on the ion energy of incidence when hitting the detector, which is given in MeV u^{-1} . The energy loss curves are deduced from tables provided by *SRIM*² (Ziegler et al., 2012).

The position of the black bars in terms of energy loss indicates the measured energy deposition of the fragments in the silicon diode, divided by $300 \mu\text{m}$ (detector thickness). The shaded region in y-direction shows the energy deposition uncertainty,

¹GEometry ANd Tracking

²The Stopping and Range of Ions in Matter, [Http://www.srim.org](http://www.srim.org)

i.e. the FWHM of the fits in Figure 5.4 (also found in Table D.5 in Appendix D). The left limit of the data represents fragmentation according to case 2, in which the fragment is produced in the end from an iron ion that has experienced energy losses in 1 cm polyethylene. It therefore always lies at 420 MeV u^{-1} . The right limit shows fragments that were produced in the beginning and lost energy in the absorber according to their energy loss function in polyethylene. The extension of the black bar in x-direction therefore represents the velocity spread of the fragments due to their different location of origin in the absorber.

For iron only the energy deposition distribution is indicated by the vertical black bar.

The fragments are well resolved by the detector, as the data points are clearly separated by the FWHM (compare also Figure 5.4). It should be noted that the values given here refer only to the mean energy loss of the ions in polyethylene. Energy loss straggling is not considered, but is naturally included in the measured data and contributes to the respective uncertainty. Also the possible error of the energy calibration is not included, which can lead to a shift of the whole data set along the ion energy axis and influence slightly the ranges given in the figure. Furthermore the energy loss in the housing material of the detector is not considered and neither are uncertainties due to production of isotopes. A more detailed investigation would include complete simulations of the experimental setup, but already with the presented simplifications the results show good consistency.

The energy deposition distribution is too broad to deduce in which part of the polyethylene absorber the fragments have been produced, due to the reasons discussed above. A reasonable assumption, however, is that the fragment production is evenly distributed over the whole range of the absorber.

5.3. SUMMARY

Measurements of fragments from iron ions verified the MDT's ability to measure energy losses of high energetic heavy ions reliably in a mixed radiation field with good resolution. The distinction of the individual fragmentation products enabled additionally the verification of the linear response of the detector system at high energies (Chapter 4).

The experiments also demonstrate effectively the importance of a portable dosimeter for astronauts, as already due to small changes in the shielding material the radiation

field can change significantly in composition and energy. In fact, the interaction of individual heavy ions of different energies with materials of different composition is still topic to discussions, simulations and experiments as not all of the complex cross sections have been measured and even in the experimental results discrepancies are observed (e.g. Zeitlin et al. 1997 and references therein). These cross sections are required to enable reliable simulations of dose estimations that include the propagation of GCR through matter. The NCRP Report No. 153 (2006) discusses this problem in detail and provides an overview of existing data.

Regarding measurements with the MDT in space, individual fragments are not expected to be distinguished with a simple two-part telescope as employed here. The energy deposition will vary with the incident energy of the particle and with the path length travelled in the detector, as the irradiation is not restricted to one direction (compare simulations in Chapter 7).

FLIGHT MEASUREMENTS

The radiation environment at aviation altitudes is complex and differs from the radiation environment on Earth as well as from the one in low Earth orbit (LEO). Nevertheless, radiation measurements in aircraft provide a good and easy accessible opportunity to test the performance of the developed detector in a mixed radiation field.

The following sections present first the measurement procedure and the general data evaluation (Sections 6.1.1 and 6.1.2). The results and their analysis are given in Section 6.2. The context within the current solar cycle is clarified (Section 6.2.1), before the measured data is presented. Count rates and their dependence on the altitude and on the geomagnetic cutoff rigidity (Sections 6.2.2 and 6.2.3) are investigated and dose rates are given in Section 6.2.4. The subsequent sections consider the measured energy deposition and linear energy transfer spectra (Sections 6.2.5 and 6.2.6, respectively). In the last section (6.2.7) quantities relevant for radiation protection are deduced and the results of the MDT are compared to measurements taken by an additional detector and to calculations. Final summary of the MDT performance and of the flight data analysis are given in Section 6.3.

In aviation, the altitude is usually expressed in flight level (FL), a barometric nominal altitude, which is given in hundreds of feet, and which is defined by the International Standard Atmosphere (ISA, e.g. NASA 1976). For a standard sea level pressure of 1.013 bar, FL300 corresponds to 30,000 ft and can be converted to meters by 30.48 m per FL. Due to barometric changes the pressure altitude does not necessarily coincides exactly with the absolute altitude. It can however immediately be converted to residual atmosphere, which has the unit g cm^{-2} and decreases with increasing altitude. For cruising altitudes residual atmosphere is a direct measure for the shielding from cosmic radiation and therefore a useful physical quantity for the description of the radiation environment. Throughout this chapter the altitude will

be mainly given in residual atmosphere.

On individual flights a flight level change corresponds due to the semicircular rule¹ usually to the increase or decrease in altitude by 2000 ft (about 600 m), which corresponds to a change in residual atmosphere between 19 g cm^{-2} to 26 g cm^{-2} .

6.1. MATERIALS AND METHODS



Figure 6.1.: Flight box with both prototypes MDT-01-001 and MDT-01-000.

6.1.1. MEASUREMENTS

Most of the measurements were conducted with the two prototypes, MDT-01-000 and MDT-01-001. Both detectors were stored within a plastic box (Figure 6.1) that was placed in the overhead storage in the cabin of the aircraft or under the front seat.

¹According to the semicircular rule, flights heading eastwards follow 'odd' flight levels (e.g. 350, 370), whereas flights heading westwards follow 'even' flight levels (e.g. 360, 380). This regulation is applied in the airspace of most nations.





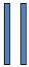

The measurements were started as soon as the aircraft reached cruising altitude and were stopped before the final descent.

The cruising altitude was obtained by noting down the information provided by the onboard entertainment program during the flight every ten to forty minutes. The time of the flight level changes was verified with data recorded by a pressure measuring device next to the detectors (not shown in the figure), as the pressure inside the cabin also changes with the decreasing outside pressure, which corresponds directly to changes in altitude.

Information on the flight route was retrieved from *FlightAware*². *FlightAware* provides time resolved geographical coordinates, which are either provided by on ground surveillance stations or – in case no data is available – are estimated. Since during the flight measurements also the flight route was observed with the entertainment program and no strong deviations have been noted, the coordinates from *FlightAware* were converted into cutoff rigidities with PLANETOCOSMICS³ for further data evaluation.

The radiation field at aviation altitudes is known to be non-isotropic. Most particles can be assumed to come from the zenith direction with a \cos^n distribution (Grieder, 2001), where n is different for the individual particle species and their energy ranges. Planar radiation detectors, like silicon diodes, and especially telescopes with planar detectors have a strong direction-dependent response (Section 3.7.3). Hence, it should be possible to observe this anisotropy of the radiation field by changing the orientation of the telescopes.

Table 6.1.: Telescope configurations of the two MDTs during flight measurements. Either both detectors face upwards (configurations 1) or one of the detectors is rotated by 90° (configurations 2a and 2b). The arrows indicate the denotation used throughout this chapter.

Configuration 1		Configuration 2a		Configuration 2b	
					
MDT-01-000	MDT-01-001	MDT-01-000	MDT-01-001	MDT-01-000	MDT-01-001
↑	↑	↑	⇒	⇒	↑

²www.flightaware.com, in the time the measurements were taken, *FlightAware* did not provide information on altitude.

³<http://cosray.unibe.ch/~laurent/planetocosmics/>; Matthiä (2009)

Three different flight configurations, defined by the orientation of the telescope axes of the two prototypes, were applied during the flights (Table 6.1). In configuration 1 the telescope axes of both detectors point upwards, in configurations 2a the axis of MDT-01-000 points upwards, while for MDT-01-001 it is rotated by 90° , pointing to the side. Configuration 2b is similar to 2a, but the orientation of the two detectors is reversed. In the following, the orientation of each detector is indicated by \uparrow (upwards) and \Rightarrow (sideways) corresponding to the orientation of the telescope axis. Table 6.1 gives an overview of the flight configurations and their denotations. For some flights an additional silicon detector, a Liulin (Dachev et al., 2007) was used, whose detector plane was always oriented upwards. Figure 6.1 shows the flight box in configuration 1.

6.1.2. DATA ANALYSIS

The detector system records every single particle event with a time stamp (Section 3.4.5) and distinguishes events detected in diode 1, in diode 2 or in both diodes (coincidences). With an energy calibration (Chapter 4) absorbed dose and linear energy transfer can be calculated. As the MDT is an active device, time resolved quantities like count rates and dose rates can also be measured.

The flux of the **energy deposition** in silicon $j(E_i)$ in $\text{cm}^{-2} \text{s}^{-1} \text{sr}^{-1} \text{MeV}^{-1}$ is calculated for each energy deposition E_i (from Equation 4.1) by Equation 6.1

$$j(E_i) = \frac{N_i}{\text{GF} \cdot T \cdot \Delta E_i}, \quad (6.1)$$

with N_i being the number of events detected at the i th bin, GF the geometry factor in $\text{cm}^2 \text{sr}$ ($\text{GF} = 3.8 \text{cm}^2 \text{sr}$ for single diodes and $\text{GF} = 1.7 \text{cm}^2 \text{sr}$ for the telescope, Section 3.7.3, Equations 3.4 and 3.5), T the total measurement time in seconds, and ΔE_i the bin width in MeV.

The uncertainty of E_i is given by the energy resolution. The statistical uncertainties of N_i are considered to follow Poisson statistics for all energy channels, in which more than 10 counts are detected. For energy bins with less counts, uncertainties are calculated following a method presented by Kraft et al. (1991). This Bayesian approach assumes that the observed system is in principle a priori known, which is true for the radiation field at flight altitudes, as it can be assumed to consist of secondary particles that are created due to the interaction of galactic cosmic radiation with the atmosphere. In this work uncertainties for a confidence interval of 0.9 are

chosen, with the assumption that no 'background particle' is detected, i.e. all detected particles originate from the expected radiation field (Kraft et al. 1991, Table 1, Row 1).

Equation 6.2 gives the **absorbed dose** D_{Si} in silicon in the unit Gy by

$$D_{\text{Si}} = \frac{K}{M} \cdot \sum_i (N_i \cdot E_i), \quad (6.2)$$

where $K = 1.602176487 \cdot 10^{-13} \text{ J MeV}^{-1}$ is the conversion factor from MeV to Joule and $M = 8.46 \cdot 10^{-5} \text{ kg}$ the mass of the detector material.

In order to obtain the absorbed dose in water $D_{\text{H}_2\text{O}}$, the dose in silicon has to be multiplied by a factor, which accounts for the different stopping power of particles in water and in silicon. Regarding the different radiation field compositions, at aviation altitudes a conversion factor of 1.2 is used, whereas for measurements in LEO a conversion factor of 1.23 is applied to account for the presence of particles with higher charge numbers (Beaujean et al., 2005).

Dose rates are calculated from Equation 6.2 for each minute. They are usually given in $\mu\text{Gy h}^{-1}$. In contrast to count rates, dose rates are not purely Poisson distributed, but also depend on the energy deposition of the particles, which can differ immensely for individual events.

For the **linear energy transfer** (LET) in $\text{keV } \mu\text{m}^{-1}$ only coincidence events are considered. The path length traversed by the particles is restricted by the opening angle of the telescope. With Monte Carlo simulations, the mean path length for particles triggering a coincidence event has been calculated to $l_m = 356 \mu\text{m}$ for an isotropic field distribution (Section 3.7.3). It should be noted that l_m changes with other dependencies on the incidence angles of particles. The LET flux in water $j(LET_i)$ is computed by

$$j(LET_i) = \frac{N_i}{\text{GF} \cdot T \cdot \Delta LET_i}, \quad (6.3)$$

where

$$LET_i = 1.2 \cdot \frac{E_i \cdot \rho_{\text{H}_2\text{O}}}{l_m \cdot \rho_{\text{Si}}} \quad (6.4)$$

and E_i , N_i , GF, and T as before; $\rho_{\text{Si}} = 2.33 \text{ g cm}^{-3}$ is the density of silicon, $\rho_{\text{H}_2\text{O}} = 1 \text{ g cm}^{-3}$ the density of water and ΔLET_i the bin width in $\text{keV } \mu\text{m}^{-1}$ for a

given LET_i .

For each LET a quality factor Q_i value is calculated from Equation 2.8 (ICRP Publication 103, 2007). The **dose equivalent** measured in coincidence mode H_c is then obtained with

$$H_c = 1.2 \cdot \frac{K}{M} \cdot \sum_i (Q_i \cdot N_i \cdot E_i). \quad (6.5)$$

Furthermore, the **mean quality factor** \bar{Q} is calculated by

$$\bar{Q} = \frac{H_c}{D_c}, \quad (6.6)$$

with D_c being the absorbed dose in silicon considering only particles detected in coincidence mode, multiplied by 1.2.

This mean quality factor is finally applied to the total absorbed dose:

$$H = \bar{Q} \cdot D_{Si} \cdot 1.2 = \bar{Q} \cdot D_{H_2O}. \quad (6.7)$$

Calculations are performed separately for high and low gain channels (low and high energy range, compare e.g. Section 4.3) of the detectors. In order to display energy deposition and LET spectra, the data for low and high gain is merged and logarithmically re-binned to account for lower fluxes at high energies.

For data analysis the software *ROOT*⁴ by Brun and Rademakers (1996) in the version 5.32/00 was employed.

6.2. LONG DISTANCE FLIGHTS

During four long distance round trip flights in the northern hemisphere measurements have been performed. The flights were conducted between three different airports (in the following labelled with A, B and C), at locations of geomagnetic cutoff rigidities of $R_c(A) \approx 3.4$ GV, $R_c(B) \approx 11$ GV and $R_c(C) \approx 4.6$ GV (compare Section 2.1.4). Three of these round trips were flown between A and B, and one between A and C. The flights on the routes A–B and C–A were eastbound, while B–A and A–C were westbound flights.

⁴<http://root.cern.ch/>

Usually both detectors MDT-01-000 and MDT-01-001 measured during the flights. During flight A–B 2, MDT-01-001 failed due to a faulty soldered joint. Because of the same reason, it also partly failed during the flights A–B 3 and B–A 3.

Routes for all flights were downloaded from *FlightAware*, except for the flight A–B 2, whose information was unavailable for unknown reasons.

Table 6.2 gives an overview of the flights, listing the individual flight routes in column one. The duration in minutes in columns two and three of this table refers to the measurement during the flights. For the flights in which MDT-01-001 measured only partly during the flight, the measurement times differ for both detectors (although for flight B–A 3 this will not be considered in the following, as the difference is less than 1%). Column four lists the flight configuration. The last column shows, if the additional silicon detector Liulin also acquired data during the flight.

The measurements were taken within a cutoff rigidity range of 0.5 GV up to 10 GV and in cruising altitudes between FL 320 (280 g cm^{-2}) and FL 410 (183 g cm^{-2})⁵

Table 6.2.: Overview of flight routes and measurement times.

Route	Duration / min		Configuration	Additional Si Detector
	MDT-01-000	MDT-01-001		
A–B 1	574	574	1 (↑ ↑)	—
B–A 1	600	600	1 (↑ ↑)	—
A–B 2	571	—	(↑)	Liulin
B–A 2	612	612	2b (⇒ ↑)	Liulin
A–B 3	620	493	2a (↑ ⇒)	Liulin
B–A 3	600	596	2b (⇒ ↑)	Liulin
A–C	543	543	2a (↑ ⇒)	Liulin
C–A	447	447	2b (⇒ ↑)	Liulin

6.2.1. SOLAR ACTIVITY DURING FLIGHT PERIOD

All flight measurements were taken within one year, in which the sun was heading towards the maximum of its eleven year solar cycle. During the individual flight periods no solar energetic particle events have been detected. Nevertheless, in order

⁵The data taken at FL 410 are excluded in the following data evaluation, since no data on the flight route is available. The altitude range for the analyzed data falls therefore between FL 320 and FL 390 (201 g cm^{-2}).

to verify that the individual measurements are comparable in terms of primary cosmic ray intensity, the variation of neutron monitor count rates within the time frame of all measurements is analyzed. The count rates of the neutron monitors in Oulu ($R_c = 0.81$ GV, Finland), Kiel ($R_c = 2.36$ GV, Germany), and Alma-Ata B (AATB, $R_c = 6.69$ GV, Kazakhstan) are taken into account. These three stations are chosen as their positions cover the cutoff rigidity range in which the flight measurements have been performed. The daily averaged count rates for the days of each flight are taken from the Neutron Monitor Database website⁶ and are listed in Table 6.3

Table 6.3.: Daily averaged neutron monitor counts for the days of the flights.

Route	Neutron Monitor Counts s^{-1}		
	Oulu	Kiel	Alma-Ata
A-B 1	107	172	1415
B-A 1	105	169	1390
A-B 2	106	169	1419
B-A 2	106	170	1439
A-B 3	104	167	1414
B-A 3	106	168	1421
A-C	104	167	1424
C-A	104	166	1401

The count rates vary within less than 4%. Hence the individual flight measurements can be compared and strong differences between the results due to cosmic ray intensity are not expected.

6.2.2. COUNT RATES

The count rates of a flight measurement give an immediate impression of the flight profile. In the following section they are investigated in detail. As it is usually not permitted to switch on electronic devices during take off and the final descent phase of a flight, the related increase and decrease, respectively, in the count rates cannot be seen in any plot discussed here. Count rate profiles including these phases can be seen in Appendix G, 'Additional Flight Measurements'. For comparison, while at cruising altitudes the count rates are in the order of 40 to 80 counts per minute, on ground the MDT detects only few – less than ten – counts per minute with one diode (compare

⁶<http://www.nmdb.eu>

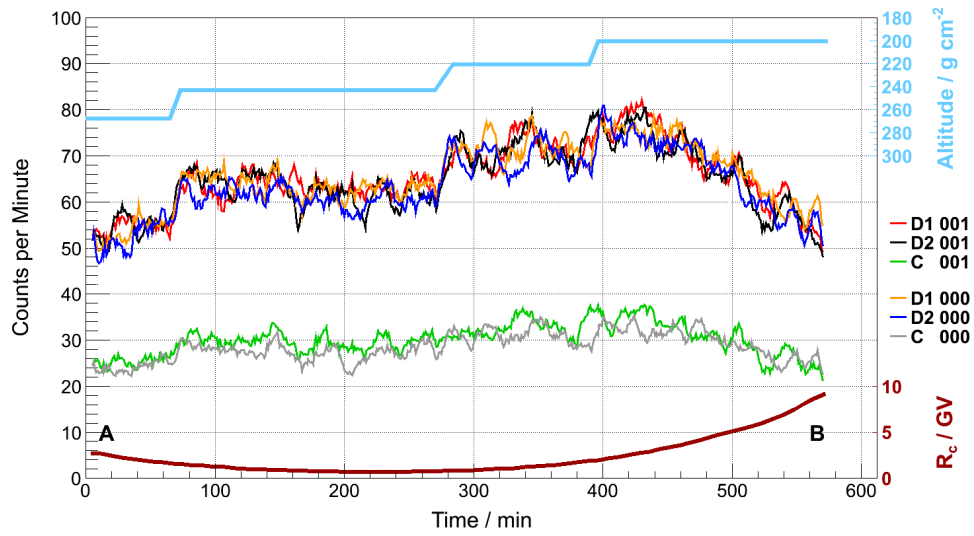
also Figure 3.14 in Section 3.6).

The count rates for diode 1, diode 2, and coincidences are distinguished and plotted versus time for both prototypes. In Figures 6.2 and 6.4 the count rates of both detectors during two round trip flights are plotted. The count rates of diode 1 (D1 001) and diode 2 (D2 001) of detector MDT-01-001 are shown in red and black, respectively, while the coincidence events (C 001) are plotted in green. For MDT-01-000 diode 1 (D1 000) is given in orange, diode 2 (D2 000) in dark blue, and the coincidence count rates (C 000) are shown in grey. The original time resolution of the detectors is set to one minute, but due to the low particle flux at aviation altitudes and the small detection area, the count rates show strong fluctuations corresponding to the Poisson distribution. Therefore, count rates are represented as a ten minutes moving average on a one minute scale. In the subsequent data analysis, however, the original time resolution is used. For comparison, Figure E.1 in Appendix E.1 shows count rates of the flight A–B 1 with the original time resolution in thin lines overlaid by the ten minutes average in thick lines. In all figures the altitude is indicated by the residual atmosphere in light blue in the upper part of the graph. In the lower part, the cutoff rigidity R_c is visible in dark red. Departure airport and destination are noted in the lower left and right corners of the figures. Analog count rate plots of the remaining flights can be found in Appendix E.1 (Figures E.2 to E.5).

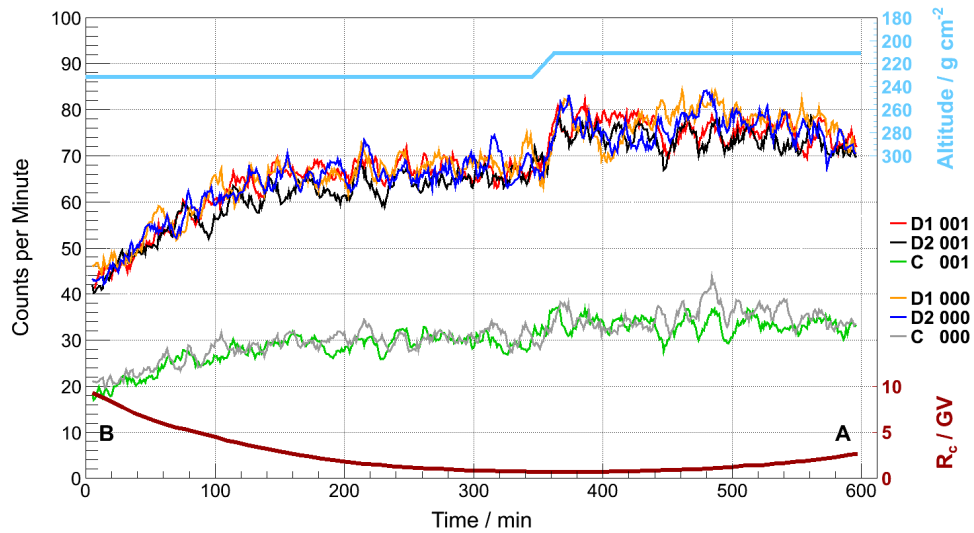
CONFIGURATION 1

The first round trip flight on the A–B route has been conducted in configuration 1 (Tables 6.1 and 6.2). In Figure 6.2 the change of the count rates with altitude can be easily followed as at higher altitudes more counts are detected due to lower atmospheric shielding. Also the dependence on the geomagnetic cutoff rigidity is visible. With increasing cutoff rigidity, fewer particles can penetrate the Earth’s magnetic field and hence less particles are detected. This is especially well seen at high geomagnetic cutoff rigidities in the vicinity of B (about the first and last 100 minutes of the related flights).

The first impression suggests that the detectors work stably and that the performance of both detectors and each diode is comparable. In order to quantify the spread of the count rates, the mean of all four diodes is calculated for each minute. The deviation of this mean for each diode is plotted in Figure 6.3. Panel (a) gives the results for flight A–B 1 and panel (b) for flight B–A 1. Count rates follow the Poisson distribution that can be approximated by a Gaussian for sufficiently large mean values λ (here



(a) Count rates A-B1 in configuration 1



(b) Count rates B-A1 in configuration 1

Figure 6.2.: Count rates for the flight **A-B1** and **B-A1** for MDT-01-000 (\uparrow) and -001 (\uparrow), both flown in configuration 1. Count rates are shown for single diodes (**D1** and **D2**) and for coincidence events (**C**) in color code for both detectors, indicated with **000** and **001**. The count rates are given with a ten minutes moving average. The cruising altitude is plotted in residual atmosphere in light blue at the top and the cutoff rigidity R_c in dark red at the bottom of each panel. **A** and **B** denote start and destination of the flights.

between 40 and 80, e.g. Parzen 1960). The standard deviation should not exceed $\sqrt{\lambda}/\lambda$, which is 11 % for $\lambda=80$ and 16 % for $\lambda=40$. The results for all diodes in both flights are within 10 %.

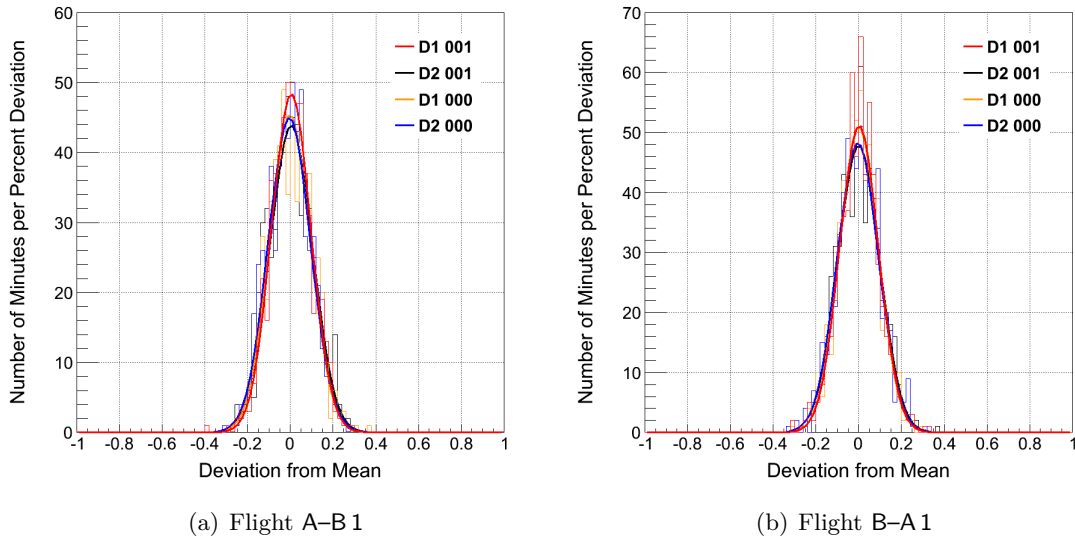


Figure 6.3.: Deviation of count rates from mean of all four diodes for the two flights performed in configuration 1. No unexpected deviation can be observed.

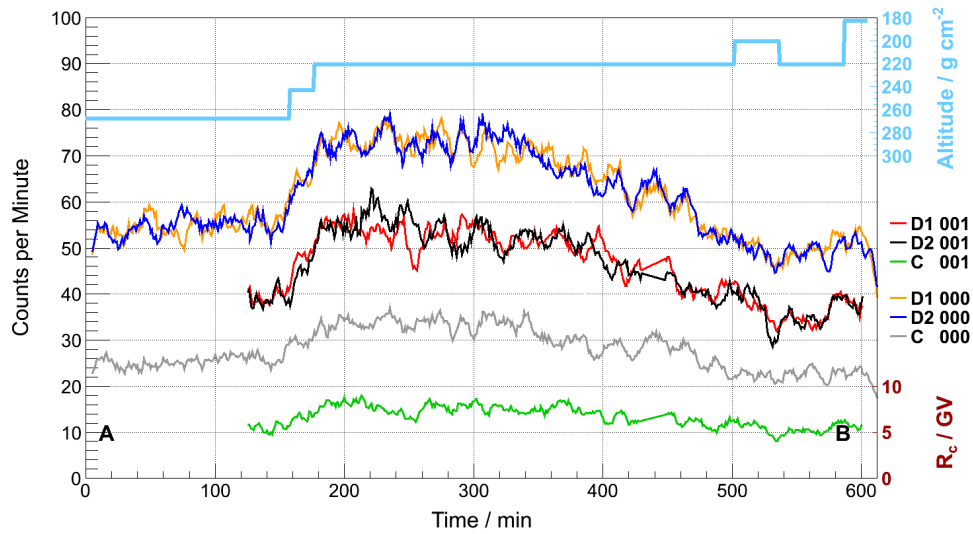
The fluctuations in the ten minutes average count rates sometimes appear to show a periodic pattern for individual diodes and even a correlation of two diodes of the same detector. Nevertheless, the fluctuations are purely statistical as proven by the cross- and autocorrelation investigation presented in Appendix G.2.

The consistent behaviour of the two prototypes presented here justifies to compare also count rate measurements, in which the two telescopes measure in different directions, i.e. measurements taken in configurations 2a and 2b.

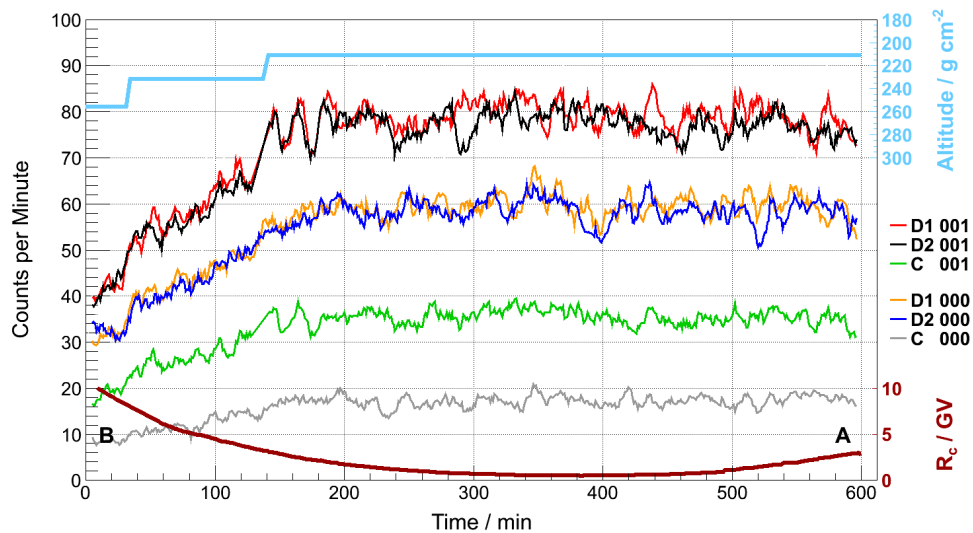
CONFIGURATIONS 2A AND 2B

After the first round trip flight, all flights starting in A were flown in configuration 2a and the return flights in configuration 2b.

As an example, the round trip A-B-A 3 is presented. For flights in configurations 2a, Figure 6.4(a), the count rates of MDT-01-000 (\uparrow) are higher than those of MDT-01-001 (\Rightarrow), as it is expected in a directed radiation field, in which the dominant component originates from the zenith. For the return flights, Figure 6.4(b),



(a) Count rates A-B 3 in configuration 2a



(b) Count rates B-A 3 in configuration 2b

Figure 6.4.: Same as in Figure 6.2 for the flights **A-B 3** flown in configuration 2a (MDT-01-000 \uparrow and MDT-01-001 \Rightarrow) and **B-A 3** flown in configuration 2b (MDT-01-000 \Rightarrow and MDT-01-001 \uparrow). During the flight A-B 3 (a) the aircraft had to change the flight route to avoid a typhoon near the destination airport. Although no recorded information on the flight route is available, the detour can be seen in the decreasing count rates as the aircraft moves to higher cutoff rigidities earlier than e.g. in Figure 6.2(a). The missing count rates for MDT-01-001 are due to partly failure of the detector, because of a faulty soldered joint.

this behaviour is reversed as the measurements were performed in configuration 2b. During the flight A–B3, the aircraft started to move to higher geomagnetic cutoff rigidities earlier around minute 310, since it had to avoid a typhoon near the destination airport. Unfortunately no information on the flight route was available on *FlightAware*, but the rerouting was verified by observations of the route during the flight and can also be seen in the count rates, which decrease with increasing cutoff rigidity as the aircraft is heading south earlier than usual for this flight route.

6.2.3. ALTITUDE AND CUTOFF RIGIDITY DEPENDENCE OF COUNT RATES

The radiation field and its intensity – and therefore the count rates – depend on both, the altitude and the geomagnetic cutoff rigidity (Section 2.1). In the following these two parameters are investigated separately, however always considering that they are not independent of each other.

ALTITUDE DEPENDENCE

Count rates increase with increasing altitude, because of less shielding from the cosmic radiation by the residual atmosphere. In order to investigate this dependence, the rates are plotted versus altitude in terms of residual atmosphere. Since the count rates also depend on the cutoff rigidity, this investigation is done for three different cutoff rigidity intervals: $0.7 \text{ GV} < R_c < 1.0 \text{ GV}$ (close to pole), $2.0 \text{ GV} < R_c < 2.9 \text{ GV}$ (close to A), and $7 \text{ GV} < R_c < 10 \text{ GV}$ (close to B). These regions are selected, as a number of measurements at different altitudes with an ascertained position is available.

Since the count rate data is comparable for MDT-01-000 and MDT-01-001 and the diodes of each detector are not correlated except for their coincidences (Section G.2.2), count rates from both detectors are combined to obtain a larger set of data. Table 6.4 lists the altitude in flight levels and residual atmosphere for the three cutoff rigidity intervals and the number of minutes measured for each cutoff rigidity and each altitude. This number is given by the sum of measurement minutes of all individual diodes (i.e. a factor of two for each prototype). Figure 6.5 shows the statistics as a bar diagram. The count rates are normalized to an area of 1 cm^2 , as the area of the silicon diodes is 1.21 cm^2 .

For a detailed investigation the number of measurements and the number of different altitudes is relatively small and due to the low particle flux at aviation altitudes (compared to space, where the MDT has been designed for) the statistics for the small

Table 6.4.: Overview of time measured at certain altitudes (in residual atmosphere and flight level) at a certain cutoff rigidity for single diodes facing upwards (\uparrow) and sideways (\Rightarrow). Dividing these numbers by two gives the time for corresponding coincidence events.

Residual Atmosphere (g cm^{-2})	FL	Measuring Time / min					
		$0.7 \text{ GeV} < R_c < 1.0 \text{ GeV}$		$2.0 \text{ GeV} < R_c < 2.9 \text{ GeV}$		$7 \text{ GeV} < R_c < 10 \text{ GeV}$	
		near pole \uparrow	\Rightarrow	near A \uparrow	\Rightarrow	near B \uparrow	\Rightarrow
280	320	154	154	—	—	100	100
268	330	—	—	160	—	—	—
256	340	—	—	32	32	62	62
243	350	362	—	98	36	—	—
232	360	328	208	78	78	80	—
221	370	482	228	110	110	60	60
211	380	732	500	164	94	—	—
201	390	—	—	204	204	154	—
Total		2058	1090	846	554	456	222

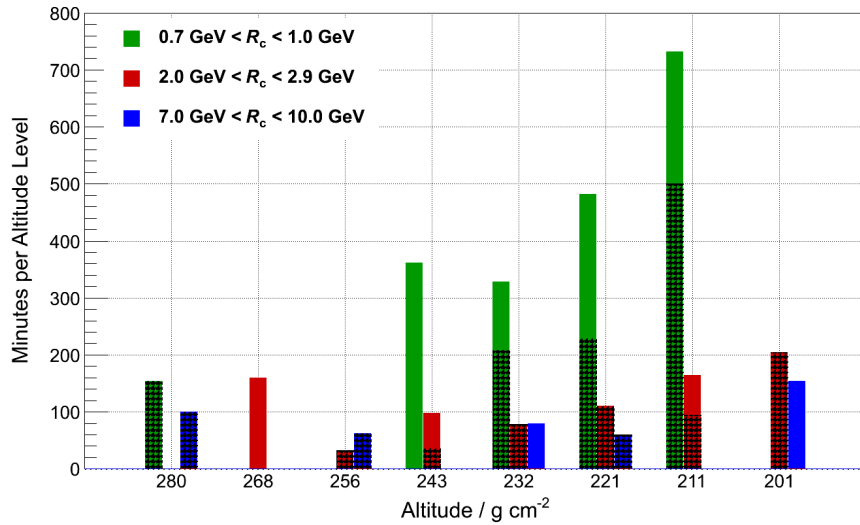


Figure 6.5.: Time measured with single diodes in upwards orientation (\uparrow) on each flight level for three different cutoff rigidity ranges, indicated by the color. The shaded parts show the amount of time measured in sideways orientation (\Rightarrow). The corresponding number of minutes for coincidence events is half the time for all data points.

detection area is low. Nevertheless, the correlation between altitude and count rates for different cutoff rigidities becomes apparent in Figure 6.6. The results shown in this

figure are for measurements with single diodes pointing upwards (\uparrow). Results for measurements with single diodes pointing sideways (\Rightarrow) and coincidence events in upward and sideways orientation can be found in Figures E.6, E.7, and E.8 in Appendix E.1. The uncertainties in y-direction follow the Poisson statistic of the count rates, which underestimates the true error, as possible error sources, like different shielding of the aircraft due to position within the plane and its detailed configuration, are not considered (see also next paragraph). Uncertainties in the residual atmosphere are chosen to $\pm 2 \text{ g cm}^{-2}$, which corresponds to some $\pm 50 \text{ m}$ in altitude (depending on the altitude).

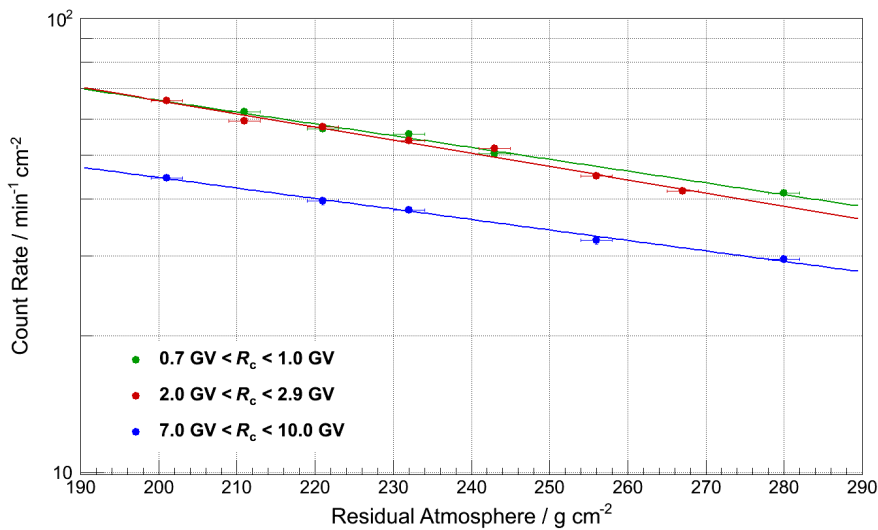


Figure 6.6.: Count rate dependence on the altitude in residual atmosphere for three different cutoff rigidity regions. The figure shows the results for single diodes facing upwards (\uparrow). Exponential fits are plotted (solid lines), the results are listed in Table 6.5.

The data recorded at low cutoff rigidities (up to 2.9 GV), are hardly distinguishable with this set of data due to the fact that the atmospheric shielding is more dominant at high latitudes. Count rates for high cutoff rigidities (averaged for R_c between 7 and 10 GV) are clearly offset, as the Earth's magnetic field has, in addition to the atmosphere, an increased influence. This feature has also been measured by e.g. Beaujean et al. (2005).

Since the cruising altitudes considered here are well below the Pfozter maximum, the count rates can be expected to follow an exponential behaviour (Beer-Lambert law). The data is fitted by Equation 6.8, where \dot{C} is the count rate in $\text{min}^{-1} \text{cm}^{-2}$ and x is the residual atmosphere in g cm^{-2} .

$$\dot{C} = b_c \cdot \exp\left(-\frac{x}{a_c}\right) \quad (6.8)$$

Table 6.5 gives the results of the fit parameters a_c and b_c .

Table 6.5.: Fit results for the exponential fits of upwards facing single diode count rates (Figure 6.6). The goodness of the fits are given by χ^2/N , where N is the number of degrees of freedom.

Cutoff Rigidity Interval	a_c (g cm^{-2})	b_c ($\text{min}^{-1} \text{cm}^{-2}$)	χ^2/N
0.7 GV – 1.0 GV	167 ± 8	222 ± 2	2.1
2.0 GV – 2.9 GV	150 ± 7	224 ± 2	2.2
7.0 GV – 10.0 GV	188 ± 11	134 ± 2	0.5

The exponential fits reproduce this dependence reasonably (compare χ^2/N in Table 6.5). This is in agreement with Beaujean et al. (2005), who report an exponential behaviour in the count rates measured with the silicon detector telescope DOSTEL. Figure E.9 in Appendix E gives an example of a normalized count rate profile (flight B–A2, detector MDT-01-001, diode 1). In this figure, all three fits are applied to the complete flight (indicated with color code of the corresponding cutoff rigidity region). The differences between these normalizations are not strong.

Figure 6.7 shows the altitude dependence for the three cutoff rigidity intervals for the count rate data of all flight configurations. It is distinguished between particles detected in each single diode in horizontal (S_{\uparrow}) and in vertical orientation (S_{\Rightarrow}) as well as between particles detected as coincidences for the telescope in horizontal (C_{\uparrow}) and vertical orientation (C_{\Rightarrow}). The large offsets between the measurements in different configurations prove clearly the strong directional dependence of the radiation field. Results for all fits are listed in Table F.1 in Appendix F.

For further analysis, an exponential fit is calculated taking into account all cutoff rigidity intervals. The results for these mean parameters a_c are given in Table 6.6. Since the normalization process requires only the exponent of the fit function, parameter b_c is not listed.

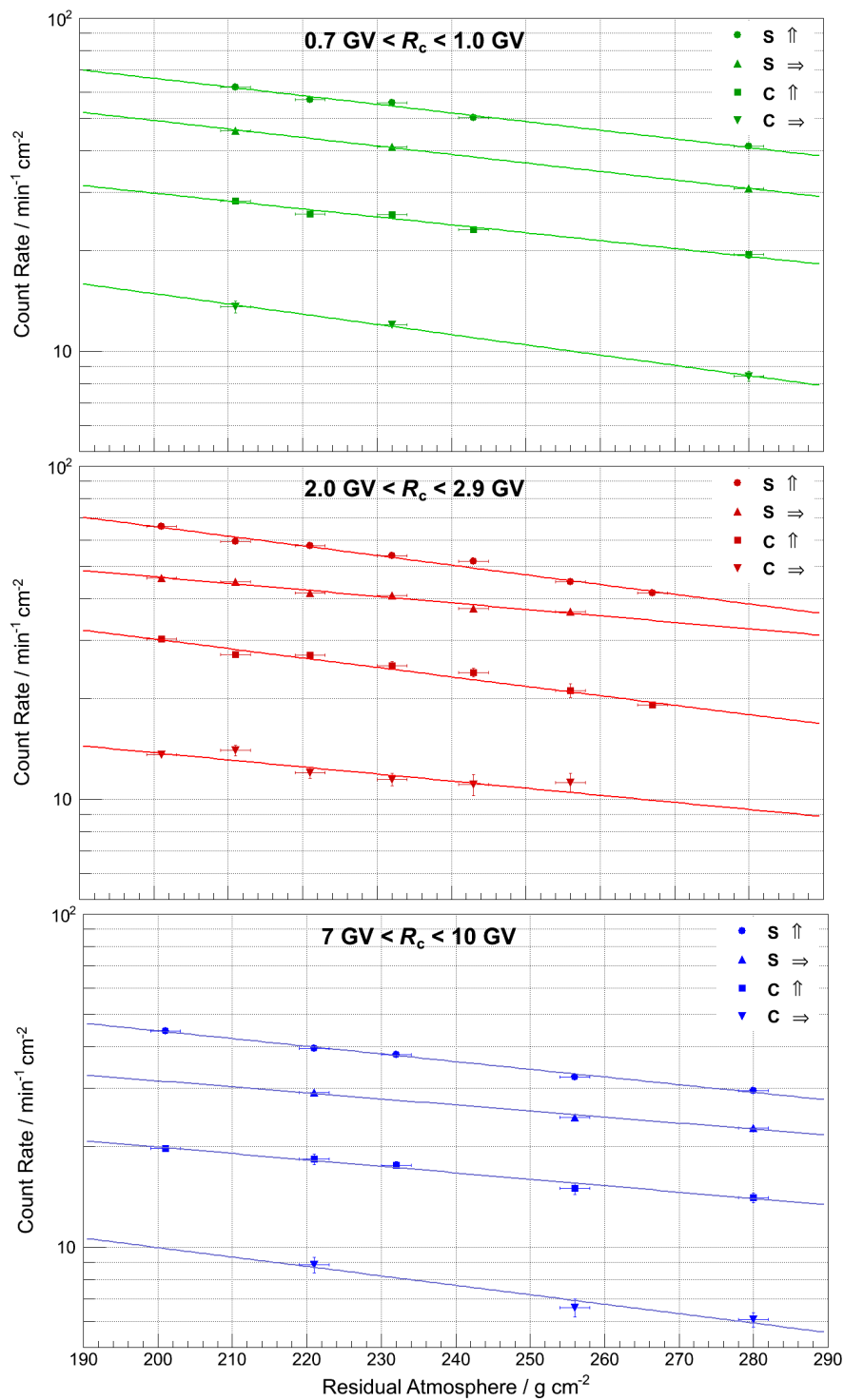


Figure 6.7.: Count rate dependence on the altitude in residual atmosphere for three individual cutoff rigidity intervals. Exponential fits are shown for $S \uparrow$ (highest count rate in each panel), followed by $S \Rightarrow$, $C \uparrow$ and $C \Rightarrow$ (with decreasing count rate).

Table 6.6.: Calculated mean values for fit parameter a_c (Equation 6.8), which is applied for normalization. It is distinguished between single diode and coincidence measurements and the orientation of the detector axis (\uparrow and \Rightarrow).

$a_c / \text{g cm}^{-2}$	\uparrow	\Rightarrow
Single Diodes	165 ± 6	195 ± 9
Coincidences	178 ± 9	152 ± 12

GEOMAGNETIC CUTOFF RIGIDITY DEPENDENCE

In order to investigate the dependence of the count rates on the geomagnetic cutoff rigidity R_c in more detail, count rates for all flights are normalized to 243 g cm^{-2} residual atmosphere (FL 350), applying the fit results given in Table 6.6.

While for small geomagnetic cutoff rigidities a large number of data points is available, the measurement time at higher cutoff rigidities often amounts to only a few minutes per flight. Table 6.7 and Figure 6.8 show the number of minutes measured in a certain cutoff rigidity region for all altitudes. In red the time for single diodes facing upwards and in grey the time for single diodes facing sideways are plotted. For the corresponding coincidence measurements, these numbers have to be divided by two. Data from flights, in which no position information was available or in which the data from *FlightAware* did not appear to be reliable (e.g. when discontinuities in the flight route were observed like in Figure E.4) are excluded.

In Figure 6.9 the normalized count rates in $\text{min}^{-1} \text{ cm}^{-2}$ are plotted versus the geomagnetic cutoff rigidity R_c in GV. Red filled circles represent data from single diodes facing upwards (S_{\uparrow}) and dark red squares the corresponding coincidence events (C_{\uparrow}). For the sideways orientation of the detector, single diodes (S_{\Rightarrow}) and coincidence (C_{\Rightarrow}) events are shown in black and grey triangles, respectively. The values are averaged over all measurements in cutoff rigidity intervals of 0.5 GV up to $R_c = 6 \text{ GV}$. Above, intervals of 1 GV are chosen to account for low statistics and to ensure to have a minimum of ten minutes measurement time in each R_c interval. The error bars in x-direction give the geomagnetic cutoff rigidity average interval plus 0.1 GV for the position uncertainty. The errors in y-direction include the standard deviation from the altitude fit errors as well as the statistical uncertainties of the count rates. It has to be noted here again that the statistical uncertainty does not account for changes in count rates due to different measurement setups in terms of shielding and scattering

Table 6.7.: Overview of time measured within a certain cutoff rigidity range, independent of flight altitude, for measurements with single diodes in two different orientations (\uparrow and \Rightarrow). The time for the corresponding coincidence events is half the number of minutes for each geomagnetic cutoff rigidity interval.

R_c Range (GV)	Time (\uparrow) (min)	Time (\Rightarrow) (min)	R_c Range (GV)	Time (\uparrow) (min)	Time (\Rightarrow) (min)
0.5 – 1.0	2894	1178	5.5 – 6.0	164	44
1.0 – 1.5	1752	690	6.0 – 6.5	132	32
1.5 – 2.0	1232	624	6.5 – 7.0	102	18
2.0 – 2.5	880	398	7.0 – 7.5	90	16
2.5 – 3.0	680	340	7.5 – 8.0	82	14
3.0 – 3.5	292	130	8.0 – 8.5	84	14
3.5 – 4.0	190	74	8.5 – 9.0	92	16
4.0 – 4.5	190	58	9.0 – 9.5	100	30
4.5 – 5.0	184	56	9.5 – 10.0	64	38
5.0 – 5.5	208	58			

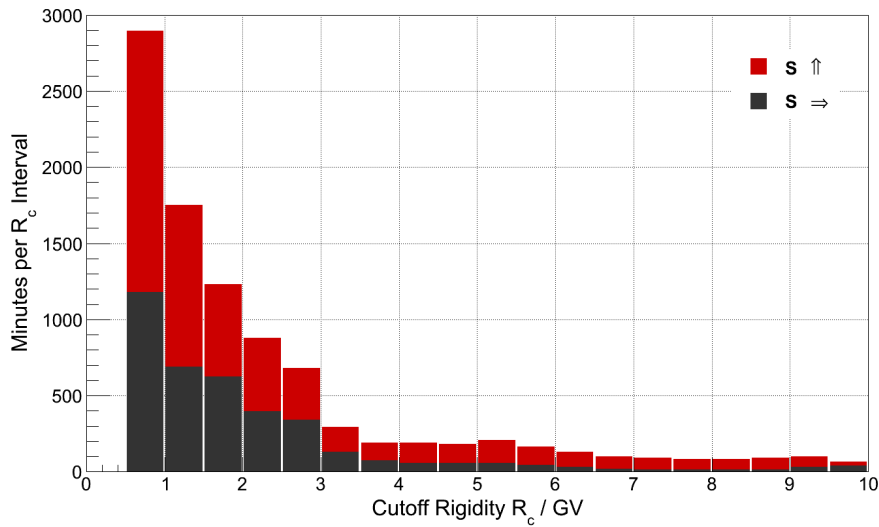


Figure 6.8.: Time measured within each geomagnetic cutoff rigidity interval including all flight altitudes for single diode measurements in two different orientations. The corresponding number of minutes for coincidence measurements is half the time for all intervals.

within the aircraft for the individual flights.

The ratios of the normalized count rates are calculated in order to investigate, if a dependence on the geomagnetic cutoff rigidity can be observed, and are shown in

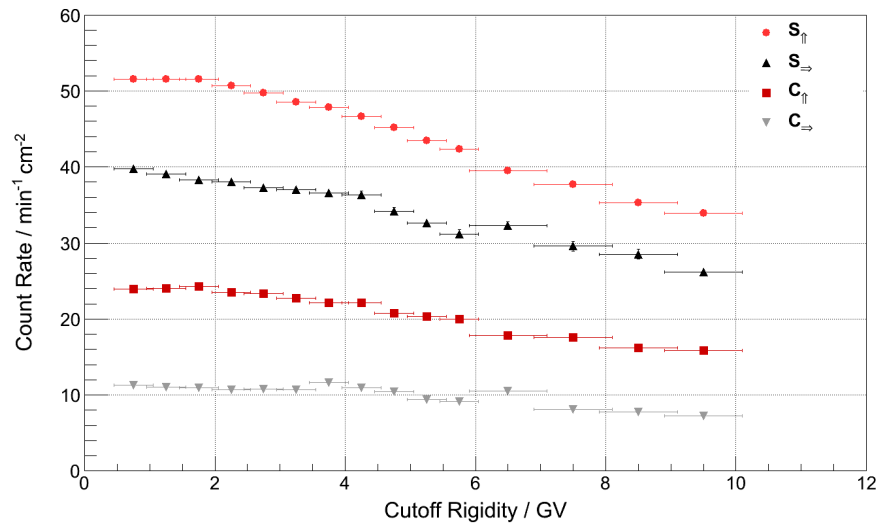


Figure 6.9.: Count rate dependence on the geomagnetic cutoff rigidity. The count rates are normalized to an altitude of 243 g cm^{-2} (FL 350).

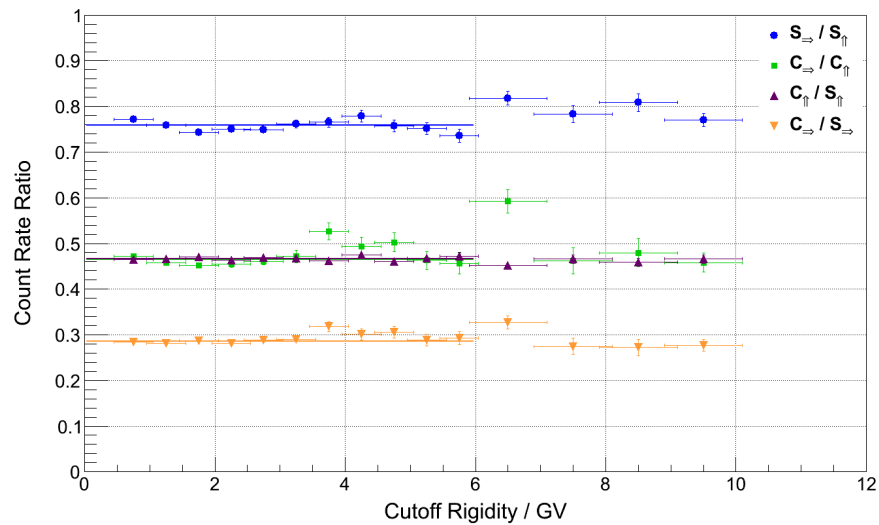


Figure 6.10.: Count rate ratio dependence on the cutoff rigidity. The solid curves show the constant fit.

Figure 6.10. In first approximation a constant ratio for the different orientation can be assumed at least up to a cutoff rigidity of 6 GV. For larger values this still holds for the ratio of coincidence to single diodes in upwards orientation (purple triangles). The other ratios are then dominated by their large uncertainty. Also Battistoni et al.

(2004) find with simulations that the angular distribution of the radiation field in an aircraft is nearly independent of the geomagnetic cutoff rigidity. Strong fluctuations due to low measurement statistics and additional not quantified error sources prevent a convincing conclusion for cutoff rigidities higher than 6 GV in the presented data set. Hence the ratios are fitted by a constant only including data, where $R_c < 6.0$ GV:

$$\frac{S_{\Rightarrow}}{S_{\Uparrow}} = 0.76 \pm 0.01 \quad (6.9)$$

$$\frac{C_{\Rightarrow}}{C_{\Uparrow}} = 0.46 \pm 0.01 \quad (6.10)$$

$$\frac{C_{\Uparrow}}{S_{\Uparrow}} = 0.47 \pm 0.01 \quad (6.11)$$

$$\frac{C_{\Rightarrow}}{S_{\Rightarrow}} = 0.29 \pm 0.01, \quad (6.12)$$

where, again, S and C represent single diodes and coincidences, respectively, and the arrows indicate the detector axis orientation. The error is given by the standard deviation.

Under the assumption that single diodes and coincidences are sensitive to the same particle species and energies, the ratio of coincidences (that see particles within an opening angle of about 70°) to single diodes (that see the whole hemisphere) gives an estimate to the angular dependence of the radiation field. Monte Carlo simulations⁷ with this purely geometrical assumption show that for an isotropic radiation field the ratio $C_{\Uparrow}/S_{\Uparrow}$ is about 0.45. As mentioned before, the radiation field at aviation altitudes is known to follow a \cos^n distribution for the incident angle θ (e.g. Grieder 2001). This directionality is confirmed by the significant lower ratio for $C_{\Rightarrow}/S_{\Rightarrow}$. A ratio of 0.47 in upwards direction would be consistent with $n = 1.2$, but this may be misleading. While coincidences detect mainly charged particles, single diodes are additionally partially sensitive to the neutral component of the radiation field, especially to photons. This leads to the assumption that n is larger than 1.2 for charged particles. It needs to be considered that the radiation field inside the aircraft is strongly influenced by the structure of the aircraft itself, including factors like position inside the aircraft as well as number of passengers and fuel (Ferrari et al., 2004). For instance Battistoni et al. (2004) present simulations of the angular dependence of different particle species within an aircraft and conclude that the charged component

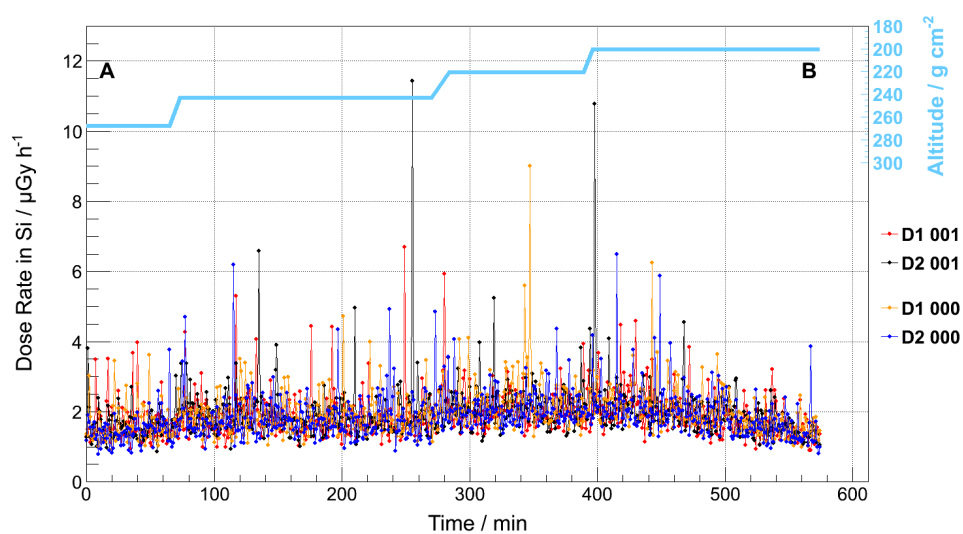
⁷Compare Section 3.7.3.

of the radiation field (electrons, protons, muons, pions) is more directed than neutrons and photons. This can be understood by considering the creation processes of these particles. Neutrons with energies less than 10 MeV are produced by evaporation, which is an isotropic process. However it has to be taken into account that silicon detectors are barely sensitive to neutrons. Photons e.g. produced in the decay of in scattering processes highly excited nuclei, do not necessarily follow the direction of incident of these nuclei. Bremsstrahlung photons from easily scattered non-relativistic electrons are radially emitted from their curved trajectories, whereas bremsstrahlung from relativistic electrons rather follows their direction of incidence. Also annihilation processes of positrons and electrons contribute to a rather isotropic photon component. Therefore the directionality of photons can be subdued. These descriptions are not intended to be exhaustive, but generally the lower energetic a secondary particle is, the more scattering processes it was subject to and the stronger can be the deviation from its incident trajectory. Subtracting the coincidence events from the single diode data, i.e. $(S_{\uparrow} - C_{\uparrow})$ and $(S_{\Rightarrow} - C_{\Rightarrow})$, shows that the resulting differences are about equal. This could support the presence of a rather isotropic neutral component, but is not necessarily the only possible explanation. Single diode data includes the whole solid angle of 4π , but with a cosine bias for the response of a planar detector. In upwards direction therefore mainly the sum of particles coming from the top and from below are seen, while the sideways measuring diodes have this bias to the horizontal component. But while for the upwards direction the radiation field can be assumed to be at least rotational symmetric (neglecting the squared shape of the diodes), this is not the case for the sideways direction, in which the cosine bias of the planar detector also includes the azimuth ϕ .

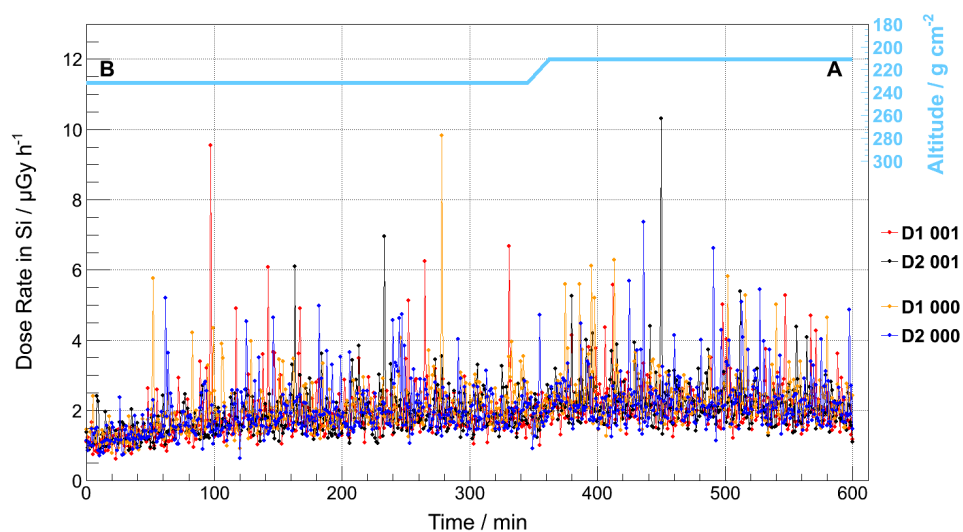
Considering these effect, from the measurements presented in this work no simplified model of the angular distribution of the radiation field at aviation altitudes is derived. For this, a detailed simulation of the aircraft structure, as well as of the response of the silicon telescope is required.

6.2.4. DOSE RATES

Dose rates are calculated as described in Section 6.1.2. Figures 6.11 and 6.12 show the dose rates for the flights A–B–A 1 and 3 (same flights as for the count rates in Section 6.2.2). The dose rates are plotted with a time resolution of one minute for each diode of both prototypes. Red dots indicate the upper diode and black dots the lower diode of MDT-01-001 (D1 and D2001, respectively). The two diodes of

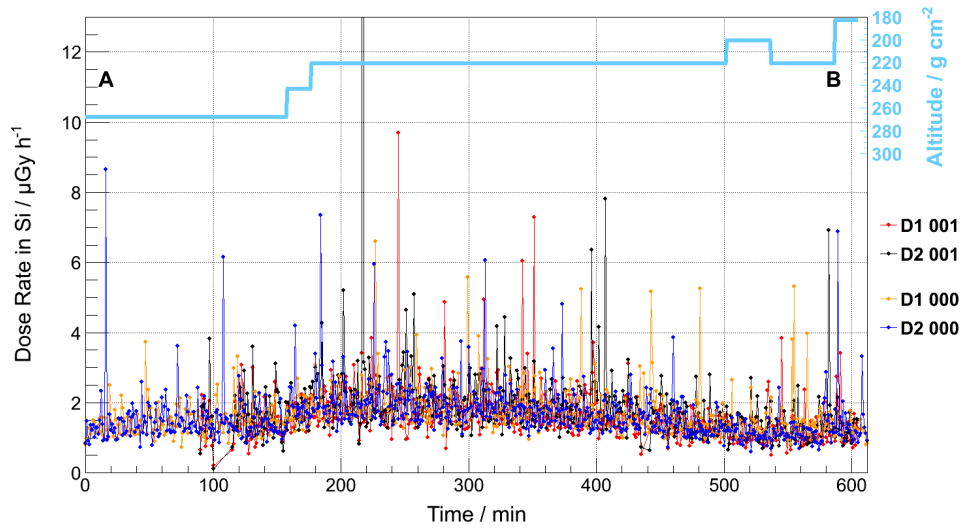


(a) Dose rates A–B 1 in configuration 1

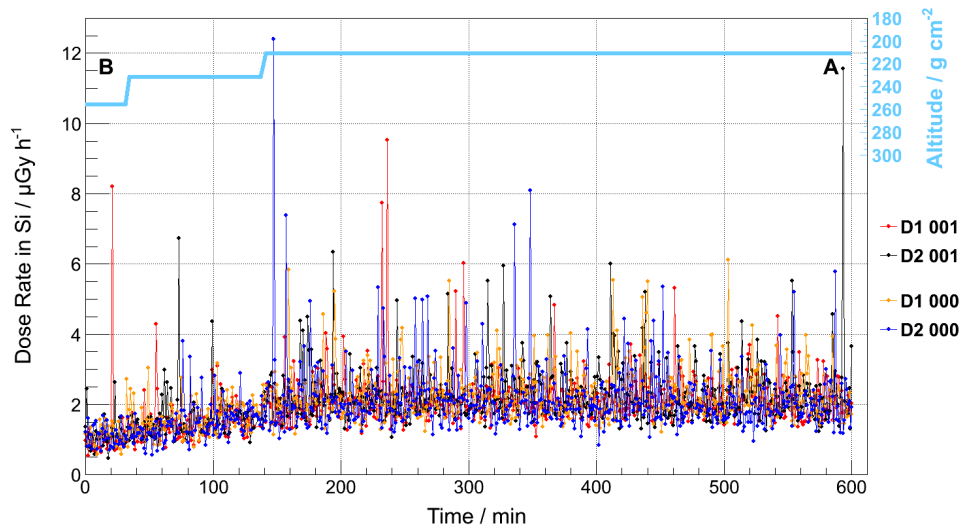


(b) Dose rates B–A 1 in configuration 1

Figure 6.11.: Dose rates for the flights **A–B 1** and **B–A 1** for MDT-01-000 (\uparrow) and -001 (\uparrow) flown in configuration 1. Dose rates are shown for single diodes (**D1** and **D2**) in color code for both detectors indicated with **000** and **001** with a time resolution of one minute. The cruising altitude is plotted in **flight levels** (light blue line) at the top of the figure. **A** and **B** denote departure and destination of this flight. Compare with count rates in Figure 6.2. The dose rate recorded in coincidence are not included for clarity.



(a) Dose rates A-B 3 in configuration 2a



(b) Dose rates B-A 3 in configuration 2b

Figure 6.12.: Same as in Figure 6.11 for the flights **A-B 3** flown in configuration 2a (MDT-01-000 \uparrow and MDT-01-001 \Rightarrow) and **B-A 3** flown in configuration 2b (MDT-01-000 \Rightarrow and MDT-01-001 \uparrow). Compare to count rates in Figure 6.4.

MDT-01-000 are labelled in orange (D1 000) and blue (D2 000). The cruising altitude is indicated in residual atmosphere in light blue.

In addition to the fluctuations following a Poisson distribution, the variation of the dose rate depends on the energy deposition of single particles. The energy deposition is dependent on the particle species, the particle energy and the energy

loss distribution in the detector. This can be seen in the short increases of the dose rates due to individual events with a high energy deposition detected in the low gain channel (corresponding to high energy depositions). In order to emphasize the contribution of these events to the absorbed dose, in Figure 6.13 the dose rates for flight B–A3 are shown separately for high and low gain for detector MDT-01-001. The dose contribution from the high gain channels are relatively even distributed, while detections in the low gain channels are rare, but can have a high impact on the dose.

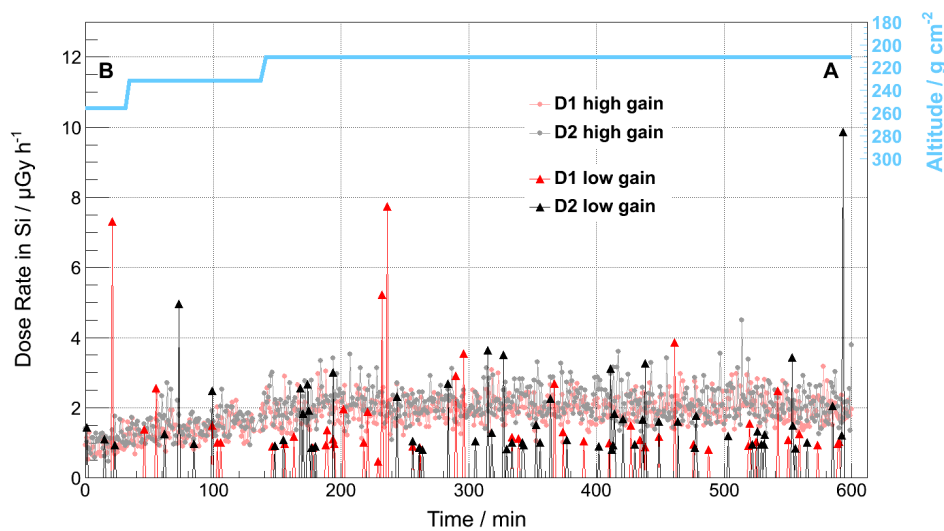


Figure 6.13.: Dose rates for the flight B–A3 (compare Figure 6.12(b)) for MDT-01-001 (\uparrow) shown separately for high and low gain.

Changes with altitude and with the geomagnetic cutoff rigidity can be seen in the dose rates, however not to such an extent as found for the count rates, which is partly due to the different scaling and the averaging of the count rates. There is no difference seen in the dose rates for different measurement configurations (see below). This however is not true for dose rates measured in coincidence, which have been excluded from the figures for the sake of clarity.

Analog dose rate plots of the remaining flights can be found in Appendix E.2 (Figures E.10 to E.13).

CONFIGURATIONS 1 AND 2 – ANGULAR DEPENDENCE OF COUNT AND DOSE RATES

Count and dose rates show a different behaviour in the different measurement configurations. In contrast to what is observed in the count rate, the dose rate measured by the single diodes is not dependent on the orientation of the telescope geometry, but only on the altitude as well as on the cutoff rigidity. This can be clearly seen by comparing Figure 6.11 measured in configuration 1 ($\uparrow\uparrow$) and Figure 6.12 measured in configurations 2a and 2b with one of the detectors pointing sideways and the corresponding count rate Figures 6.2 and 6.4, respectively.

Count rates consider the pure intensity of radiation and the geometrical response of the detector, which follows a cosine distribution in the incidence angle θ for a planar detector. Dose rates on the other hand, depend additionally on the energy deposition of the particles. This energy deposition is the product of the linear energy transfer (LET) and the path length travelled in the detector. The path length is given by $d \cdot \cos^{-1}(\theta)$, where d is the detector thickness ($300 \mu\text{m}$) and θ the incident angle of the particle.

As these two effects compensate each other, the dose rate – and hence the dose – is independent of the radiation field geometry and therefore also does not depend on the detector orientation within any radiation field.

Naturally the dose rates measured in coincidence show a different behaviour, as the opening angle of incoming particles is restricted by the telescope configuration omitting large energy deposition events due to long path lengths.

ALTITUDE AND CUTOFF RIGIDITY DEPENDENCE OF DOSE RATES

Figure 6.14 shows the single diode dose rate in silicon in $\mu\text{Gy h}^{-1}$ plotted versus residual atmosphere in g cm^{-2} for the same three geomagnetic cutoff rigidity intervals as for the count rates (compare previous section, Figure 6.6). Dose rates from all measurements in both orientations are included. The uncertainty in the dose rate is given by the standard deviation. As for the count rates, the difference with altitude as well as with the geomagnetic cutoff rigidity is apparent. The dose rates are exponentially fitted by

$$\dot{D} = b_d \cdot \exp\left(-\frac{x}{a_d}\right) \quad (6.13)$$

where \dot{D} is the dose rate in $\mu\text{Gy h}^{-1}$ and x the residual atmosphere in g cm^{-2} . The

fit parameters a_d and b_d are listed in Table 6.8.

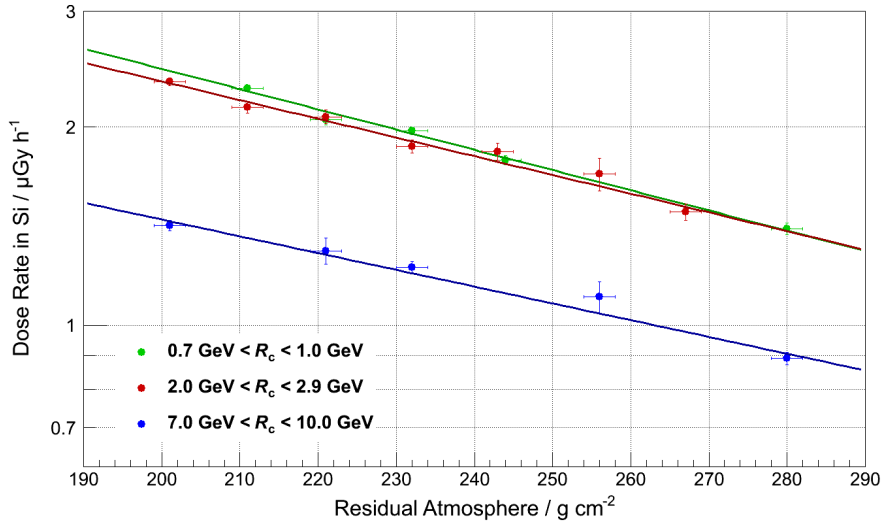


Figure 6.14.: Dose rate dependence on the altitude in residual atmosphere for three different geomagnetic cutoff rigidity regions. The solid lines represent exponential fits and their results are listed in Table 6.8.

Table 6.8.: Fit results for the exponential fits of dose rates (Figure 6.14). The goodness of the fits are given by χ^2/N , where N is the number of degrees of freedom.

Cutoff Rigidity Interval	a_c (g cm^{-2})	b_c ($\mu\text{Gy h}^{-1}$)	χ^2/N
0.7 GV – 1.0 GV	142 ± 9	2.3 ± 0.1	0.7
2.0 GV – 2.9 GV	152 ± 10	2.2 ± 0.1	0.6
7.0 GV – 10.0 GV	170 ± 12	1.5 ± 0.1	0.9

Due to the large uncertainty, all fit results show a rather low χ^2/N , which implies in this case that also other fits, e.g. linear functions, could be an appropriate solution. A linear dependence for this altitude range has for example been proposed by Schrewe (2000) and Wissmann (2006) for TEPC measurements of ambient dose equivalent rates.

Figure 6.15 shows the altitude dependence of the dose rates for the three different geomagnetic cutoff rigidity intervals including the results of the coincidence dose rates in both configurations (C_{\uparrow} and C_{\Rightarrow}). Although the data is fitted exponentially, it is

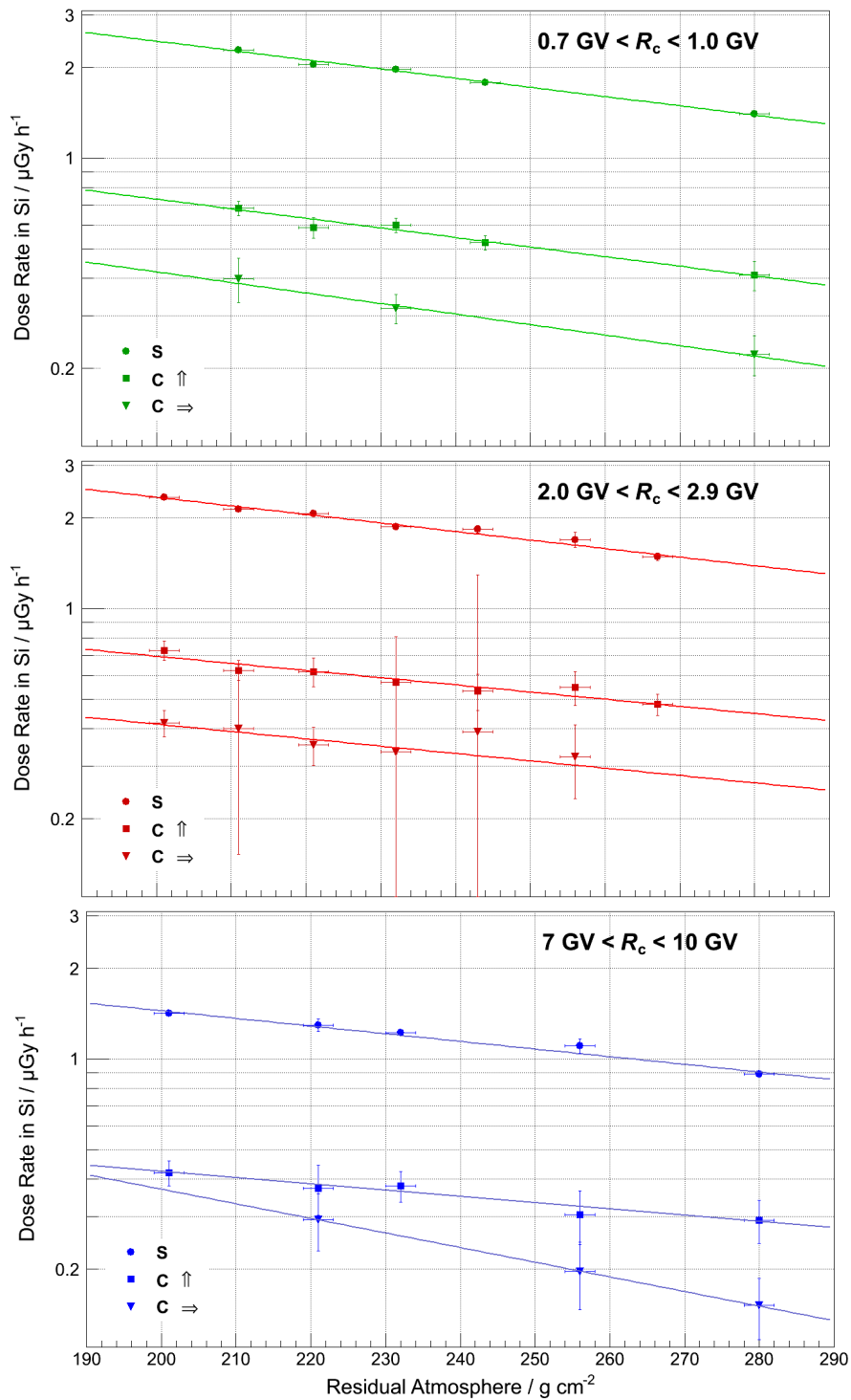


Figure 6.15.: Dose rate dependence on the altitude in residual atmosphere for three individual cutoff rigidity intervals. Exponential fits are shown for single diodes in both configurations (S, highest count rate in each panel), followed by C_{\uparrow} and C_{\Rightarrow} (with decreasing dose rate). Especially the data for the coincidence events rather gives a qualitative impression that as the count rates, also the dose rates are dependent on the geomagnetic cutoff rigidity. The exponential fits serve here as a guidance for the eye and the quantitative fit results are not expected to reflect reliable data.

apparent that rather a qualitative impression than quantitative reliable results can be seen. Nevertheless for completeness the fit results are given in Table F.2 in Appendix F.

It would be interesting to investigate the dose rate behaviour in dependence of the geomagnetic cutoff rigidity in a similar way as it has been done for the count rates and to compare the results. Results for such an analysis of the ambient dose equivalent rate are shown for example by Wissmann et al. (2010), showing a similar trend with R_c as the count rates in Figure 6.9. Regarding however the angular dependence, especially the dependence of count and dose rates for high geomagnetic cutoff rigidity values seems to be stronger dependent on altitude for coincidence measurements in sidewards orientation (C_{\Rightarrow}) than for the other configurations and could be an effect worth looking more into. But this dependence is statistically not significant and requires a larger set of data for investigation.

In general the number of measurements is small and statistics is low due to the small detection area and the low particle flux at aviation altitudes compared to what would be expected in space. Since dose rates additionally depend strongly on the energy loss of the particles within the detector, which varies enormously, the analysis of the dependence of dose rates on the geomagnetic cutoff rigidity does not lead to convincing results and is therefore not performed in this work.

6.2.5. ENERGY DEPOSITION SPECTRA

Energy deposition spectra are calculated applying Equation 6.1 to the complete energy deposition spectrum. Figure 6.16(a) shows the energy deposition spectra in silicon of all four diodes. The color code is chosen as in the previous sections, i.e. diode 1 (D1) and diode 2 (D2) of MDT-01-001 in red and black and of MDT-01-000 in orange and blue, respectively. Data from all flights in which the respective diodes have measured in upwards direction are accumulated for better statistics. This is justified as most flights have been conducted on the same flight route and all have been performed in the northern hemisphere within a limited geomagnetic cutoff rigidity interval (compare previous sections). The spectra are binned logarithmically, choosing larger bin widths from 3 MeV energy deposition upwards. From 0.1 MeV on the error bars in x-direction give the bin width, while below the energy resolution determines the uncertainty. In the following the spectra are analyzed according to the configuration (i.e. upwards \uparrow and sidewards \Rightarrow orientation) they have been recorded in. In order to

show that differences observed between the configurations are not due to electronic abnormalities or statistics, Figure 6.16(b) shows the spectra from Figure 6.16(a) multiplied by a power law with index 2.7. Up to energy depositions of about 2 MeV the spectra agree well, justifying comparison of the different configurations. For energies above, large deviations are visible due to low fluxes.

The energy deposition spectra for all individual flights can be found in Figure E.14 to Figure E.21 in Appendix E.3.

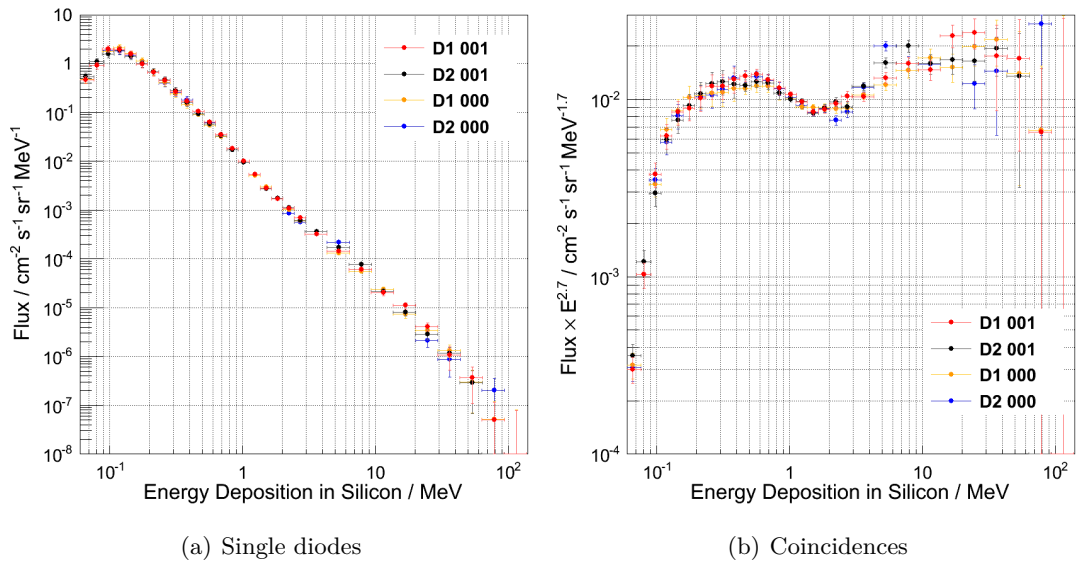


Figure 6.16.: Energy deposition spectra of single diodes in upwards orientation accumulated for all flights for each diode separately. Panel (a) shows the flux in usual display, panel (b) shows the flux multiplied by a power law with index 2.7 for better comparison of the diodes.

Note: The uncertainties in y-direction for energy depositions below 1 MeV are not only given by Poisson statistic, but also account for the non-linearities in the low energy regime that can influence the number of events detected in an energy bin. The MDTs work at the very edge of the electronic performance in order to cover 3.5 decades of energy deposition with low power consuming operational amplifiers and two amplifications stages (compare Section 3.4). That caused some problems in the non-linear low energy regime in which the response of the detector was not completely stable. The effect can be seen in the energy deposition spectra from the flights A–B–A 1-3 (Figures E.14 to E.19 in Appendix E.3) as the spectra seem to be slightly distorted in the low energy range. The additional uncertainty is deduced from linearity measurements presented in Section 3.7.2.

This does not affect the count rates, as the amplitude of the signals might not have been acquired

correctly, but as these particles still have been registered.

The problem was minimized before flight A–C–A for MDT-01-001 by inserting baseline shifts and passive shapers in front of the peak detector in the high gain (low energy) channel.

Figure 6.17 shows the energy deposition spectra detected by single diodes (a) and in coincidence (b). Spectra for events detected in upwards and sideways orientation are given. As before for the count rates (Section 6.2.3) the data is merged from all diodes in the respective configuration. Symbols and color code are chosen according to Figure 6.9.

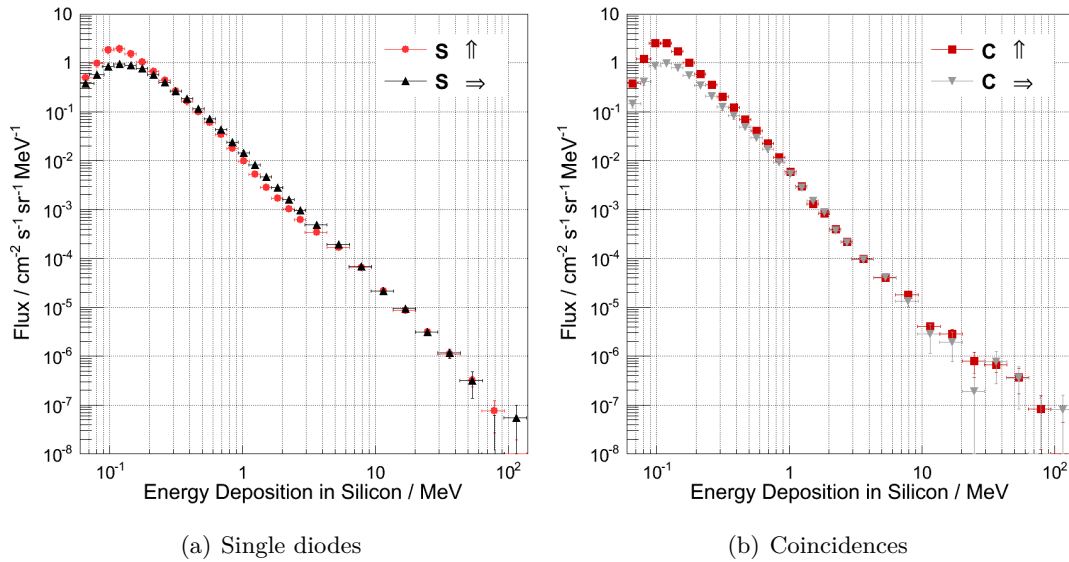


Figure 6.17.: Energy deposition spectra accumulated for all flights. Panel (a) shows the flux detected in every single diode (S), while panel (b) shows the results that have been detected in coincidence mode (C). The arrows in the figures indicate the orientation of the telescope axis.

The overall shape of all spectra is dominated by the peak between 80 keV and 180 keV and the steep decrease of the flux towards higher energy depositions.

In order to make a simple estimation for the origin of this shape and the composition of the spectra, the individual constituents of the radiation field are considered. In altitudes between 180 g cm^{-2} and 300 g cm^{-2} the most abundant particle species are protons, electrons (including positrons), muons, photons, neutrinos, and neutrons (e.g. Beringer et al. (PDG) 2012a, Grieder 2001). From these neutrinos can be neglected due to their small interaction cross sections. Neutrons are only considered to contribute rarely and therefore can also be neglected for the energy deposition

range in which the spectra peak.

The different contributions due to the individual particle species for the lower end of energy depositions is estimated by the energy loss of minimal ionizing particles (with energies E_{\min}) in silicon (compare also Roos 1997). Path lengths within the detector range from $300\ \mu\text{m}$ for particles traversing perpendicularly through the diode over $356\ \mu\text{m}$ for the mean path length for coincidences in an isotropic radiation field, up to $877\ \mu\text{m}$ for coincidence events (Section 3.7.3). The maximum incident angle for coincidences is 70° . For single diodes the maximum path length would be $1.56\ \text{cm}$, although this number only refers to the extremely rare event of a particle traversing a diode parallel and diagonally.

The mean energy loss in silicon of minimal ionizing electrons with energies $1\ \text{MeV} < E_{\min} < 2\ \text{MeV}$ lies between $0.35\ \text{keV}\ \mu\text{m}^{-1}$ and $0.37\ \text{keV}\ \mu\text{m}^{-1}$ (*ESTAR*⁸, Berger et al. 2005). This corresponds to a mean energy loss of $108\ \text{keV}$ in $300\ \mu\text{m}$ silicon.

For minimal ionizing protons of E_{\min} between 2 and $3\ \text{GeV}$ the mean energy loss is $0.39\ \text{keV}\ \mu\text{m}^{-1}$ (calculated with *SRIM*⁹, Ziegler et al. 2012), resulting in energy depositions of $117\ \text{keV}$ in $300\ \mu\text{m}$.

Minimal ionizing muons have a mean energy loss in silicon of $0.39\ \text{keV}\ \mu\text{m}^{-1}$ (Beringer et al. (PDG), 2012b), which is similar to protons.

The most probable energy loss of all particles is considerably lower than the mean energy loss due to the asymmetric energy loss distribution and peaks at almost $100\ \text{keV}$ for all three particle species. The peak flux observed in the spectra is shifted to slightly higher energy depositions due to longer mean path lengths in the detector and due to not minimal ionizing particles.

In the following the differences between the individual spectra are discussed qualitatively in more detail.

SINGLE DIODES AND COINCIDENCES \uparrow

Figures 6.17(a) and (b), red circles and dark red squares. The flux in the peak position of the coincidence spectra seems to exceed the flux of the single diode spectra by a factor 1.5, although all data of the coincidence events are included in the single diode data. In order to scale the flux to the solid angle, it is divided by the corre-

⁸Stopping-power and range tables for electrons,

<http://physics.nist.gov/PhysRefData/Star/Text/ESTAR.html>

⁹The Stopping and Range of Ions in Matter, <http://www.srim.org>

sponding geometry factor for a single detector ($GF = 3.8 \text{ cm}^2 \text{ sr}$) and for a telescope ($GF = 1.7 \text{ cm}^2 \text{ sr}$, Equation 6.1). This, however, assumes an isotropic field distribution, which is not present at aviation altitudes. The fact that the coincidence flux exceeds the single diode flux confirms a directed radiation field component along the telescope axis. Generally the telescope cannot distinguish between particles coming from the zenith and from below (but compare Figure 6.18 and respective discussion), however simulations show that the amount of particles travelling through the diodes from the bottom is only about 5% of all particles¹⁰.

The slope of the coincidence event spectrum is steeper towards both, lower and higher energy depositions with respect to the peak. Considering the low energy part, this is assumed to arise from relatively low energetic photons, depositing their energy in one diode and from particles that graze one of the diodes at the edge. Towards energy depositions larger than the peak position the ratio of coincidence to single diode flux drops below one at 200 keV and goes down to one half at around 1 MeV. The reason is that the path length – and therefore the possibility to deposit energy – of each particle is restricted by the opening angle. Additionally single diodes also detect particles that usually do not trigger coincidences, like high energetic photons and neutrons¹¹. Especially neutron interactions can deposit a large amount of energy at once, e.g. when they interact with a silicon nucleus resulting in fragmentation of the latter. These effects lead to a higher flux in the larger energy deposition range for single diode measurements compared to the corresponding coincidences.

SINGLE DIODES \uparrow AND \Rightarrow

Figure 6.17(a). The most significant difference in the flux is in the peak region, where the peak of the diodes in sideways orientation seems to be smeared out to higher energies due to the longer mean path length in the directed radiation field. It is about half the flux of the diodes in upwards orientation, but this ratio increases with de- and increasing energy depositions. From around 300 keV energy deposition the flux in sideways orientation exceeds the upwards orientation flux and goes up to 1.5 times the flux in upwards orientation at around 1 MeV. Up to 10 MeV the flux ratio stays between one and 1.5, before the fluxes seem to become the same above 10 MeV. This strengthens the assumption that most of the high energy depositions are due to nuclear reactions from neutrons or fragmentation processes as these are assumed to

¹⁰Considering charged particles only, D. Matthiä (2012), private communication

¹¹These particles can occasionally trigger coincidences, compare quality factor paragraph in Section 6.2.7.

be of rather isotropic origin (compare discussion in last paragraph of Section 6.2.3) and the interaction products are usually short ranged particles. At very high energy depositions statistics do not allow a convincing analysis.

SINGLE DIODES AND COINCIDENCES \Rightarrow

Figures 6.17(a) and (b), black and grey triangles. The peak fluxes of single diodes and coincidences are comparable, but the peak in coincidence is more pronounced due to the path length restriction towards higher energies and low energetic photons towards lower energies. For energy deposition above 300 keV the coincidence flux drops below half the single diode flux. Compared to the single diode to coincidence ratio in upwards direction this hints that especially higher energetic ionizing charged particles that can trigger coincidences originate from the zenith direction, which is in accordance with what is expected.

COINCIDENCES \uparrow AND \Rightarrow

Figure 6.17(b). As for the single diodes in sideways orientation, the corresponding coincidence peak flux is slightly smeared out towards higher energy deposition compared to the upwards spectrum due to generally longer path lengths in the detector. The ratio for the coincidence fluxes is minimal at the peak position, where the flux of the sideways orientation is about one third of the upwards orientation flux. The ratio increases towards higher energy depositions, where the path lengths in the detector become similar in both configurations. At higher energy depositions, also more isotropic interactions can contribute for events in which particles trigger coincidences by production of secondaries (compare also quality factor paragraph in Section 6.2.7). Above few MeV statistics are too low to allow comparison.

Plotting the coincidence spectra of diode 2 versus diode 1 gives a more detailed insight. Figure 6.18 shows these two-dimensional plots for C_{\uparrow} (left) and C_{\Rightarrow} (right). The intensity in color code is given by the number of counts that is arbitrarily normalized to 1000 counts for C_{\uparrow} . For C_{\Rightarrow} the maximum is additionally scaled by Equation 6.10, the ratio for $C_{\uparrow}/C_{\Rightarrow} = 0.46$ resulting from count rate analysis in Section 6.2.3.

The rather broad distribution up to 1 MeV energy deposition can be explained by minimal ionizing electrons, muons and protons (compare previous paragraphs) that lose energy in the diodes close to Landau distributions, for which it can happen that a large energy loss in one diode (high energy tail of distribution) corresponds to a low

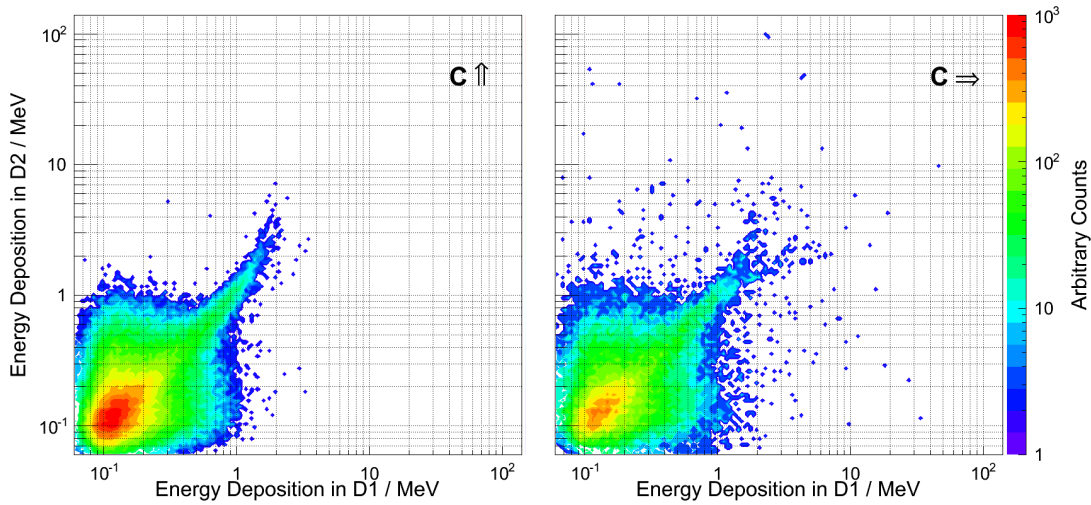


Figure 6.18.: Energy deposition in silicon in diode 2 (D2) versus diode 1 (D1) measured in coincidence, accumulated of all flights in upwards (left) and sideways orientation (right). The figures share the same axis labelling and range, the number of counts in z-direction is arbitrarily normalized to 1000 counts for C_{\uparrow} and additionally scaled by the $C_{\Rightarrow}/C_{\uparrow}$ count rate ratio of 0.46 for C_{\Rightarrow} .

energy deposition in the other (most probable energy loss of distribution, compare Section 2.2.3).

Considering the range of possible angles of incidence and the mentioned particle species, only protons below some 100 MeV are able to deposit more than 1 MeV in each silicon diode. The extended tail towards higher energies arises mainly due to lower energetic protons. The maximum energy deposition of protons lies at about 6 MeV for particles stopping in one of the detectors.

In the panel showing the measurements taken in upwards orientation (C_{\uparrow}), this tail shows a deviation from the angle bisector (45° line) of the plot. These particles can be identified as slowing down particles originating from the zenith direction, as, while slowing down, they start to lose more energy in diode 2, the lower diode of the telescope. With an increased number of flight measurements it might be possible to reveal even stopping protons that would appear in the plot as the deviated tail structure up to about 3 MeV in diode 1 and 6 MeV in diode 2, before the energy deposition in diode 2 would decrease, while still slightly increase in diode 1 (as an example a simulation of this is shown in Figure E.22 in Appendix E.3).

Interestingly the energy loss in both diodes is symmetric for the case of measurements taken with the silicon telescope axis pointing sideways (C_{\Rightarrow} , right panel of Fig-

ure 6.18). A fish-tail like structure is visible mirroring the energy deposition structure discussed above along the angle bisector proving this feature to be real and that the radiation field is rotational symmetric in first approximation. Statistics and measurement setup (no consistent aligning of the telescope axis along the cardinal direction) do not allow discussion of possible asymmetries like the East-West effect (Rossi, 1930).

Together with the count rate analysis of the individual configurations, this set of data provides an excellent starting point for the verification of the radiation field simulations within an aircraft at flight altitudes investigated with a silicon detector. Despite the fact that the statistics is not perfect, important general features could be shown.

6.2.6. LET SPECTRA

Figure 6.19 shows the accumulated LET spectra for all flights like for the energy deposition spectra in the previous section. Dark red squares show data measured during flights in upwards direction and grey triangles show the LET spectra for the sideways orientation. The LET spectra are calculated from the energy deposition spectra of the coincidence events (Figure 6.17(b)) and show therefore the same features as discussed above.

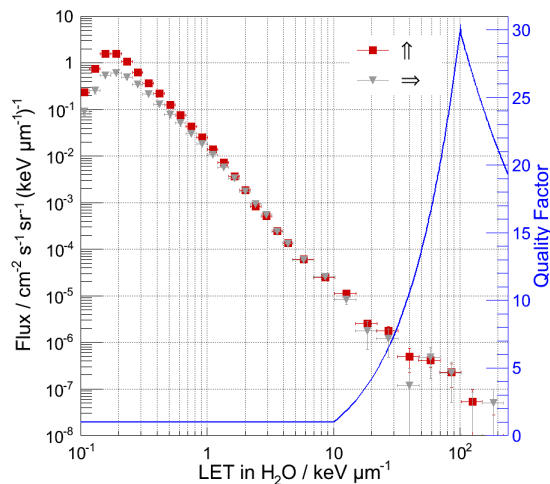


Figure 6.19.: Linear energy transfer spectra accumulated for all flights. The arrows in the figure indicate the orientation of the telescope axis. In blue the quality factor is shown as a function of the linear energy transfer defined by ICRP Publication 103 (2007) and as given in Equation 2.8.

For clarity the quality factor as a function of the linear energy transfer following ICRP Publication 103 (2007) is included in the figure. It can be distinguished between low-LET ($\leq 10 \text{ keV } \mu\text{m}^{-1}$) and high-LET ($> 10 \text{ keV } \mu\text{m}^{-1}$) particles. Low-LET particles are considered to be directly ionizing electrons, positrons, high energetic protons, and muons as well as secondary electrons from photon interactions. The high-LET part results from nuclear interaction of protons and neutrons that produce short range secondary particles (e.g. ICRU Report 84 2010). But especially these short range secondary particles are hardly seen in the measured LET spectra, since they usually do not trigger coincidences. Deriving the quality factor from these data will underestimate its real value (compare Section 6.2.7).

LET spectra for the individual flights of both detectors are shown in Figures E.24 to E.31 in Appendix E.4.

6.2.7. ABSORBED DOSE, QUALITY FACTOR, AND DOSE EQUIVALENT

The MDT was designed to eventually serve as a personal dosimeter. For dosimetric purposes therefore the relevant quantities absorbed dose, quality factor, and dose equivalent are considered in the following paragraphs.

ABSORBED DOSE

The absorbed dose in silicon is calculated from the energy deposition spectra using Equation 6.2. The results for all measurements are listed in Table 6.9, giving the flight route and number in the first column, followed by the detector (MDT-01-000 and -001) and the diode (1 and 2 for upper and lower). Column four lists the absorbed dose in μGy in the high gain channel (low energy range, up to 7 MeV energy deposition, compare e.g. Section 4.3.3), column five the low gain channels and column six the total absorbed dose in the diode. In the last column the mean dose rate is given in $\mu\text{Gy h}^{-1}$. The errors in dose include the energy resolution of the detector system and the statistical uncertainty of detected particles.

Most of the absorbed dose is detected in the high gain channels of the detectors. The low gain channels measure usually less than 10 % of the total dose.

Not all results for each diode and detector are consistent within the error for the individual flight measurements, due to possible systematic deviations, but also due to difficulties in the electronics in the beginning, as discussed before (Section 6.2.5).

Table 6.9.: Results for absorbed dose in silicon are given for each flight (column 1). For both detectors (column 2) the values of the individual diodes (column 3) are listed separately. It is distinguished between high and low gain in columns 4 and 5. The total absorbed dose for the complete energy range is given in column 6. The dose rates (column 7) refer to the mean value for the complete flight. Errors of the mean dose rate can be directly derived from the errors of the total absorbed dose, but are too small to be listed here.

Flight	Detector	Diode	Absorbed Dose in Si			Mean Dose Rate
			High Gain (μGy)	Low Gain (μGy)	Total (μGy)	in Si ($\mu\text{Gy h}^{-1}$)
A-B 1	000	1	17.6 ± 0.3	1.2 ± 0.2	18.9 ± 0.4	2.0
		2	16.6 ± 0.3	1.4 ± 0.2	18.0 ± 0.4	1.9
	001	1	17.0 ± 0.3	1.2 ± 0.2	18.2 ± 0.4	1.9
		2	17.3 ± 0.3	1.3 ± 0.3	18.7 ± 0.4	2.0
B-A 1	000	1	19.9 ± 0.3	1.6 ± 0.3	21.5 ± 0.4	2.2
		2	18.7 ± 0.3	2.2 ± 0.3	20.9 ± 0.4	2.1
	001	1	18.1 ± 0.3	1.6 ± 0.3	19.7 ± 0.4	2.0
		2	18.6 ± 0.3	1.3 ± 0.3	20.0 ± 0.4	2.0
A-B 2	000	1	16.7 ± 0.3	1.9 ± 0.3	18.6 ± 0.4	2.0
		2	16.4 ± 0.3	1.2 ± 0.2	17.7 ± 0.4	1.9
B-A 2	000	1	14.4 ± 0.3	1.1 ± 0.2	15.4 ± 0.3	1.5
		2	14.2 ± 0.3	1.7 ± 0.3	15.9 ± 0.4	1.6
	001	1	14.1 ± 0.3	1.3 ± 0.2	15.4 ± 0.4	1.5
		2	15.1 ± 0.3	1.3 ± 0.2	16.4 ± 0.4	1.6
A-B 3*	000	1	15.9 ± 0.3	1.1 ± 0.2	17.1 ± 0.4	1.7
		2	15.3 ± 0.3	1.6 ± 0.3	16.9 ± 0.4	1.6
	001	1	12.3 ± 0.3	1.3 ± 0.3	13.6 ± 0.4	1.7
		2	13.7 ± 0.3	1.7 ± 0.4	15.3 ± 0.5	1.9
B-A 3	000	1	19.4 ± 0.3	1.6 ± 0.2	21.0 ± 0.4	2.1
		2	17.9 ± 0.3	2.0 ± 0.4	19.9 ± 0.5	2.0
	001	1	18.3 ± 0.3	1.7 ± 0.3	20.0 ± 0.4	2.0
		2	19.1 ± 0.4	2.0 ± 0.3	21.1 ± 0.5	2.1
A-C	000	1	18.5 ± 0.3	1.5 ± 0.3	20.0 ± 0.4	2.2
		2	19.1 ± 0.3	0.8 ± 0.2	19.9 ± 0.4	2.2
	001	1	18.6 ± 0.3	1.4 ± 0.3	20.0 ± 0.4	2.2
		2	18.0 ± 0.3	1.3 ± 0.2	19.3 ± 0.4	2.1
C-A	000	1	14.9 ± 0.3	1.1 ± 0.2	15.3 ± 0.4	2.1
		2	15.4 ± 0.3	0.7 ± 0.2	16.1 ± 0.4	2.2
	001	1	15.5 ± 0.3	1.0 ± 0.2	16.5 ± 0.4	2.2
		2	15.1 ± 0.3	1.1 ± 0.2	16.2 ± 0.4	2.2

* The measurement time here is different for MDT-01-000 and -001. Compare Table 6.2

Since the two MDT detectors are prototypes, these measurements can be employed to estimate a systematic error for dose measurements during long duration flights in the northern temperate zone with coming detectors of MDT-kind. For each flight, the mean dose is calculated from the two diodes of each detector considering the corresponding uncertainty by error propagation. The values for each flight are consistent within less than $\pm 5\%$, which is a good result for dosimetric applications and satisfying for the prototype setup of the detector system.

These final results are compared to the available measurements with the additional silicon detector (Table 6.2), the Liulin, which has been designed as a portable dosimeter. The absorbed dose in silicon is calculated from the energy deposition spectra of the Liulin. Figure E.23 in Appendix E.3 shows the energy deposition spectra of MDT-01-001 and Liulin for flight A–C. The energy range of the Liulin is restricted to about 16 MeV to 17 MeV energy deposition, but goes down to 40 keV. Table 6.10 shows the results for both MDTs and the Liulin. The uncertainty of the MDT is the error calculated as described above. The error calculation for the Liulin includes only the statistical uncertainty and the energy resolution deduced from the energy deposition spectra, as there is no systematic error given.

Table 6.10.: Comparison of absorbed dose in silicon measured with MDTs and the Liulin, respectively, and calculated with the model by D. Matthiä. Errors for the MDTs are systematic errors as described in the text. For the Liulin the errors include statistical uncertainties and the energy resolution, only. It should be noted that the energy range of the Liulin is smaller compared to the MDT (see text). As no flight route information was available for flight A–B3, no calculations were performed for this flight.

Flight	Absorbed Dose in Si (μGy)			
	MDT-01-000	MDT-01-001	Liulin	Calculation
A–B1	18.5 ± 0.7	18.5 ± 0.7	—	18.5
B–A1	21.2 ± 0.7	19.9 ± 0.7	—	19.4
A–B2	18.2 ± 0.6	—	17.4 ± 0.1	18.5
B–A2	15.7 ± 0.7	15.9 ± 0.7	15.2 ± 0.1	16.4
A–B3*	17.0 ± 0.6	(14.5 ± 0.6)	15.6 ± 0.1	—
B–A3	20.5 ± 0.8	20.6 ± 0.8	19.1 ± 0.2	20.6
A–C	20.0 ± 0.7	19.7 ± 0.7	18.2 ± 0.2	19.5
C–A	15.7 ± 0.7	16.4 ± 0.7	14.8 ± 0.2	15.9

* The measurement time here is different for MDT-01-000 and -001. Compare Table 6.2.

It is apparent that the absorbed dose measured by the Liulin is lower than the MDT values by 4% to 9% for all flights. One reason is that the measurement range is significantly lower than for the MDT. Comparing the Liulin results with the corresponding energy range of the MDT leads to reasonable agreement between the two detector systems. Nevertheless other possible systematic uncertainties might possible and further investigation, e.g. comparative measurements with the MDTs and the Liulin with defined radiation sources and further measurements in mixed fields, as well as comparisons with other established silicon detectors and dosimeters are desirable. Still, values for dose measurements within less than 20% deviation is an acceptable result for a dosimeter (ICRU Report 84, 2010) and shows that the measurements of the MDTs are reasonable.

Additionally the measured results are compared with simulations performed by D. Matthiä (2013, private communication) with GEANT4 and PLANETOCOSMIC simulations of a silicon detector at the respective flight altitudes and routes, based on Matthiä (2009). The results are shown in column five of Table 6.10. Given few exceptions, the dose values are in excellent agreement with the measured data from the MDTs.

QUALITY FACTOR

The individual mean quality factors for the flights are derived applying Equation 6.5 and Equation 6.6. Calculations are performed for the upper diode of the telescope only, since most particles come from above. This reduces the probability to consider particles stopping in the diode, which is more likely for the lower diode, if the particle is detected in coincidence.

The quality factors vary strongly for the different flights between values of 1 and 2 (Table F.3, Appendix F), as few detected high LET events have a high influence on the calculated mean quality factors. These uncertainties also exceed possible variations due to the different flight configurations (\uparrow and \Rightarrow). Since most of the measurements were taken on the same flight route (i.e. A–B–A) and all flights were flown within the north temperate zone, a mean quality factor, weighted by the flight duration, is calculated from all flights resulting in

$$\bar{Q} = 1.37 \pm 0.33$$

This result is in good agreement with the quality factor measured with the silicon telescope DOSTEL by Beaujean et al. (2005).

Quality factors derived from measurements with a silicon detector mostly account for charged particles, as these trigger coincidences by traversing both diodes of the telescope. The contribution of neutral particles is hardly reflected, although coincidences can be triggered by high energetic photons that interact via pair production or by fragments catapulted into the second diode as a result from nuclear interactions with neutrons.

However, nuclear interaction of both, neutrons and protons, generally produce particles with a short range and large energy depositions. The linear energy transfer of these particles is not accounted for, if they do not hit the second diode, and therefore leads to a further underestimation of the mean quality factor (Beaujean et al., 1998). These factors prevent to deduce a quantitative measure of the underestimation of the mean quality factor.

DOSE EQUIVALENT

The dose equivalent for all flights and each detector is calculated by applying the mean quality factor of $\bar{Q} = 1.4$ to the absorbed dose in water (Equation 6.7). As discussed above, this quality factor underestimates the mean quality factor of the radiation field. Applying it to the total absorbed dose leads to the additional uncertainty that the total absorbed dose does not only include contributions from charged particles – that are accounted for in this quality factor – but also contributions from neutral particles that were not detected in coincidence.

In order to compare the measurements to calculations, the public available tool EPCARD¹² (Roesler et al., 2002) is employed. EPCARD calculates the effective dose following Equation 2.10, considering the date of flight, the route, and the time spent on each flight level. Although effective dose is in principle not comparable with dose equivalent, and especially not for a silicon detector, it is convenient to verify, if the overall trend is constant for the radiation exposure by comparing the ratios. These are shown in column five and six of Table 6.11 for both MDTs, together with the dose equivalent results of the MDTs and the corresponding effective dose calculated with EPCARD.

The dose equivalent measured with the MDTs is between 40 % and 50 % of the values EPCARD calculates. This ratio is stable within the uncertainty. Assuming the missing dose to be contributed by neutrons that are hardly seen in the detector, this is a

¹²European Program Package for the Calculation of Aviation Route Doses,
<http://www.helmholtz-muenchen.de/epcard-portal/dosisberechnung-auf-einer-reise/index.html>

Table 6.11.: The dose equivalent results for each flight is given for both MDTs. The fourth column gives the effective dose for each flight calculated with EPCARD. For comparison, their ratio is given in the last columns.

Flight	Dose Equivalent (μSv)		Effective Dose (μSv) EPCARD	MDT / EPCARD	
	MDT-01-000	MDT-01-001		MDT-01-000	MDT-01-001
A-B 1	31.0 ± 5.6	31.0 ± 5.6	64	0.48 ± 0.09	0.48 ± 0.09
B-A 1	35.6 ± 6.4	33.3 ± 6.0	71	0.50 ± 0.09	0.47 ± 0.09
A-B 2	30.5 ± 5.5	—	63	0.48 ± 0.09	—
B-A 2	26.3 ± 4.8	26.7 ± 4.9	58	0.45 ± 0.09	0.46 ± 0.09
A-B 3*	28.6 ± 5.2	(24.3 ± 4.4)	63	0.45 ± 0.09	—
B-A 3	34.4 ± 6.2	34.5 ± 6.3	70	0.49 ± 0.09	0.49 ± 0.09
A-C	33.5 ± 6.1	33.0 ± 6.0	74	0.45 ± 0.09	0.45 ± 0.09
C-A	26.4 ± 4.8	27.5 ± 5.0	63	0.42 ± 0.08	0.44 ± 0.08

* The measurement time here is different for MDT-01-000 and -001. Compare Table 6.2.

reasonable result according to Goldhagen (2000) for the altitude range of the presented measurements (9 km to 12.5 km) and according to Wilson (2000) for their latitudes.

6.3. SUMMARY

The radiation field at aviation altitudes is complex and provides a suitable and easy accessible environment for field tests.

The overall performance of the two MDT prototypes MDT-01-000 and MDT-01-001 was tested, including sensitivity to radiation field parameters, stability of the electronics, comparability of derived dose quantities to other measurements and calculations, respectively, as well as the general handling of the developed device.

PERFORMANCE OF THE MDT

The overall performance of the MDT was satisfying. No microphonic effects and no unexpected electronic noise were observed during the measurements. Both devices work stably, despite the fact that MDT-01-000 is rather a breadboard system than a prototype. The data was recorded reliably on the μSD card, no data was lost due to any digital process in the electronics. The displays of the detectors were not monitored continuously, but whenever they were checked, they worked fine. The power consumption did not exceed expected values and the battery runtime was found to be

sufficient.

A possible periodicity and correlation in the count rates that might have been induced by the electronics (e.g. by the saving process), could be excluded. No cross talk between the two detection channels, i.e. diodes, was found.

The speed of the electronics did not induce any dead time effects, as it was expected for these low intensities.

The general handling of the MDTs during the flights turned out to be as easy and convenient as intended. The Mobile Dosimetric Telescope successfully completed field tests in a mixed radiation field.

MEASUREMENTS IN THE RADIATION FIELD AT FLIGHT ALTITUDES

The MDT is sufficiently sensitive to verify important features of the radiation field at flight altitudes. Flight level changes that correspond to a change in altitude of 1000 ft (300 m) – in practice usually 2000 ft (600 m) – could be tracked in the count rate as well as in the dose rate profiles of a flight. With data of several flight measurements the exponential behaviour of the radiation field intensity with altitude has been shown. The dominance of the atmospheric cutoff over the geomagnetic cutoff at high latitudes has been seen in both rates.

Exploiting the strong directional response of the telescope setup, the directional dependence of the radiation field was validated.

Furthermore it was shown that the angular distribution of the radiation field at these altitudes does not change significantly with the geomagnetic cutoff rigidity, although the data presented here does not exclude slight changes.

The spectra show that the charged component of the radiation field consists to a large fraction of minimal – or close to minimal – ionizing particles. Investigating the angular dependence of the radiation field, it does not seem to follow a simple cosine law, as it is a complex superposition of different particle species with different energies, all subject to a large number of interaction processes and possibly including isotropic components. Additionally it could be shown that the main fraction of protons arises from the zenith. Since the detector generally does not distinguish between particle species, a simple geometrical model is not derived from the measured radiation field parameters.

However this data set can provide a valuable starting point to investigate the radiation field within aircraft in detail in dependence on the particle energy and incident direction.

DOSE MEASUREMENTS

The dose results are consistent with the Liulin within less than 10 %, which is a good result for dosimeters that by ICRU recommendation (ICRU Report 84, 2010) are supposed to correlate within 20 %.

The quality factor derived is in excellent agreement with previously results found with the silicon detector telescope DOSTEL. It is however not recommended to identify a quality factor from a single flight, since few high energetic events in the detector have a large influence, especially considering the small detector size.

The ratio of the dose equivalent derived from absorbed dose in silicon and the obtained quality factor, to the calculated effective dose values from EPCARD proved to be stable.

A systematic error that also accounts for statistical uncertainties for dose measurements for long duration flights is derived for the MDT and adds to $\pm 5\%$.

The newly developed detector MDT has proven the ability to measure important dose quantities reliably.

SIMULATIONS

The Mobile Dosimetric Telescope (MDT) has been designed to serve as an astronaut's dosimeter, e.g. in low Earth orbit (LEO). The verification of the device in space, however, cannot easily be performed. Therefore alternatives and approximations for calibration and testing need to be considered. In the previous chapters the MDT's detection capability of monoenergetic heavy ions and of their fragmentation products, as well as its the performance in the mixed radiation field of Earth's atmosphere were shown. However, heavy ions in space are not monoenergetic and the radiation field at aviation altitudes does not cover the energy range and particle species variety found in space. In order to estimate that the MDT will be capable to work reliably as an astronaut's dosimeter, an approach with basic simulations is presented.

These simulations should not be understood as a complete characterization of the interaction of galactic cosmic rays (GCR) with the detector system, which would result in a separate work. The following discussion is solely supposed to give an idea of what the MDT will be able to detect in space and what its limits are.

The following sections present the simulation setup (Section 7.1) and the results (Section 7.2) considering the energy depositions of the telescope on coincidence mode (Section 7.2.1) and in dependence on the energy of the detected particles (Section 7.2.2). The results are compared to measurements of a silicon detector (Section 7.2.3) before Section 7.3 provides concluding remarks.

7.1. MATERIALS AND METHODS

Figure 2.8 shows the contribution of individual GCR particle species to the absorbed dose and the dose equivalent at solar minimum. The large contribution of heavy nuclei to the dose emphasizes the necessity to cover the complete particle spectrum up to iron ions with measurements for the dose estimation of astronauts, as iron still contributes significantly to the dose equivalent.

In order to estimate, what the MDT will measure in space with its telescope

configuration, basic simulations are performed with the GEANT4¹ Monte-Carlo framework (Agostinelli et al. 2003, Allison et al. 2006). The simulations only include the geometrical setup of two silicon diodes corresponding to the size and arrangement of the MDT that is placed within a volume filled with air. No additional shielding is applied². This setup is separately irradiated with protons, oxygen and iron ions of an isotropic field distribution using the GEANT4 General Particle Source (GPS)³. Iron has been chosen as it is the heaviest ion with a significant abundance in the GCR and therefore benchmarks a sensible upper limit for what still needs to be detected. Oxygen gives an example of an important heavy ion in the medium energy range and protons are the most abundant species. Figure 7.1 shows the input spectra for the simulations of the discussed ions in the range from 100 MeV u^{-1} to 1000 GeV u^{-1} .

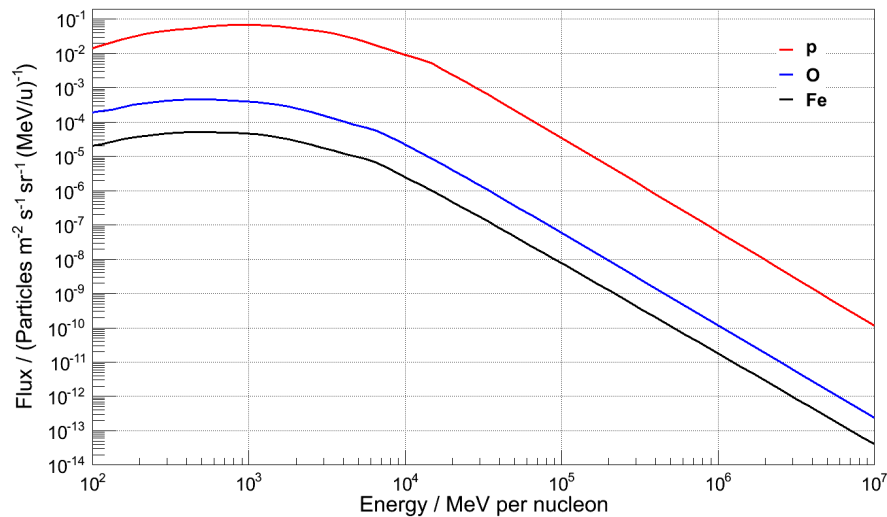


Figure 7.1.: Flux of input spectra for protons, oxygen, and iron at an altitude of 350 km.

The energies of the ions are chosen according to their energetic distribution in LEO, applying theoretical input spectra provided by the Badhwar-O’Neill GCR model (O’Neill, 2010) for the year 1998, which was right after the solar minimum between the solar cycles 22 and 23. The begin of 1998 has been chosen, since the model coincides well with measured data for this time (Mrigakshi et al., 2012). These spectra are modified

¹GEometry ANd Tracking, <http://geant4.cern.ch/>

²The simulation setup was provided by J.Köhler; the GEANT4 physics list QGSP_BERT was used (http://geant4.cern.ch/support/proc_mod_catalog/physics_lists/referencePL.shtml).

³<http://reat.space.qinetiq.com/gps/>

by the geomagnetic transport function from the programming tool CREME96⁴ (Tylka et al., 1997) to represent the energy distribution at an altitude of 350 km and an inclination of 51.6 degrees with respect to the equatorial plane of Earth. This corresponds to a possible orbit of the International Space Station (ISS)⁵. Input energies are chosen to above 100 MeV, as particles with energies below hardly contribute to dose at ISS orbit altitudes (e.g. Mrigakshi et al. 2013).

7.2. RESULTS

7.2.1. ENERGY DEPOSITION OF COINCIDENCE EVENTS

In Figure 7.2 the energy deposition in diode 2 (D2) is plotted versus the energy deposition in diode 1 (D1). Only events measured in coincidence, i.e. detected in both diodes with energy depositions above 0.06 MeV, are considered. The color coded z-axis gives the number of events in arbitrary units in logarithmic scale and for reasons of displaying normalized to a maximum of 1000 counts per bin. For comparison Figure 7.2(a) shows accumulated data recorded during flight measurements in configuration 1 (compare Section 6.2.5 and Figure 6.18(a)). Panels (b), (c), and (d) of the same figure give the results from simulations of protons, oxygen and iron ions, respectively. The sensitive range of the MDT spans from 0.06 MeV up to 140 MeV of energy depositions (Chapter 4). The plots start at the lower limit and the upper limit of this energy range is indicated by the red bars in the panels. Every entry that is above the measurement range would be detected in an overflow channel of the detector.

The term angle of incidence used in the following discussion is defined with respect to the telescope axis of the detector setup, i.e. a particle with an incident angle of zero follows the direction of the telescope axis.

The shape of the aircraft flight energy deposition spectrum has been discussed in the previous chapter (Figure 6.18, Section 6.2.5). It is apparent how the results differ in terms of energy depositions between measurements at cruising altitudes and what the detector would measure in space due to the significantly different radiation environment.

The simulation with protons is dominated by energy depositions at rather low energies

⁴Cosmic Ray Effects on Micro-Electronics, <https://creme.isde.vanderbilt.edu/>

⁵The modified spectra were provided by A.I. Mrigakshi.

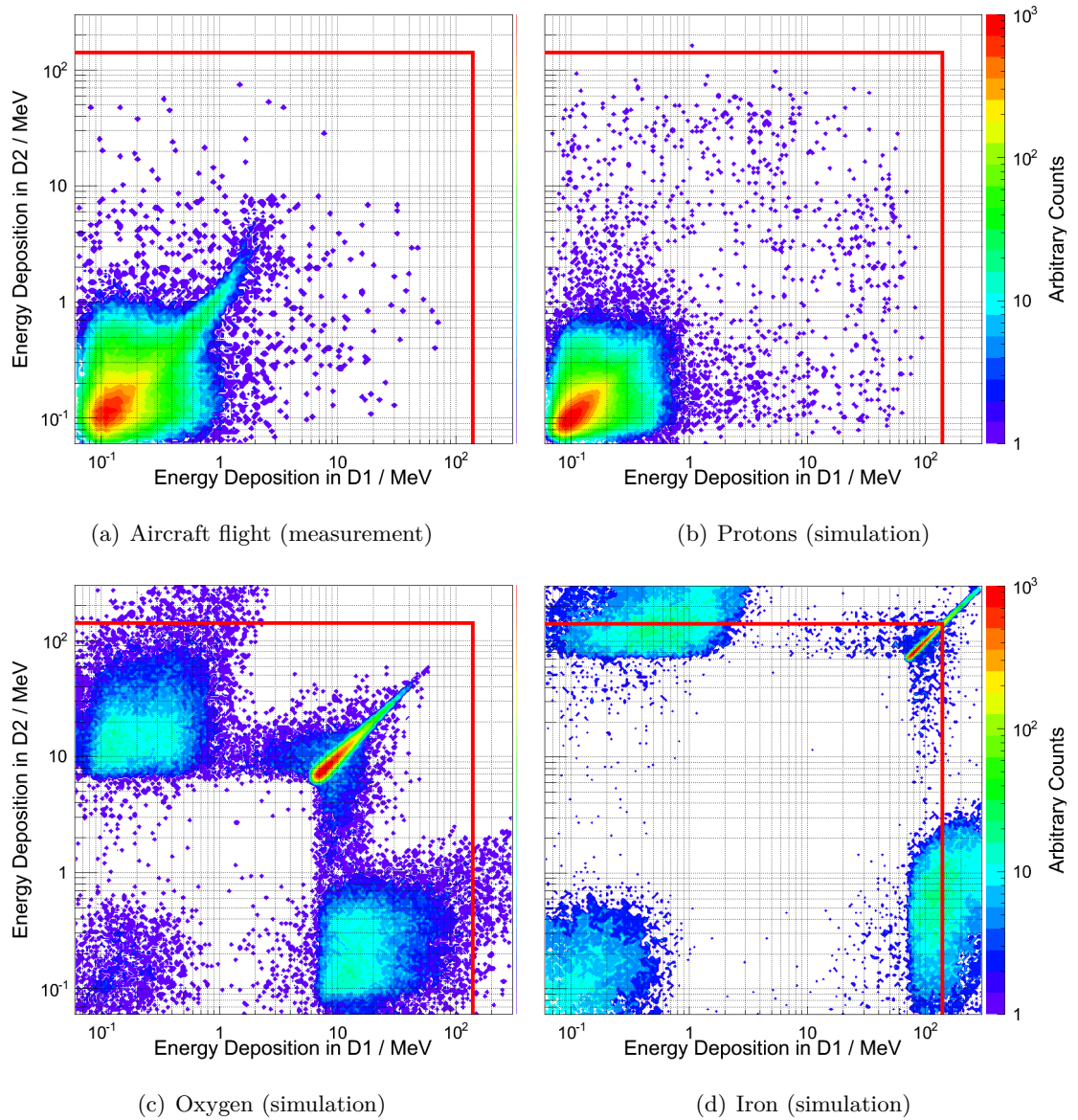


Figure 7.2.: Energy deposition in diode 2 (D2) plotted versus the energy deposition in diode 1 (D1) for measurements taken during flights at aviation altitudes (Section 6.2.5 and Figure 6.18(a)) in panel (a) and for simulations of isotropic irradiation with protons (b), oxygen (c), and iron ions (d) in accordance with their energetic distribution at an altitude of 350 km (Figure 7.1). The upper limit of the MDT measurement range (140 MeV) is indicated by red bars. All panels share the same corresponding y- and z-axis. The maximum intensity in z-direction is normalized to 1000 counts.

up to about one MeV due to the opening angle of the telescope. For protons traversing both diodes under the maximal opening angle of 70° the maximal energy deposition

adds to about 1.2 MeV for 100 MeV protons. Few entries are found at higher energies, partly due to protons with a large angle of incidence that travel a long path in one diode and produce secondary electrons that are detected in the second diode, and partly due to nuclear reactions with secondary particle production. The slight spread in the direction of the x- and y-axes of the plot arises from the fact that the energy loss distribution for protons in the silicon detectors is close to a Landau distribution. Hence larger energy depositions in one detector can correspond to smaller values in the other detector, both directly deposited by the primary proton.

The energy depositions from protons in LEO fall well within the MDT measurement range.

Most entries for oxygen and iron follow the angle bisector (45° line) of the plot. This feature arises from the superposition of two effects. For a monoenergetic particle beam along the telescope axis of the detector setup, a single spot is seen. The elongated structure along the angle bisector is partly due to the broad energy spectrum of the ions, as the energy transfer is dependent on the primary energy of the particle. The other contribution to the elongated structure as well as energy depositions apart from the angle bisector arise because of the isotropic irradiation of the setup. Particles lose energy according to their path length in the detector. For iron it is observed that the energy depositions start at about 70 MeV. This corresponds to minimal ionizing iron ions passing the $300 \mu\text{m}$ thick silicon detectors with a small angle of incidence as the mean energy loss of minimal ionizing iron ions in silicon calculates to $254 \text{ keV } \mu\text{m}^{-1}$ corresponding to an energy deposition of 76.2 MeV. Due to binning as well as due to energy loss straggling in the detector, this limit is shifted to slightly lower energies in the figure. Energies below are hardly seen and are due to particles brushing the detectors rather than traversing it completely and due to secondary particles. The same feature arises in the oxygen data for minimal ionizing oxygen ions with an energy loss of $24 \text{ keV } \mu\text{m}^{-1}$, where the limit is at about 6 MeV.

Additional islands of energy depositions are seen above these limits in one detector, while the energy deposition in the other detector is only up to the low MeV range. These are coincidences of a primary particle with a secondary particle, usually an electron (delta ray), produced by the primary and scattered into the second detector, which is not hit by the primary particle (Figure 7.3). Structures connecting these islands to the main peak can be results from a full energy deposition in one and an edge hit in the second diode.

All energy depositions below these strongly defined features discussed, arise due to

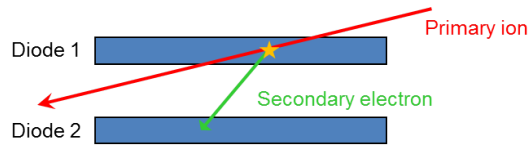


Figure 7.3.: Simplified sketch of an interaction process in which a heavy ion traverses one of the diodes in the telescope and produces a secondary particle that is detected in the second diode.

interactions of the primary ion with the air surrounding the detector setup in which the produced secondary particles trigger coincidences.

7.2.2. DEPENDENCE ON ION ENERGY

Figure 7.4 shows the energy deposition in one detector (here diode 1) in dependence of the input spectra of oxygen and iron, in order to visualize the contribution of the input energies to the detected signals. All hits above 0.06 MeV energy deposition are considered. Again, the red bars indicate the measurement range of the MDT and the data is normalized to a maximum entry of 1000 counts.

As the plot represents basically the energy loss of particles in silicon in dependence

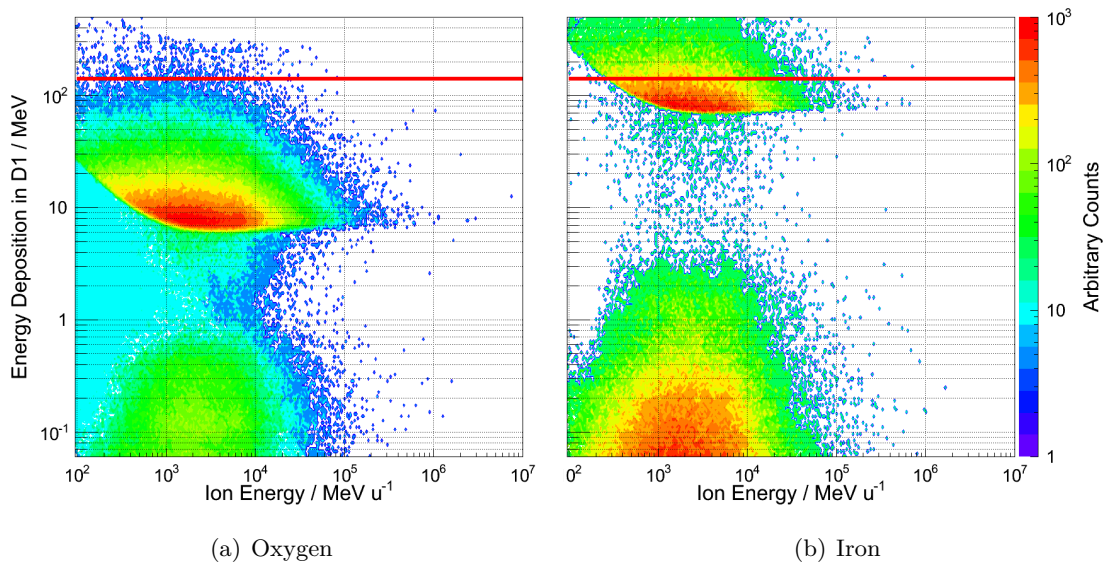


Figure 7.4.: Energy deposition in the silicon diode from oxygen and iron in space plotted versus the input spectra. All events below the red bar can be detected by the MDT. The figures share the same axis labelling and range, the intensity in z-direction is normalized to 1000 counts.

of their energy, the typical run of the energy loss curve according to the Bethe-Bloch formula (Equation 2.2) can be estimated above 6 MeV energy deposition for oxygen and above 70 MeV for iron describing the same feature that has been discussed in the previous paragraph. It restricts energy deposition mainly to values above the curve, which is given by the energy loss of the ions in $300\ \mu\text{m}$ of silicon. All events found below the curve are again due to processes (production of secondary radiation, edge hits) as discussed in Section 7.2.1. The curve itself is smeared out to higher energy depositions up to energies that lie outside the MDT measurement range. These entries are not restricted to particles of a certain incidence energy, but result from path length variations in the silicon diode. By enlarging the distance between the two diodes of the telescope, this behaviour could be improved for coincidence events, but at the cost of statistics.

7.2.3. COMPARISON WITH MEASUREMENTS

Figure 7.5 shows the energy deposition spectra of all three presented ions in one diode considering coincidences only. Red shows protons, blue oxygen and black iron ions. The flux of the individual ions is arbitrarily scaled to their relative abundance (compare Figure 7.1). Additionally displayed is a GCR spectrum from DOSTEL-1 (for

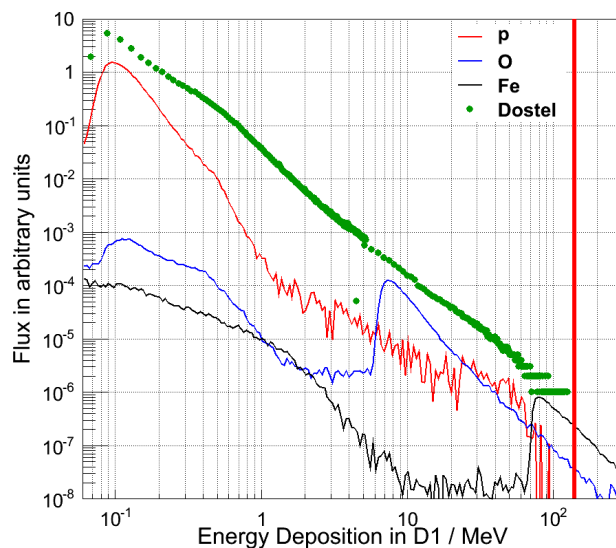


Figure 7.5.: Energy deposition spectra for protons, oxygen and iron ions simulated for the MDT and data from DOSTEL-1 measurements onboard ISS.

DOSTEL detectors see e.g. Section 2.3.3 and Beaujean et al. 1999) recorded in coincidence within the DOSIS 3D experiment (Burmeister et al., 2012). As DOSTEL-1 covers this broad energy range with only one of its silicon diodes, data from this detector channel is shown. The simulation results are scaled to fit below the DOSTEL data and the red bar in the high energy part of the spectrum indicates the MDT energy range.

Despite the fact that the simulations are limited to only three ions, it is clearly visible that the sum of the energy depositions of all ions results in a spectrum like the recorded DOSTEL spectrum. The slope of the spectrum towards higher energies is dominated by the peaks of the minimal ionizing ions. As seen before, the MDT is able to detect the important part of the spectrum, although the spectrum continues to higher energy depositions. In practice it is known from DOSTEL measurements that the number of particles detected in the overflow channel is low (Burmeister 2013, private communication).

7.3. SUMMARY

Since large energy depositions of the GCR heavy ions are the limiting factor for the high energy range of the detector, Monte Carlo simulations with three representative ions – protons, oxygen and iron – and their according energy distribution in LEO were performed. The simulations were restricted to the basic silicon telescope geometry in an isotropic radiation field distribution to give an estimate of possible energy depositions in the detector.

The results showed satisfactorily that the energy coverage of the MDT is sufficient to measure the main GCR contributions and therefore to give a reliable estimate of the dose, as it has been envisaged in the detector design.

It should be noted that depending on the coincidence criterion the linear energy transfer (LET) spectra can show contributions from secondary radiation that does not reflect the LET of the actual heavy ion. Depending on what is desired to measure this criterion could be for example that energy depositions in one diode are within a certain fraction (e.g. 50%) of the other diode, which would reject the coincidences triggered by secondary radiation. These secondary particles should however be considered for dosimetric purposes.

CONCLUSION

With the Mobile Dosimetric Telescope – MDT – a prototype for a new active personal dosimeter has been developed. The small size battery driven device is based on silicon detector technology and is specially designed to match the requirements for radiation measurements in space onboard the International Space Station.

Two prototypes – MDT-01-000-DLR-CAU and MDT-01-001-DLR-CAU – were built and the response of the electronics characterized. The electronics in both prototypes is the same, but they differ in their housing shape. The calibration has been performed with radioactive isotopes and heavy ions. Measurements of ion fragments have been conducted and field tests onboard aircraft in the mixed radiation field of the atmosphere have successfully been done. Figure 8.1(a) shows prototype MDT-01-001-DLR-CAU.

TECHNICAL SUMMARY

Two silicon diodes are placed in a telescope arrangement, enabling not only the measurement of absorbed dose, but also of the linear energy transfer (LET) by restricting the path length of an ionizing particle in the detector setup by the telescope opening angle. To prevent microphonic effects, the telescope itself is mechanically decoupled from the rest of the detector.

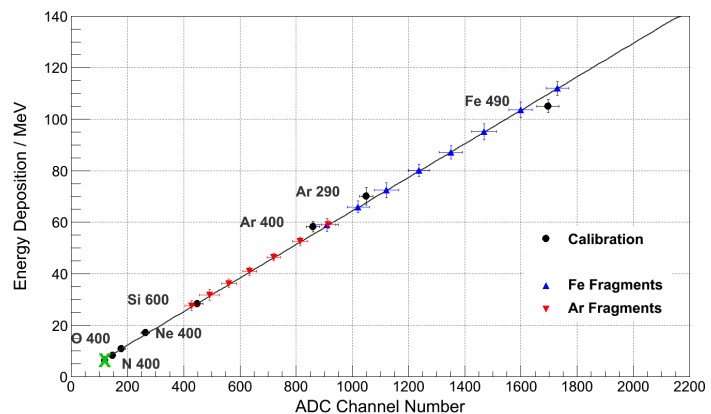
The electronics has been developed from scratch resulting in eight electronics board versions from which two – the latest preamplifier and the latest signal processing board – are in use.

In order to minimize power consumption, the signal processing is kept as simple as possible. The battery voltage drives the internal power supply unit that provides the required outputs, i.e. the bias voltage for the silicon detectors and the supply voltages for analog and digital signal processing. The front end, consisting of both silicon diodes and their preamplifiers, is placed in a separate electromagnetically shielded compartment to reduce electronic noise. The preamplifier signals are processed in

two amplification stages (low and high gain) and digitized for data evaluation. The onboard microcontroller manages the signal processing, including controlling and read-out of the analog to digital converters, monitoring the battery voltage and the communication with the interfaces. The large dead time of $440 \mu\text{s}$ for each event is a concession to realize the low power consumption, but is still more than sufficient to match the count rates in low Earth orbit (LEO) at its maximum in the region of the South Atlantic Anomaly. User interfaces of the MDT are the switch to turn the device on and off, a push-button for data saving before switching off, a display, a μSD card, a programming and a mini-USB interface. The battery can either be replaced or charged using the USB interface. Currently the MDT records single events with a time stamp and coincidence flag, which enables a detailed data evaluation, including the generation of energy deposition spectra for individual diodes or both (two-dimensional plots), linear energy transfer spectra, count and dose rates. The case of the system is carefully designed to provide a stable and well electromagnetically shielded environment, while at the same time being sufficiently flexible to enable detailed testing of the electronics of this prototype. The mechanical decoupling of the silicon diodes from the rest of the system resulted in a vibration resistant setup in which during normal daily life activity and in vibration tests within a shaking incubator no microphonic effects are observed.



(a) MDT-01-001-MDT-CAU



(b) MDT low gain calibration curve

Figure 8.1.: MDT-01-001-DLR-CAU (a) is shown (Chapter 3) next to a μSD card for size comparison and the low gain calibration curve of one detector channel (Chapter 4, Figure 4.10) including results from fragmentations measurements (Chapter 5) can be seen (b).

After characterizing the response to input signals and the electronic resolution, the MDT is calibrated with photons, electrons and alpha particles from isotope sources, proving the excellent energy resolution of the device. Accomplishment of calibration measurements with heavy ions shows that the MDT is able to detect energy depositions over 3.5 decades (Figure 8.1b). Monte Carlo simulations of measurements with selected heavy ions showed that the MDT thereby matches the requirements to measure most of the radiation field in LEO.

Table 8.1 lists the properties of the calibrated and tested prototype MDT-01-001-DLR-CAU.

Table 8.1.: Key data of the Mobile Dosimetric Telescope (MDT-01-001-DLR-CAU).

Detector setup	Telescope of 2 diodes
Sensitive detector area	$2 \times 1.21 \text{ cm}^2$
Diode thickness	$300 \mu\text{m}$
Geometry factor	$3.8 \text{ cm}^2 \text{ sr}$ (single diode) $1.7 \text{ cm}^2 \text{ sr}$ (telescope)
Size	$14 \times 6 \times 3.9 \text{ cm}^3$
Weight	290 g (including battery)
Supply voltage	3.7 V battery
Power consumption	40 mA, 160 mW
Battery runtime	> 40 h
System clock	1.8432 MHz
Dead time	440 μs
Interfaces	Display, mini-USB, μSD card
Dynamic range	60 keV – 140 MeV
LET range	0.1 – 208 keV μm^{-1} in water
Energy resolution	20 keV (high gain) 70 keV (low gain)
Uncertainty for dose measurements*	$\pm 5 \%$

* Uncertainty for dose measurements during long distance flights at altitudes between 5 and 12 km within the northern hemisphere.

PERFORMANCE SUMMARY AND MEASUREMENT RESULTS

Field tests onboard aircraft were performed with both prototypes. The MDTs showed their ability to measure reliably in the mixed and complex radiation environment of the Earth's atmosphere and to derive important radiation field parameters. Altitude and geomagnetic cutoff rigidity dependence of count and dose rates as well as the

strong directionality of the radiation field were observed and quantified. Figure 8.2 shows for example count rate profiles of a flight (a) and LET spectra (b), both with results for measurements in which the telescope axis of the detectors have been oriented towards the zenith (\uparrow) and rotated by 90° pointing sideways (\Rightarrow). Already these plots indicate immediately altitude and geomagnetic cutoff rigidity dependence (in the count rates) as well as the directionality (count rates and LET spectra) of the radiation field. It was furthermore shown that this directionality at aviation altitudes does not seem to be subject to strong changes with the geomagnetic cutoff rigidity. From the energy deposition spectra a rather low energetic directed proton component could be identified. Reasonable values for the dose quantities absorbed dose, quality factor and dose equivalent were obtained that could be compared to other measurements as well as to calculations. From the measurements a preliminary systematic error of the detector system was deduced.

In order to extend performance tests to higher energies and to simulate a rudimentary mixed radiation field at these energies, fragmentation measurements of heavy ions were conducted. The experiments lead to convincing results, showing the good response of the detector system at these energies in terms of resolution and stability.

Not only the measurement capability, but also the easy handling of the devices during all tests was consistently satisfying.

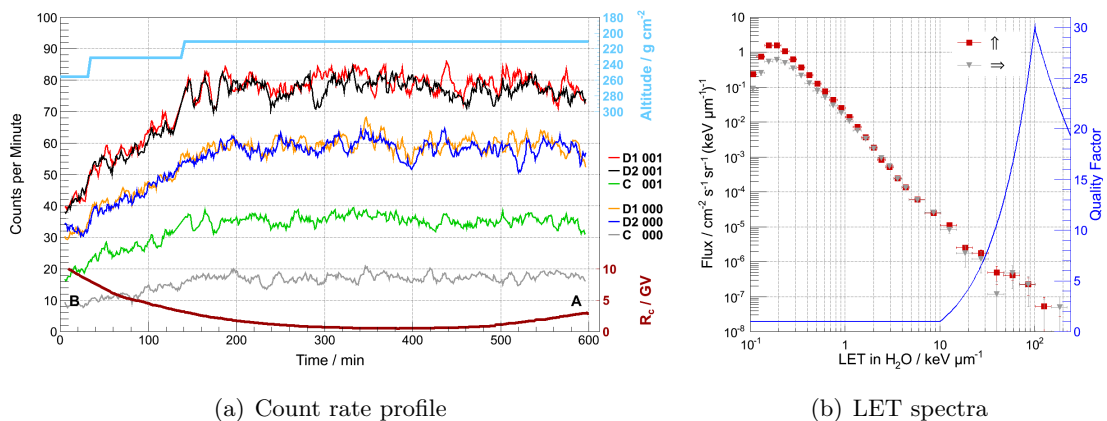


Figure 8.2.: Examples of successful tests with the MDT prototypes during flight measurements in which one detector measured towards the zenith, while the other was rotated by 90° to the side (Chapter 6, Figures 6.4 and 6.19).

APPLICATION AND OUTLOOK

Despite the fact that the MDT performed well in the radiation field of the Earth's atmosphere, the small detector size limits the measurement accuracy in this environment. The detector system is especially designed for the application in the stronger radiation field in LEO, providing sufficient counting statistics while at the same time the signal processing speed can be kept low in order to reduce power consumption enabling the detector to run on battery supply.

This is an advantage compared to other excellent detector systems currently working onboard the International Space Station (ISS), as due to different shieldings, the radiation environment changes within the space station and therefore also the radiation exposure of astronauts changes.

The continuous radiation exposure monitoring of astronauts is currently performed by passive personal dosimeters. The MDT is not to replace these well established and failure-safe detectors, but rather to improve the radiation monitoring of astronauts with an active device. Thereby it is possible to act accordingly in case a certain dose rate threshold is exceeded. The recording of dose rates is important for scientific as well as for medical purposes. It is known that the radiation environment inside ISS does not threaten the astronauts' health immediately in terms of deterministic effects. However, little is known about the biological effects of a continuous exposure of humans with doses that might be below deterministic thresholds, but that at the same time exceed the natural radiation environment of Earth by a factor of 100. Late effect like cataracts are already recorded. Extension of this knowledge with detailed measurements will help to improve this knowledge and thereby also improve the risk estimation for humans in space.

BIBLIOGRAPHY

- Ackermann, M., Ajello, M., Allafort, A. et al., Feb. 2013. Detection of the Characteristic Pion-Decay Signature in Supernova Remnants. *Science* 339 (6121), 807–811.
- Agostinelli, S., Allison, J., Amako, K. et al., (Geant4 Collaboration), Jul. 2003. Geant4 – a simulation toolkit. *Nuclear Instruments and Methods in Physics Research A* 506, 250–303.
- Allison, J., Amako, K., Apostolakis, J. et al., Feb. 2006. Geant4 developments and applications. *Nuclear Science, IEEE Transactions on* 53 (1), 270–278.
- Battistoni, G., Ferrari, A., Pelliccioni, M., Villari, R., 2004. Monte Carlo calculation of the angular distribution of cosmic rays at flight altitudes. *Radiation Protection Dosimetry* 112 (3), 331–343.
- Beaujean, R., Burmeister, S., Petersen, F., Reitz, G., 2005. Radiation exposure measurement onboard civil aircraft. *Radiation Protection Dosimetry* 116 (1-4 Pt 2), 312–315.
- Beaujean, R., Kopp, J., Reitz, G., 1999. Active dosimetry on recent space flights. *Radiation Protection Dosimetry* 85 (1-4), 223–226.
- Beaujean, R., Kopp, J., Roos, F., Reitz, G., 1998. Measurements of radiation exposure in civil aircraft. *Acta Astronautica* 43 (3-6), 271–275.
- Berger, M., Coursey, J., Zucker, M., , Chang, J., 2005. ESTAR, PSTAR, and ASTAR: Computer Programs for Calculating Stopping-Power and Range Tables for Electrons, Protons, and Helium Ions (version 1.2.3), [2013, 01]. National Institute of Standards and Technology, Gaithersburg, MD 116.
URL <http://physics.nist.gov/Star>
- Berger, M. J., Coursey, J. S., Zucker, M. A., Chang, J., 1998. XCOM: Photon Cross Sections Database. NIST Standard Reference Database.
URL <http://physics.nist.gov/PhysRefData/Xcom/Text/XCOM.html>
- Berger, T., 2008. Radiation dosimetry onboard the International Space Station ISS. *Zeitschrift für medizinische Physik* 18, 265–275.
- Berger, T., Hajek, M., Bilski, P., Horwacik, T., Puchalska, M., Körner, C., Yukihiro, E., Benton, E., Gaza, R., Pálfalvi, J. K., Szabó, J., Hager, L., Yasuda, N., Uchihori, Y., Kitamura, H., Kodaira, S., Nagamatsu, A., Shurshakov, V. A., Burmeister, S., Sihver, L., Petrov, V. M., Reitz, G., Sep. 2012. MATROSHKA – Results from the exposure inside the Japanese KIBO Module – and comparison with previous missions. 17th WRMIS, Austin, Texas.
- Beringer et al. (PDG), J., 2012a. 26. Cosmic Rays. *Phys. Rev. D* 86, 010001.
URL <http://pdg.lbl.gov>

- Beringer et al. (PDG), J., 2012b. 30. Passage of Particles Through Matter. Phys. Rev. D86, 010001.
URL <http://pdg.lbl.gov>
- Biermann, L., 1951. Kometenschweife und solare Korpuskularstrahlung. Zeitschrift für Astrophysik 29, 274.
- Brun, R., Rademakers, F., 1996. ROOT - An Object Oriented Data Analysis Framework, Proceedings AIHENP'96 Workshop, Lausanne, Sep. 1996, Nucl. Inst. & Meth. in Phys. Res. A 389 (1997) 81-86.
URL <http://root.cern.ch/>
- Burmeister, S., Labrenz, J., Beaujean, R., Kortmann, O., Berger, T., Boehme, M., Haumann, L., Reitz, G., Sep. 2012. The DOSIS and DOSIS 3D Experiments onboard the International Space Station – Results From Active DOSTEL Instruments. 17th WRMISS, Austin, Texas.
- Cucinotta, F., Manuel, F., Jones, J., Iszard, G., Murrey, J., Djojonegro, B., Wear, M., 2001. Space radiation and cataracts in astronauts. Radiation Research 156 (5 Pt 1), 460–6.
- Dachev, T., Dimitrov, P., Tomov, B., Matviichuk, Y., 2007. Technical description of the LET spectrometer Liulin-6G.
- Ferrari, A., Pelliccioni, M., Villari, R., 2004. Evaluation of the influence of aircraft shielding on the aircrew exposure through an aircraft mathematical model. Radiation Protection Dosimetry 108 (2), 91–105.
- Gaimard, J. J., Schmidt, K. H., 1991. A reexamination of the abrasion-ablation model for the description of the nuclear fragmentation reaction. Nuclear Physics A 531, 709–745.
- Goldhagen, P., 2000. Overview Of Aircraft Radiation Exposure And Recent Er2 Measurements. Health Physics 79, 526–544.
- Grieder, P. K. F., 2001. Cosmic Rays at Earth: Researcher's Reference Manual and Data Book. North-Holland, Amsterdam.
- Hale, G. E., Nicholson, S. B., Nov. 1925. The Law of Sun-Spot Polarity. Astrophysical Journal 62, 270.
- Hall, E. J., Giaccia, A. J., 2011. Radiobiology for the Radiologist; 7th ed. Lippincott Williams & Wilkins, Philadelphia, PA.
- Hassler, D. M., Zeitlin, C., Wimmer-Schweingruber, R. F. et al., Sep. 2012. The Radiation Assessment Detector (RAD) Investigation. Space Science Reviews 170, 503–558.
- Heber, B., 2011. Cosmic Rays Through the Solar Hale Cycle. Space Science Reviews, online first article, 1–14.
- Heber, B., Potgieter, M. S., 2006. Cosmic Rays at High Heliolatitudes. Space Science Reviews 127, 117–194.
- Hellweg, C. E., Baumstark-Kahn, C., 2007. Getting ready for the manned mission to Mars: the astronauts' risk from space radiation. Naturwissenschaften 94, 517–526.

- Herbst, K., 2012. Interaction of Cosmic Rays with the Earth's Magnetosphere and Atmosphere. Dissertation, Kiel.
- Hess, V. F., 1912. Über Beobachtungen der durchdringenden Strahlung bei sieben Freiballonfahrten. *Physikalische Zeitschrift* 13, 1084–1094.
- Hüfner, J., Schäfer, K., Schürmann, B., Dec. 1975. Abrasion-ablation in reactions between relativistic heavy ions. *Phys. Rev. C* 12, 1888–1898.
- ICRP Publication 103, 2007. The 2007 Recommendations of the International Commission on Radiological Protection. ICRP Publication 103. *Ann. ICRP* 37 (2-4).
- ICRP Publication 60, 1991. 1990 Recommendations of the International Commission on Radiological Protection. ICRP Publication 60. *Ann. ICRP* 21 (1-3).
- ICRU Report 84, 2010. Reference Data for the Validation of Doses from Cosmic-Radiation Exposure of Aircraft Crew. ICRU Report 84 (prepared jointly with ICRP). *Journal of the ICRU* 10 (2).
- ICRU Report 85, Oct. 2011. Fundamental Quantities and Units for Ionizing Radiation (*Revised*). *Journal of the ICRU* 11 (1).
- Jadrníčková, I., Tateyama, R., Yasude, N., Kawashima, H., Kurano, M., Uchihori, Y., Kitamura, H., Akatov, Y., Shurshakov, V., Kobayashi, I., Ohguchi, H., Koguchi, Y., Spurný, F., 2009. Variation of absorbed doses onboard of ISS Russian Service Module as measured with passive detectors. *Radiation Measurements* 44 (9-10), 901–904.
- Knoll, G. F., 1999. Radiation Detection and Measurement. John Wiley & Sons, Inc. Third Edition.
- Kraft, R. P., Burrows, D. N., Nousek, J. A., Jun. 1991. Determination of confidence limits for experiments with low numbers of counts. *The Astrophysical Journal* 374, 344–355.
- La Tessa, C., 2007. Fragmentation Cross Sections: Measurement, Systematics and Model Development. Dissertation, Göteborg, Sweden.
- Landau, L., 1944. On the energy loss of fast particles by ionization. *Journal of Physics (USSR)* 8, 201–205.
- Leo, W. R., 1994. Techniques for Nuclear and Particle Physics Experiments. Springer Verlag Second Revised Edition.
- Lewis, B., Desormeaux, M., Green, A., Bennett, L., Butler, A., McCall, M., Vergara, J. S., September 2004. Assessment of aircrew radiation exposure by further measurements and model development. *Radiation Protection Dosimetry* 111, 151–171.
- Matthiä, D., 2009. The Radiation Environment in the Lower Atmosphere – A Numerical Approach. Dissertation, Kiel.
- Matthiä, D., Heber, B., Reitz, G., Meier, M., Sihver, L., Berger, T., Herbst, K., 2009. Temporal and spatial evolution of the solar energetic particle event on 20 January 2005 and resulting radiation doses in aviation. *Journal of Geophysical Research* 114.

- Mocchiutti, E., Adriani, O., Barbarino, G., Bazilevskaya, G., Bellotti, R. et al., 2009. The PAMELA Space Experiment.
- Mrigakshi, A., Matthiä, D., Berger, T., Reitz, G., Wimmer-Schweingruber, R. F., 2012. Assessment of Galactic Cosmic Ray models. *Journal of Geophysical Research*.
- Mrigakshi, A., Matthiä, D., Berger, T., Reitz, G., Wimmer-Schweingruber, R. F., 2013. How Galactic Cosmic Ray models affect the estimation of radiation exposure in space. *Advances in Space Research* 51 (5), 825 – 834.
- Musiol, G., Ranft, J., Reif, R., Seeliger, D., 1988. *Kern- und Elementarteilchenphysik*. VCH Verlagsgesellschaft.
- Narici, L., Belli, F., Bidoli, V., et al., 2004. The ALTEA/ALTEINO projects: studying functional effects of microgravity and cosmic radiation. *Advances in Space Research* 33, 1352–1357.
- NASA, 1976. U.S. Standard Atmosphere (NASA-TM-X-74335) National Aeronautics and Space Administration.
- NCRP Report No.132, 2000. Radiation Protection Guidance for Activities in Low-Earth Orbit. Recommendations of the National Council on Radiation Protection and Measurements.
- NCRP Report No.142, 2002. Operational Radiation Safety Program for Astronauts in Low-Earth Orbit: A Basic Framework. Recommendations of the National Council on Radiation Protection and Measurements.
- NCRP Report No. 153, 2006. Information Needed to Make Radiation Protection Recommendations for Space Missions Beyond Low-Earth Orbit. Recommendations of the National Council on Radiation Protection and Measurements.
- O'Neill, P., Dec. 2010. Badhwar-O'Neill 2010 Galactic Cosmic Ray Flux Model – Revised. *Nuclear Science, IEEE Transactions on* 57 (6), 3148–3153.
- Parker, E. N., Nov. 1958. Dynamics of the Interplanetary Gas and Magnetic Fields. *Astrophysical Journal* 128, 664.
- Parzen, E., 1960. *Modern probability theory and its applications*. (A Wiley Publication in Mathematical Statistics.) New York and London: John Wiley & Sons, Inc. XV, 464 p.
- Perez-Nunez, D., Braby, L. A., 2011. Replacement tissue-equivalent proportional counter for the International Space Station. *Radiation Protection Dosimetry* 143 (2-4), 394–397.
- Pfotzer, G., 1936. Dreifachkoinzidenzen der Ultrastrahlung aus vertikaler Richtung in der Stratosphäre. *Zeitschrift für Physik* 102.
- Picozza, P., Marcelli, L., Adriani, O. et al., 2013. Cosmic Ray Study with the PAMELA Experiment. *Journal of Physics: Conference Series* 409.
- Potgieter, M., 2011. Cosmic Rays in the Inner Heliosphere: Insights from Observations, Theory and Models. *Space Science Reviews*, online first article, 1–12.

- Potgieter, M. S., Vos, E. E., Boezio, M., De Simone, N., Di Felice, V., Formato, V., 2013. Modulation of galactic protons in the heliosphere during the unusual solar minimum of 2006 to 2009. ArXiv: 1303.1284.
- Pröls, G. W., 2004. Physik des erdnahen Weltraums: Eine Einführung. Springer Verlag Zweite Auflage.
- Reitz, G., 2008. Characteristic of the radiation field in low earth orbit and in deep space. Zeitschrift für Medizinische Physik 18 (4), 233–243.
- Reitz, G., Beaujean, R., Benton, E., Burmeister, S., Dachev, T., Deme, S., Luszik-Bhadra, M., Olko, P., 2005. Space radiation measurements on-board ISS — the DOSMAP experiment. Radiation Protection Dosimetry 116 (1-4), 374–379.
- Roesler, S., Heinrich, W., Schraube, H., 2002. Monte Carlo calculation of the radiation field at aircraft altitudes. Radiation Protection Dosimetry 98 (4), 367–88.
- Roos, F., 1997. Messung der Strahlenexposition in Verkehrsflugzeugen mit einem Halbleiterdetektor. Diplomarbeit, Kiel.
- Rossi, B., Aug 1930. On the Magnetic Deflection of Cosmic Rays. Phys. Rev. 36, 606–606.
- Santen, N., Meier, M., Matthiäe, D., 2012. The Importance of Space Weather Awareness for Airborne Radiation Monitoring after the Nuclear Disaster of Fukushima. Space Weather Week, Boulder.
- Schrewe, U., 2000. Global Measurements of the Radiation Exposure of Civil Air Crews from 1997 to 1999. Radiation Protection Dosimetry 91 (4), 347–364.
- Schwabe, S. H., 1843. Solar Observations During 1843. Astronomische Nachrichten 20 (495).
- SIDC-team, 1957-2012. The International Sunspot Number. Monthly Report on the International Sunspot Number, online catalogue.
URL <http://www.sidc.be/sunspot-data/>
- Sihver, L., 2008. Transport calculations and accelerator experiments needed for radiation risk assessment in space. Zeitschrift für Medizinische Physik 18 (4), 253–64.
- Simpson, J. A., 1983. Elemental and Isotopic Composition of the Galactic Cosmic Rays. Annual Review of Nuclear and Particle Science 33, 323–382.
- Simpson, J. A., Jul. 2000. The Cosmic Ray Nucleonic Component: The Invention and Scientific Uses of the Neutron Monitor - (Keynote Lecture). Space Science Reviews 93, 11–32.
- Singer, S. F., Sep. 1958a. "Radiation Belt" and Trapped Cosmic-Ray Albedo. Physical Review Letters 1, 171–173.
- Singer, S. F., Sep 1958b. Trapped Albedo Theory of the Radiation Belt. Physical Review Letters 1, 181–183.

- Smart, D. F., Shea, M. A., 2005. A review of geomagnetic cutoff rigidities for earth-orbiting spacecraft. *Advances in Space Research* 36, 2012–2020.
- Straube, U., Berger, T., Reitz, G., Facius, R., Fuglesang, C., Reiter, T., Damann, V., Tognini, M., Apr. 2010. Operational radiation protection for astronauts and cosmonauts and correlated activities of ESA Medical Operations. *Acta Astronautica* 66, 963–973.
- Sullivan, J. D., 1971. Geometrical factor and directional response of single and multi-element particle telescopes. *Nuclear Instruments and Methods* 95, 5.
- Sullivan, J. D., 1972. Errata. *Nuclear Instruments and Methods* 98 (1), 187.
- Tylka, A., Adams, J.H., J., Boberg, P., Brownstein, B., Dietrich, W., Flueckiger, E., Petersen, E., Shea, M., Smart, D., Smith, E., Dec. 1997. CREME96: A Revision of the Cosmic Ray Effects on Micro-Electronics Code. *Nuclear Science, IEEE Transactions on* 44 (6), 2150–2160.
- van Allen, J. A., McIlwain, C. E., Ludwig, G. H., Mar. 1959. Radiation Observations with Satellite 1958e. *Journal of Geophysical Research* 64, 271–286.
- Vavilov, P. V., 1957. Ionization losses of high-energy heavy particles. *Soviet Physics JETP* 5, 749–751.
- Westfall, G. D., Wilson, L. W., Lindstrom, P. J., Crawford, H. J., Greiner, D. E., Heckman, H. H., Apr. 1979. Fragmentation of relativistic ^{56}Fe . *Phys. Rev. C* 19, 1309–1323.
- Wilson, J. W., 2000. Overview Of Radiation Environments And Human Exposures. *Health Physics* 79, 470–494.
- Wilson, J. W., Nealy, J. E., Dachev, T. P., Tomov, B. T., Cucinotta, F. A., Badavi, F. F., Angelis, G. D., Atwell, W., Leutke, N., 2007. Time serial analysis of the induced LEO environment within the ISS 6A. *Advances in Space Research* 40 (11), 1562–1570.
- Wissmann, F., 2006. Long-term measurements of $\text{H}^*(10)$ at aviation altitudes in the northern hemisphere. *Radiation Protection Dosimetry* 121 (4), 347–57.
- Wissmann, F., Reginatto, M., Möller, T., 2010. The ambient dose equivalent at flight altitudes: a fit to a large set of data using a Bayesian approach. *Journal of Radiological Protection* 30 (3), 513.
URL <http://stacks.iop.org/0952-4746/30/i=3/a=006>
- Zeitlin, C., Guetersloh, S., Heilbronn, L., Miller, J., Elkhayari, N., Empl, A., LeBourgeois, M., Mayes, B. W., Pinsky, L., Christl, M., Kuznetsov, E., 2008. Shielding experiments with high-energy heavy ions for spaceflight applications. *New Journal of Physics* 10 (7), 075007.
- Zeitlin, C., Heilbronn, L., Miller, J., Rademacher, S. E., Borak, T., Carter, T. R., Frankel, K. A., Schimmerling, W., Stronach, C. E., Jul. 1997. Heavy fragment production cross sections from 1.05 GeV/nucleon ^{56}Fe in C, Al, Cu, Pb, and CH_2 targets. *Phys. Rev. C* 56, 388–397.
- Zeitlin, C., Heilbronn, L., Miller, J., Schimmerling, W., Townsend, L. W., Tripathi, R. K., Wilson, J. W., 1996a. The fragmentation of 510 MeV/nucleon iron-56 in polyethylene. II. Comparisons between Data and a Model. *Radiation Research* 145 (6), 666–672.

- Zeitlin, C., Miller, J., Heilbronn, L., Frankel, K., Gong, W., Schimmerling, W., 1996b. The fragmentation of 510 MeV/nucleon iron-56 in polyethylene. I. Fragment fluence spectra. *Radiation Research* 145 (6), 655–665.
- Zhou, D., Semones, E., Gaza, R., Johnson, S., Zapp, N., Lee, K., George, T., 2009. Radiation measured during ISS-Expedition 13 with different dosimeters. *Advances in Space Research* 43 (8), 1212–1219, *space Life Sciences*.
- Ziegler, J. F., Ziegler, M., Biersack, J., 2012. SRIM - The stopping and range of ions in matter. *Nuclear Instruments and Methods in Physics Research Section B: Beam Interactions with Materials and Atoms* 268 (11-12), 1818–1823.

LIST OF DATASHEETS

A250FNF	Preamplifier http://www.amptek.com/a250fn.html
AD5252	Digital potentiometer http://www.analog.com/static/imported-files/data_sheets/AD5251_5252.pdf
AD7864-2	Analog to digital converter http://www.analog.com/static/imported-files/data_sheets/AD7864.pdf
ADM8829	Voltage inverter http://www.analog.com/static/imported-files/data_sheets/ADM8828_8829.pdf
ADR291	2.5 V Voltage reference http://www.analog.com/static/imported-files/data_sheets/ADR291_292.pdf
ADS1174	Analog to digital converter http://www.ti.com/lit/ds/symlink/ads1174.pdf
AT45DB161D	Flash memory http://www.adestotech.com/at45db161d
ATmega16	Microcontroller http://www.atmel.com/Images/doc2466.pdf
ATmega1284P	Microcontroller http://www.atmel.com/Images/doc8059.pdf
DOGM163L	Display http://www.lcd-module.com/eng/pdf/doma/dog-me.pdf
DS1339U	Real time clock http://datasheets.maximintegrated.com/en/ds/DS1339-DS1339U.pdf
FT232RL	USB to UART interface http://www.ftdichip.com/Support/Documents/DataSheets/ICs/DS_FT232R.pdf
MAX1811	Battery charger http://datasheets.maximintegrated.com/en/ds/MAX1811.pdf
MAX3221EUE	RS-232 Transceiver http://datasheets.maximintegrated.com/en/ds/MAX3221-MAX3243.pdf
PC250F	Commercial test board for preamplifier A250FNF http://www.amptek.com/a250fn.html
REG71055	5.5 V charge pump http://www.ti.com/lit/ds/symlink/reg71055.pdf
S	Gel bush http://docs-europe.electrocomponents.com/webdocs/0b52/0900766b80b52934.pdf
S3590-19	Silicon diode http://www.hamamatsu.com/resources/pdf/ssd/s3590-08_etc_kpin1052e09.pdf
S2744-08	Silicon diode (Liulin) http://www.hamamatsu.com/resources/pdf/ssd/s2744-08_etc_kpin1049e06.pdf

SI	Shaking incubator http://www.infors-ht.com/index.php/de/produkte/schuettler/inkubationsschuettler/multitron-standard
STK600	Commercial test board for Atmel microcontrollers http://www.kamami.pl/dl/stk600_user_guide.pdf
TPS77030	Low-dropout voltage regulator http://www.ti.com/lit/ds/symlink/tps77030.pdf
TS5A3166	Analog switch http://www.ti.com/lit/ds/symlink/ts5a3166.pdf

As of May 2013

LIST OF ABBREVIATIONS

ADC	Analog to digital converter
Amp	Amplifier
AMS	Alpha Magnetic Spectrometer
BfS	Bundesamt für Strahlenschutz
CAD	Computer-aided design
CAU	Christian-Albrechts-Universität zu Kiel
CNES	French National Center for Space Studies
CRAND	Cosmic Ray Albedo Neutron Decay
CREME	Cosmic Ray Effects on Micro-Electronics
CSA	Charge sensitive preamplifier
DLR	Deutsches Zentrum für Luft- und Raumfahrt (German Aerospace Center)
DOSIS	Dose Distribution Inside the ISS
DOSTEL	Dosimetry Telescope
ESA	European Space Agency
ESR	Equivalent series resistance
FL	Flight level
FWHM	Full width at half maximum
GCR	Galactic cosmic rays
GEANT	Geometry And Tracking
GF	Geometry factor
GPS	General Particle Source
HIMAC	Heavy Ion Medical Accelerator
I ² C	Inter-Integrated Circuit
ICRP	International Commission on Radiological Protection
ICRU	International Commission on Radiation Units & Measurements
ISA	International Standard Atmosphere
IEAP	Institute for Experimental and Applied Physics
ISS	International Space Station
JTAG	Joint Test Action Group – Standard Test Access Port and Boundary-Scan Architecture
LAT	Large Area Telescope
LEO	Low Earth Orbit
LET	Linear energy transfer
MDT	Mobile Dosimetric Telescope
μ C	Microcontroller
μ SD card	Micro secure digital card
NCRP	National Council on Radiation Protection and Measurements
NIRS	National Institute of Radiological Sciences

OBF	Oberpfaffenhofen
PAMELA	Payload for Antimatter Matter Exploration and Light-nuclei Astrophysics
PCB	Printed circuit board
PDG	Particle Data Group
PD	Peak detector
PE	Polyethylene
PNTD	Plastic nuclear track edge detector
PWM	Pulse-width-modulation
RTC	Real time clock
SAA	South Atlantic Anomaly
SEP	Solar energetic particle
SG	Signal generator
SHA	Shaper
SPI	Serial Periphery Interface
TEPC	Tissue equivalent proportional counter
TLD	Thermoluminescence detector
USART	Universal Synchronous/Asynchronous Receiver/Transmitter
USB	Universal Serial Bus

LIST OF FIGURES

1.1. Aurora Australis	2
2.1. Galactic cosmic ray spectrum	6
2.2. Anti-correlation of neutron monitor count rates and sun spot numbers	7
2.3. Geomagnetic cutoff rigidity	9
2.4. Proton flux in dependence on geomagnetic cutoff rigidity	9
2.5. Radiation belts	10
2.6. Energy loss distribution	15
2.7. Quality factor	20
2.8. Contribution of galactic heavy ions to dose	22
3.1. Telescope Setup	26
3.2. Detector principle – block diagram 1	27
3.3. Detector principle – block diagram 2	28
3.4. Analog signal processing – CSA, SHA, Amp	29
3.5. Analog signal processing – Amp, PD, Comp, Threshold	29
3.6. Board versions 00.xx to 05.01	31
3.7. Board version 08.01	33
3.8. Silicon diode	35
3.9. Detector principle – block diagram 3	38
3.10. MDT-01-000-DLR-CAU	40
3.11. MDT-01-001-DLR-CAU – open	41
3.12. MDT-01-001-DLR-CAU	42
3.13. Countermeasure for microphonic effects	42
3.14. Count rate profile for microphonic countermeasure (1)	43
3.15. Vibration test of MDT-01-001	44
3.16. Count rate profile for microphonic countermeasure (2)	44
3.17. Electronic resolution	46
3.18. Response for linear input of the MDT-01-001 1B	46
3.19. Telescope with definition of θ and ϕ	48
3.20. Geometrical response – dependence on θ and ϕ (1)	49
3.21. Geometrical response – dependence on θ and ϕ (2)	50

4.1.	^{241}Am γ - MDT-01-001 diode 1	52
4.2.	^{241}Am α - MDT-01-001 diode 1	53
4.3.	^{241}Am α - MDT-01-001 diode 1 (covered diode)	53
4.4.	Active volume of silicon diode with aluminium frame	54
4.5.	^{207}Bi electrons - MDT-01-001 diode 1	55
4.6.	Irradiation setup at HIMAC	56
4.7.	Heavy ions - MDT-01-001 diode 1	58
4.8.	Vavilov fits of heavy ions	59
4.9.	High gain calibration curve - MDT-01-001 diode 1	61
4.10.	Low gain calibration curve - MDT-01-001 diode 1	62
4.11.	Calibration curves - MDT-01-001 diode 1	64
5.1.	Irradiation setup of fragment measurement	66
5.2.	Fragment measurements	67
5.3.	Charge spectrum	69
5.4.	Fragments – energy pulse height spectrum	71
5.5.	Fragment production in PE absorber	71
5.6.	Energy loss of fragments in silicon	72
6.1.	Flight setup	76
6.2.	Count rates – A–B–A 1	84
6.3.	Deviation of count rates from mean	85
6.4.	Count rates – A–B–A 3	86
6.5.	Time measured on flight level	88
6.6.	Count rates vs. residual atmosphere – S_{\uparrow}	89
6.7.	Count rates vs. residual atmosphere	91
6.8.	Time measured within R_c interval	93
6.9.	Count rates vs. cutoff rigidity	94
6.10.	Count rate ratios vs. cutoff rigidity	94
6.11.	Dose rates A–B–A 1	97
6.12.	Dose rates A–B–A 3	98
6.13.	Separate dose rates MDT-01-001 B–A 3	99
6.14.	Dose rates vs. residual atmosphere	101
6.15.	Dose rates vs. residual atmosphere	102
6.16.	Energy deposition spectra – all diodes	104
6.17.	Energy deposition spectra – all configurations	105

6.18. Energy deposition spectra – Coincidences	109
6.19. LET spectra	110
7.1. Heavy ion spectra in low Earth orbit	120
7.2. Simulation of energy deposition in telescope in space	122
7.3. Sketch of coincidence with secondary particles	124
7.4. Simulation of energy deposition in dependence of input energy	124
7.5. Energy deposition spectra – ion simulation	125
8.1. Conclusion – technical summary	128
8.2. Conclusion – performance summary	130
A.1. Board version 01.01 with vacuum chamber	156
A.2. Board version 05.01 and 06.01	158
B.1. Circuit diagram – battery charger and USB interface	161
B.2. Circuit diagram – bias voltage	161
B.3. Circuit diagram – analog supply voltage	162
B.4. Circuit diagram – digital supply voltage	162
B.5. Circuit diagram – charge sensitive preamplifier	162
B.6. Circuit diagram – shaper and amplification	163
B.7. Circuit diagram – peak hold detector	163
B.8. Circuit diagram – ADC	164
B.9. Circuit diagram – digital electronics	165
B.10. Technical drawing of case – MDT-01-001	166
B.11. Technical drawing of case – MDT-01-001 – main case	167
B.12. Technical drawing of case – MDT-01-001 – top cover	168
B.13. Technical drawing of case – MDT-01-001 – front end carrier I	169
B.14. Technical drawing of case – MDT-01-001 – front end carrier II	170
B.15. Technical drawing of case – MDT-01-001 – diode cage	171
C.1. ^{241}Am γ – MDT-01-000 diode 1	173
C.2. ^{241}Am γ – MDT-01-000 diode 2	174
C.3. ^{241}Am γ – MDT-01-001 diode 2	174
C.4. ^{241}Am α – MDT-01-000 diode 1	175
C.5. ^{241}Am α – MDT-01-000 diode 2	175
C.6. ^{241}Am α – MDT-01-001 diode 2	176
C.7. ^{207}Bi electrons – MDT-01-000 diode 1	176

C.8. ^{207}Bi electrons – MDT-01-000 diode 2	177
C.9. ^{207}Bi electrons – MDT-01-001 diode 2	177
C.10. Heavy ions – MDT-01-000 diode 1	178
C.11. Heavy ions – MDT-01-000 diode 2	179
C.12. Heavy ions – MDT-01-001 diode 2	180
C.13. High gain calibration curve – MDT-01-000 diode 1	181
C.14. High gain calibration curve – MDT-01-000 diode 2	181
C.15. High gain calibration curve – MDT-01-001 diode 2	182
C.16. Low gain calibration curve – MDT-01-000 diode 1	182
C.17. Low gain calibration curve – MDT-01-000 diode 2	183
C.18. Low gain calibration curve – MDT-01-001 diode 2	183
E.1. Count rates – A–B 1 – original resolution	189
E.2. Count rates – A–B 2	190
E.3. Count rates – B–A 2	190
E.4. Count rates – A–C	191
E.5. Count rates – C–A	191
E.6. Count rates vs. residual atmosphere – S_{\Rightarrow}	192
E.7. Count rates vs. residual atmosphere – C_{\uparrow}	192
E.8. Count rates vs. residual atmosphere – C_{\Rightarrow}	193
E.9. Count rates – B–A 2 (normalized exponentially)	193
E.10. Dose rates – A–B 2	194
E.11. Dose rates – B–A 2	194
E.12. Dose rates – A–C	195
E.13. Dose rates – C–A	195
E.14. Energy deposition spectra – MDT-01-000 – A–B–A 1	196
E.15. Energy deposition spectra – MDT-01-001 – A–B–A 1	197
E.16. Energy deposition spectra – MDT-01-000 – A–B–A 2	198
E.17. Energy deposition spectra – MDT-01-001 – A–B–A 2	199
E.18. Energy deposition spectra – MDT-01-000 – A–B–A 3	200
E.19. Energy deposition spectra – MDT-01-001 – A–B–A 3	201
E.20. Energy deposition spectra – MDT-01-000 – A–C–A	202
E.21. Energy deposition spectra – MDT-01-001 – A–C–A	203
E.22. Energy deposition spectra – simulation of protons	204
E.23. Energy deposition spectra – MDT-01-001 and Liulin – C–A	205
E.24. LET spectra – MDT-01-000 – A–B–A 1	206

E.25.LET spectra – MDT-01-001 – A–B–A 1	206
E.26.LET spectra – MDT-01-000 – A–B–A 2	207
E.27.LET spectra – MDT-01-001 – A–B–A 2	207
E.28.LET spectra – MDT-01-000 – A–B–A 3	208
E.29.LET spectra – MDT-01-001 – A–B–A 3	208
E.30.LET spectra – MDT-01-000 – A–C–A	209
E.31.LET spectra – MDT-01-001 – A–C–A	209
G.1. Flight route – OBF-Braunschweig-OBF	214
G.2. Count rates – OBF-Braunschweig-OBF	214
G.3. Parabolic maneuver	216
G.4. Count rates – parabolic flight	217
G.5. Auto- and cross-correlation count rates – parabolic flight	217
G.6. Autocorrelation of count rates – long distance flights	218
G.7. Cross-correlation of count rates – long distance flights	219

LIST OF TABLES

3.1. Electronic development steps of detector system	32
4.1. Ion energies for calibration	57
4.2. Calibration results	64
6.1. Flight configurations	77
6.2. Overview of flight routes	81
6.3. Neutron monitor count rates during flight measurements	82
6.4. Overview of flights	88
6.5. Results – Fits	90
6.6. Fit parameter a_c	92
6.7. Overview of flights	93
6.8. Results – Fits	101
6.9. Absorbed dose results	112
6.10. Absorbed dose results – comparison with Liulin and calculations	113
6.11. Dose equivalent results – comparison with EPCARD	116
8.1. MDT properties	129
B.1. μC pin allocation table	172
D.1. Energies and fit results for calibration with isotopes	185
D.2. Calculated energy depositions and fit results for calibration with heavy ions	186
D.3. Calibration fit parameters	187
D.4. Fragment measurement results – ADC channel fits	187
D.5. Fragment measurement results – energy fits	188
F.1. Flight measurement results – count rate fits	211
F.2. Flight measurement results – dose rate fits	212
F.3. Flight measurement results – quality factors	212

Appendices

MDT – DEVELOPMENT STEPS

Figure 3.6 and Table 3.1 in Section 3.3 give an overview of the development steps of the MDT. In the following each board version number is described in more detail.

As long as no power supply is implemented on the boards, the electronics described in this section is powered by external power supply units.

Links to the datasheets for all electronic components in squared brackets can be found in the list of datasheets on page 141.

Version **00.xx**: With a simple experimental breadboard (orange, Figure 3.6) and the test board [PC250F] for the preamplifier (green) provided by Amptek, the first tests with the monolithic charge sensitive preamplifier [A250FNF], shaper, and peak detector are performed. The setup design with two amplification stages (low and high gain) is chosen to cover the desired dynamic range and the peak detector, consisting of two operational amplifiers is tested.

The first two self-designed boards have the version number **01.01**. The preamplifier board is designed in a way that it fits with two diodes and two preamplifiers into a well shielded box. The analog board is equipped with two signal paths, including an active shaper with amplification, a shifter to provide a baseline shift to small negative voltages, while a comparator compares the signal from the shifter to ground. Behind the peak detector, four different possibilities to discharge the storage capacitor of the peak detector are implemented to test the most effective solution with the smallest charge injection: an analog switch, an opto-coupler, a bilateral CMOS switch, and a simple FET, from which the analog switch [TS5A3166] performed best. Both, analog and preamplifier boards are connected via a D-Sub9 connector directly or with a short cable to enable measurements with the preamplifier board inside a small vacuum chamber for measurements with alpha particles (Figure A.1). On the other side of the analog board outputs for several signals, e.g. from the shaper, peak detector, and supply voltage, are realized by a D-Sub25 connector.

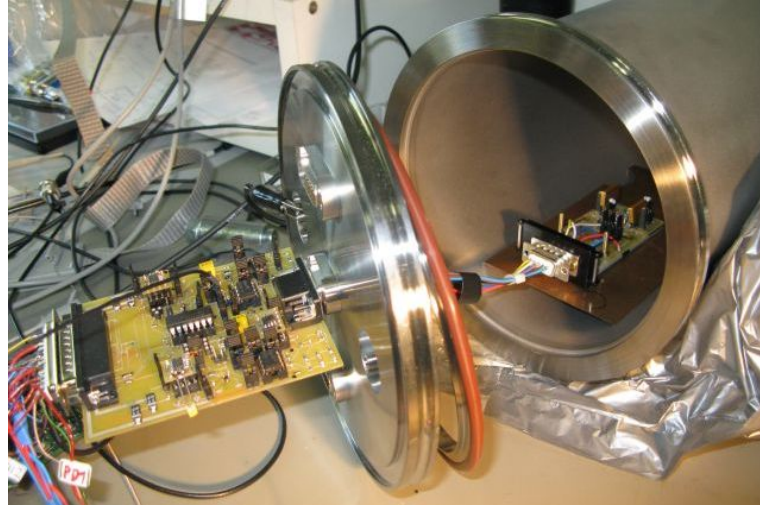


Figure A.1.: Board version 01.01 with the preamplifier board inside the vacuum chamber, while the analog board is outside to enable signal measurements with the oscilloscope.

Version **02.01** replaces the analog board of 01.01 and is connected to the preamplifier board of the previous version. The active shaper is replaced by a passive shaper and two parallel amplifiers with different amplification factors. Instead of the shifter a digital potentiometer [AD5252] is employed to define the detection threshold for the comparator. A four channel simultaneously sampling ADC [ADS1174] is tested and a 2.5 V voltage reference [ADR291] for the ADC is implemented. Logic components (AND, OR, D-flipflop) detect possible coincidences and reset the peak detector. Pinheaders are placed on the board to connect 02.01 to the commercial test board [STK600] for *Atmel*¹ microcontrollers (μ Cs). Thereby the digital signals (setting the detection threshold with the digital potentiometer, read out of ADC and coincidence logic, reset of peak detectors) are controlled. The μ C used for first testing is *Atmel*'s [ATmega16] (8-bit μ C with 16 kBytes in-system programmable flash).

On version **03.01** a toroidal transformer is tested to serve as an isolated DC-DC converter to create ± 5.5 V. Additionally, because of a better performance, the ADC is replaced by a another simultaneously sampling ADC with a parallel output [AD7864-2].

¹<http://www.atmel.com>

The 'digital board', version **04.01**, serves to test several digital devices. The μC is placed in a socket and is connected to the STK600 for programming via a JTAG² header. The RS-232 interface (USART communication, [MAX3221EUE]) provides communication with a PC terminal program via a COM port on the computer. The SPI interface of the μC communicates with the μSD card as well as with the low power consuming display [DOGM163L] with an additional chip select pin. A real time clock [DS1339U] using the I²C communication protocol is implemented. The power consumption of the whole analog part is estimated to only several tens of milliamperes. As the transformer on 03.01 is not efficient enough at this operating point, a charge pump for 5.5 V [REG71055] and an inverter to create from this the negative 5.5 V [ADM8829] are tested.

Version **05.01** merges the analog board 03.01 and the digital board 04.01. Since on version 04.01 the charge pump for +5.5 V showed a strong switching noise, the board layout on 05.01 is designed more carefully to ensure lowest possible interference and capacitors with a low ESR (equivalent series resistance) are employed in the charge pump circuitry. The generation of the bias voltage for the silicon diodes is implemented by step-up voltage converter in discontinuous mode, consisting of an inductor, charged by field effect transistor that is switched by the μC . The μC is replaced by the low power version with 128 kBytes in-system programmable flash [ATmega1284P].

The redesign of the preamplifier board results in version **06.01**. The two front-ends are not placed on one board, but on separate boards, one for each channel, each with a separate ground plane. The size is decreased as much as possible and the layout designed such that parasite capacities from the board are minimized, as they would influence the signal amplification in the most critical phase of signal processing.

Board versions 05.01 and 06.01 result in the first version of the detector system developed within the frame of this work that has been calibrated with heavy ions and has also been tested during a short flight (compare Appendix G.1). Figure A.2 shows the flight box with front end (06.01, small black box on the left) and the signal processing electronics (05.01, larger black box on the right).

Version **07.01** is the first attempt to decrease the area of the board as much as possible. All electronic components are chosen in their smallest package available

²JTAG stands for Joint Test Action Group, which is a standard test access port and boundary-scan architecture.



Figure A.2.: Setup of board version 05.01 with preamplifier board 06.01 for measurements during flights (compare Section G.1).

(e.g. MSOP instead of SOIC for the operational amplifiers). Both PCB sides – top and bottom – are completely assembled. The analog amplification chains for the two detector channels are placed separately on top and on bottom of the board to avoid cross-talking between the channels. The two amplification stages in each chain are arranged in sequence to gain a larger dynamic range. The D-Sub connectors to the preamplifier boards are replaced by pinheader sockets to shorten the signal paths and to obtain a small and stable, but still flexible detector setup. A flash memory [AT45DB161D] is placed on the board to store data immediately and not on the μ SD card, which is slower and more power consuming (up to 90 mA during the writing process). The upper 8 bit of the 12 bit parallel output of the ADC are processed by a shift register that is read out serially by the SPI interface of the μ C. This saves I/O pins at the μ C. A Schottky diode is placed at the input power line to avoid accidental polarity reversal and a mechanical switch is added for switching power on and off. One of the internal ADCs of the μ C is connected directly to the battery supply line via a voltage divider to monitor the battery voltage. A push button is connected to the μ C to serve as possible user interface. Furthermore the digital supply voltage is stabilized to 3.0 V by a low-dropout voltage regulator (LDO [TPS77030]). This

voltage is carefully chosen as the individual periphery devices like e.g. μ SD card, data flash, and display require a stable voltage within a defined range of input voltages. The RS-232 interface is replaced by a mini USB connector using a USB to UART chip [FT232RL], because of the smaller size and since the battery is charged via the USB interface.

Figure 3.7 shows top and bottom of the **final board version 08.01**, indicating the different parts of the electronics. Minor changes, including some passive filters, are applied to this version. A battery charging regulator [MAX1811] is used to charge the battery through the USB interface.

B

MDT – CIRCUIT DIAGRAMS, TECHNICAL DRAWINGS, TABLES

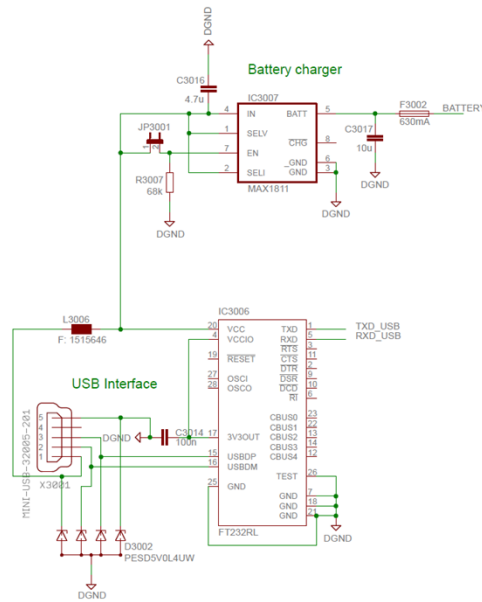


Figure B.1.: Circuit diagram – battery charger and USB interface (Section 3.4.1 and 3.4.5).

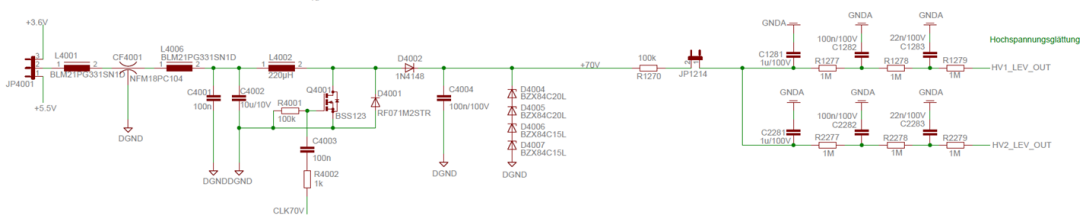


Figure B.2.: Circuit diagram – bias voltage for silicon diodes (Section 3.4.1).

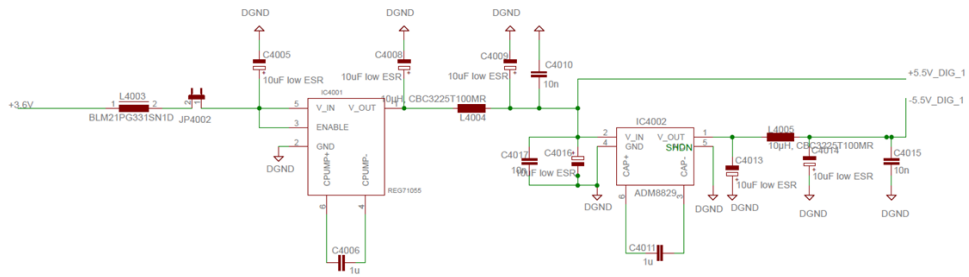


Figure B.3.: Circuit diagram – analog supply voltage (Section 3.4.1).

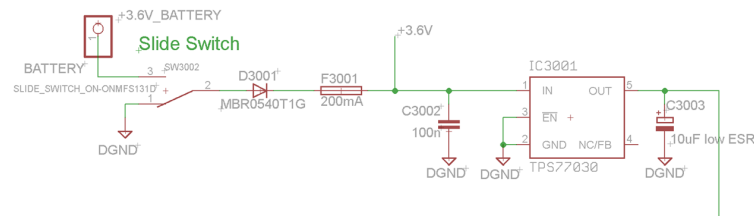


Figure B.4.: Circuit diagram – digital supply voltage (Section 3.4.1).

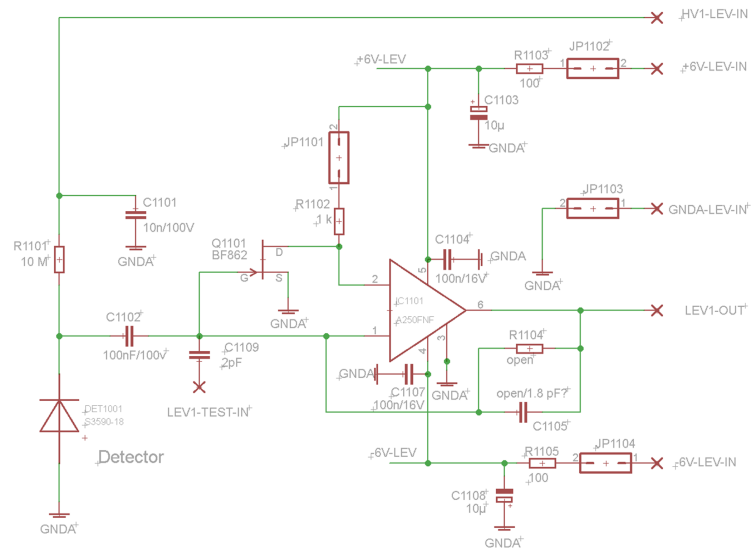


Figure B.5.: Circuit diagram – charge sensitive preamplifier with silicon diode (Section 3.4.4).

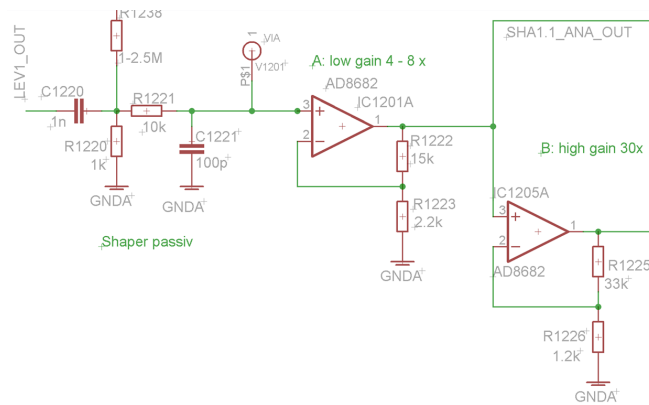


Figure B.6.: Circuit diagram – shaper and amplification (Section 3.4.4).

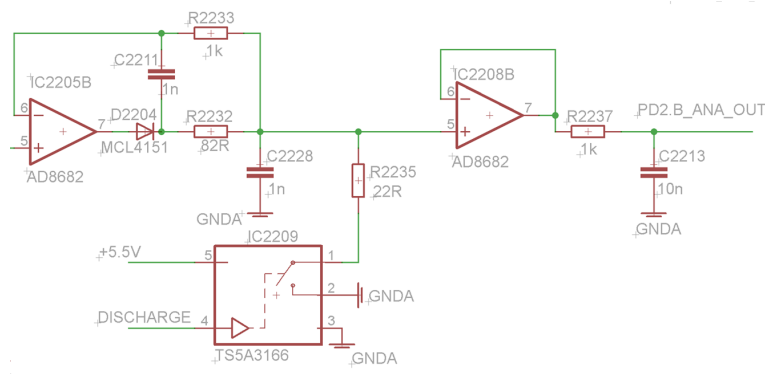


Figure B.7.: Circuit diagram – peak hold detector (Section 3.4.4).

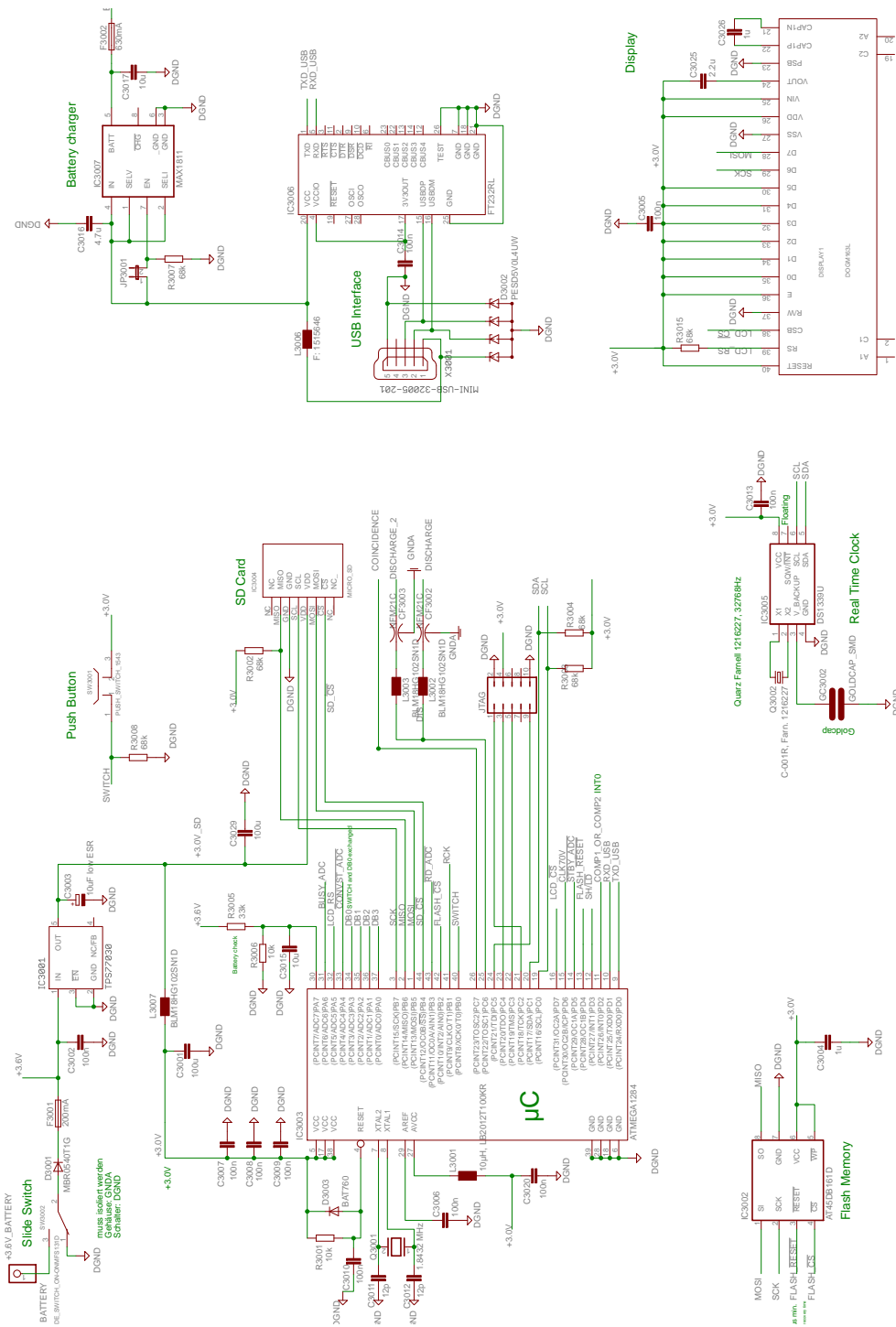


Figure B.9.: Circuit diagram – digital electronics (Section 3.4.5).

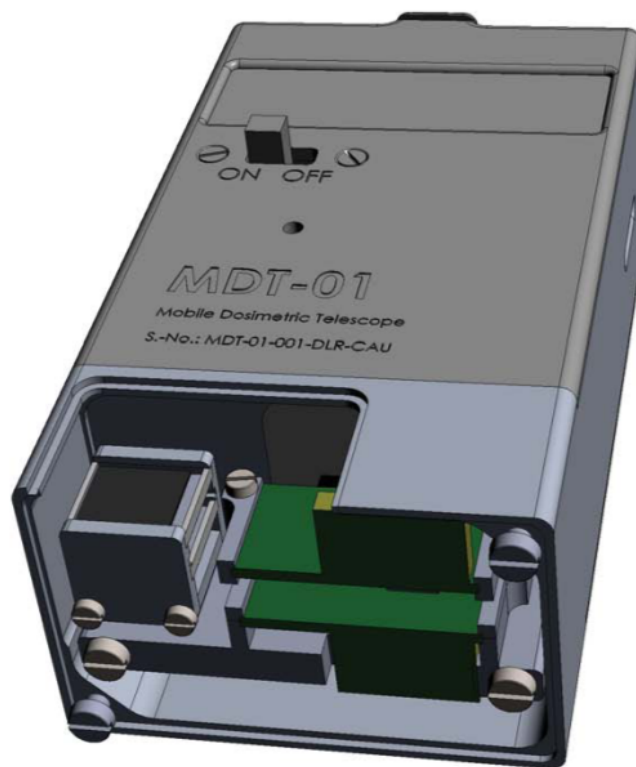


Figure B.10.: Technical drawing of the MDT-01-001 case.

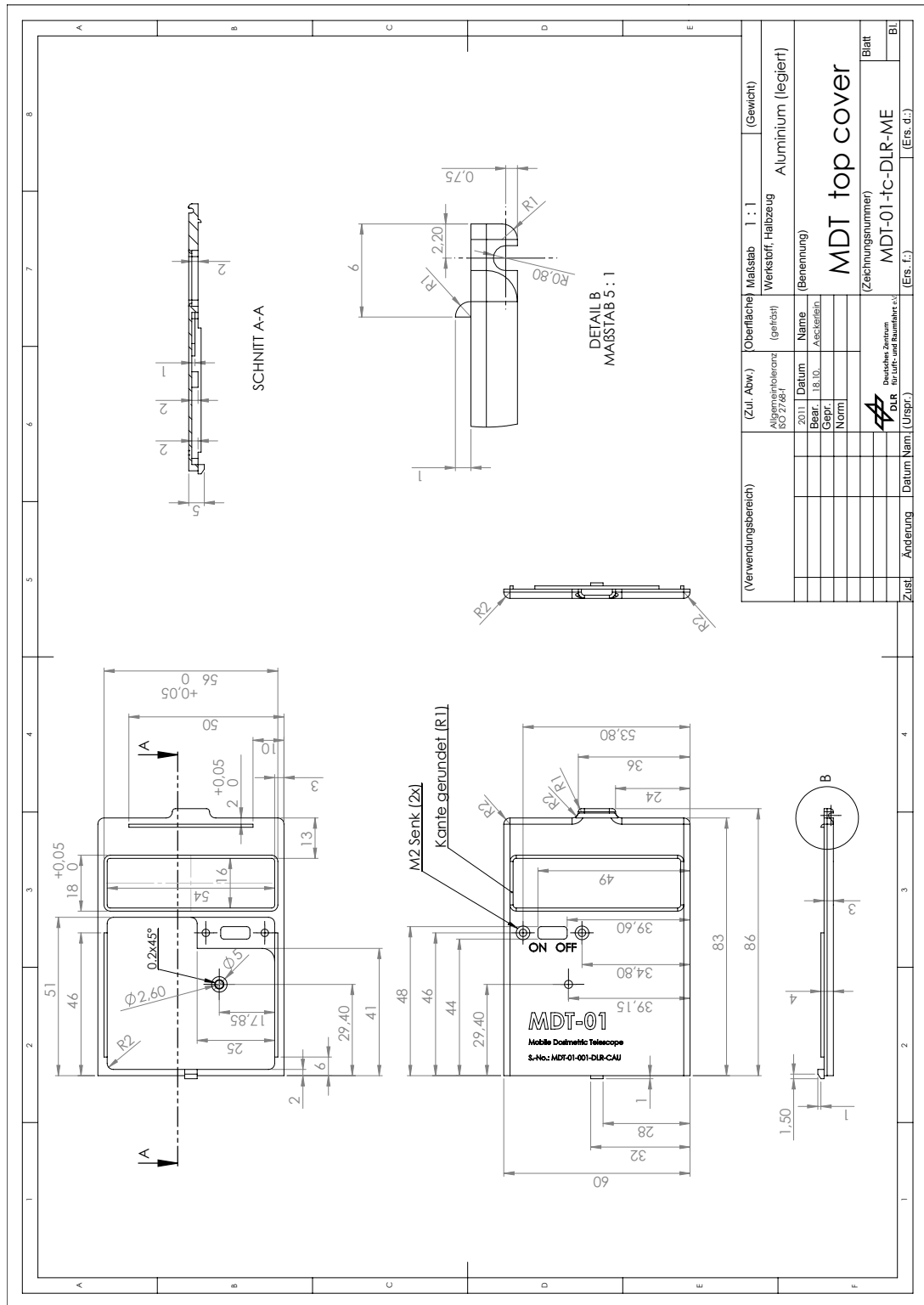


Figure B.12.: Technical drawing of the MDT-01-001 case – top cover (Section 3.5.2).

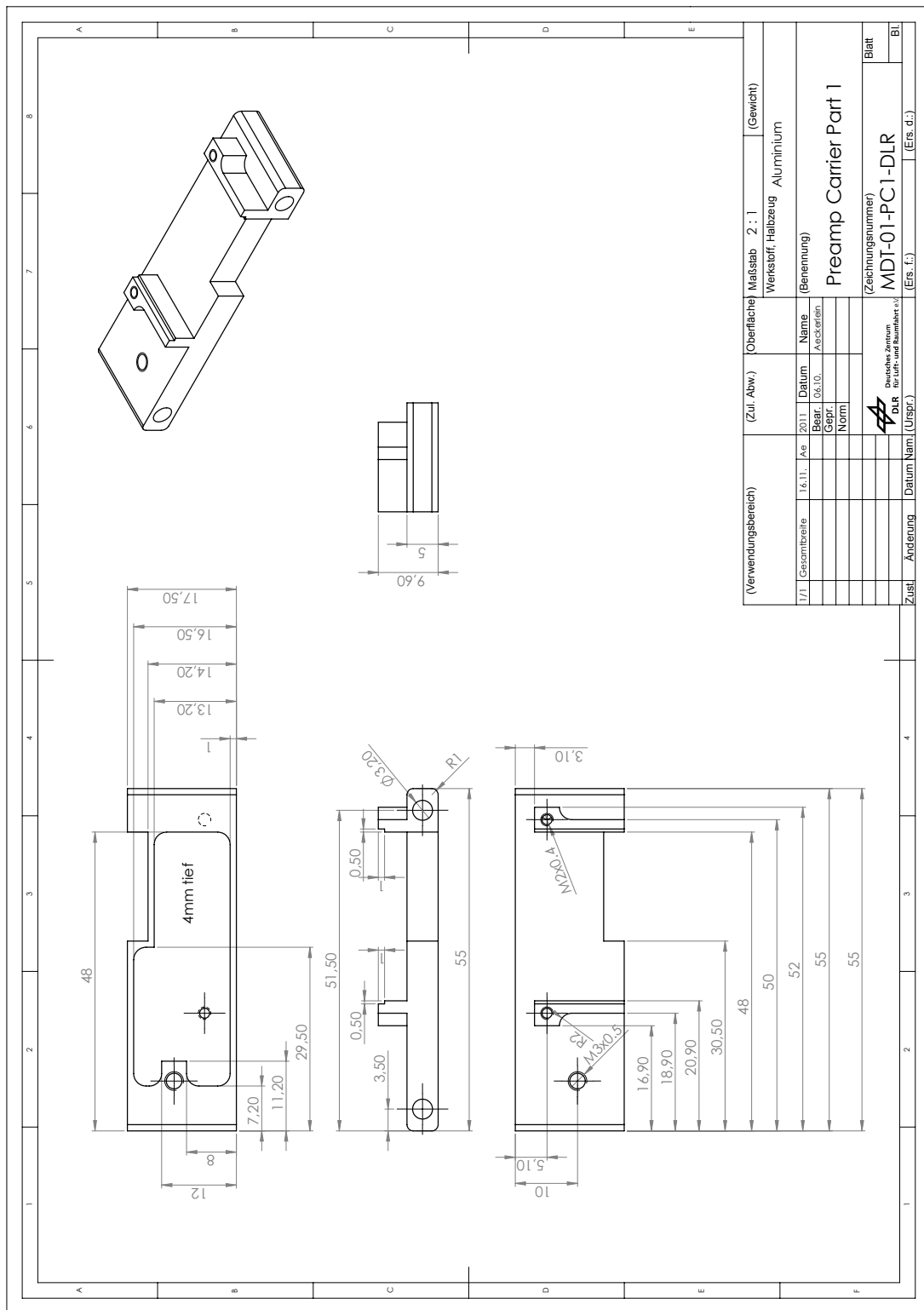


Figure B.13.: Technical drawing of the MDT-01-001 case – front end carrier I (Section 3.5.2).

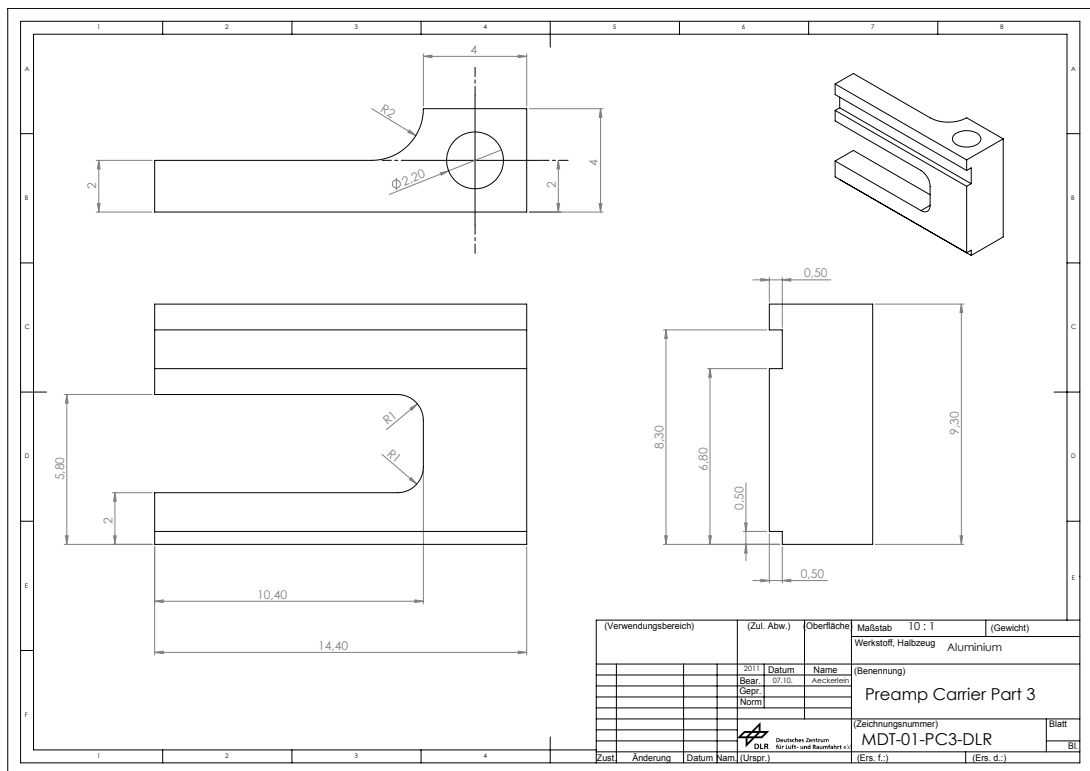
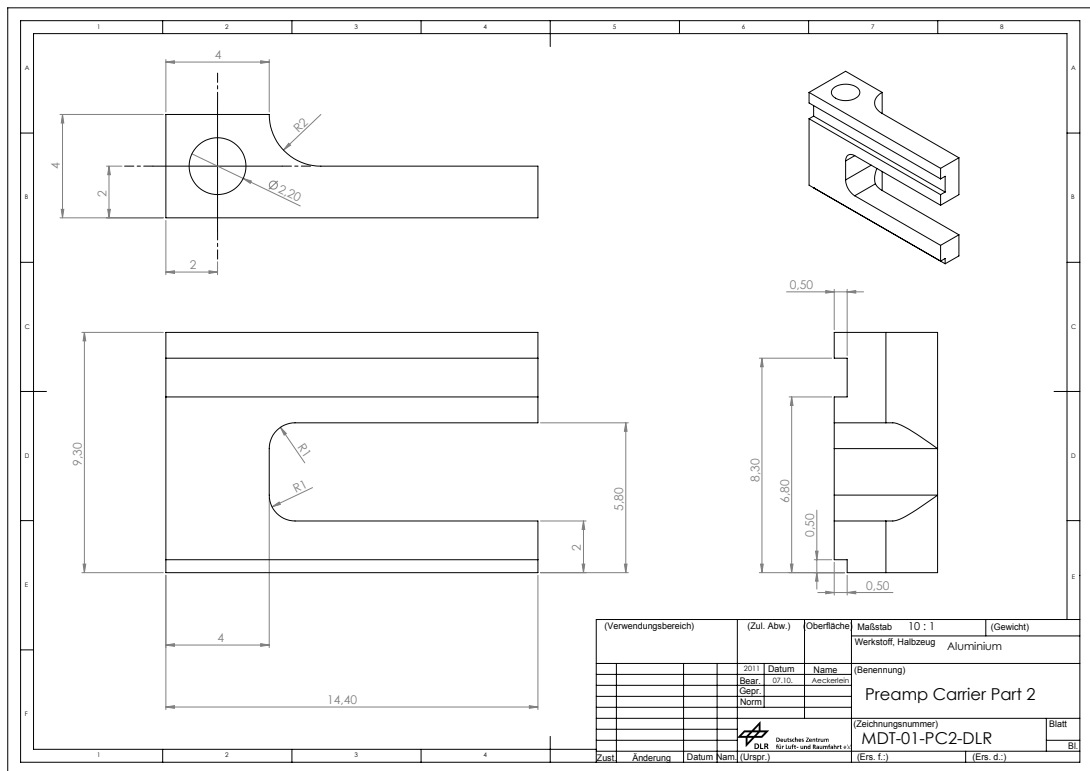


Figure B.14.: Technical drawing of the MDT-01-001 case – front end carrier II (Section 3.5.2).

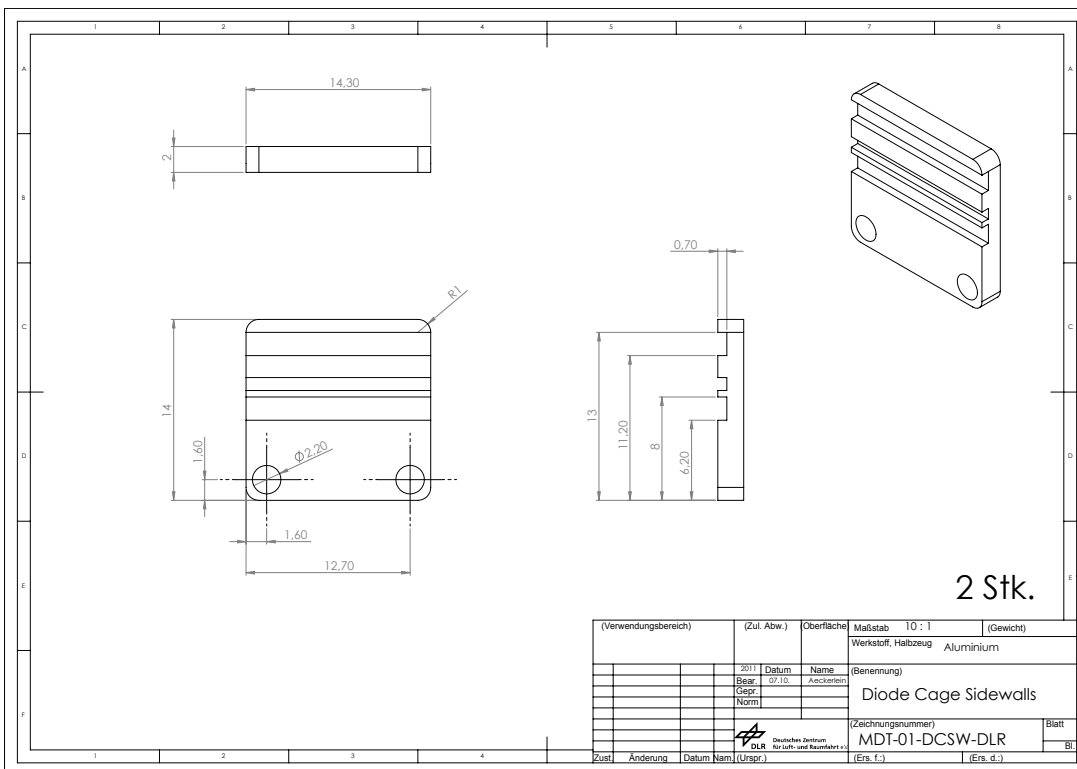
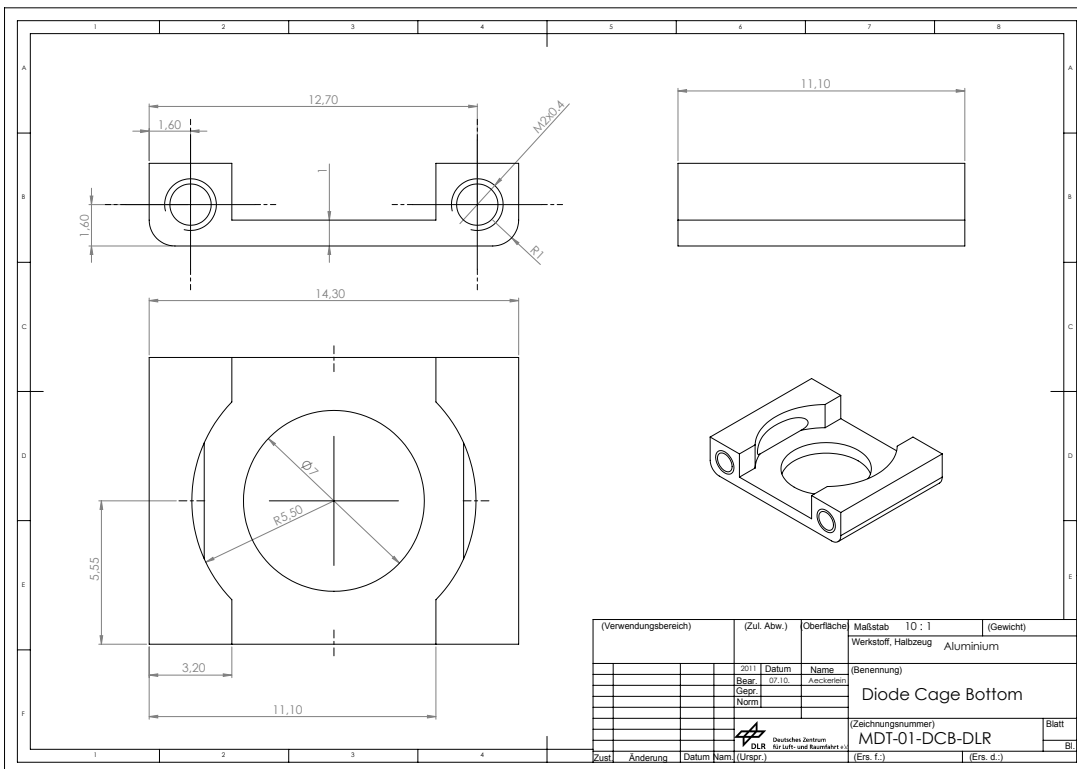


Figure B.15.: Technical drawing of the MDT-01-001 case – diode cage (Section 3.5.2).

Table B.1.: Pin allocation table for μC 1284P employed in the MDT prototypes (Section 3.4.5). Port and pin label are given in the first two columns. The signal name in the third column refers to the label in the circuit diagrams (Figures B.1 to B.9). I/O denotes, if a pin is input or output and the last column gives a short explanation of to where the signal belongs and its purpose.

PORT	PIN	Signal	I/O	Remark
A	7	Battery check	I	
	6	BUSY_ADC	I	
	5	LCD_RS	O	Display register select
	4	!CONVST_ADC	O	ADC conversion start
	3	DB0	I	ADC data
	2	DB1	I	ADC data
	1	DB2	I	ADC data
	0	DB3	I	ADC data
B	7	SCK	O	SPI
	6	MISO	I	SPI
	5	MOSI	O	SPI
	4	SD!CS	O	SPI
	3	!RD_ADC	O	ADC read
	2	FLASH!CS	O	SPI
	1	RCK	O	Shift register clock
	0	SWITCH	I	Push button
C	7	COINCIDENCE	I	
	6	DISCHARGE	O	
	5	TDI		JTAG
	4	TDO		JTAG
	3	TMS		JTAG
	2	TCK		JTAG
	1	SDA	I/O	TWI
	0	SCL	O	TWI
D	7	LCD!CS	O	SPI
	6	CLK70V	O	Bias voltage
	5	!STBY_ADC	O	ADC standby
	4	FLASH!RESET	O	
	3	SH!/LD	O	Shift register shift/load
	2	OR	I	INT0 (particle interrupt)
	1	TXD	O	RS-232 / USB
	0	RXD	I	RS-232 / USB

CALIBRATION – FIGURES

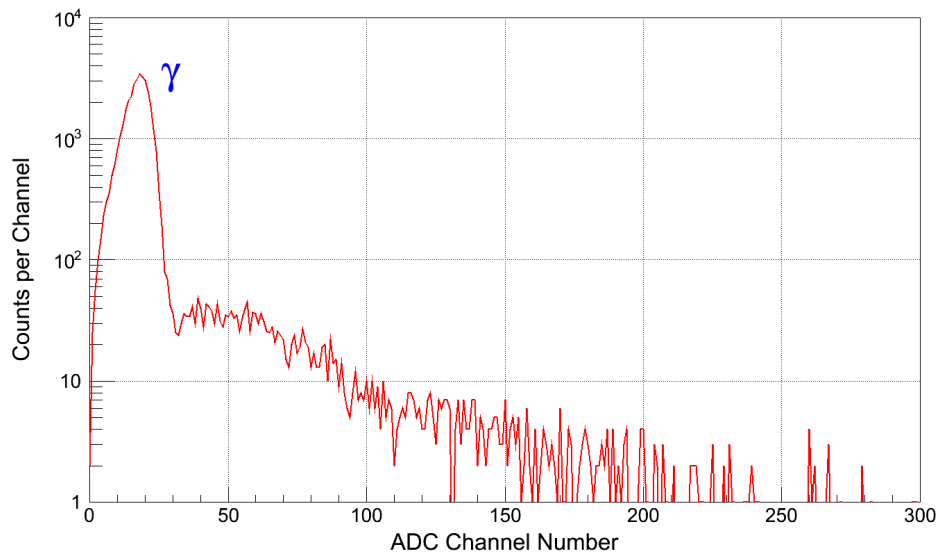


Figure C.1.: ^{241}Am γ measurement for detector **MDT-01-000 diode 1** high gain (Section 4.1.1). Fit results are given in Table D.1 in Appendix D.

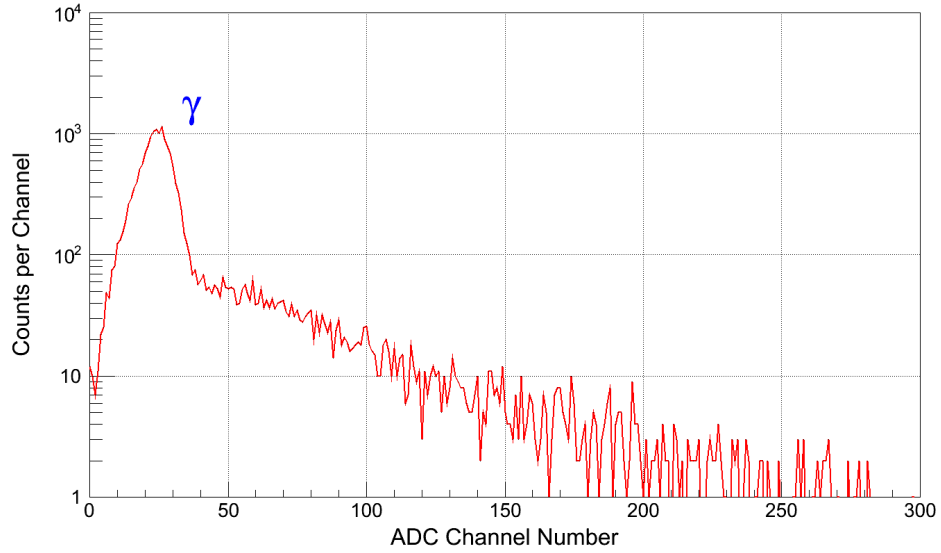


Figure C.2.: ^{241}Am γ measurement for detector **MDT-01-000 diode 2** high gain (Section 4.1.1). Fit results are given in Table D.1 in Appendix D.

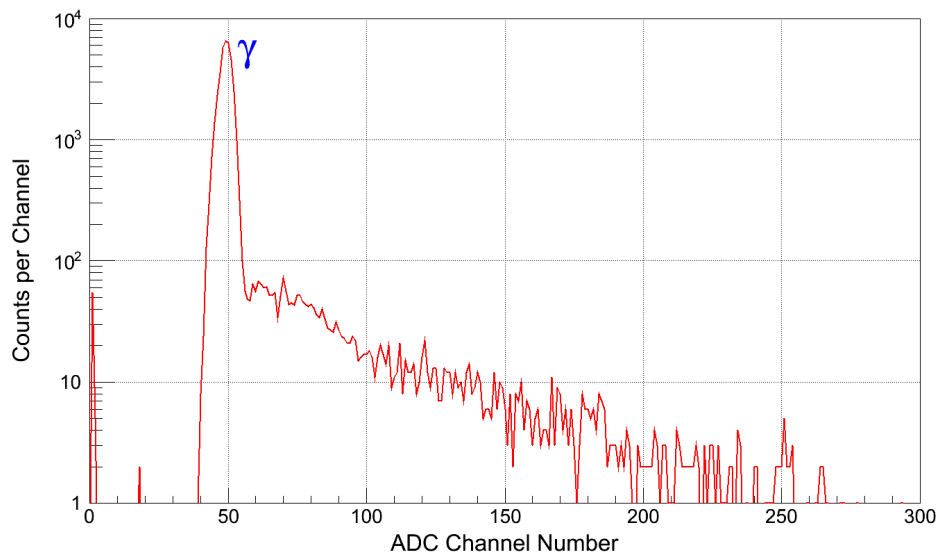


Figure C.3.: ^{241}Am γ measurement for detector **MDT-01-001 diode 2** high gain (Section 4.1.1). Fit results are given in Table D.1 in Appendix D.

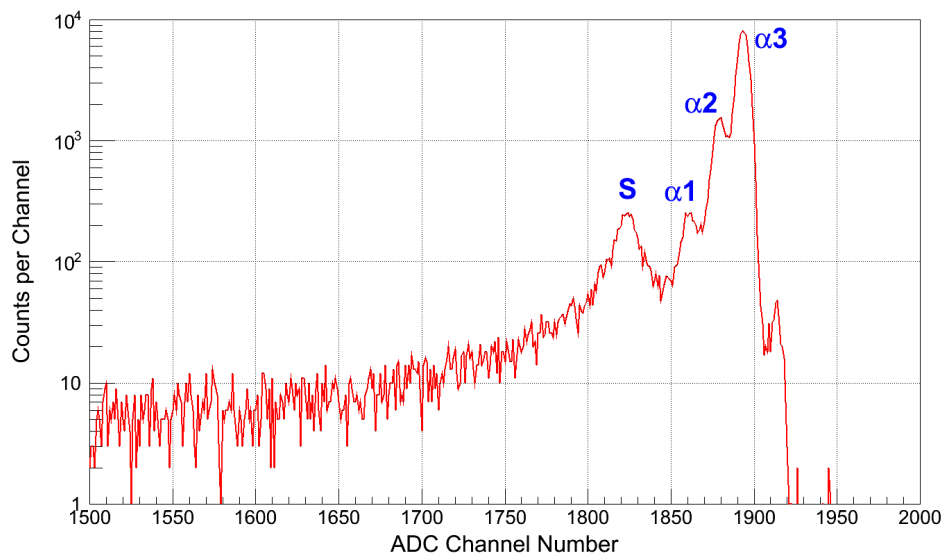


Figure C.4.: ^{241}Am α particles for detector MDT-01-000 diode 1 high gain (Section 4.1.1).
Fit results are given in Table D.1 in Appendix D.

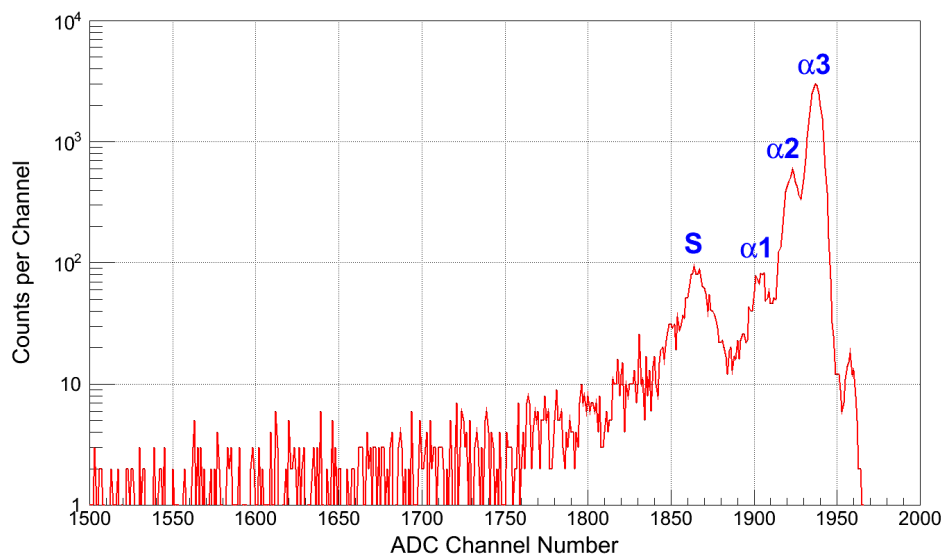


Figure C.5.: ^{241}Am α particles for detector MDT-01-000 diode 2 high gain (Section 4.1.1).
Fit results are given in Table D.1 in Appendix D.

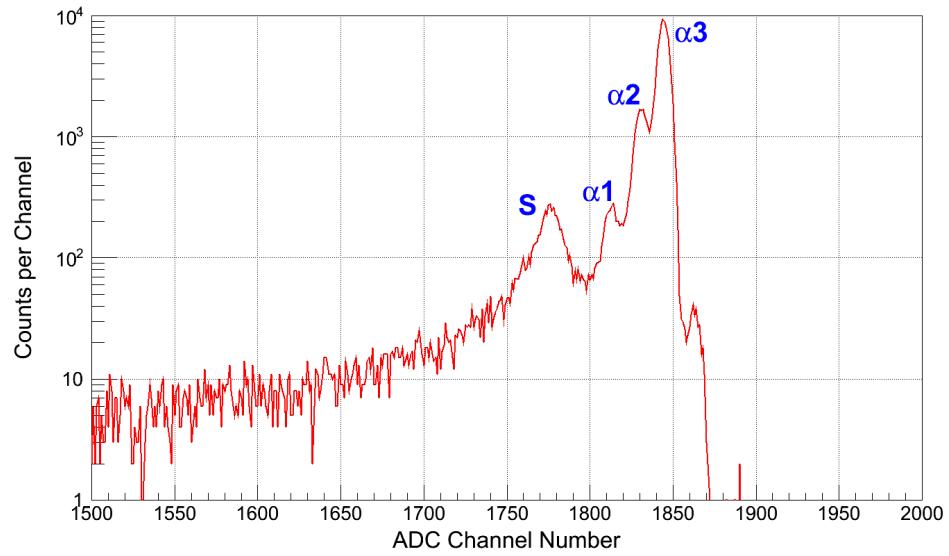


Figure C.6.: ^{241}Am α particles for detector **MDT-01-001 diode 2** high gain (Section 4.1.1). Fit results are given in Table D.1 in Appendix D.

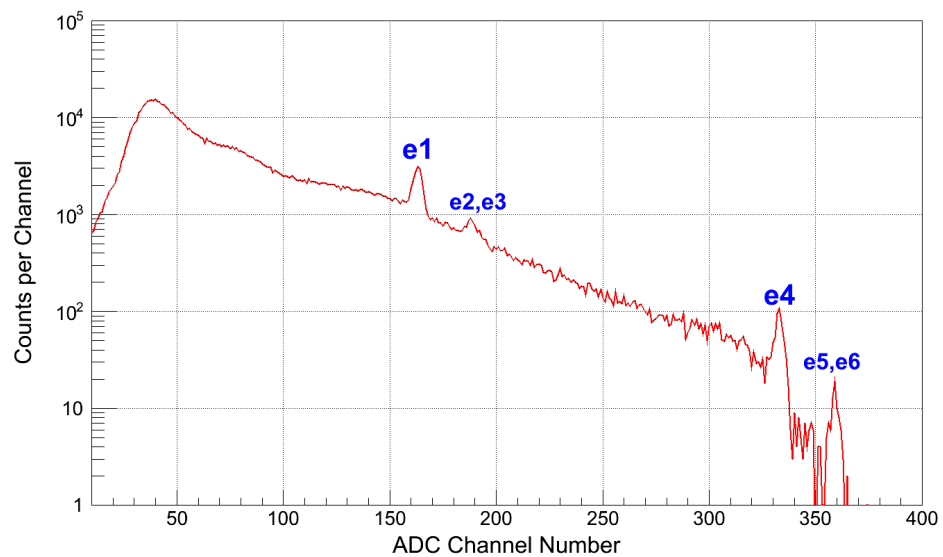


Figure C.7.: ^{207}Bi measurement for detector **MDT-01-000 diode 1** high gain (Section 4.1.2). Fit results are given in Table D.1 in Appendix D.

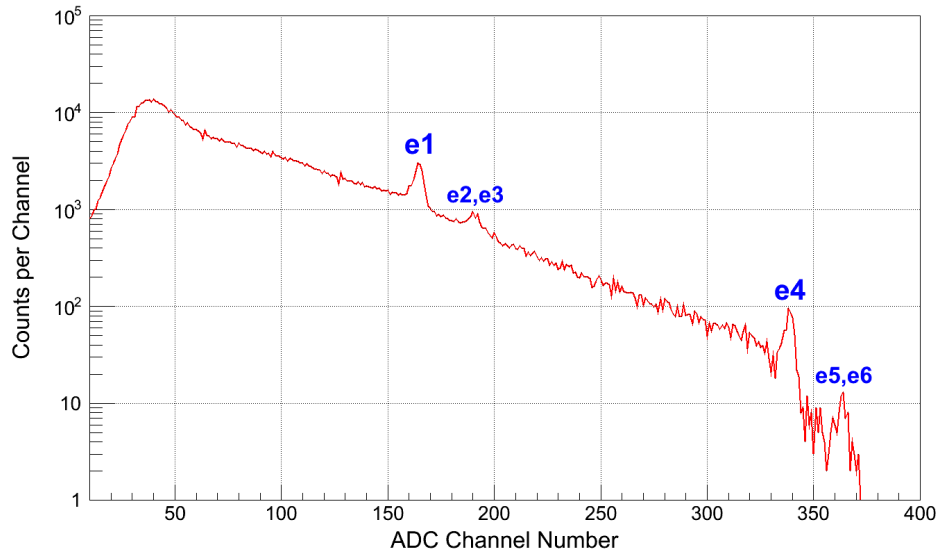


Figure C.8.: ^{207}Bi measurement for detector **MDT-01-000 diode 2** high gain (Section 4.1.2). Fit results are given in Table D.1 in Appendix D.

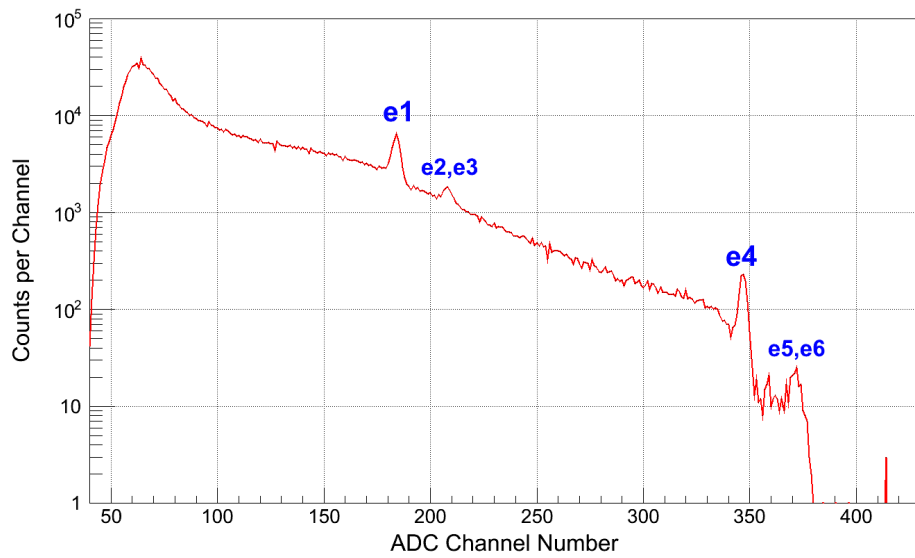
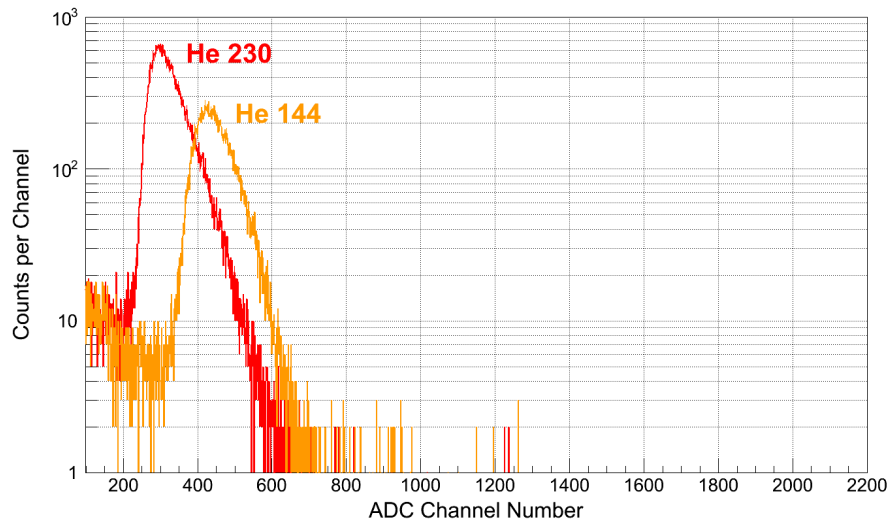
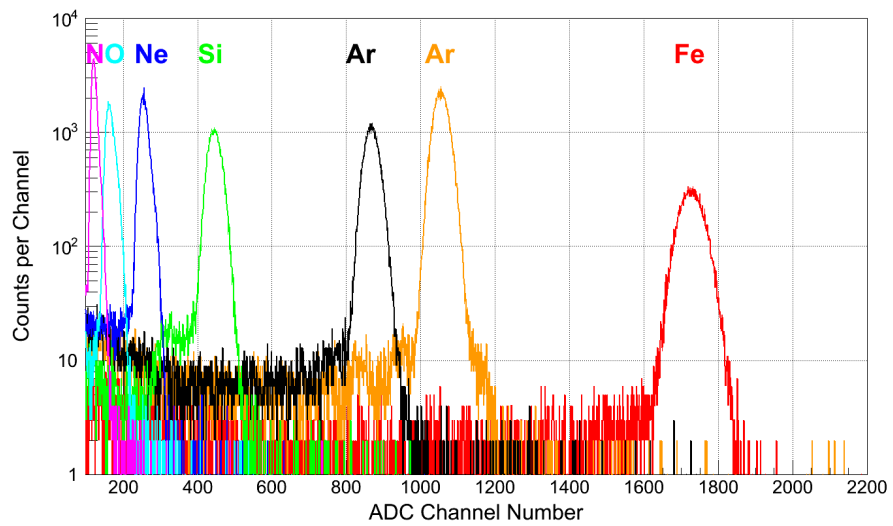


Figure C.9.: ^{207}Bi measurement for detector **MDT-01-001 diode 2** high gain (Section 4.1.2). Fit results are given in Table D.1 in Appendix D.

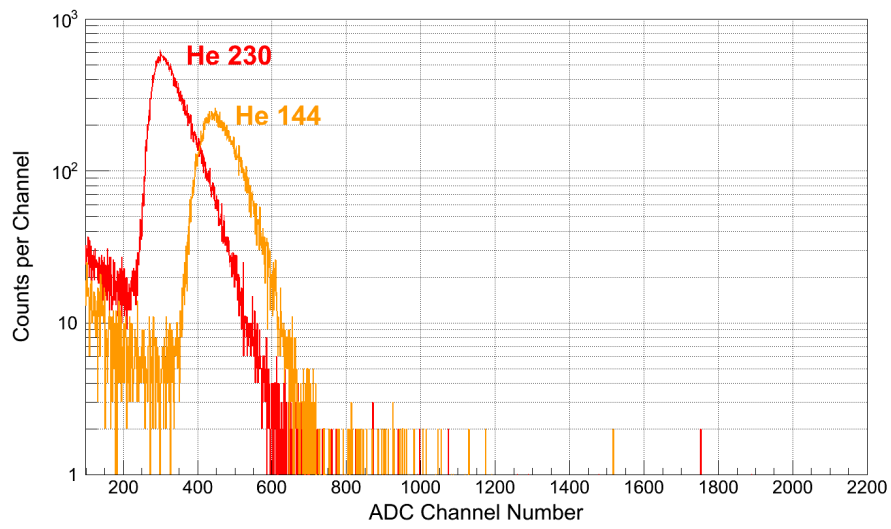


(a) High gain

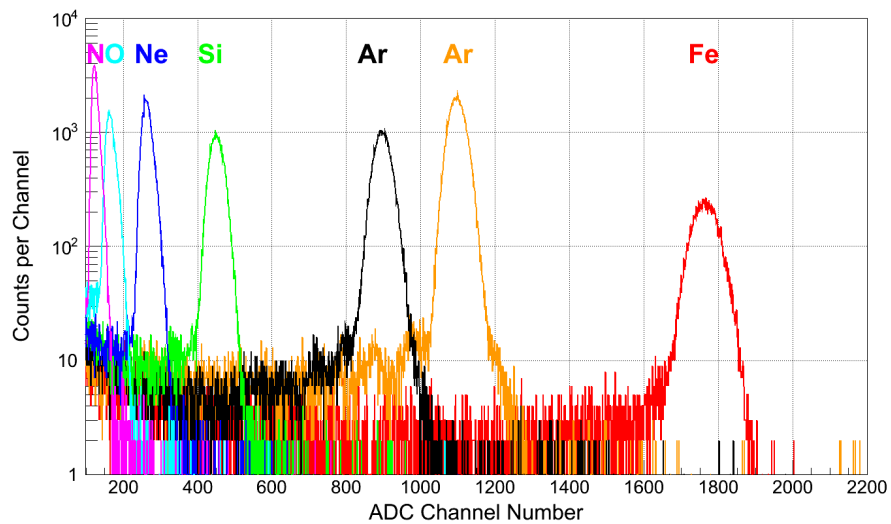


(b) Low gain

Figure C.10.: Pulse height spectra of measured ions for **MDT-01-000 diode 1** in the high gain (a) and in the low gain channel (b) (Section 4.2). The corresponding ion energies, the energy depositions in the detector, and the fit results are listed in Table D.2.

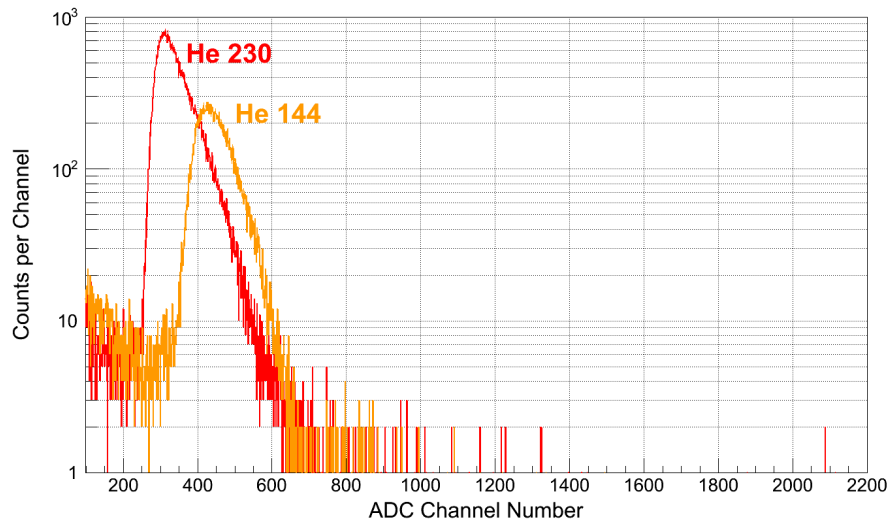


(a) High gain

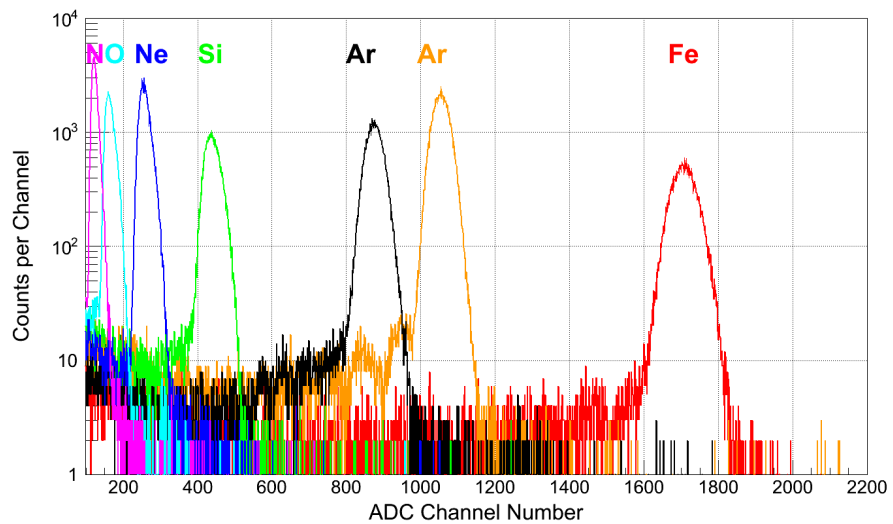


(b) Low gain

Figure C.11.: Pulse height spectra of measured ions for **MDT-01-000 diode 2** in the high gain (a) and in the low gain channel (b) (Section 4.2). The corresponding ion energies, the energy depositions in the detector, and the fit results are listed in Table D.2.



(a) High gain



(b) Low gain

Figure C.12.: Pulse height spectra of measured ions for **MDT-01-001 diode 2** in the high gain (a) and in the low gain channel (b) (Section 4.2). The corresponding ion energies, the energy depositions in the detector, and the fit results are listed in Table D.2.

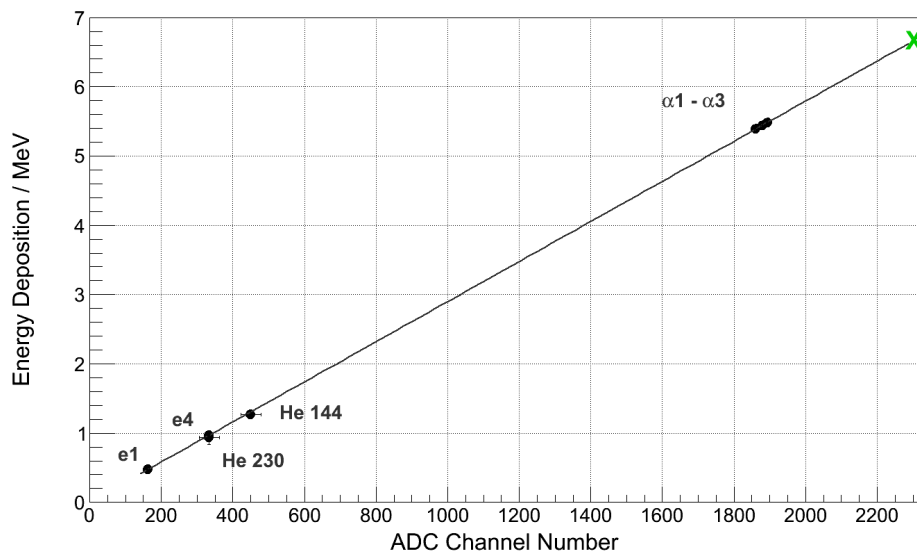


Figure C.13.: High gain calibration curve for detector MDT-01-000 diode 1 (Section 4.3.1).

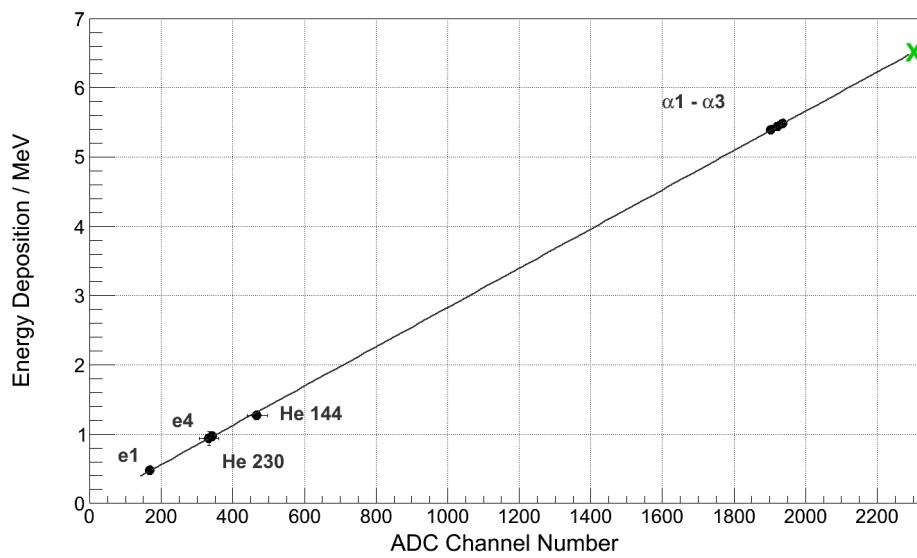


Figure C.14.: High gain calibration curve for detector MDT-01-000 diode 2 (Section 4.3.1).

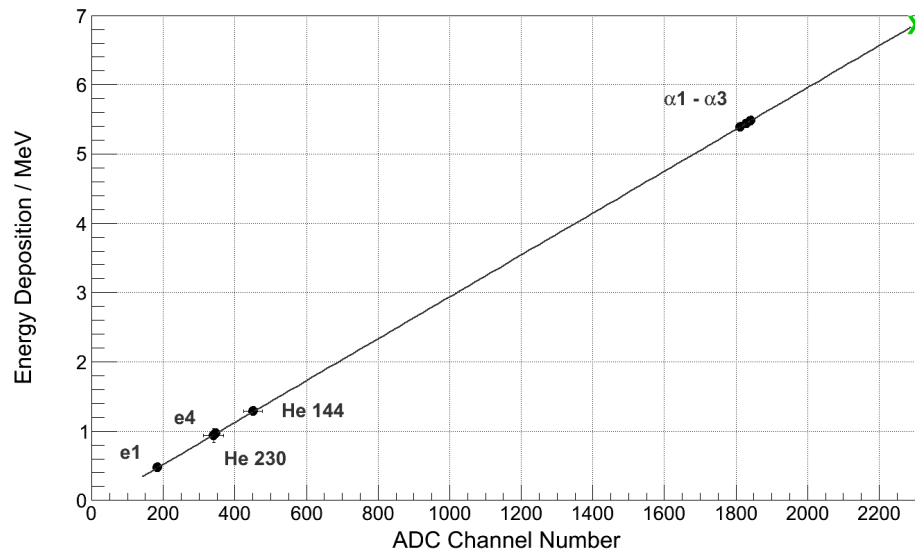


Figure C.15.: High gain calibration curve for detector MDT-01-001 diode 2 (Section 4.3.1).

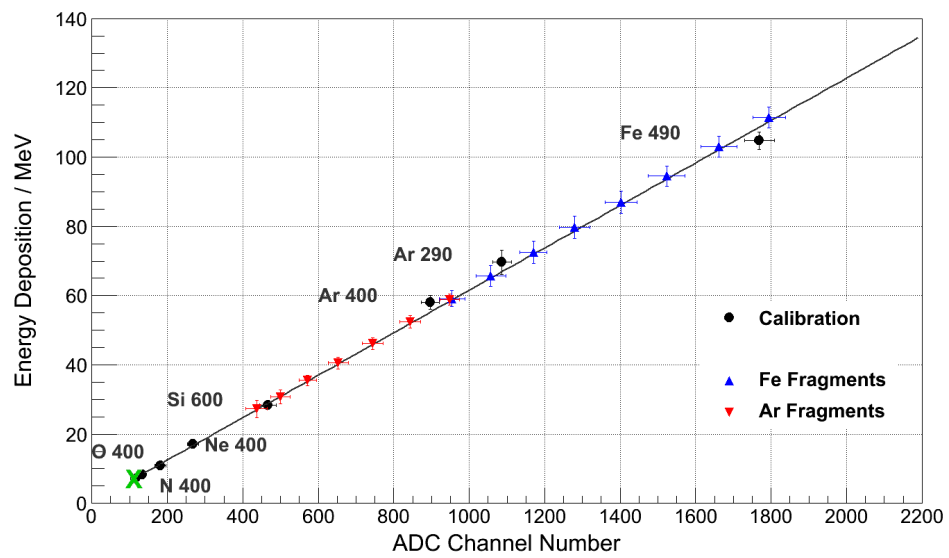


Figure C.16.: Low gain calibration curve for detector MDT-01-000 diode 1 (Section 4.3.2).

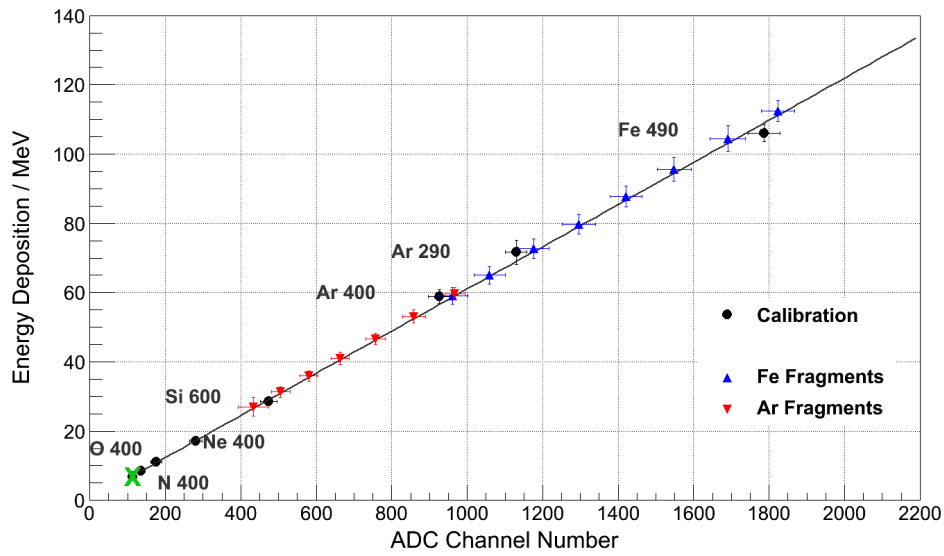


Figure C.17.: Low gain calibration curve for detector MDT-01-000 diode 2 (Section 4.3.2).

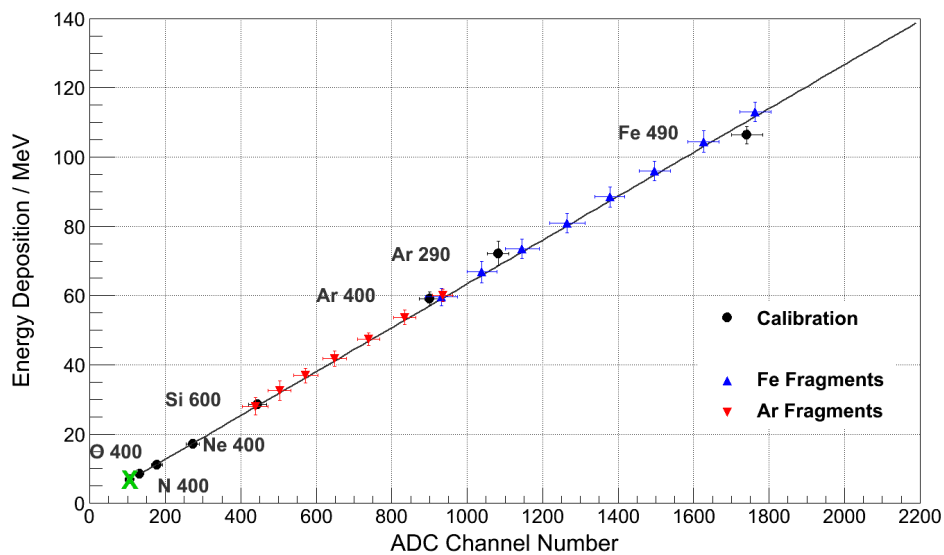


Figure C.18.: Low gain calibration curve for detector MDT-01-001 diode 2 (Section 4.3.2).

D

CALIBRATION – TABLES

Table D.1.: Fit results for high gain calibration (Section 4.1).

Source	Energy (MeV)	Fit Results in ADC Channels				
		MDT-01-000		MDT-01-001		
		Diode 1	Diode 2	Diode 1	Diode 2	
^{241}Am	γ	0.06	20.1 ± 6	26.0 ± 6	39.9 ± 3	48.0 ± 4
^{207}Bi	e1	0.481	162.7 ± 4	168.3 ± 4	174.6 ± 3	184.4 ± 4
	e4	0.975	332.3 ± 3	343.1 ± 3	337.1 ± 3	347.4 ± 3
^{241}Am	$\alpha 1$	5.389	1861.0 ± 5	1904.0 ± 6	1797.2 ± 5	1813.2 ± 6
	$\alpha 2$	5.443	1879.4 ± 4	1923.0 ± 5	1815.8 ± 4	1831.1 ± 5
	$\alpha 3$	5.486	1893.5 ± 4	1937.0 ± 4	1828.9 ± 4	1844.4 ± 4

Table D.2.: List of heavy ions with their respective energy (column 1 and 2), the with *SRIM* calculated energy depositions in $300\ \mu\text{m}$ of silicon in MeV (columns 3 to 6) and Vavilov fit results (columns 7 to 10) for all heavy ions and each diode for both prototypes (Section 4.2). Energies in MDT-01-000 are a bit lower than in -001 due to the different thickness of the aluminum case of 1.5 mm and 2.0 mm, respectively.

Ion	Energy (MeV u^{-1})	Energy Deposition in MeV				Fit Results in ADC Channels			
		MDT-01-000		MDT-01-001		MDT-01-000		MDT-01-001	
		Diode 1	Diode 2	Diode 1	Diode 2	Diode 1	Diode 2	Diode 1	Diode 2
He	230 ± 20	0.934 ± 0.1	0.938 ± 0.1	0.935 ± 0.1	0.939 ± 0.1	333 ± 28	333 ± 28	341 ± 27	341 ± 27
He	144 ± 1	1.267 ± 0.06	1.281 ± 0.06	1.271 ± 0.06	1.285 ± 0.06	450 ± 26	468 ± 28	447 ± 25	451 ± 26
N	400 ± 20	8.358 ± 0.4	8.403 ± 0.4	8.37 ± 0.4	8.418 ± 0.4	133 ± 9	136 ± 11	146 ± 11	133 ± 10
O	400 ± 20	10.947 ± 0.4	11.013 ± 0.4	10.965 ± 0.4	11.031 ± 0.4	182 ± 15	177 ± 15	178 ± 14	178 ± 15
Ne	400 ± 20	17.028 ± 0.6	17.172 ± 0.6	17.064 ± 0.6	17.208 ± 0.6	268 ± 15	282 ± 17	264 ± 16	274 ± 18
Si	600 ± 20	28.395 ± 0.5	28.527 ± 0.5	28.428 ± 0.5	28.56 ± 0.5	467 ± 22	474 ± 22	448 ± 21	445 ± 25
Ar	400 ± 20	58.14 ± 2	58.92 ± 2	58.35 ± 2	59.13 ± 2	896 ± 24	926 ± 28	860 ± 24	901 ± 29
Ar	290 ± 20	69.6 ± 3.5	71.61 ± 3.5	70.11 ± 3.5	72.18 ± 3.5	1087 ± 25	1130 ± 28	1050 ± 25	1082 ± 28
Fe	490 ± 20	103.77 ± 2.5	105.09 ± 2.5	104.1 ± 2.5	105.45 ± 2.5	1769 ± 40	1787 ± 43	1696 ± 39	1741 ± 41

Table D.3.: List of the fit parameters for the linear fit for the calibration of MDT-01-000 and MDT-01-001 (Section 4.3.3).

Detector	Diode	Amplification Channel	Fit Parameter	Fit Parameter
			a / MeV	b / MeV
MDT-01-000	1	high (B)	0.0029 ± 0.0001	0.0041 ± 0.0097
		low (A)	0.0618 ± 0.0026	0.1731 ± 1.0822
	2	high (B)	0.0028 ± 0.0001	-0.0054 ± 0.0100
		low (A)	0.0613 ± 0.0027	0.1026 ± 1.1851
MDT-01-001	1	high (B)	0.0030 ± 0.0001	-0.0890 ± 0.0099
		low (A)	0.0647 ± 0.0024	-0.0711 ± 0.5867
	2	high (B)	0.0030 ± 0.0001	-0.0847 ± 0.0111
		low (A)	0.0636 ± 0.0025	0.0423 ± 0.5871

Table D.4.: Results from fragment measurements for MDT-01-000 and MDT-01-001: fits of the ADC pulse height spectra (Section 4.3.3 and Section 5.2).

Primary Ion	Ion / Fragment	Pulse Position in ADC Channels			
		MDT-01-000		MDT-01-001	
		Diode 1	Diode 2	Diode 1	Diode 2
Ar 400 MeV u ⁻¹ behind 2 cm PE	Ar	949 ± 26	967 ± 27	914 ± 25	935 ± 26
	Cl	844 ± 28	859 ± 31	815 ± 28	835 ± 29
	S	744 ± 28	757 ± 26	721 ± 24	739 ± 29
	P	653 ± 27	664 ± 24	635 ± 24	649 ± 31
	Si	572 ± 23	581 ± 24	561 ± 26	572 ± 32
	Al	500 ± 26	506 ± 24	492 ± 35	503 ± 30
	Mg	436 ± 29	434 ± 40	429 ± 24	438 ± 34
Fe 490 MeV u ⁻¹ behind 1 cm PE	Fe	1795 ± 43	1823 ± 44	1729 ± 41	1763 ± 42
	Mn	1662 ± 48	1691 ± 47	1598 ± 42	1626 ± 42
	Cr	1523 ± 49	1548 ± 45	1468 ± 44	1497 ± 42
	V	1402 ± 43	1420 ± 42	1351 ± 42	1378 ± 39
	Ti	1279 ± 40	1296 ± 43	1237 ± 38	1265 ± 47
	Sc	1170 ± 37	1176 ± 40	1122 ± 44	1145 ± 45
	Ca	1058 ± 39	1059 ± 42	1021 ± 40	1039 ± 39
K	954 ± 34	961 ± 40	909 ± 42	931 ± 43	

Table D.5.: Results from fragment measurements for MDT-01-000 and MDT-01-001: fits of the calibrated energy deposition spectra (Section 4.3.3 and Section 5.2).

Primary Ion	Ion / Fragment	Energy Deposition in MeV			
		MDT-01-000		MDT-01-001	
		Diode 1	Diode 2	Diode 1	Diode 2
400 MeV u ⁻¹ behind 2 cm PE	Ar	58.9 ± 1.6	59.7 ± 1.7	59.0 ± 1.6	60.0 ± 1.8
	Cl	52.5 ± 1.8	53.1 ± 1.9	52.6 ± 1.7	53.7 ± 2.1
	S	46.2 ± 1.8	46.7 ± 1.6	46.5 ± 1.5	47.5 ± 1.8
	P	40.5 ± 1.7	41.0 ± 1.7	41.1 ± 1.6	41.8 ± 2.2
	Si	35.5 ± 1.5	35.9 ± 1.4	36.2 ± 1.7	36.9 ± 2.0
	Al	30.8 ± 2.0	31.3 ± 1.5	31.8 ± 2.1	32.6 ± 2.8
	Mg	27.3 ± 2.5	27.0 ± 2.7	27.6 ± 1.8	28.1 ± 2.4
490 MeV u ⁻¹ behind 1 cm PE	Fe	111.5 ± 2.9	112.5 ± 3.1	112.0 ± 2.8	113.1 ± 2.8
	Mn	103.0 ± 3.1	104.5 ± 3.8	103.6 ± 3.1	104.5 ± 3.1
	Cr	94.6 ± 2.9	95.6 ± 3.5	95.1 ± 3.1	96.0 ± 2.9
	V	87.0 ± 3.2	87.8 ± 3.0	87.2 ± 2.6	88.5 ± 2.9
	Ti	79.7 ± 3.2	79.7 ± 2.8	80.1 ± 2.4	80.9 ± 2.8
	Sc	72.5 ± 3.2	72.6 ± 2.8	72.4 ± 2.9	73.5 ± 2.8
	Ca	65.6 ± 3.0	65.0 ± 2.5	66.0 ± 2.2	66.8 ± 3.1
	K	59.1 ± 2.3	59.0 ± 2.4	59.0 ± 2.5	59.6 ± 2.6

E

FLIGHT MEASUREMENTS – FIGURES

E.1. COUNT RATES

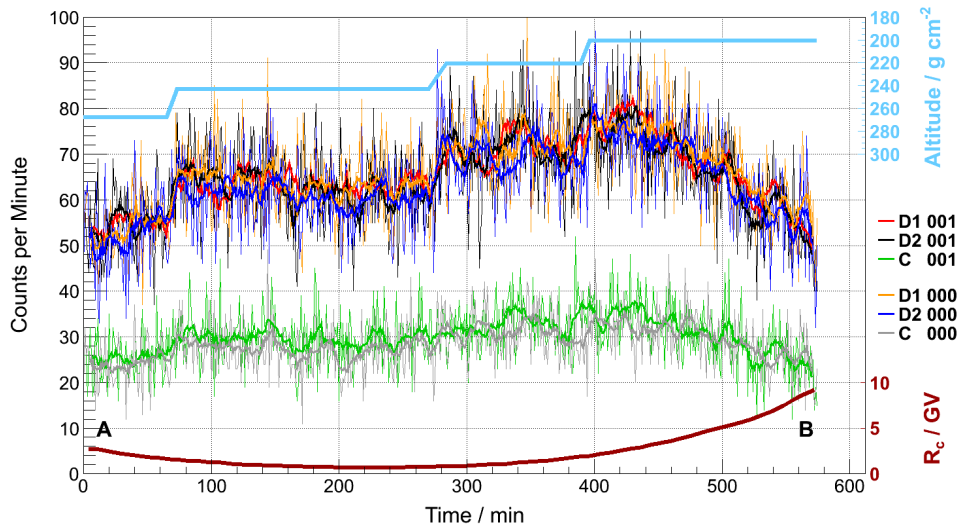


Figure E.1.: Count rates for flight **A–B 1** for MDT-01-000 and -001, Section 6.2.2 (compare Figure 6.2(a)). Count rates are shown for single diodes (**D1** and **D2**) and for coincidence events (**C**) in color code for both detectors, indicated with **000** and **001**. The count rates are given in the original resolution of one minute (thin lines), overlaid with a ten minutes moving average (thick lines). The cruising **altitude** is plotted in residual atmosphere in light blue at the top and the **cutoff rigidity** R_c in dark red at the bottom. **A** and **B** denote start and destination of the flights. The measurements have been conducted in configuration 1 (MDT-01-000 \uparrow and MDT-01-001 \uparrow).

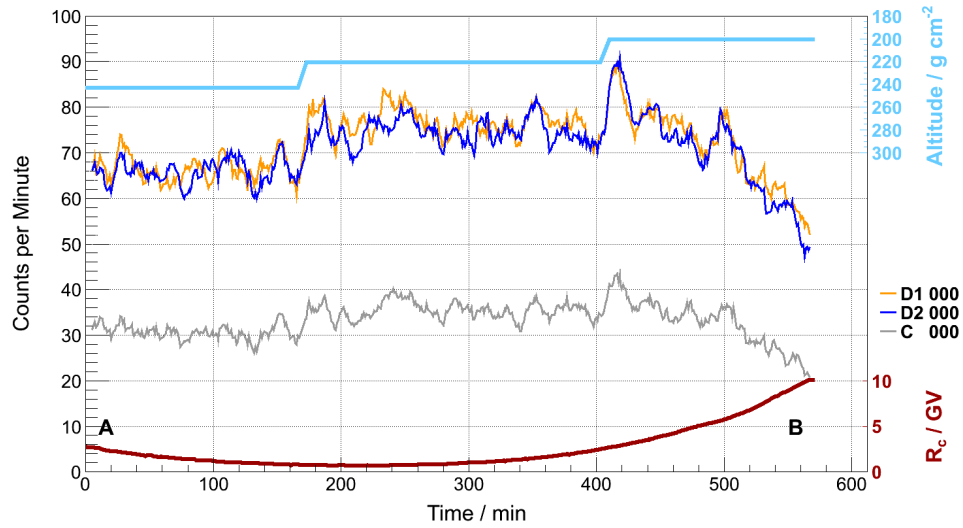


Figure E.2.: Same as in Figure 6.2(a) in Section 6.2.2 for the flight **A–B 2**. The measurements have been conducted in configuration 2a (MDT-01-000 \uparrow and MDT-01-001 \Rightarrow), but MDT-01-001 failed due to a faulty soldered joint.

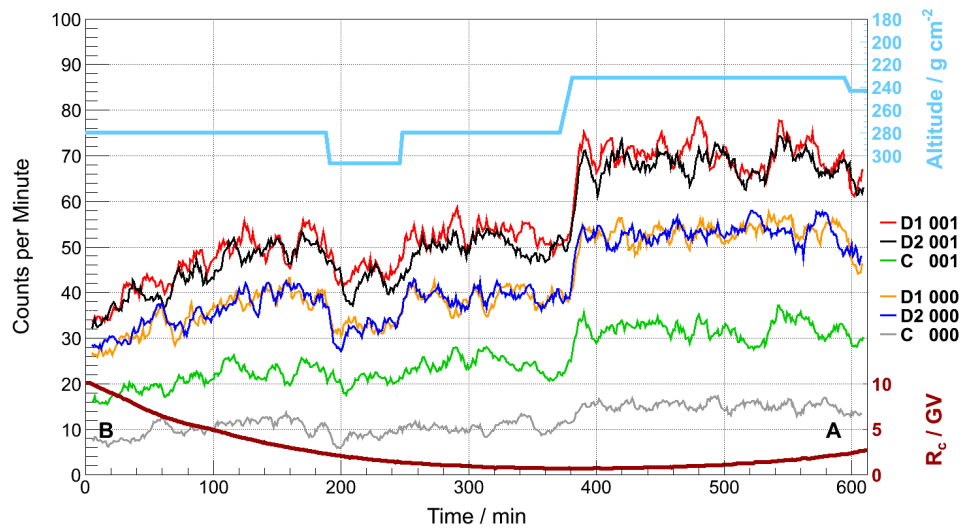


Figure E.3.: Same as in Figure 6.2(a) in Section 6.2.2 for the flight **B–A 2**. The measurements have been conducted in configuration 2b (MDT-01-000 \Rightarrow and MDT-01-001 \uparrow).

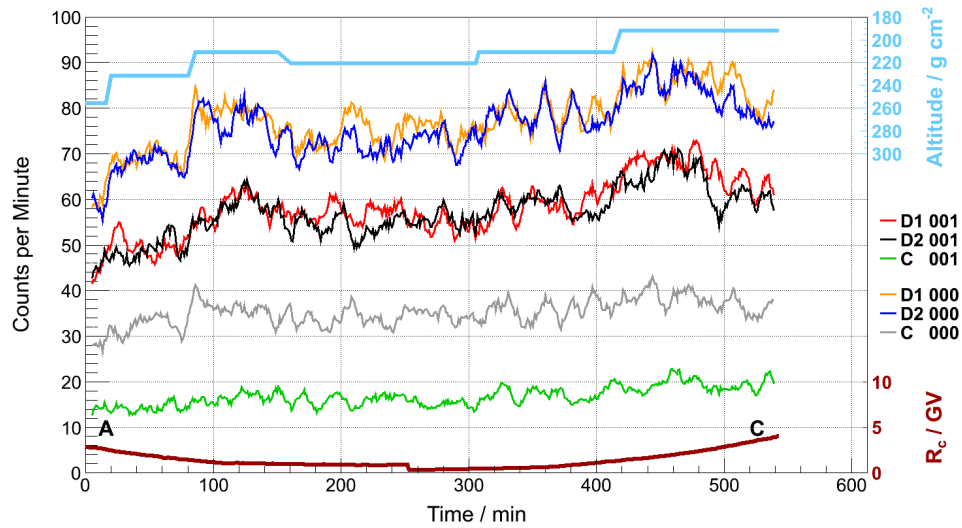


Figure E.4.: Same as in Figure 6.2(a) in Section 6.2.2 for the flight **A–C**. The measurements have been conducted in configuration 2a (MDT-01-000 \uparrow and MDT-01-001 \Rightarrow).

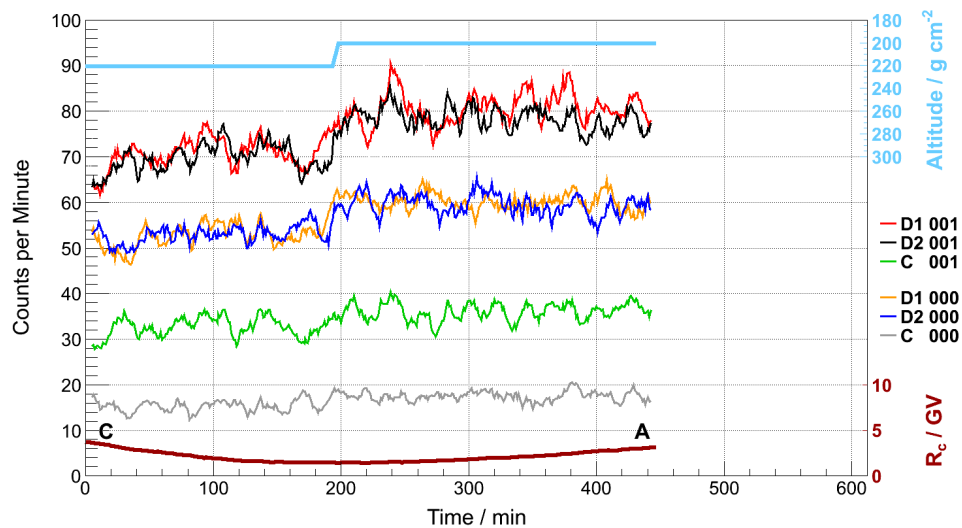


Figure E.5.: Same as in Figure 6.2(a) in Section 6.2.2 for the flight **C–A**. The measurements have been conducted in configuration 2b (MDT-01-000 \Rightarrow and MDT-01-001 \uparrow).

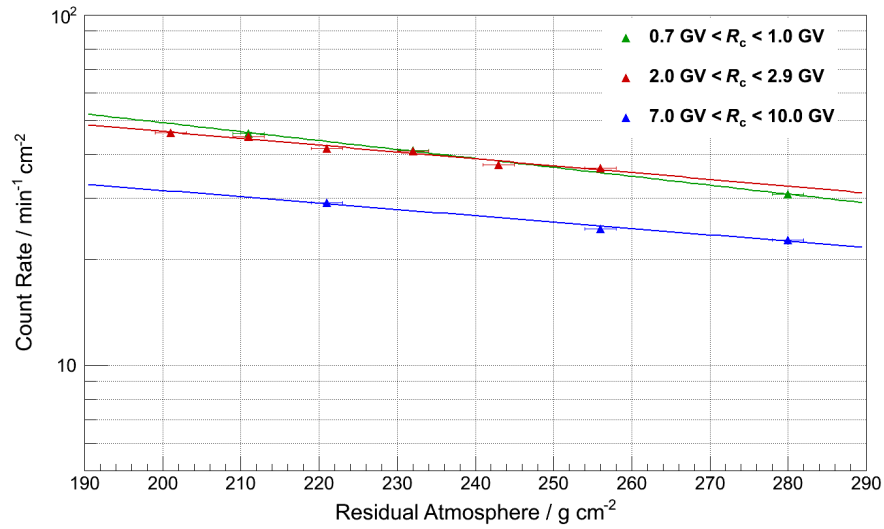


Figure E.6.: Count rate dependence on the altitude in residual atmosphere for three different cutoff rigidity regions (Section 6.2.3). The plots show the results for single diodes in configuration 2 (\Rightarrow). The solid lines are exponential fits and the results are listed in Table F.1 in Appendix F.

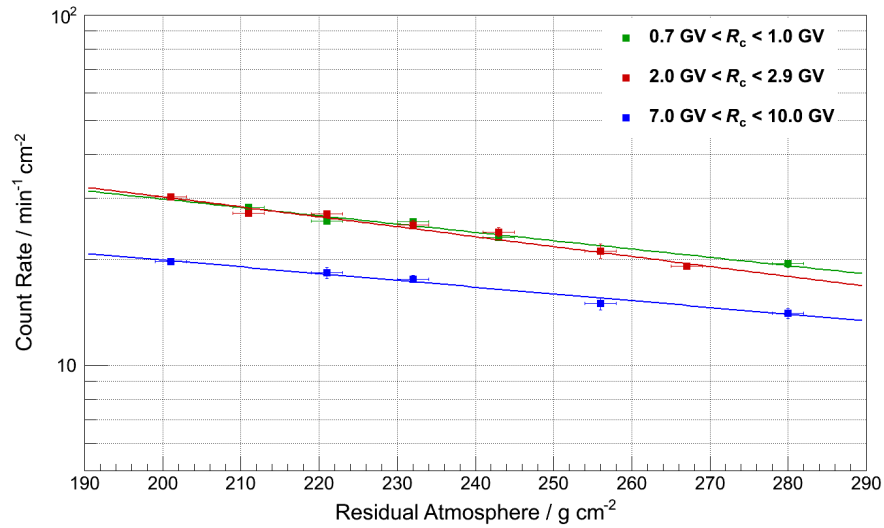


Figure E.7.: Count rate dependence on the altitude in residual atmosphere for three different cutoff rigidity regions (Section 6.2.3). The plots show the results for coincidence events in configuration 1 (\Uparrow). The solid lines are exponential fits and the results are listed in Table F.1 in Appendix F.

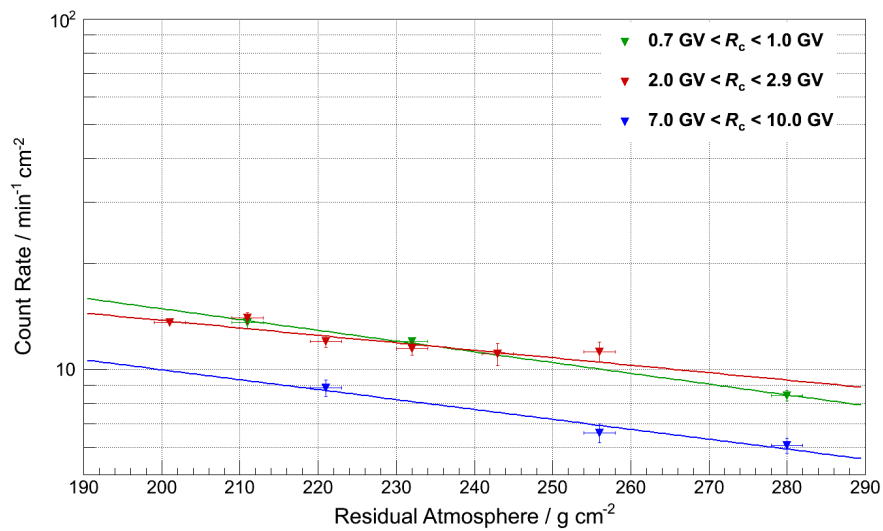


Figure E.8.: Count rate dependence on the altitude in residual atmosphere for three different cutoff rigidity regions (Section 6.2.3. The plots show the results for coincidence events in configuration 2 (\Rightarrow). The solid lines are exponential fits and the results are listed in Table F.1 in Appendix F.

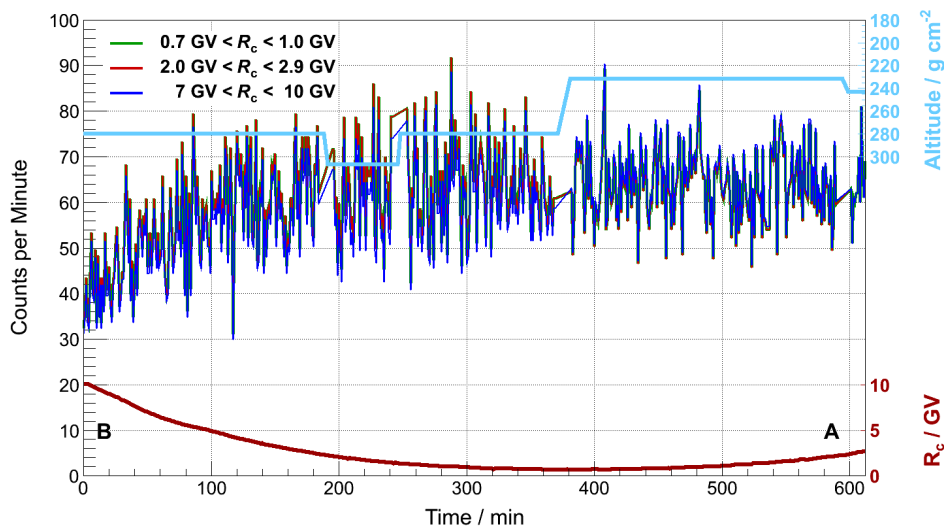


Figure E.9.: Count rates – B–A2 for MDT-01-001 diode 1 (\uparrow), normalized with exponential fit (Section 6.2.3 and Figure E.3) in the original time resolution of one minute.

E.2. DOSE RATES

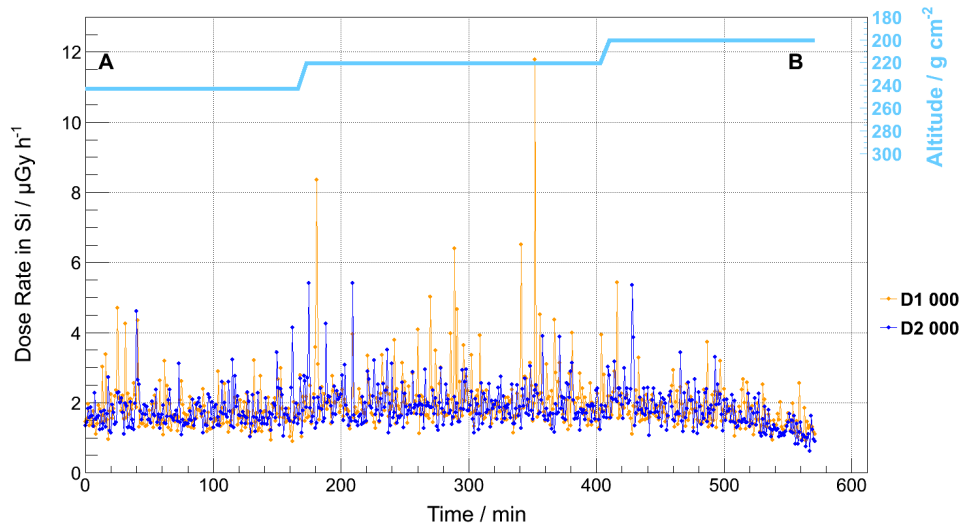


Figure E.10.: Same as in Figure 6.11(a) in Section 6.2.4 for the flight **A–B 2**. The measurements have been conducted in configuration 2a (MDT-01-000 \uparrow and MDT-01-001 \Rightarrow), but MDT-01-001 failed due to a faulty soldered joint.

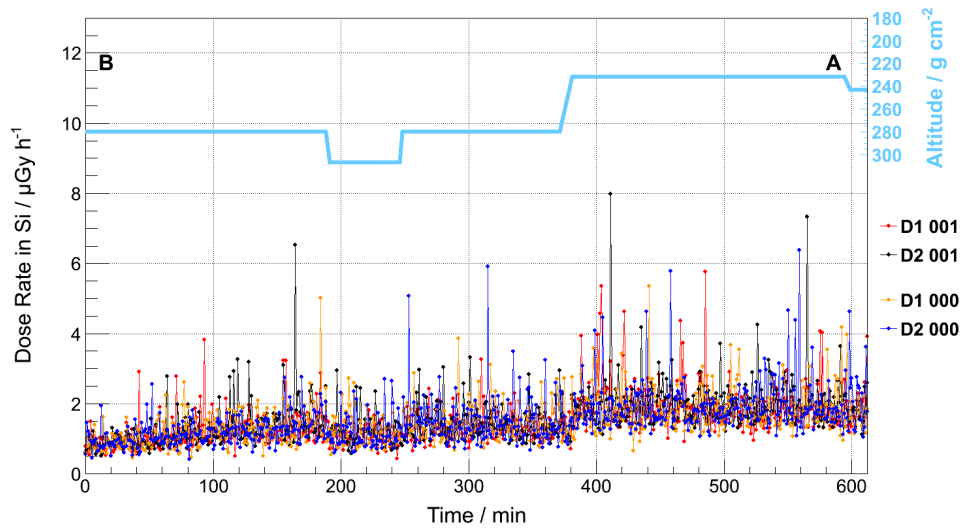


Figure E.11.: Same as in Figure 6.11(a) in Section 6.2.4 for the flight **B–A 2**. The measurements have been conducted in configuration 2b (MDT-01-000 \Rightarrow and MDT-01-001 \uparrow).

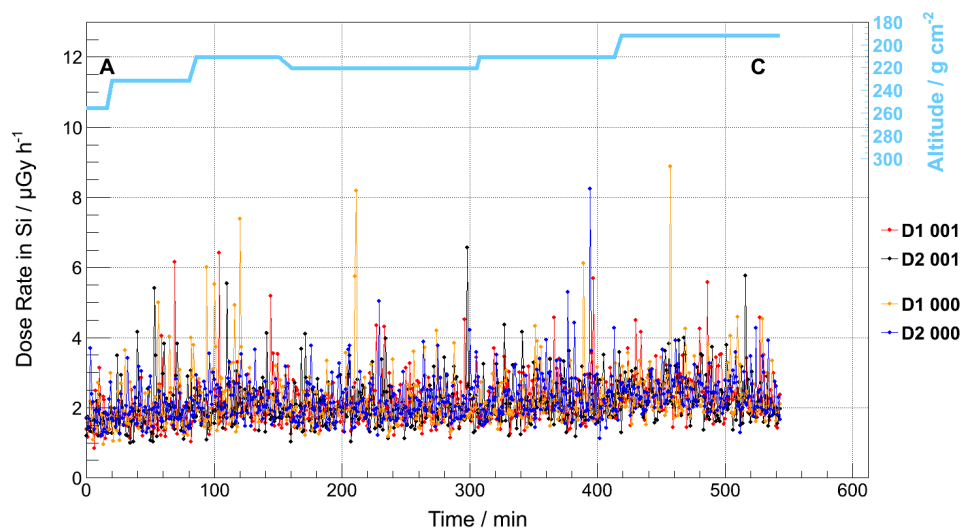


Figure E.12.: Same as in Figure 6.11(a) in Section 6.2.4 for the flight **A–C**. The measurements have been conducted in configuration 2a (MDT-01-000 \uparrow and MDT-01-001 \Rightarrow).

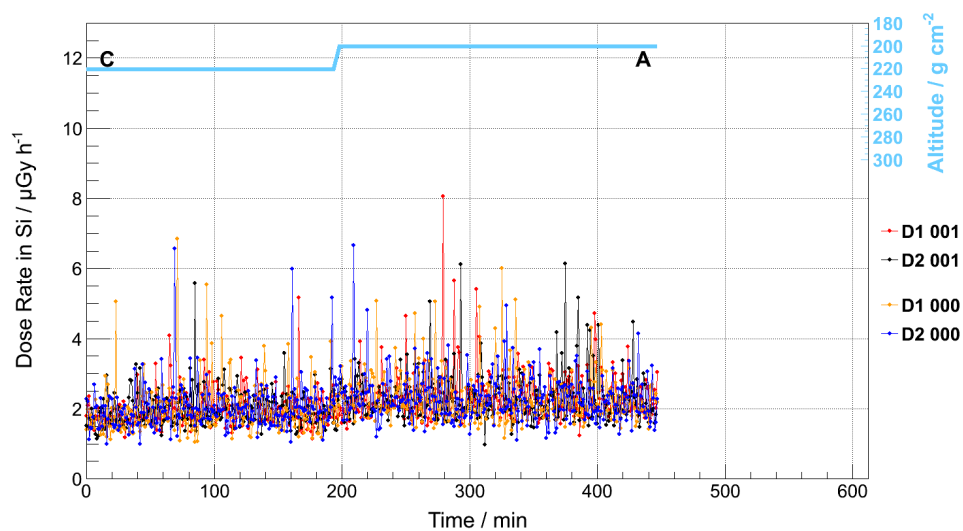


Figure E.13.: Same as in Figure 6.11(a) in Section 6.2.4 for the flight **C–A**. The measurements have been conducted in configuration 2b (MDT-01-000 \Rightarrow and MDT-01-001 \uparrow).

E.3. ENERGY DEPOSITION SPECTRA

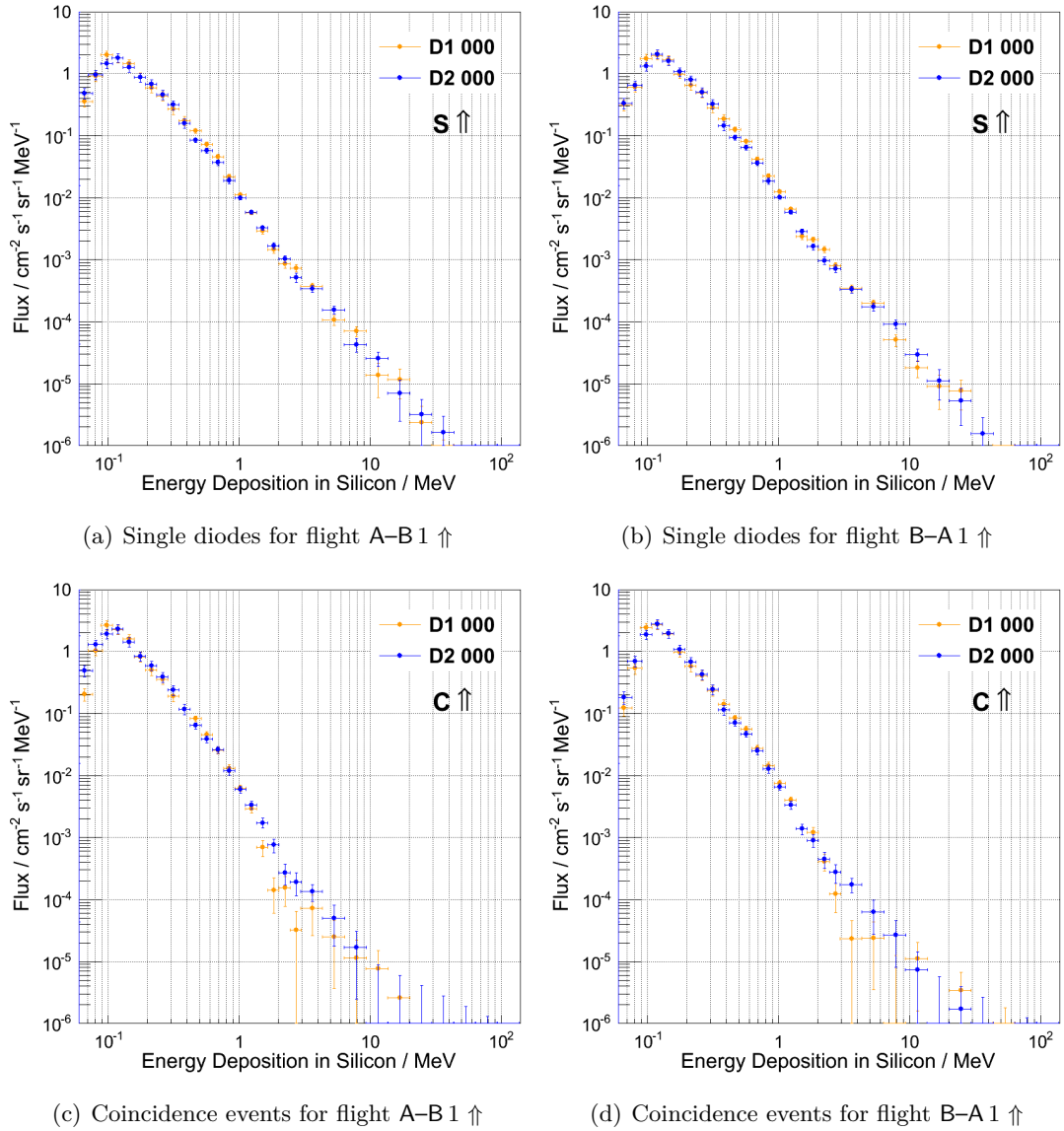


Figure E.14.: Energy deposition spectra for diode 1 (D1) and diode 2 (D2) of detector **MDT-01-000** for the flights A-B1 (left) and B-A1 (right). The two panels at the top show the flux detected in every single diode, while the two panels at the bottom show the results that have been detected in coincidence mode. The arrows indicate the orientation of the telescope axis (Section 6.2.5).

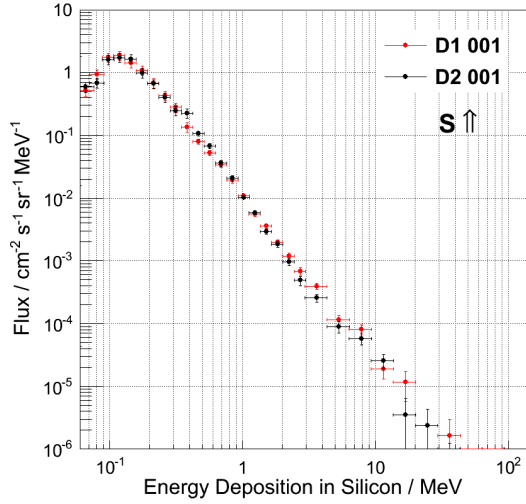
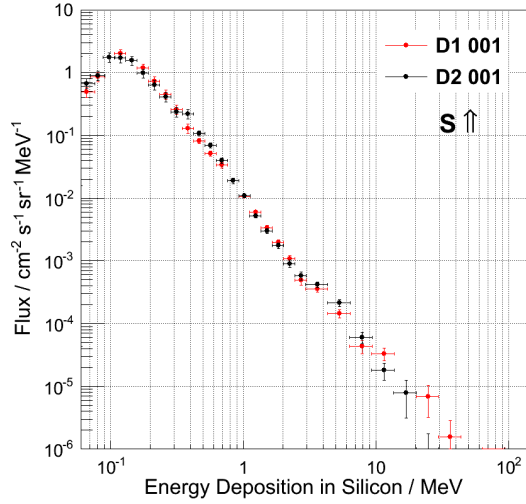
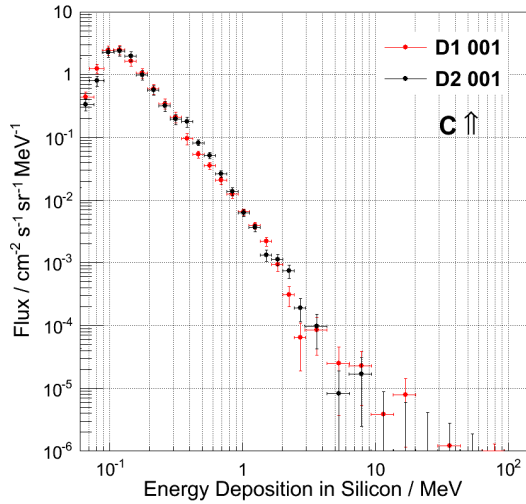
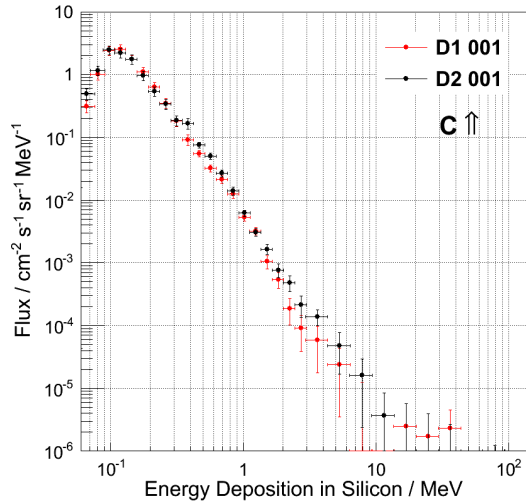
(a) Single diodes for flight A-B 1 \uparrow (b) Single diodes for flight B-A 1 \uparrow (c) Coincidence events for flight A-B 1 \uparrow (d) Coincidence events for flight B-A 1 \uparrow

Figure E.15.: Energy deposition spectra for diode 1 (D1) and diode 2 (D2) of detector **MDT-01-001** for the flights A-B 1 (left) and B-A 1 (right). The two panels at the top show the flux detected in every single diode, while the two panels at the bottom show the results that have been detected in coincidence mode. The arrows indicate the orientation of the telescope axis (Section 6.2.5).

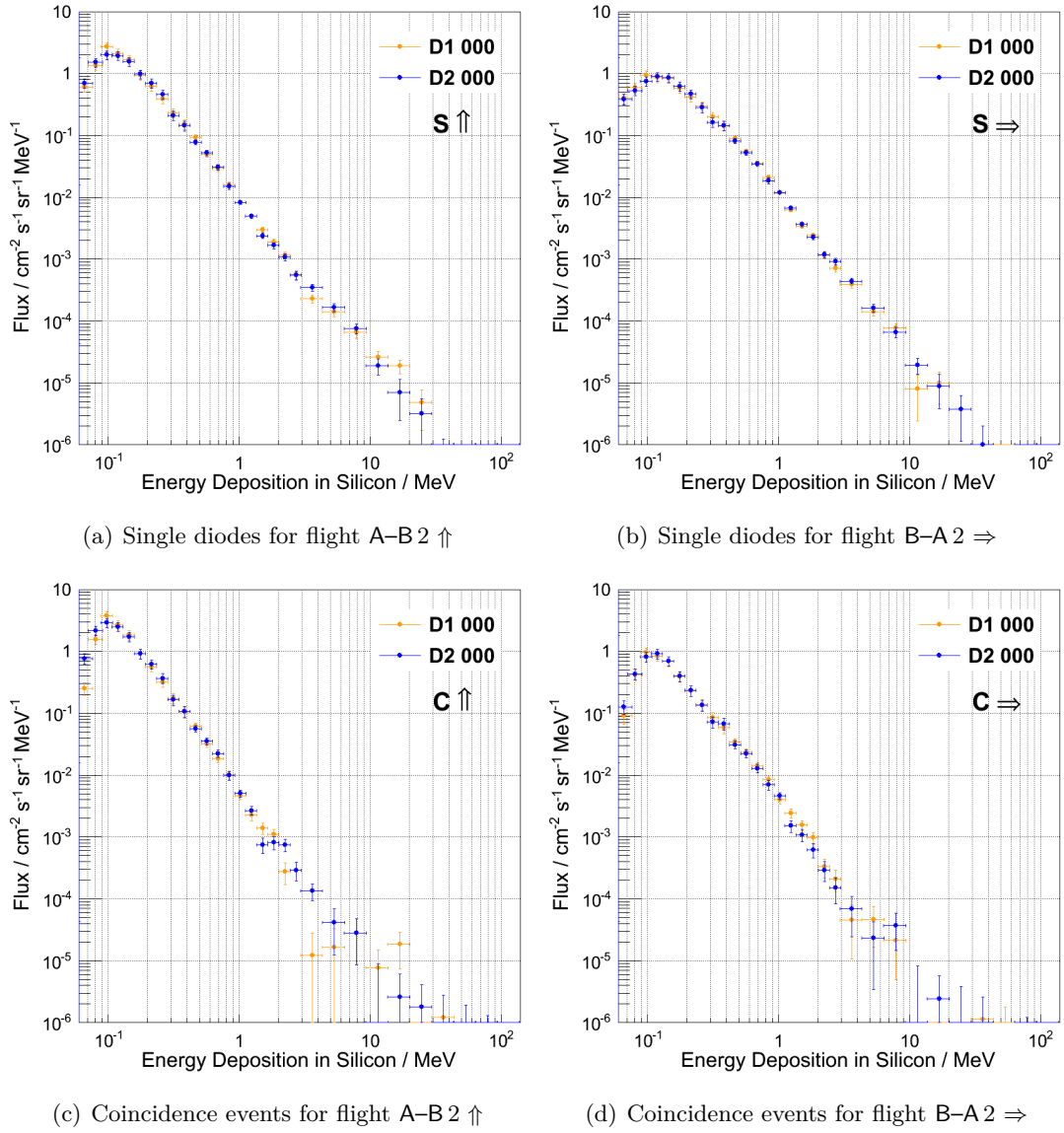


Figure E.16.: Energy deposition spectra for diode 1 (D1) and diode 2 (D2) of detector **MDT-01-000** for the flights A–B 2 (left) and B–A 2 (right). The two panels at the top show the flux detected in every single diode, while the two panels at the bottom show the results that have been detected in coincidence mode. The arrows indicate the orientation of the telescope axis (Section 6.2.5).

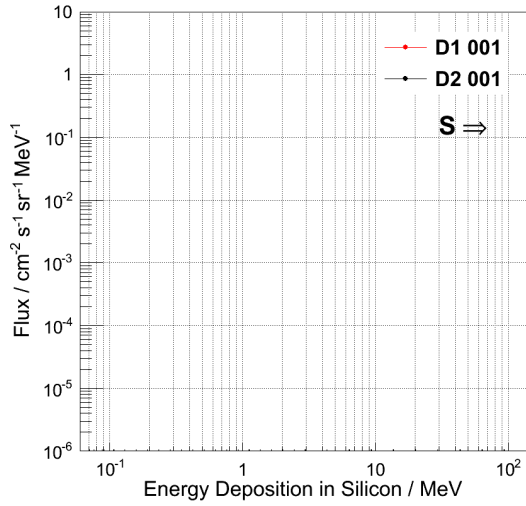
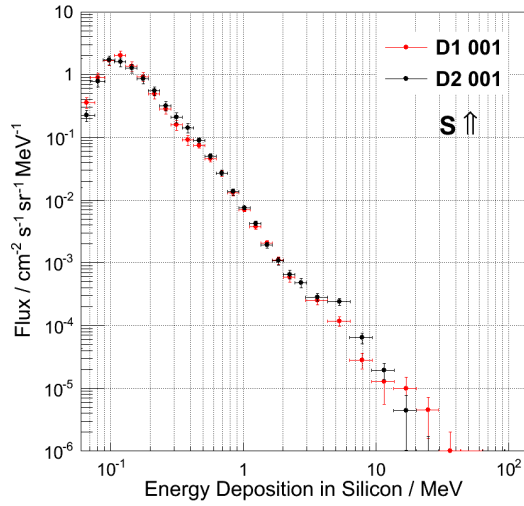
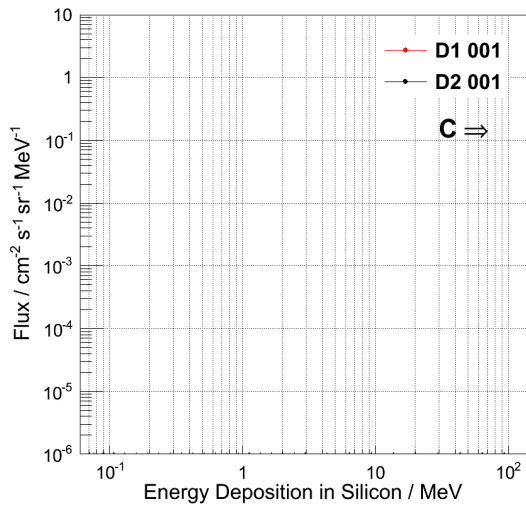
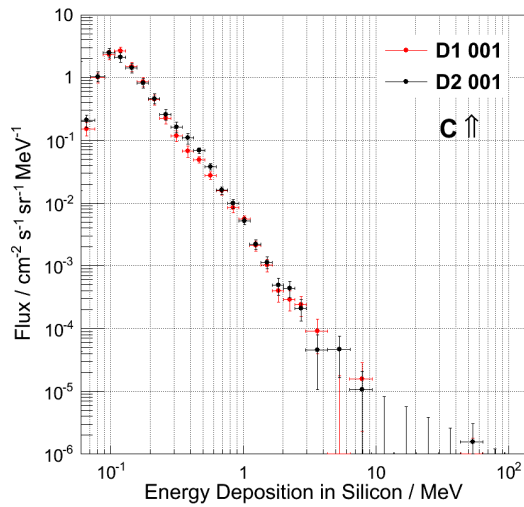
(a) Single diodes for flight A-B 2 \Rightarrow (b) Single diodes for flight B-A 2 \Uparrow (c) Coincidence events for flight A-B 2 \Rightarrow (d) Coincidence events for flight B-A 2 \Uparrow

Figure E.17.: Energy deposition spectra for diode 1 (D1) and diode 2 (D2) of detector **MDT-01-001** only for flight B-A 2 (right). The two panels at the top show the flux detected in every single diode, while the two panels at the bottom show the results that have been detected in coincidence mode. The arrows indicate the orientation of the telescope axis (Section 6.2.5). The detector failed during flight A-B 2 due to a faulty soldered joint.

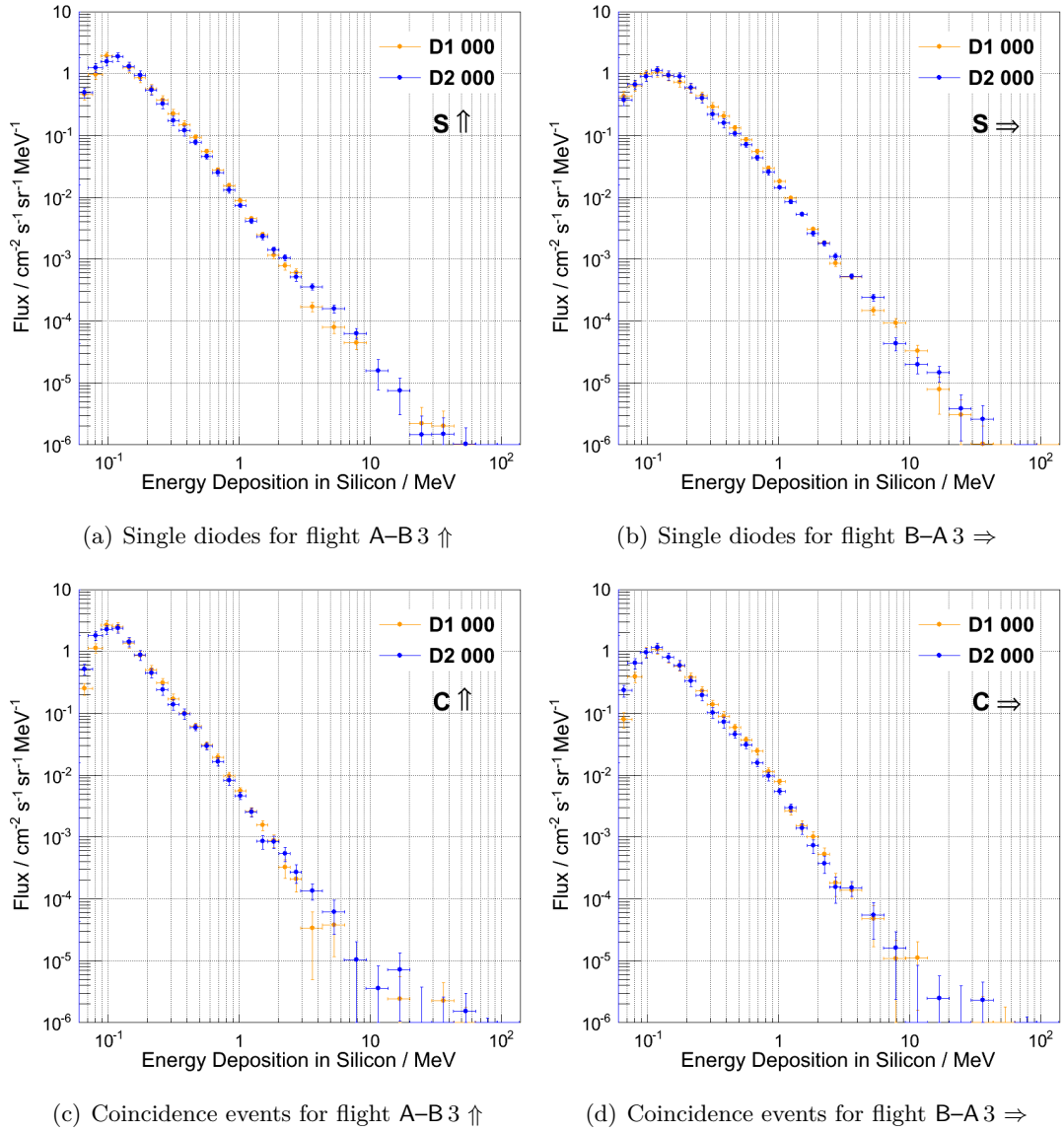


Figure E.18.: Energy deposition spectra for diode 1 (D1) and diode 2 (D2) of detector **MDT-01-000** for the flights A-B 3 (left) and B-A 3 (right). The two panels at the top show the flux detected in every single diode, while the two panels at the bottom show the results that have been detected in coincidence mode. The arrows indicate the orientation of the telescope axis (Section 6.2.5).

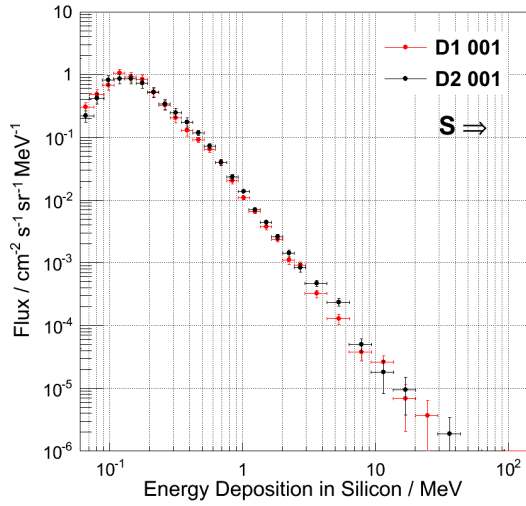
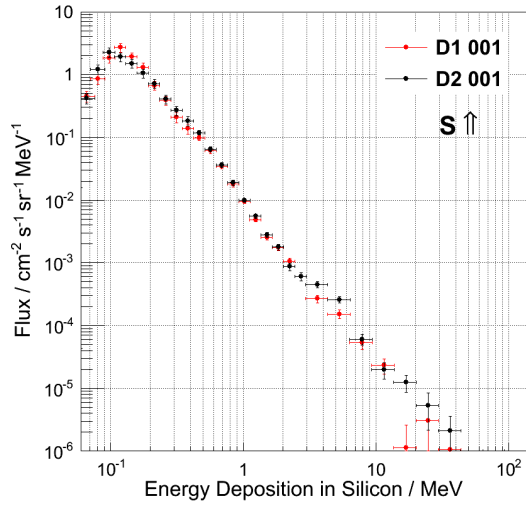
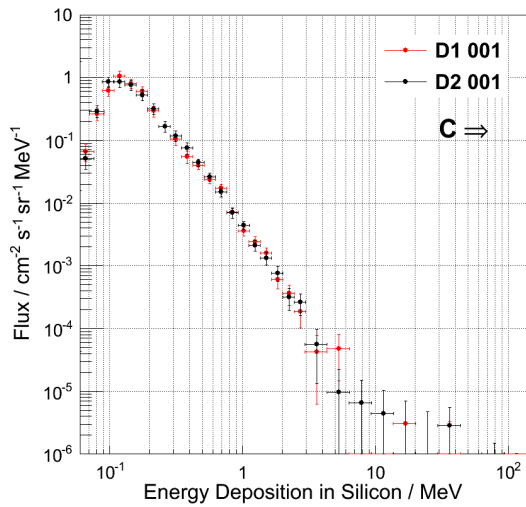
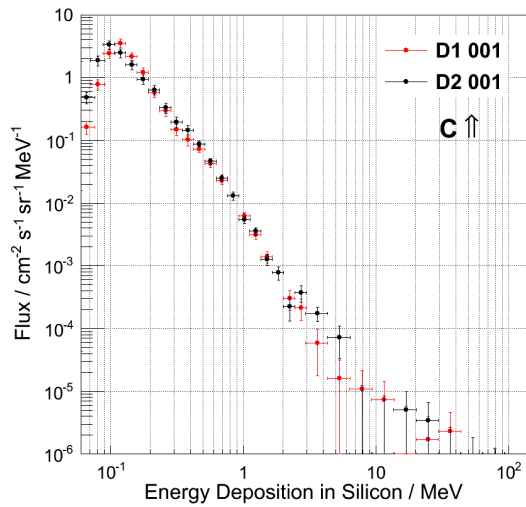
(a) Single diodes for flight A-B 3 \Rightarrow (b) Single diodes for flight B-A 3 \uparrow (c) Coincidence events for flight A-B 3 \Rightarrow (d) Coincidence events for flight B-A 3 \uparrow

Figure E.19.: Energy deposition spectra for diode 1 (D1) and diode 2 (D2) of detector **MDT-01-001** for the flights A-B 3 (left) and B-A 3 (right). The two panels at the top show the flux detected in every single diode, while the two panels at the bottom show the results that have been detected in coincidence mode. The arrows indicate the orientation of the telescope axis (Section 6.2.5).

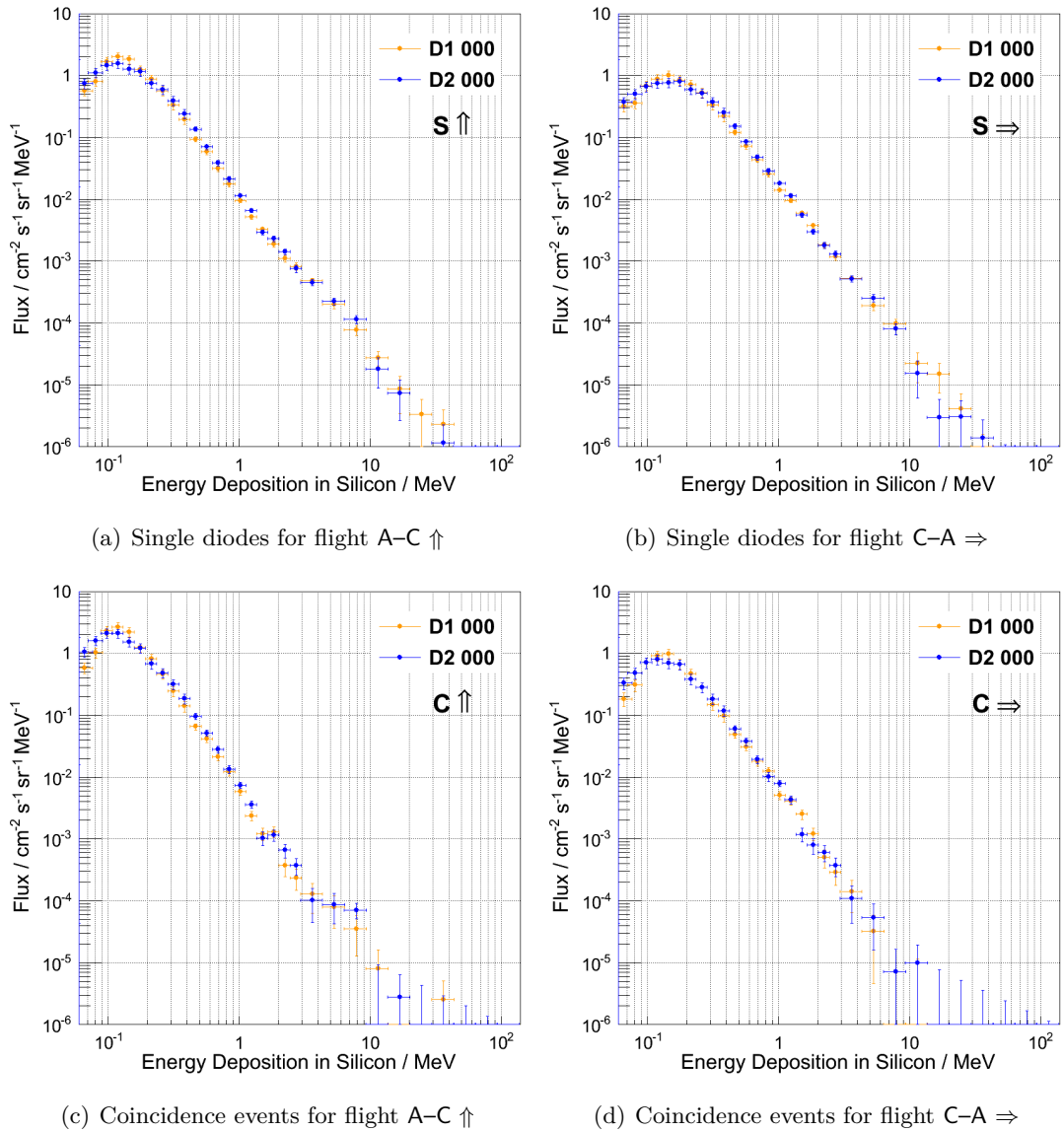


Figure E.20.: Energy deposition spectra for diode 1 (D1) and diode 2 (D2) of detector MDT-01-000 for the flights A-C (left) and C-A (right). The two panels at the top show the flux detected in every single diode, while the two panels at the bottom show the results that have been detected in coincidence mode. The arrows indicate the orientation of the telescope axis (Section 6.2.5).

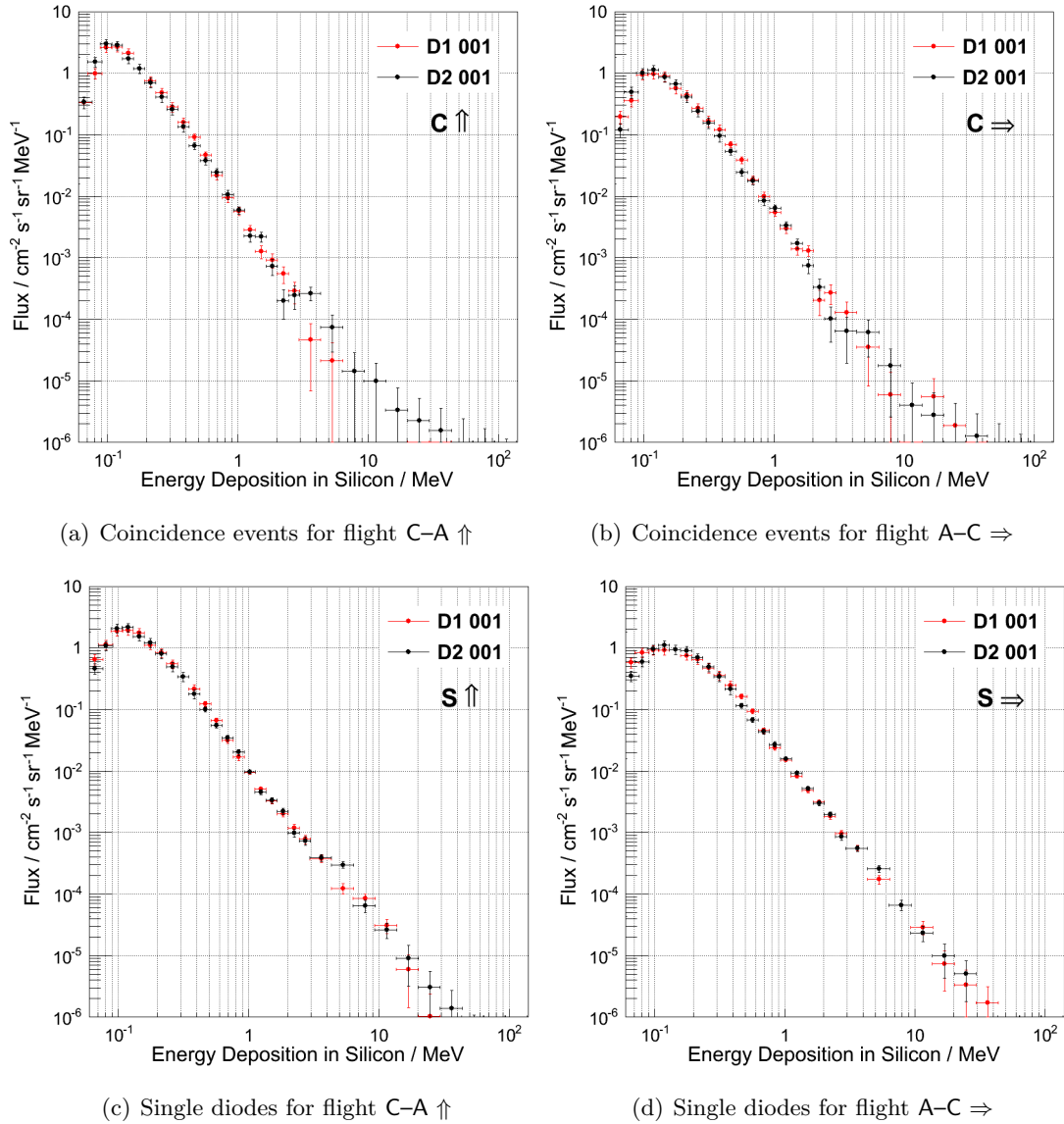


Figure E.21.: Energy deposition spectra for diode 1 (D1) and diode 2 (D2) of detector MDT-01-001 for the flights A-C (left) and C-A (right). The two panels at the top show the flux detected in every single diode, while the two panels at the bottom show the results that have been detected in coincidence mode. The arrows in the figure caption indicate the orientation of the telescope axis (Section 6.2.5).

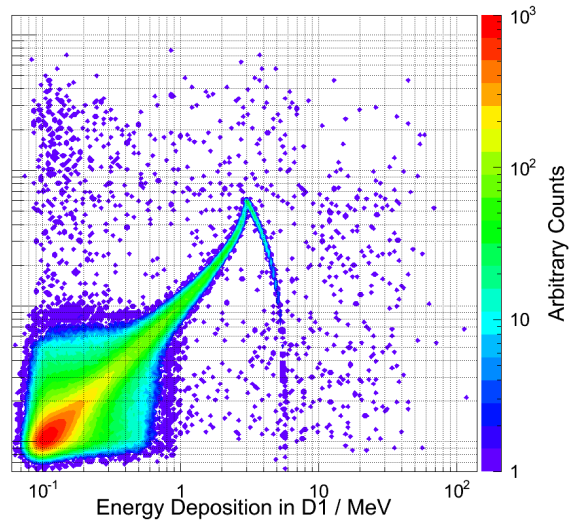


Figure E.22.: Simulation of energy deposition spectra from a proton beam of equally distributed energies between 1 MeV and 100 MeV in a silicon telescope corresponding to the MDT size and configuration (see discussion of energy depositions recorded during flight measurements in coincidence mode in Section 6.2.7, Figure 6.18). The plot is to clarify the difference between slowing down protons that traverse diode 1 (D1) first (energy deposition in the tail structure up to 3 MeV in D1 and 6 MeV in D1) and stopping protons that deposit energies according to the structure seen above 3 MeV in D1 and below 6 MeV in D2. For a description of the simulation setup and method compare Chapter 7.

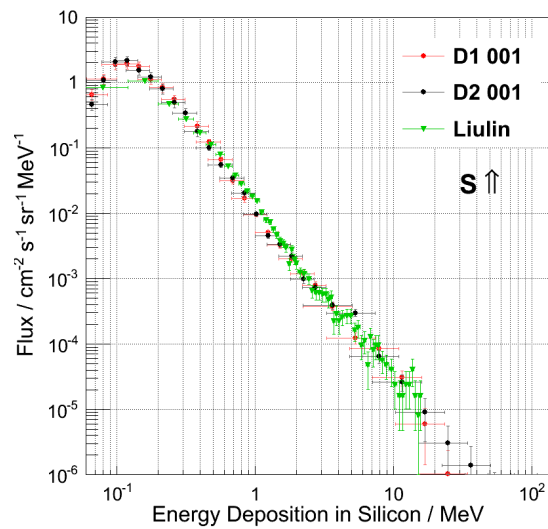


Figure E.23.: Energy deposition spectra for detector **MDT-01-001** (single diodes) and **Liulin** for the flight C-A, both detectors in upwards orientation (\uparrow). While for the MDT from the third data point on the error bar in x-direction is given by the logarithmic binning, the Liulin spectrum has not been rebinned, showing the original resolution. It can be seen that energy range of the Liulin does not include high energy depositions (Section 6.2.7).

E.4. LINEAR ENERGY TRANSFER SPECTRA

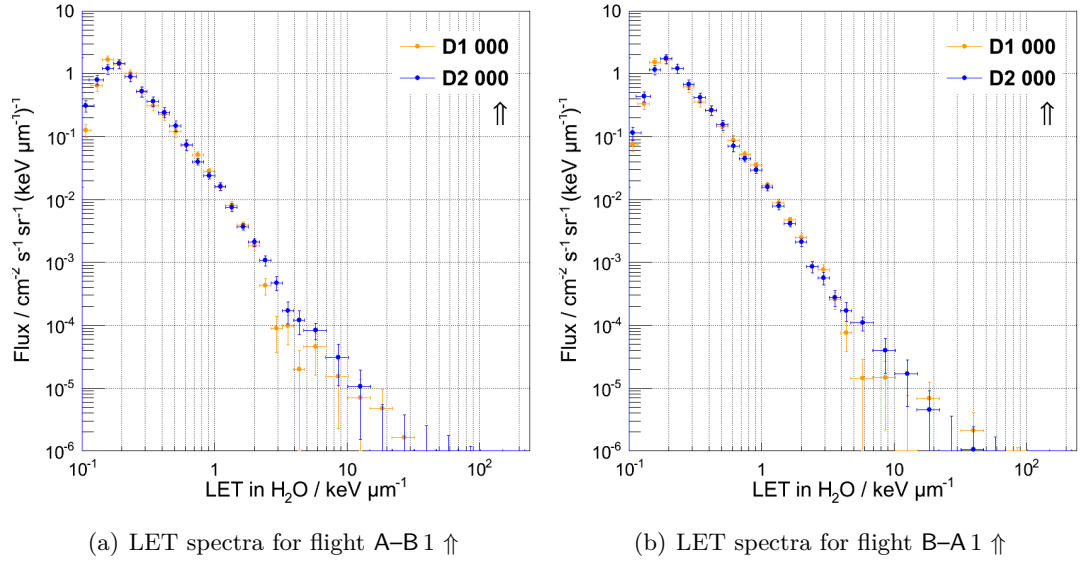


Figure E.24.: Linear energy transfer spectra for diode 1 (D1) and diode 2 (D2) of detector MDT-01-000 for the flights A-B 1 (left) and B-A 1 (right). The arrows indicate the orientation of the telescope axis (Section 6.2.6).

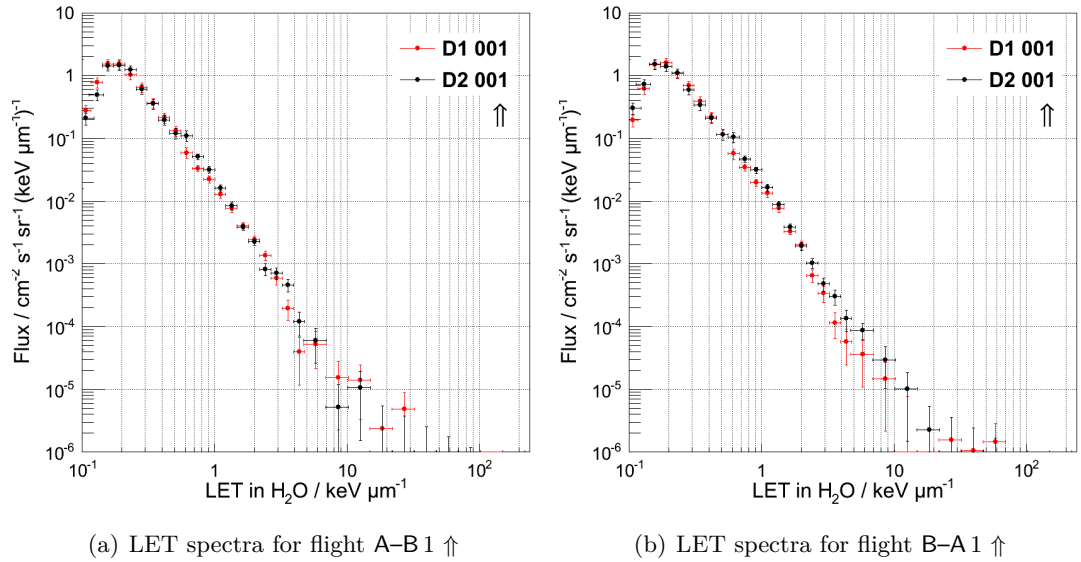


Figure E.25.: Linear energy transfer spectra for diode 1 (D1) and diode 2 (D2) of detector MDT-01-001 for the flights A-B 1 (left) and B-A 1 (right). The arrows indicate the orientation of the telescope axis (Section 6.2.6).

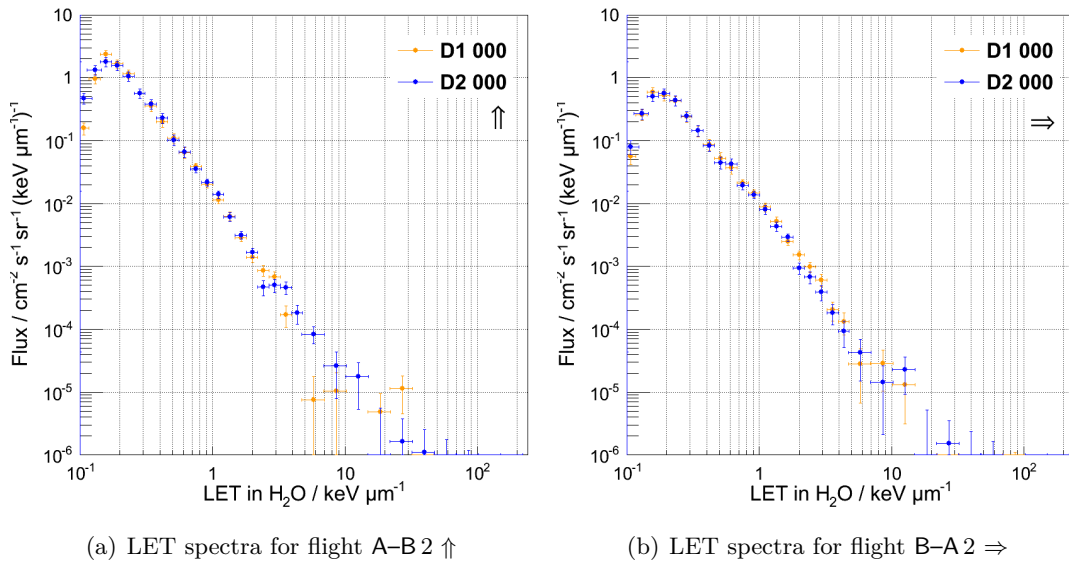


Figure E.26.: Linear energy transfer spectra for diode 1 (D1) and diode 2 (D2) of detector **MDT-01-000** for the flights A-B 2 (left) and B-A 2 (right). The arrows indicate the orientation of the telescope axis (Section 6.2.6).

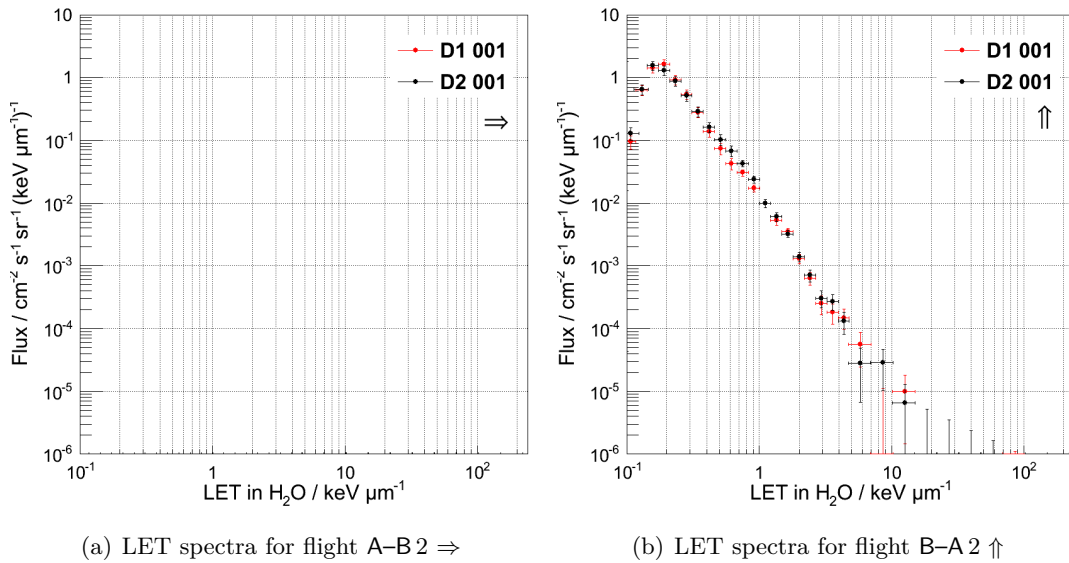


Figure E.27.: Linear energy transfer spectra for diode 1 (D1) and diode 2 (D2) of detector **MDT-01-001** only for flight B-A 2 (right). The detector failed during flight A-B 2 due to a faulty soldered joint. The arrows indicate the orientation of the telescope axis (Section 6.2.6).

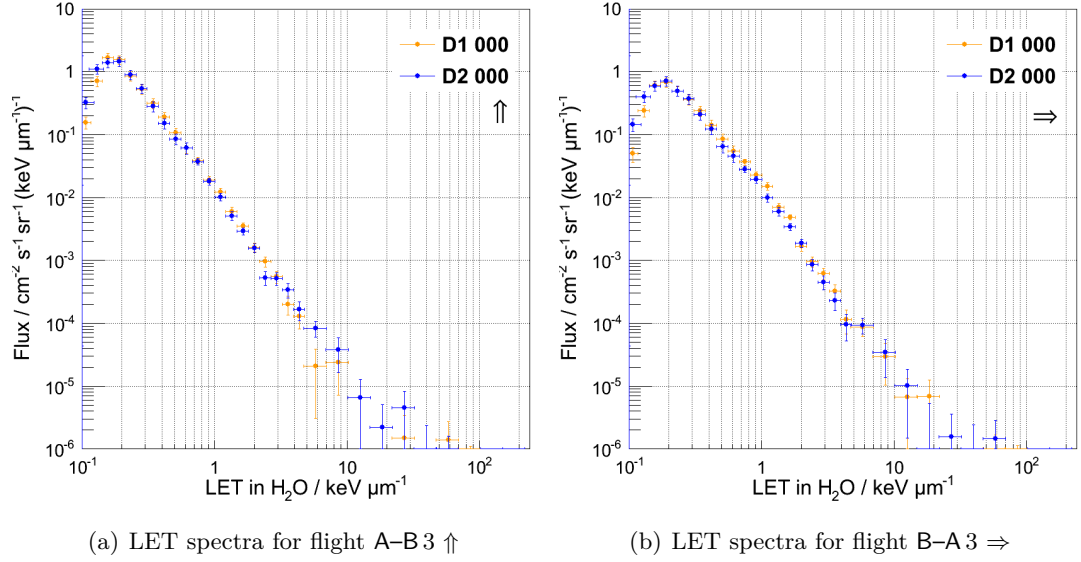


Figure E.28.: Linear energy transfer spectra for diode 1 (D1) and diode 2 (D2) of detector MDT-01-000 for the flights A-B 3 (left) and B-A 3 (right). The arrows indicate the orientation of the telescope axis (Section 6.2.6).

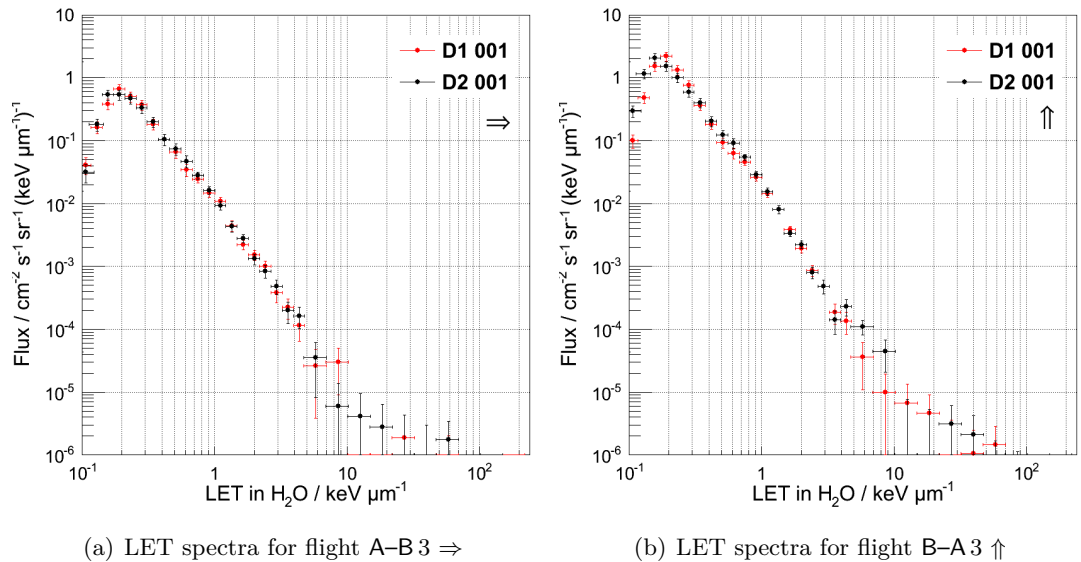


Figure E.29.: Linear energy transfer spectra for diode 1 (D1) and diode 2 (D2) of detector MDT-01-001 for the flights A-B 3 (left) and B-A 3 (right). The arrows indicate the orientation of the telescope axis (Section 6.2.6).

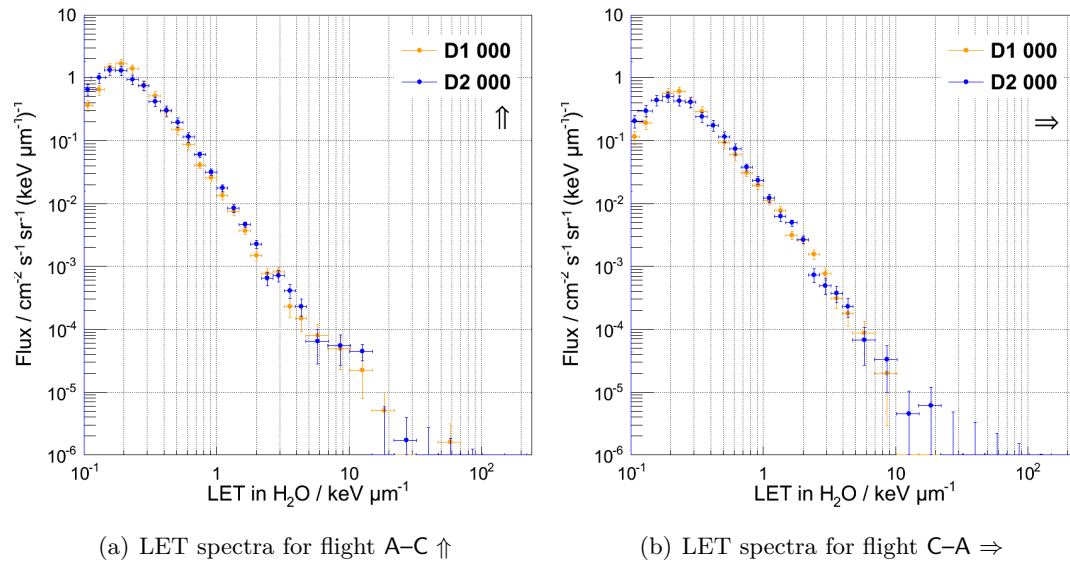


Figure E.30.: Linear energy transfer spectra for diode 1 (D1) and diode 2 (D2) of detector **MDT-01-000** for the flights A-C (left) and C-A (right). The arrows indicate the orientation of the telescope axis (Section 6.2.6).

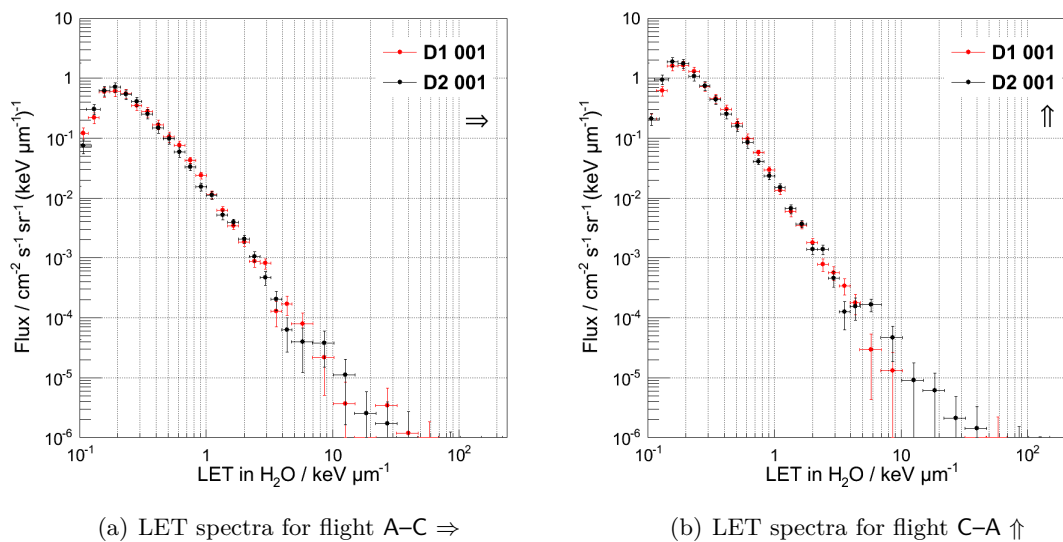


Figure E.31.: Linear energy transfer spectra for diode 1 (D1) and diode 2 (D2) of detector **MDT-01-001** for the flights A-C (left) and C-A (right). The arrows in the figure caption indicate the orientation of the telescope axis (Section 6.2.6).

F

FLIGHT MEASUREMENTS – TABLES

Table F.1.: Fit results for exponential fits of count rates vs. residual atmosphere (Figures 6.7, 6.6, Section 6.2.3 and Figures E.6, E.7, E.8, Appendix E.1) following Equation 6.8 in Section 6.2.3. The first column gives the geomagnetic cutoff rigidity region, the second the configuration, in which S stands for single diodes and C for coincidence data, the arrows label the telescope axis orientation. Column three, four and five give the fit parameters of the exponential fits including the goodness of the fit by χ^2/N , where N is the number of degrees of freedom. Compare also Table 6.5 in the respective section.

Cutoff Rigidity Interval	Configuration	a_c (g cm^{-2})	b_c ($\text{min}^{-1} \text{cm}^{-2}$)	χ^2/N
0.7 GV – 1.0 GV	S \uparrow	167 ± 8	222 ± 2	2.1
	S \Rightarrow	171 ± 11	164 ± 2	0.2
	C \uparrow	183 ± 14	90 ± 2	1.9
	C \Rightarrow	141 ± 16	60 ± 2	0.3
2.0 GV – 2.9 GV	S \uparrow	150 ± 7	224 ± 2	2.2
	S \Rightarrow	223 ± 22	110 ± 2	1.3
	C \uparrow	153 ± 10	110 ± 2	1.5
	C \Rightarrow	204 ± 44	37 ± 2	1.5
7.0 GV – 10.0 GV	S \uparrow	188 ± 11	134 ± 2	0.5
	S \Rightarrow	240 ± 31	74 ± 2	0.8
	C \uparrow	225 ± 25	49 ± 2	0.5
	C \Rightarrow	153 ± 32	37 ± 2	1.0

Table F.2.: Fit results for exponential fits of dose rates vs. residual atmosphere (Figures 6.14 and 6.15), following Equation 6.13 in Section 6.2.4. The first column gives the geomagnetic cutoff rigidity region, the second the configuration, in which S stands for single diodes (combined data for both configurations) and C for coincidence data, for which the arrows label the telescope axis orientation. Column three, four and five give the fit parameters of the exponential fits including the goodness of the fit by χ^2/N , where N is the number of degrees of freedom. Compare also Table 6.8 in the respective section.

Cutoff Rigidity Interval	Configuration	a_d (g cm^{-2})	b_d ($\mu\text{Gy h}^{-1}$)	χ^2/N
0.7 GV – 1.0 GV	S	142 ± 9	2.3 ± 0.1	0.7
	C \uparrow	136 ± 31	1.2 ± 0.4	0.4
	C \Rightarrow	124 ± 50	0.7 ± 0.8	0.1
2.0 GV – 2.9 GV	S	153 ± 12	2.2 ± 0.2	0.7
	C \uparrow	182 ± 51	0.7 ± 0.4	0.2
	C \Rightarrow	178 ± 167	0.2 ± 1.2	0.0
7.0 GV – 10.0 GV	S	171 ± 12	1.5 ± 0.1	0.9
	C \uparrow	210 ± 99	0.1 ± 0.6	0.1
	C \Rightarrow	89 ± 44	1.2 ± 1.4	0.0

Table F.3.: Calculated quality factors for individual flights (Section 6.2.7).

Flight	Detector	\bar{Q}
MDT-01-		
A–B 1	000	1.06 ± 0.05
	001	1.23 ± 0.14
B–A 1	000	1.65 ± 0.51
	001	1.94 ± 0.59
A–B 2	000	1.34 ± 0.15
B–A 2	000	1.30 ± 0.30
	001	1.01 ± 0.03
A–B 3	000	1.33 ± 0.22
	001	1.69 ± 0.65
B–A 3	000	1.09 ± 0.07
	001	2.01 ± 0.58
A–C	000	1.66 ± 0.43
	001	1.20 ± 0.15
C–A	000	1.00 ± 0.04
	001	1.05 ± 0.05
Mean		1.37 ± 0.33

G

ADDITIONAL FLIGHT MEASUREMENTS

G.1. FIRST SYSTEM CHECK

The first measurement onboard an aircraft was performed with the setup including breadboard versions 05.01 and 06.01 (compare Section 3.3, Figure A.2) and one detection channel, i.e. one diode, only. This served as a first test run to verify that the system is functioning correctly. The setup has been preliminary calibrated with ^{241}Am and heavy ions at the Heavy Ion Medical Accelerator (HIMAC)¹.

The measurement flight was conducted by the flight facility of the German Aerospace Center (DLR) in Oberpfaffenhofen (OBF) in order to monitor the German airspace for radioactive pollution after the incidence in the Japanese nuclear power plant in Fukushima in March 2011. The flight was performed with the aircraft Dassault Falcon 20E / D-CMET at the end of March.

Figure G.1 outlines the flight route from OBF to Braunschweig (left) and back (right) with a color code indicating the altitude.

RESULTS

Figure G.2 shows the count rates in counts per minute in red and the altitude in meters in light blue. Microphonics is observed, which can be seen as an unexpected increase in the count rates (e.g. in the first 30 minutes after starting the measurement and in minute 77 during the first flight). For this test setup the microphonic countermeasure described in Section 3.6 had not been implemented yet.

The calculated dose rate for the three and the one hour flight was $1.7 \mu\text{Gy h}^{-1}$ and $0.3 \mu\text{Gy h}^{-1}$, respectively. This is in acceptable agreement with the other silicon detector (Liulin, Dachev et al. 2007) that measured dose rates of $1.9 \mu\text{Gy h}^{-1}$ and $0.3 \mu\text{Gy h}^{-1}$ during the two flights. With silicon detectors, no excess radiation expo-

¹The heavy ions were helium (100 MeV u^{-1}), carbon, and oxygen (both 400 MeV u^{-1}). The results are not shown in this work, but the calibration process is the same as it has been applied for the final prototypes (compare Chapter 4).

sure has been detected (Santen et al., 2012).

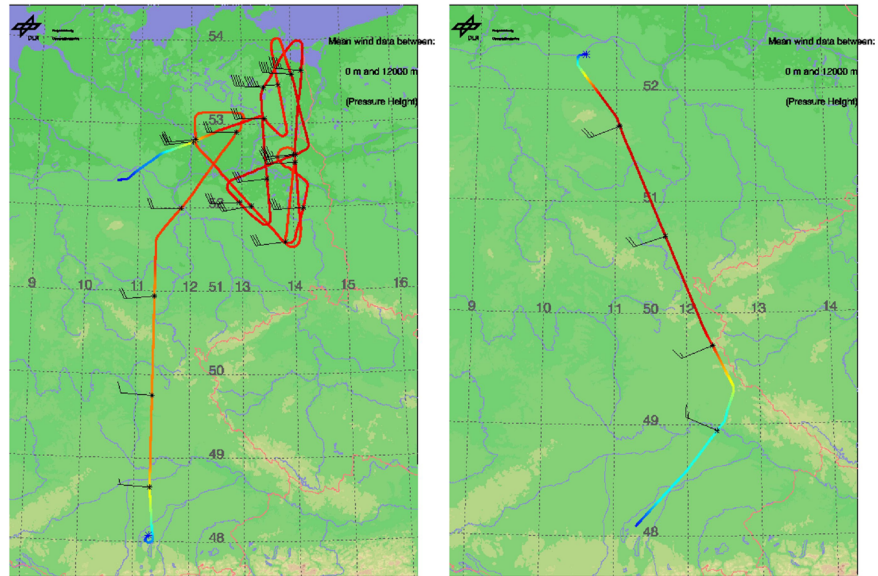


Figure G.1.: Flight route OBF-Braunschweig-OBF (figure credit: DLR Oberpfaffenhofen)

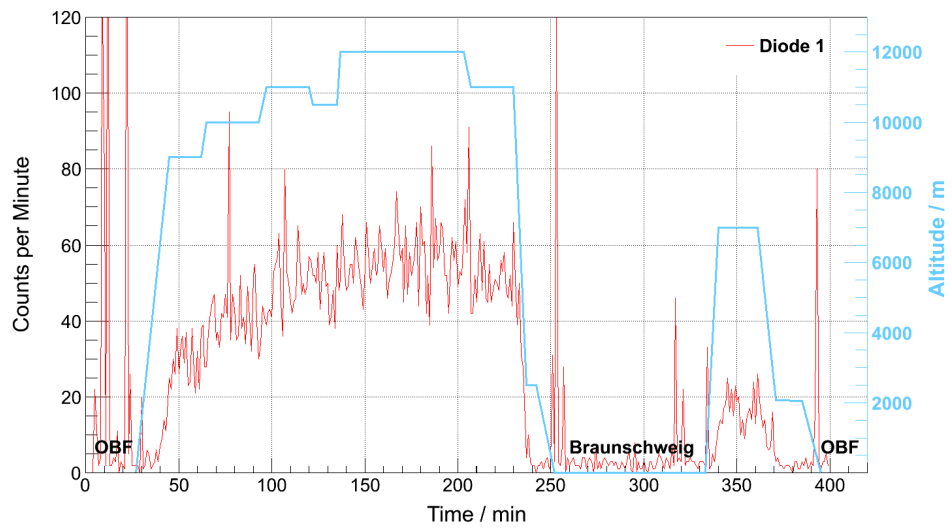


Figure G.2.: Count rates OBF-Braunschweig-OBF

G.2. PERIODIC BEHAVIOUR OF COUNT RATES

The ten minutes averaged count rates in Figures 6.2 and 6.4 of Section 6.2.2 raise the suspicion that a periodic pattern or at least a correlation between the two diodes of one detector is present. In order to investigate this appearance, cross-correlation of count rates from two different diodes should be a suitable tool for possible correlation between the two. Autocorrelation (in principle the cross-correlation of a function with itself) of the count rates can additionally reveal periodic behaviour within the function. The resulting correlation coefficient R of both methods has values between -1 and 1 and shows the relationship strength of the functions for a given time shift. $R=0$ is consistent with no correlation.

For every autocorrelation $R=1$ at the origin, as naturally the function is identical with itself.

In order to show that cross- and autocorrelation are indeed suitable tools to investigate relationship and periodicity of count rates, results of these methods are presented for a parabolic flight in which a recurring variation is expected due to the cyclic change in altitude (Section G.2.1).

Examples of auto- and cross-correlations for count rates recorded during long distance flights (Section 6.2) are shown in Section G.2.2.

G.2.1. COUNT RATES OF PARABOLIC FLIGHT

In the context of field tests the MDT-01-001 and the Liulin were flown on a parabolic flight. These campaigns are organized by the European Space Agency (ESA), the German Aerospace Center (DLR), and the French National Center for Space Studies (CNES) in order to provide a platform for scientific experiments in microgravity.

For a parabolic maneuver (Figure G.3) the aircraft flies with maximum speed and pulls up under an angle of 47° . During this phase, gravity inside the plane almost doubles. The power of the engines is reduced, while the aircraft climbs to the top of an approximate bombtrajectory before the vertical acceleration component turns into a free fall motion. This time period of microgravity lasts for about 22 seconds, before the engines are boosted to counteract the free fall and the flight attitude is stabilized. In this phase gravity increases again to about 1.8 g. Two minutes later the next parabola is started. The total time from the beginning of one parabola to the beginning of the next adds to some three minutes. In this process the flight altitude varies between 6.1 km and 8.5 km.

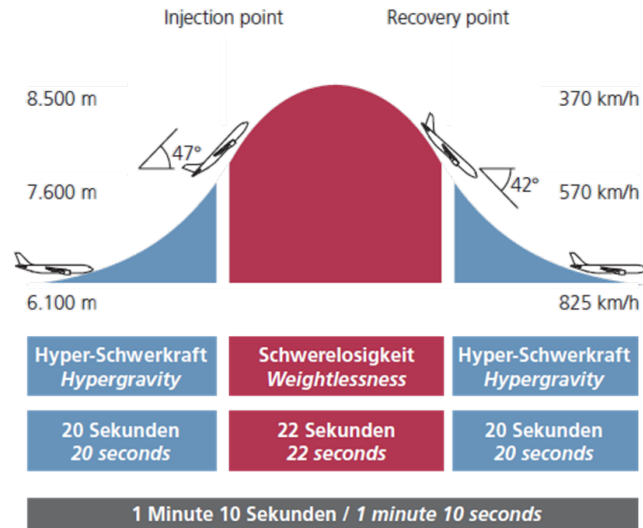


Figure G.3.: Sketch of a parabolic maneuver. The figure is taken from the DLR homepage².

During the flight 33 parabolas in two phases of 17 and 16 parabolas were flown. Figure G.4 shows the count rates of MDT-01-001 in red and of the Liulin in black in a time resolution of one minute. The two time periods in which parabolic maneuvers have been performed are indicated by blue bars. In order to improve statistics, the count rate of the MDT is the sum the two diodes, neglecting the double consideration of the few coincidence events. The detector size of the Liulin is about twice the detector size of one MDT diode. According to the Nyquist-Shannon theorem the time resolution of one minute is sufficient to resolve the three-minute periodicity of the parabolic maneuvers.

At first appearance the count rates do not show a periodic pattern. A slight correlation between the count rates of the two detectors, however, can be assumed (e.g. around minute 140).

Figure G.5 gives the results for the autocorrelation of MDT-01-001 for the first flight period and the cross-correlation between the MDT and the Liulin for the second flight period. Both correlations show a strong periodic pattern with a period of about three minutes, which is the time for an individual parabola. Especially the high values of the correlation coefficient in Figure G.5(b) indicate that this pattern is a real

²http://www.dlr.de/rd/Portaldata/28/Resources/dokumente/rw/Broschuere_Parabelflug_hires.pdf

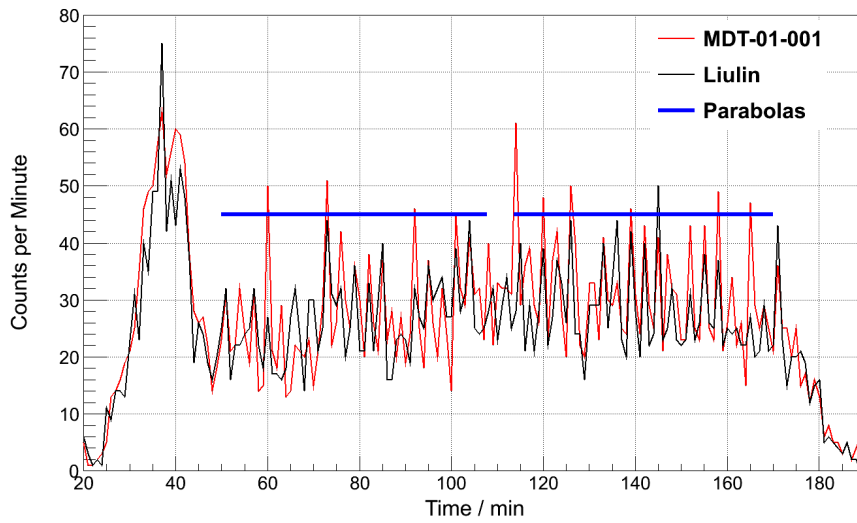
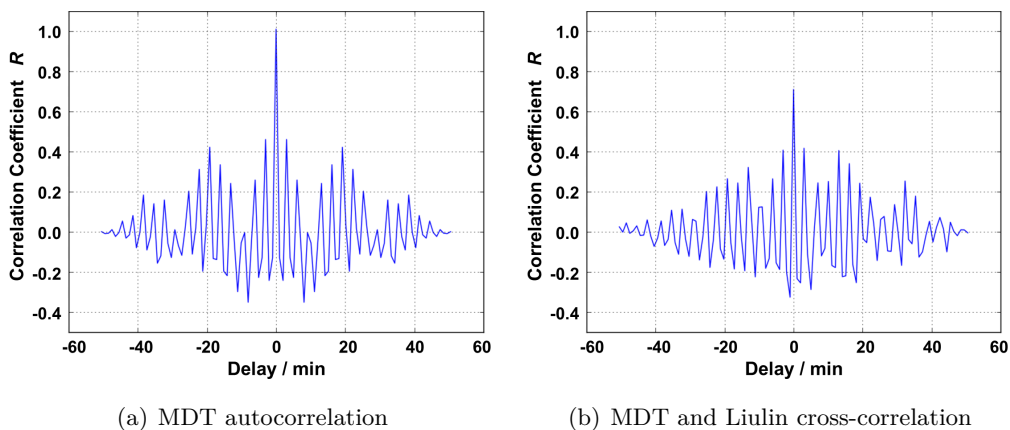


Figure G.4.: Count rates for the parabolic flight for MDT-01-001 and Liulin. The blue bars indicate the time period, in which parabolos have been flown.

feature, as two separate and independent devices measure the same periodicity. The additional harmonic in Figure G.5(a) occurs due to not completely removed general altitude change e.g. around minute 50 that can be seen in Figure G.4.

Fourier analysis of the count rates resulted in a periodicity of 3 minutes and 11 seconds, which is in perfect agreement with the course of the parabolic flight.



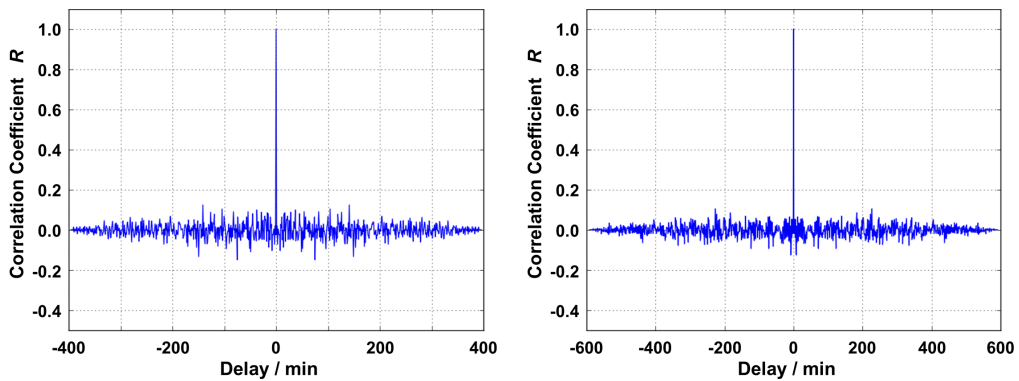
(a) MDT autocorrelation

(b) MDT and Liulin cross-correlation

Figure G.5.: Panel (a) shows the autocorrelation of MDT count rates for the first time period (Figure G.4), in which parabolos have been flown. In panel (b), the cross-correlation for the second time period for the MDT and the Liulin is plotted.

G.2.2. COUNT RATES OF LONG DISTANCE FLIGHTS

Before the correlations for the count rates are calculated, known and expected effects are removed. The count rates are normalized to one flight level by applying the exponential fits presented in Section 6.2.3. The coincidence count rates are subtracted from the single diode data, since the coincidences are an intended correlation. Finally a polynomial fit is computed and subtracted from the count rates to account for geomagnetic cutoff rigidity effects. The residual data is distributed around zero and should be consistent with noise, in case no correlation or periodic pattern is present. The procedure is applied to count rates in the original time resolution of one minute. Hence calculation of the auto- and cross-correlation will reveal all patterns with a time resolution larger than two minutes.

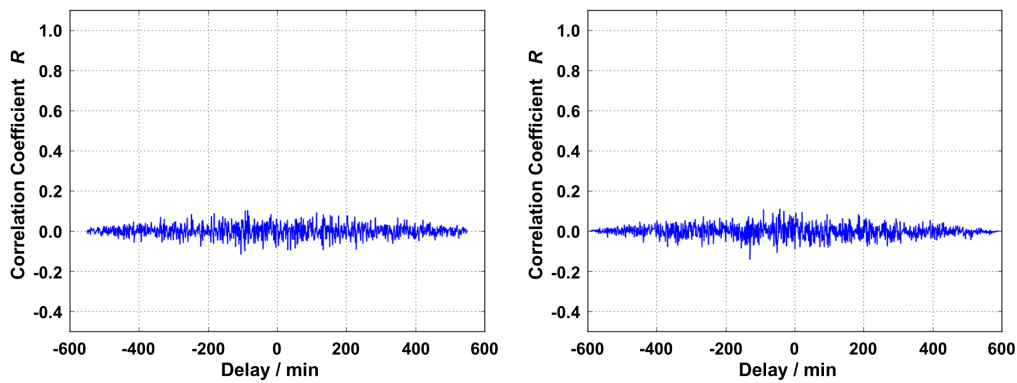


(a) Autocorrelation of count rates diode 2, MDT-01-000, flight A-B 3
 (b) Autocorrelation of count rates diode 1, MDT-01-001, flight B-A 3

Figure G.6.: The autocorrelation of these two examples show that no periodic pattern found in the count rates.

The autocorrelations in Figure G.6 and the cross-correlations in Figure G.7 give examples for individual flights, but are representative for all long duration flights. The autocorrelations show the characteristic spike for R at zero delay and no additional enhancement that would hint to a periodicity. Figure G.7 features no correlation between the two diodes in either of the detector systems.

It has been shown that auto- and cross-correlation are suitable tools to investigate periodic or correlated behaviour in count rates, even at low altitudes. The apparent periodicity and correlation for count rates during normal flights could be excluded.



(a) Cross-correlation of count rates for diode 1 and 2 of MDT-01-000, flight A-B 1

(b) Cross-correlation of count rates for diode 1 and 2 of MDT-01-001, flight B-A 3

Figure G.7.: The cross-correlation of these two examples show that after subtraction of the coincidence counts, no correlation is found between the two diodes of one detector system.

ACKNOWLEDGEMENT

I thank Prof. Dr. Bernd Heber, Dr. Günther Reitz and Dr. Thomas Berger for providing me the opportunity to work on this project within the frame of the Helmholtz Space Life Sciences Research School (SpaceLife) and for the possibility to perform my thesis work in the Radiation Biology Department at the German Aerospace Center in Köln. I am grateful for your strong support during this time.

I appreciate PD Dr. Frank Wissmann for his encouragement and his willingness to be available as a second referee.

I am especially thankful to Dr. Karel Maršálek for being an excellent teacher with endless patience. Without him, probably this work could not have even started.

Moreover, I am particularly indebted to Dr. Thomas Berger for continuous guidance and supervision, and to Dr. Sönke Burmeister for scientific discussions and helpful comments as well as for sharing his beam time at HIMAC.

I acknowledge the Helmholtz Association and the German Aerospace Center for funding in equal parts the SpaceLife program and I would like to convey my gratitude to PD Dr. Christine Hellweg for the excellent organization of this program. As part of SpaceLife I furthermore thank to Prof. Dr. Rupert Gerzer, Anna-Maria Trautmann and my mentor Dr. Christa Baumstark-Kahn.

I appreciate the assistance of Hisashi Kitamura and the HIMAC staff for the excellent organisation of the beam times. The experiments were performed in the frame of the HIMAC Research Project 11H233.

I furthermore thank ...

- ... Dr. Daniel Matthiä and Dr. Nicole Santen for their critical reviews and for fruitful discussions.
- ... Joachim Aeckerlein for providing his mechanical engineering expertise.
- ... Dr. Jan Köhler for his support with simulations and Thomas Möller for valuable arguments.
- ... Dr. Matthias Meier for providing the first flight opportunity.
- ... Dr. Anja Bauermeister for the parabolas.
- ... the Radiation Biology Department and specifically the Biophysics Group for a good working climate.
- ... the Extraterrestrik at Kiel University, who have been welcoming and supportive during my short stays in Kiel.
- ... all SpaceLife students, particularly Dr. Tina Koch and Petra Schwendner, for a great time.

Specifically I thank my dear friend and colleague Alankrita Isha Mrigakshi for the last years we spent together.

I am deeply indebted to my family – my parents, my brothers and especially to Johannes – for continuous support in every respect.

CURRICULUM VITAE

PERSONAL DATA

NAME: **Birgit Ritter**
PLACE OF BIRTH: Duisburg, Germany
DATE OF BIRTH: 13 March 1984
NATIONALITY: German

EDUCATION

SINCE JULY 2009 **Christian-Albrechts-University Kiel**, Kiel, Germany
Institute of Experimental and Applied Physics
Department of Extraterrestrial Physics

German Aerospace Center (DLR), Cologne, Germany
Institute of Aerospace Medicine
Department of Radiation Biology, Biophysics Group

Doctoral Student in the SpaceLife Program
Funded by the Helmholtz Association and DLR
Doctoral Thesis: *The Mobile Dosimetric Telescope*

MAY 2009 **Rheinische Friedrich-Wilhelms-University Bonn**, Bonn,
Germany
Diploma in Physics (very good)
Subjects: Astronomy (major), Nuclear Medicine (minor), Mineralogy (additional)
MAY 2008 – MAY 2009: Diploma Thesis at the
Max-Planck-Institute for Radio Astronomy (MPIfR),
Bonn, Germany
Diploma Thesis: *Radio Interferometry Observations of Maser Sources in High-Mass Star Forming Regions*

JUNE 2003 **Landfermann Gymnasium** (High School), Duisburg, Germany
Abitur / A-Levels (1.4)
Subject: Mathematics, Physics, (Spanish, History)

 ADDITIONAL TRAINING, OCCUPATIONS AND INTERNSHIPS

- AUG. 2011 **ISWI-Europe Summer School in Space Sciences**,
Tatranská Lomnica, Slovakia
Organized by the International Space Weather Initiative (ISWI)
- MAY 2008 – MAY 2009 **MPIfR**, Bonn, Germany
Student Assistant in the Millimeter and Sub-millimeter Astronomy Group
- JAN. 2008 **TIARA Winter School on Exoplanets**, Hsinchu, Taiwan
Organized by the Theoretical Institute for Advanced Research in Astrophysics (TIARA)
- OCT. – DEC. 2007 **University of New South Wales (UNSW)**, Sydney, Australia
Internship in the field of astrobiology in the Department of Astrophysics
- AUG. – SEPT. 2007 **Academia Sinica Institute of Astronomy & Astrophysics (ASIAA)**, Taipei, Taiwan
Internship in the Star Formation Group
- NOV. 2006 – JULY 2007 **MPIfR**, Bonn, Germany
Student Assistant in the Millimeter and Sub-millimeter Astronomy Group
- JUNE – OCT. 2006 **MPIfR**, Bonn, Germany
Student Assistant in Public Relations, speaker for public visitors at the 100 m radio telescope in Effelsberg, Germany

 HONORS AND GRANTS

- JULY 2012 **62th Lindau Nobel Laureate Meeting** dedicated to Physics, Lindau, Germany
Participation as 'Young Researcher'
- 2011 **Amelia Earhart Fellowship**
Award recipient of the annual Fellowship from the Zonta International Foundation to women pursuing doctoral degrees in aerospace related sciences and engineering
- since JULY 2009 **SpaceLife Program**
Recipient of the scholarship for the interdisciplinary PhD program in space life sciences from the Helmholtz Space Life Sciences Research School

AUG. – SEPT. 2007 **Taiwan Summer Institute Program**

Recipient of the scholarship for master students in natural sciences and engineering for a two month internship at a research institute in Taiwan, funded by the German Academic Exchange Service (DAAD) and the National Science Council (NSC, Taiwan)

SEPT. 2001 Second winner in the German finals of the European competition for high school students 'Life in the Universe' (scientific), organized by ESA and others

EIDESSTATTLICHE ERKLÄRUNG

Die vorliegende Abhandlung ist, abgesehen von der Beratung durch die Betreuer, nach Inhalt und Form meine eigene Arbeit.

Sie hat weder ganz noch zum Teil an anderer Stelle im Rahmen eines Prüfungsverfahrens vorgelegen und ist weder ganz noch teilweise veröffentlicht oder zur Veröffentlichung eingereicht worden.

Die Arbeit ist unter Einhaltung der Regeln guter wissenschaftlicher Praxis der Deutschen Forschungsgemeinde entstanden.

Frühere Promotionsversuche wurden von mir nicht vorgenommen.

Kiel, den _____

Birgit Ritter